Excitonic properties of low-dimensional semiconductors

Magnetic field effects and impurity bound excitons

Have, Jonas

Publication date:
2019

Document Version
Publisher's PDF, also known as Version of record

EXCITONIC PROPERTIES OF LOW-DIMENSIONAL SEMICONDUCTORS

MAGNETIC FIELD EFFECTS AND
IMPURITY BOUND EXCITONS

BY
JONAS HAVE

DISSERTATION SUBMITTED 2019

AALBORG UNIVERSITY
DENMARK

Excitonic properties of low-dimensional semiconductors: Magnetic field effects and impurity bound excitons

Ph.D. Dissertation

Jonas Have

Dissertation submitted August, 2019

Dissertation submitted: August, 2019

PhD supervisor: Proffesor Thomas Garm Pedersen
Aalborg University

PhD Co-supervisor: Proffesor Horia Decebal Cornean
Aalborg University

PhD committee: Associate Professor Morten Grud Rasmussen (chair.)
Aalborg University

Associate Professor Christian Flindt
Aalto University

Professor Klaus Mølmer
University of Aarhus

PhD Series: Faculty of Engineering and Science, Aalborg University

Department: Department of Materials and Production

ISSN (online): 2446-1636
ISBN (online): 978-87-7210-480-5

Published by:
Aalborg University Press
Langagervej 2
DK – 9220 Aalborg Ø
Phone: +45 99407140
aauf@forlag.aau.dk
forlag.aau.dk

Printed in Denmark by Rosendahls, 2019

English abstract

This thesis deals with excitonic effects in low-dimensional semiconductors. Excitons are quasi-particles present in semiconductors and insulators. They are generated when an electron from the valence band is excited to the conduction band, usually through photon absorption. This leaves an unoccupied state in the valence band, called a hole. The electron and hole are attracted through Coulomb interactions and can form a bound state with energy below the non-interacting band gap. This bound state is called an exciton. For the usual types of bulk semiconductors, such as III-V semiconductors, the binding energy of excitons is on the order of a few meV. Thus, thermal dissociation occurs at room temperature. In low-dimensional semiconductors the situation is different. The reduced dimensionality and screening result in strongly bound excitons, with binding energies on the order of 0.5-1 eV. Consequently, the optical properties of low-dimensional semiconductors are dominated by excitonic effects. Examples of such low-dimensional semiconductors include, but are not limited to, carbon nanotubes (CNTs), graphene nanoribbons (GRNs), hexagonal boron nitride, and transition metal dichalcogenides (TMDs). To accurately model the optical response of such systems, the inclusion of excitonic effects is necessary. The thesis focuses on modeling two different excitonic systems: Impurity bound excitons and Magnetoexcitons.

The majority of the results in this thesis deals with the theoretical description of magnetoexcitons, which are excitons in a material perturbed by an external magnetic field. The presence of an external magnetic field severely complicates the calculations of excitonic properties. This is, in part, because the translation symmetry of the system is broken by the field. Recently, many experimental studies of magnetoexcitons in both CNTs and TMDs have been conducted and, consequently, the field of magnetoexcitons would benefit from a theoretical study. In the thesis, the magneto-optics of CNTs, GNRs, and TMDs are studied using a tight-binding model to describe the single-particle properties and the Bethe-Salpeter equation to calculate excitonic properties. Additionally, magnetoexcitons in TMDs are also studied using an equation-of-motion approach and the Wannier model. Such quantities as the diagonal optical conductivity, the Hall conductivity, and the diamagnetic shift are com-

puted for the different materials.

The remaining results presented in this thesis deal with impurity bound excitons. When materials are grown or exfoliated they will in practice always contain impurities. In semiconductors, excitons can bind to such impurities through electrostatic Coulomb attraction. This bound state consisting of electron, hole, and impurity is what is denoted an impurity bound exciton. Such phenomena have been observed for several different materials, including TMDs. In this thesis, the existence of impurity bound excitons is studied as a function of the impurity charge. This is done for a very simple one-dimensional toy-model, but using a rigorous mathematical approach. The results show that, for a sufficiently small impurity charge, such a system is stable and a bound state exists. On the other hand, it is also proven that a critical charge exists, such that when the impurity charge is larger than the critical charge no impurity bound excitons exist.

Danish abstract

I denne afhandling behandles exciton effekter i lav-dimensionelle halvledere. Excitoner er kvasi-partikler i halvledere og isolatorer. De genereres når en elektron eksiteres fra et valensbånd til et ledningsbånd. Typisk sker dette ved absorption af en foton. Dette efterlader en ubesat tilstand i valensbåndet, som kaldes for et elektronhul. Elektronhullet og den eksiterede elektron tiltrækkes af hinanden gennem Coulomb kræfter, hvilket resulterer i at der dannes en bundet tilstand med lavere energi end det ikke-interagerende båndgab. Denne bundne tilstand kaldes for en exciton. For de sædvnalige typer af halvledere, som for eksempel III-V halvledere, er excitonens bindings energi af størrelsesorden en til ti meV og termisk dissociation kan derfor forekomme ved stuetemperatur. I lav-dimensionelle halvledere er situationen anderledes. Den reducerede skærmning og dimension giver anledning til stærkt bundne excitoner med en typisk bindingsenergi på mellem 0.5-1 eV. Den høje bindingsenergi resulterer i at de optiske egenskaber af lav-dimensionelle halvledere er domineret af exciton effekter. Eksempler på lav-dimensionelle halvledere inkluderer kulstof nanorør (CNTs), grafen nanoribbons, hexagonal bornitrid, og overgangsmetal dikalkogenider (TMDs). For at kunne modellere de optiske egenskaber af sådanne systemer korrekt er det nødvendigt at inkludere exciton effekter. I denne afhandling fokuseres der på to forskellige exciton systemer: Excitoner bundet til urenheder og excitoner i magnetfelter.

Størstedelen af resultaterne i denne afhandling omhandler den teoretiske beskrivelse excitoner i magnetfelter. Udregningen af excitonernes egenskaber kompliceres af det eksterne magnetfelt. Dette skyldes delvist at translationssymmetrien af systemet brydes af det eksterne felt. I de senere år er mange eksperimentelle studier af magnetoexcitoner i TMDs og CNTs blevet publiceret, og området kunne derfor gavne fra et grundigt teoretisk studie. I denne afhandling, studeres de magneto-optiske egenskaber af CNTs, GNRs og TMds ved hjælp af en tight-binding model, og excitoner inkluderes gennem Bethe-Salpeter ligningen. Derudover studeres magnetoexcitoner i TMDs også både ved hjælp af en tilgang baseret på en bevægelses-ligning samt ved hjælp af Wannier modellen. De opnåede resultater omhandler kvantiteter som den diagonale optiske ledningsevne, Hall ledningsevnen, og det diamagnetiske skift.

De resterende resultater, der er præsenteret i denne afhandling, omhandler excitoner bundet til urenheder. Når virkelige materialer bliver produceret, indeholder de typisk urenheder. For halvledere gælder det at excitoner kan bindes til sådanne urenheder gennem elektrostatisk Coulomb tiltrækning. Denne bundne tilstand bestående af elektron, hul og urenhed er hvad der kaldes en urenheds bundet exciton. Sådanne tilstande er blevet observeret i en række forskellige materialer, eksempelvis TMDs. I denne afhandling studeres eksistensen af urenheds bundne excitoner som funktion af ladningen på urenheden. Det er gjort for en simpel legetøjsmodel, men ved hjælp af stringente matematiske metoder. Resultaterne viser at når ladningen på urenheden er tilstrækkeligt lille, så kan der eksistere urenheds bundne excitoner. På den anden side, det bevises også at en kritisk ladning eksisterer. For den kritiske ladning gælder det, at når urenhedens ladning er større end den kritiske ladning, så eksisterer der ikke længere urenheds bundne excitoner.

Contents

English abstract iii

Danish abstract v

Thesis Details ix

Preface xi

1 Introduction 1
- 1.1 This work . . . 4
  - 1.1.1 Impurity bound excitons . . . 4
  - 1.1.2 Magnetoexcitons in quasi-1D semiconductors . . . 5
  - 1.1.3 Magneto-optics of transition metal dichalcogenides . . . 7

2 Theory and Methods 11
- 2.1 Tight-binding method . . . 12
  - 2.1.1 The Peierls substitution . . . 14
- 2.2 Excitonic effects . . . 16
  - 2.2.1 The Wannier model . . . 19
- 2.3 Optical response . . . 22
  - 2.3.1 Single-particle response . . . 22
  - 2.3.2 Excitonic response . . . 23

3 Summary of results 27
- 3.1 Impurity bound excitons . . . 27
- 3.2 Magnetoexcitons in quasi-1D systems . . . 31
- 3.3 Magneto-optics of transition metal dichalcogenides . . . 36
  - 3.3.1 Equation of motion approach . . . 36
  - 3.3.2 From nanoribbons to 2D response . . . 44

4 Conclusions 49

References 51

Publications **59**

A On the existence of impurity bound excitons in one-dimensional systems with zero range interactions **61**

B Magnetoexcitons and Faraday rotation in single-walled carbon nanotubes and graphene nanoribbons **79**

C Monolayer transition metal dichalcogenides in strong magnetic fields: Validating the Wannier model using a microscopic calculation **89**

D Optical orientation with linearly polarized light in transition metal dichalcogenides **103**

E Excitonic magneto-optics in monolayer transition metal dichalcogenides: From nanoribbons to two-dimensional response **121**

Thesis Details

Thesis title:	Excitonic effects in low-dimensional semiconductors
Ph.D student:	Jonas Have
Supervisor:	Thomas Garm Pedersen
Co-Supervisor:	Horia Decebal Cornean

The main body of this thesis consists of the following papers:

(**A**). **J. Have**, H. Kovařík, T. G. Pedersen, and H. D. Cornean, "On the existence of impurity bound excitons in one-dimensional systems with zero range interactions", J. Math. Phys. **58**, 052106 (2017).

(**B**). **J. Have** and T. G. Pedersen, "Magnetoexcitons and Farday rotation in single-walled carbon nanotubes and graphene nanoribbons", Phys. Rev. B. **97**, 115405 (2018).

(**C**). **J. Have**, G. Catarina, T. G. Pedersen, and N. M. R. Peres, "Monolayer transition metal dichalcogenides in strong magnetic fields", Phys. Rev. B **99**, 035416 (2019).

(**D**). G. Catarina, **J. Have**, J. Fernández-Rossier, and N. M. R. Peres, "Optical orientation with linearly polarized light in transition metal dichalcogenides", Phys. Rev. B **99** 125405 (2019).

(**E**). **J. Have**, N. M. R. Peres and T. G. Pedersen, "Excitonic magneto-optics in monolayer transition metal dichalcogenides: From nanoribbons to two-dimensional response", Phys. Rev. B **100** 045411 (2019).

This thesis has been submitted for assessment in partial fulfillment of the Ph.D degree. The thesis is based on the submitted or published scientific papers which are listed above. Parts of the papers are used directly or indirectly in the summary in the thesis. As part of the assessment, co-author statements have been made available to the assessment committee and are also available at the Faculty.

Preface

The present thesis is the result of the work I have conducted as a PhD student at the Department of Materials and Production and the Department of Mathematical Sciences at Aalborg University, over the period August 2016 to July 2019. My work was funded by the QUSCOPE Center of Excellence and for this, I am very grateful.

First of all, I would like to thank my supervisor Thomas Garm Pedersen for offering me the possibility of doing a PhD under his supervision. Attending his Quantum Mechanics II course in the spring of 2015 was my first real encounter with both Thomas and quantum mechanics, and both have played a large part in my work in the subsequent years. Thomas mathematical reasoning, attention to detail, and passion for physics have been very inspiring and I am certain I will benefit from the time spend under his supervision in my future career. I also owe thanks to Horia Cornean for his co-supervision and, especially, his willingness to share a drink. I would also like to express my gratitude towards Nuno Peres for making my visit at the University of Minho, Braga, both possible and pleasant. I thoroughly enjoyed the time spend working together with Nuno in Portugal and the numerous times we had lunch at the Grill. Finally, all the different PhD students and postdocs working in Thomas group have contributed to a great and ever-changing working environment, and for that, I am very grateful. I will fondly remember the discussions with my office mates Rene Petersen, Morten Rishøj Thomsen, and Enok Skjølstrup.

This section would not be complete without mentioning my family and, in particular, my wife Caroline Have. I am immensely grateful for the support you all have provided me over the years, not just during the past three years. Going from being a potentially poor car mechanic to completing my masters degree and a PhD in physics would not have been possible without your support and patience. Finally, I should thank my 5 months old son Theodor Have for not ruining my sleep too much while I was writing this thesis.

Jonas Have
Aalborg University, August 18, 2019

Chapter 1

Introduction

In this chapter, a brief introduction to the topic of excitons in low-dimensional semiconductors is given. First, the concept of an exciton is explained. Then an overview of the development of exciton theory is provided. In the last part of the chapter, an introduction to the specific systems and topics that are studied in this thesis is provided. These topics include excitons in an external magnetic field, also called magnetoexcitons, and impurity bound excitons. The rest of the thesis is organized as follows: In Chp. 2, the theoretical foundation for the thesis is presented. In Chp. 3, a summary of the results obtained is given. This summary is based on the papers that were written as part of the thesis. In Chp. 4, the conclusions of the study are drawn. Finally, in the last part of the thesis, all papers that were published during the PhD study are provided.

To explain the concept of an exciton, consider a semiconductor or insulator. At low temperature, the valence bands of such a system are completely occupied, while the conduction bands are empty. When light is shined on the material an electron from the valence band can be excited to the conduction band. The excited electron leaves a single unoccupied state in the valence band called a hole. The properties of the hole are similar to those of the electron. However, the charge of the hole has opposite sign compared to the charge of the electron. Due to the opposite sign, the electron and the hole are attracted through Coulomb interactions and can form a bound state. Such an electron-hole pair can be considered a quasi-particle with zero charge. It is exactly this quasi-particle which is called an exciton. The energy of the exciton is below that of the non-interacting band gap, which causes light absorption at photon energies below the band gap energy. The difference between the non-interacting band gap energy and the exciton energy is called the exciton binding energy and is the energy needed for the dissociation of an exciton into a free electron and hole. The generation of an exciton is illustrated in Fig. 1.1 for the two-dimensional (2D) material phosphorene (monolayer black phosphorus).

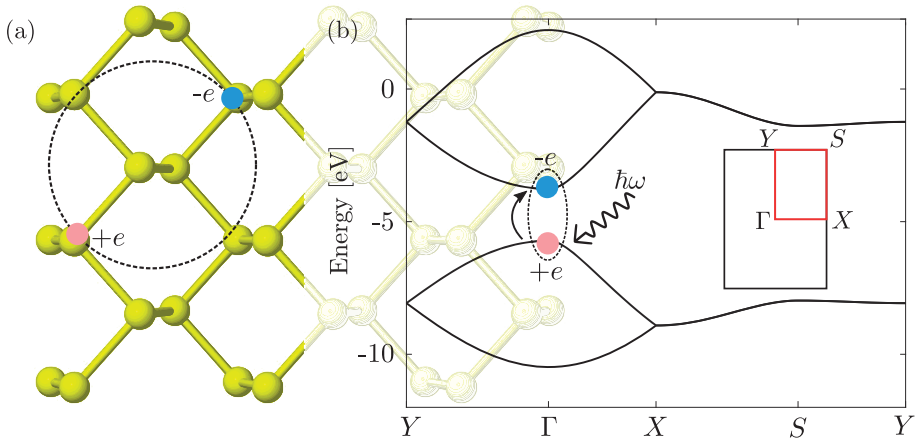

Fig. 1.1: (a) Exciton on the lattice of phosphorene. The blue (red) particle is the electron (hole). (b) Excitation of electron to the conduction band of phosphorene by absorption of photon with energy $\hbar\omega$. The excited electron and the hole in the valence band generate an exciton. The inset illustrates the Brillouin zone of phosphorene.

Phosphorene is not one of the materials considered in the published results, but it will be used in the thesis to illustrate certain aspects relating to excitons.

The concept of excitons was first introduced by Y. I. Frenkel in a series of papers dealing with the transformation of light into heat in solids [1, 2]. In these papers, he studied elementary excitations of the electronic subsystem of a molecular crystal, and in [3] he used the term *excitons* to denote waves of excitation on the crystal lattice without charge transfer. The exciton model proposed by Frenkel, and later together with R. Peierls [4], is suited for describing excitons, which are strongly bound, have a small exciton radius, and are typically located on a single molecule in the crystal. Frenkel's exciton model has been found to accurately describe excitons in organic solids, such as pentacene and naphthalene [5].

Another approach to modelling excitons was proposed by G. H. Wannier and N. F. Mott a few years after Frenkel's work on excitons was published [6, 7]. In the work by Wannier and Mott, the radius of the exciton is assumed to be very large compared to the crystal unit cell. In this setting, they proposed an exciton model in which the effect of the lattice potential was included using the effective mass approximation. This approach leads to an extremely simple and useful exciton model, where the excitons are described as hydrogen-like atoms. The only differences between the Wannier-Mott model and the hydrogen atom are different masses and screening. Adding to the usefulness of the Wannier-Mott model is the simplicity in which the optical response of the excitons can be computed [8]. The model suggested by Wannier and Mott is suited for materials with a large dielectric constant and has been found to be a good

model for excitons in traditional bulk semiconductors such as III-V and II-VI semiconductors [9–11].

The Frenkel and Wannier-Mott exciton models describe two extremes of the same physical phenomenon and are still actively used in condensed matter research today. However, a general unified theory of excitons was made possible by the equation for bound-state problems derived by E. E. Salpeter and H. A. Bethe, the so-called Bethe-Salpeter equation (BSE) [12]. It was later shown that this equation can be applied to describe excitons and that the Wannier-Mott exciton model is a special case of the BSE [13]. This general framework also allowed for calculations of the excitonic optical properties as shown by W. Hanke in [14]. Frenkel's model for excitons can also be expressed as a special case of this more general theory [15]. Modern-day *ab-initio* calculations of excitonic effects are also based on the BSE. The typical approach for *ab-initio* calculations was suggested in [16] and consists of the following steps: (1) The single-particle properties are calculated using density functional theory (DFT). (2) The electronic properties calculated using DFT are self-energy corrected using the GW approximation [17]. (3) The excitonic properties are computed from the GW corrected band structure using the BSE. This approach has been found to provide very accurate estimates of the excitonic properties for a wide number of materials, including conjugated polymers [18], carbon nanotubes (CNTs) [19], phosphorene [20], monolayer transition metal dichalcogenides (TMDs) [21], and various III-V semiconductors [22].

In traditional bulk semiconductors, such as type III-V and II-VI semiconductors, the exciton binding energy is in the range from a few meV to tens of meV [9–11, 22]. Therefore, when doing theoretical modelling of the optical response of such materials, electron-hole interactions only amount to a small correction of the single-particle properties and can typically be ignored. While this holds for the typical bulk semiconducting materials, it is in general not correct for low-dimensional semiconducting materials. Here, low-dimensional materials refer to materials which can be modelled as being finite in one, two, or three directions and infinite in the remaining directions. These types of materials include quantum dots, quantum wires, and atomically thin layers also called monolayers. The reduced dimensionality and screening of such materials cause the excitons to see a significant increase in binding energy [23–25]. For some low-dimensional semiconductors, exciton binding energies up to several eV are found [26–30]. In this case, the inclusion of excitons is no longer just a small correction but a necessity if accurate theoretical predictions of the optical properties are to be expected.

The topic of excitons in low-dimensional systems have grown increasingly important in the past decades, as advancements in methods for synthesis and production of materials have led to the discovery of a wide range of interesting low-dimensional materials. These include both quasi-one-dimensional (quasi-1D) materials, such as carbon nanotubes and graphene nanoribbons, and 2D

materials, such as TMDs. Many of these new materials have shown promising applications in areas such as electronics and optoelectronics [31–38]. However, to use these materials for applications and even to inspire new applications, it is necessary to have a solid understanding of the different excitonic properties of these materials. This includes how excitons are affected by impurities in the material and by external perturbations. The two most important external perturbations are perturbation by an external electric and perturbation by a magnetic field. An external electric field can be used to cause exciton dissociation and to change the optical absorption associated with excitons [39–43]. Similarly, an external magnetic field can be used to probe the physical properties of excitons, such as their spatial extent and mass [44, 45]. In addition, magnetic fields also alter the electronic and optical properties of a material and can cause it to exhibit new optical effects. These includes the emergence of Landau levels (LLs) in the optical-response, the magneto-optical Kerr effect, and Faraday rotation.

1.1 This work

The goal of this thesis is to study the following two aspects of excitons in low-dimensional semiconductor systems: Impurity bound excitons and Magnetoexcitons. In addition to being important from the viewpoint of applications and experimental research, they also pose interesting theoretical problems. For various reasons, the topics studied in the thesis prove difficult to treat using the *ab-initio* approach described above. Instead, other theoretical methods must be used. These include the Wannier-Mott exciton model, also called the Wannier model, and a framework based on a tight-binding description of the single-particle properties coupled with the BSE to compute the excitonic properties. In the following, an introduction to the topics studied is provided.

1.1.1 Impurity bound excitons

The first topic treated in the thesis is impurity bound excitons. In practice, all materials, independent of the method used to produce it contains some impurities and defects. This can be vacancies, adatoms, dopants, and so on. In some cases, an exciton can bind to an impurity, which is the so-called impurity bound exciton. This has been predicted theoretically and confirmed experimentally for a wide range of semiconducting materials [46–52]. The presence of impurity bound excitons will affect both the optical response and the electronic properties of the material. Thus, it is important to have a solid understanding of this type of system if such materials are to be used for optoelectronics and other applications. In the thesis, the existence of impurity bound excitons in a 1D system is studied as a function of the impurity charge. Using a simple

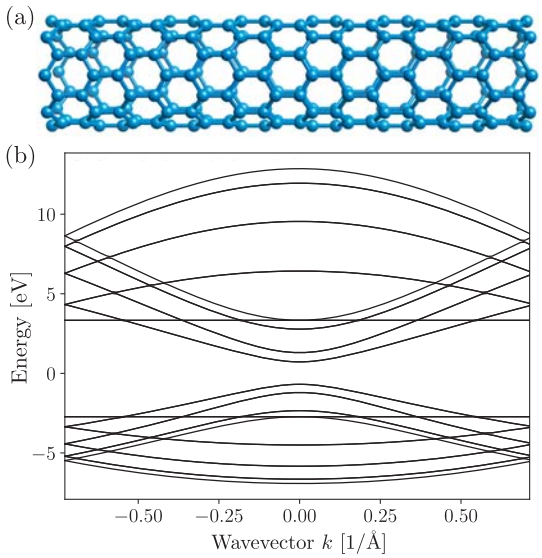

Fig. 1.2: (a) Atomic structure of a zigzag $(8, 0)$ CNT. (b) Electronic band structure of $(8, 0)$ CNT calculated using the tight-binding model in [53].

Wannier model to describe the three-body system of an electron, a hole, and an impurity, the existence of impurity bound excitons will be studied using a rigorous mathematical approach in addition to numerical computations. To do so, the Coulomb interactions will be modelled by Dirac delta functions. This provides a very simple and clear description of impurity bound excitons. Due to the simplicity of the model, the goal is not to describe excitonic properties such as the binding energy or the size of the complex for some given material. Instead, the goal is to provide valuable physical and mathematical insights regarding impurity bound excitons.

In addition to the simple 1D model, the more realistic case of impurity bound excitons in monolayer TMDs is also studied using a Wannier model. In the case of impurity bound excitons in TMDs, the focus is on computing the binding energy and the structure of such a complex. For this, the rigorous mathematical approach must be replaced by numerical computations.

1.1.2 Magnetoexcitons in quasi-1D semiconductors

The next topic treated in the thesis is the effect of excitons on the magneto-optical response of semiconducting carbon nanotubes (CNTs) and graphene nanoribbons (GNRs). CNTs consist of carbon atoms organized in a hexagonal lattice, which is rolled-up into a cylinder. The geometric structure of carbon nanotubes is described by a pair of indices (n, m), which determine the diame-

ter and the helicity of the CNT. The atomic structure and the band structure of CNTs are illustrated in Fig. 1.2. The electronic structure of CNTs is such that some CNTs are semiconducting and others are metallic depending on the diameter and helicity of the CNT [54, 55]. The material was first synthesized in 1991 by S. Iijima [56], and subsequently, several improved manufacturing methods have been developed [57–59]. Due to the exceptional physical properties exhibited by CNTs, the system has been the subject of a large amount of research in the past decades. The interesting physical properties of CNTs include good conductivity, high charge carrier mobility, high surface per mass ratio, and exceptional mechanical properties [55, 60–62]. These properties have inspired the use of CNTs in a wide range of electronic and optoelectronic applications, including electrodes, capacitors, and light-emitting diodes [62, 63]. The optical absorption spectra are also used to evaluate the quality and purity of manufactured CNTs [64]. The excitonic binding energy and the optical response, including excitonic effects, have been studied both theoretically and experimentally. The reduced dimension and screening have been shown to give rise to strongly bound excitons with binding energies on the order of several hundreds of meV [19, 26, 65], which leads to dominant excitonic effects in the optical response [66]. This has been studied in various theoretical frameworks, including the Wannier model and more general *ab-initio* frameworks, and has been verified experimentally [67, 68]. Perturbation by an external magnetic field has been predicted to significantly change the optical response of CNTs. The changes include Ajiki-Ando splitting of the absorption peaks and a Faraday rotation of the polarization of incoming light [69–73]. These interesting magneto-optical phenomena have also been observed experimentally [74–80].

In contrast to CNTs, the amount of research done on the properties of GNRs is more limited. Just as CNTs, GNRs is a carbon-based material and can be considered as thin strips of graphene. For years GNRs were predicted to have interesting edge-dependent electronic and optical properties [81, 82]. However, research into the properties of GNRs was limited to theoretical studies as no actual method for synthesis of the material existed. The rediscovery of graphene by K. S. Nososelov and A. K. Geim in 2004 [83] made it possible to construct GNRs by lithography of graphene [84]. Soon after, methods for chemical production of GNRs were also developed [85, 86]. The geometry and the electronic band structure of an armchair graphene nanoribbon (AGNR) are illustrated in Fig. 1.3. Comparing to the atomic structure and the band structure of CNTs in Fig. 1.2 it becomes apparent that the two materials have many similarities. In practice, GNRs can be regarded as, and even produced from, unrolled CNTs [87, 88]. The electronic properties of GNRs are strongly dependent on the type of edges present on the nanoribbon and the width and, similar to CNTs, can be either metallic or semiconducting [82]. This property provides a method for tuning the electric and optical properties and have inspired the use of GNRs in a range of electronic applications [31, 89]. Just as in

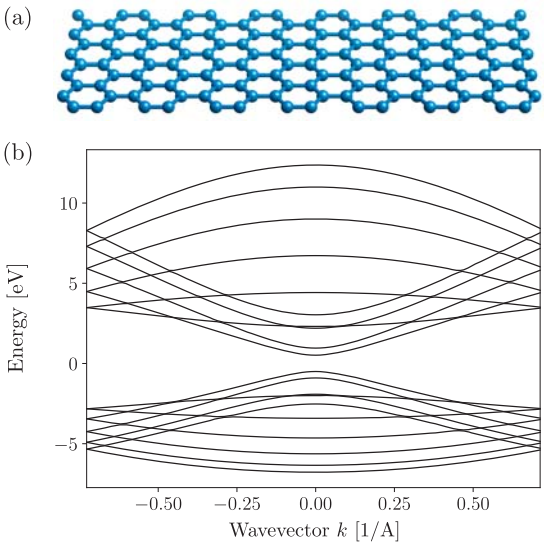

Fig. 1.3: (a) Atomic structure of an armchair GNR. (b) Electronic band structure of a semiconducting armchair GNR with a width of 10 dimer calculated using the tight-binding model in [53].

the case of CNTs, the optical response of GNRs is also dominated by excitonic effects, with exciton binding energies in the range from 0.5 eV to more than 1 eV [27, 90, 91]. The effect of an external magnetic field on the properties of GNRs has also been studied theoretically and has been found to cause changes in both the optical and electronic properties of GNRs [92–94].

The existing theoretical studies of the magneto-optical response of CNTs and AGNRs is either performed in the independent particle approximation, i.e. without excitonic effects, or important magneto-optical properties, such as the Hall conductivity, are disregarded. The Hall conductivity is intimately related with the magneto-optical Kerr effect and the Faraday rotation. In the thesis, the effect of excitons on the magneto-optical response of CNTs and AGNRs is studied using a tight-binding model to describe the single-particle properties of CNTs and AGNRs perturbed by a magnetic field. The excitonic effects are included by using the BSE. The work on magnetoexcitons in quasi-1D materials will also be useful when the related problem of magnetoexcitons in 2D systems is considered later in the thesis.

1.1.3 Magneto-optics of transition metal dichalcogenides

The final topic considered in the thesis is magnetoexcitons and magneto-optics of monolayer TMDs. Monolayer TMDs is one of several different 2D semiconducting materials discovered in the wake of the exfoliation of graphene in 2004.

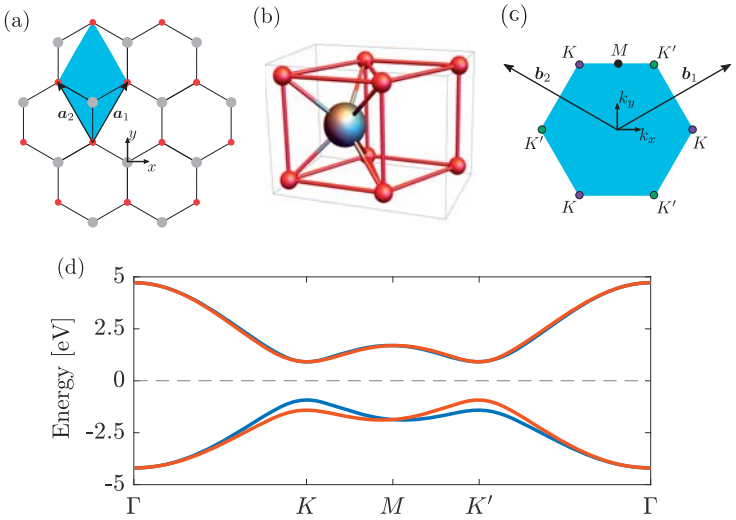

Fig. 1.4: (a) Hexagonal crystal lattice of a monolayer TMD. The red dots and grey dots correspond to transition metal atoms and chalcogen atoms, respectively. The shaded blue area correspond to the primitive unit cell. (b) Structure of the primitive monolayer TMD unit cell. (c) Brillouin zone of monolayer TMDs. (d) Band structure of WSe_2 calculated using the tight-binding model in [95]. The blue and red lines correspond to spin up and down, respectively.

The lack of a band gap in intrinsic graphene limits the use of graphene for transistors and optoelectronics. This led to the search for other 2D materials with similar properties, but with a band gap. Monolayer TMDs became available when atomically thin MoS_2 was successfully exfoliated in 2010 [96]. The unit cell of TMDs consists of a single transition metal atom, typically Mo or W, and two chalcogen atoms, usually S, Se, or Te. While bulk TMDs have an indirect band gap, the band gap transitions from indirect to direct as the number of layers decrease [97]. The crystal lattice, unit cell, and band structure of a monolayer TMD material are illustrated in Fig. 1.4. As illustrated by the band structure in Fig. 1.4, the valence band is spin-split. The conduction bands are also spin-split, although the splitting is much smaller than for the valence bands. This spin-splitting is caused by a strong spin-orbit coupling in TMDs and broken inversion symmetry [98–101]. Another fascinating property of TMDs is the possibility of selectively probing the valleys by using circular polarized light [102, 103]. In line with other low-dimensional semiconducting materials, monolayer TMDs also exhibit rich excitonic effects with exciton binding energies in the range from 0.5 eV to 1 eV [21, 104, 105]. The properties of monolayer TMDs perturbed by an external magnetic field have been the subject of many experimental studies. These studies have shown that monolayer TMDs exhibit interesting magneto-optical properties, such as valley

polarized Landau levels, valley Zeeman splitting, and excitonic diamagnetic shifts [44, 45, 106–115].

In this thesis, magnetoexcitons and the magneto-optical properties of monolayer TMDs will be studied theoretically. While there has been a considerable amount of resources devoted to the experimental study of TMDs perturbed by an external magnetic field, the amount of theoretical work on the subject is limited. Previous theoretical work on magnetoexcitons has been limited to applications of the Wannier model [116]. However, the Wannier model does not provide the correct Landau level structure and cannot be used to compute the Hall conductivities of TMDs. To avoid these issues, a theoretical method that goes beyond the effective mass approximation is needed. But computing the magnetoexcitonic properties in a framework that incorporates the fully periodic 2D structure of the system is difficult computationally. The cause of this difficulty will be explained in detail in the following chapter. In this thesis, two different approaches are used to overcome this. One approach uses a Dirac-type Hamiltonian to describe the single-particle properties and then uses an equation-of-motion approach to compute the properties of the magnetoexcitons. The other approach is based on using a tight-binding description of a monolayer, which is infinite in one direction and finite in the other (basically a nanoribbon geometry). This allows for the computation of the magneto-optical response of TMDs including excitonic effects.

Chapter 2

Theory and Methods

This chapter will serve as an introduction to the theoretical methods and models applied in the published work. In the papers, only the most important details of the theory are provided. To keep the thesis as self-contained as possible an in-depth introduction is provided here. The first section introduces the tight-binding model for calculation of the electronic band structure. Many of the published results deal with the effects of an external magnetic field. Thus, in the first section, it is also explained how to include the effect of an external magnetic field in a tight-binding model. In the next section, the theoretical framework for calculating excitonic properties is introduced. This includes both the Bethe-Salpeter equation and the Wannier model. In the final section, the focus is on the calculation of the optical response functions.

Before delving into the actual models, a few general considerations are made. The materials studied in this thesis consist of a very large number of particles. Thus, a naive approach to describing the properties of such a material would be to first try to solve the time-independent Schrödinger equation $\hat{H}\Psi = E\Psi$, where $\hat{H}$ is the many-body Hamiltonian given by

$$\begin{aligned}\hat{H} = &\sum_n \frac{\hat{\boldsymbol{P}}_n}{2M_n} + \sum_i \frac{\hat{\boldsymbol{p}}_i}{2m_e} + \frac{1}{2}\sum_{n\neq m} Z_n Z_m V(\mathbf{R}_n - \mathbf{R}_m) \\ &- \sum_{n,i} Z_n V(\mathbf{r}_i - \mathbf{R}_n) + \frac{1}{2}\sum_{i\neq j} V(\mathbf{r}_i - \mathbf{r}_j). \end{aligned} \tag{2.1}$$

Here, $\hat{\boldsymbol{P}}_n$, M_n and Z_m are the momentum operator, mass and charge of the n'th nuclei (in units of e), respectively, and n runs over all nuclei. Similarly, $\hat{\boldsymbol{p}}_i$, m_e, and $-e$ are the momentum operator, mass and charge of the i'th electron, respectively, and i runs over all electrons. Finally, V is the Coulomb interaction potential. In an ideal world, the Schrödinger equation for the many-body Hamiltonian can be solved and all properties of the material, including

its geometric structure, its electrical and optical properties, and so on, could be extracted from the solution. Unfortunately, the world is not ideal and such a solution is not feasible mathematically or numerically. Thus, the problem has to be simplified. Applying the Born-Oppenheimer approximation, the problem can be simplified by assuming that the nuclei are in a stationary configuration [117]. Then the terms in Eq. (2.1) related purely to the nuclei simply gives a constant energy shift and, consequently, they can be disregarded. Additionally, the term

$$U(\mathbf{r}_i) = -\sum_n Z_n V(\mathbf{r}_i - \mathbf{R}_n) \tag{2.2}$$

defines a periodic potential for the electrons, with same periodicity as the crystal lattice. This leaves the following expression for the many-body Hamiltonian

$$\hat{H} = \sum_i \left(\frac{\hat{\boldsymbol{p}}_i}{2m_e} + U(\mathbf{r}_i) \right) + \frac{1}{2} \sum_{i \neq j} V(\mathbf{r}_i - \mathbf{r}_j). \tag{2.3}$$

The first term is the sum over single-particle Hamiltonians and the second term defines the electron-electron interaction. In the next section, the tight-binding method for solving the Schrödinger equation for the single-particle Hamiltonian is introduced. Thereafter, electron-electron interactions are included to describe excitonic effects.

2.1 Tight-binding method

The theoretical outset for much of the work presented in this thesis is a tight-binding (TB) model. The TB model is a convenient and relatively simple model for quantum mechanics calculations. It is a semi-empirical model, meaning it is dependent on parameters that need to be determined by fitting to either experimental measurements or first-principles calculations such as density functional theory band structures. When the TB parameters have been determined, the model is computationally inexpensive and is suitable for calculating the electronic band structure and the single-particle wavefunctions of the chosen system. In addition, the presence of an external magnetic field is easily included in a TB model by the use of the Peierls substitution [118], which we will derive in Sec. 2.1.1.

To find the tight-binding bandstructure and wavefunctions, the Schrödinger equation $\hat{H}_0\psi(\mathbf{r}) = E\psi_n(\mathbf{r})$ for the single-particle Hamiltonian $\hat{H}_0$ should be solved. Here, ψ is the wavefunction corresponding to the energy E. The single-particle Hamiltonian is given by

$$\hat{H}_0 = \frac{\mathbf{p}^2}{2m_e} + U(\mathbf{r}). \tag{2.4}$$

Here, $\mathbf{p} = i\hbar\nabla$ is the momentum operator, m_e is the free electron mass, and $U(\mathbf{r})$ is the periodic potential due to the crystal lattice, as defined in Eq. (2.2).

The TB model then relies on the assumption that electrons in solids are localized near the atomic cores. Thus, the wavefunction $\psi(\mathbf{r})$ can be assumed to be a linear combination of atomic orbitals. Writing $\varphi_\alpha(\mathbf{r})$ for the α'th orbital in the unit cell, the TB wavefunction takes the following form

$$\psi(\mathbf{r}) = \sum_{\alpha,\mathbf{R}} C_{\mathbf{R},\alpha}\varphi_\alpha(\mathbf{r}-\mathbf{R}), \tag{2.5}$$

where $\mathbf{R}$ denotes the unit cell location and $C_{\mathbf{R},\alpha}$ are expansion coefficients to be determined. The sum runs over all orbitals in the unit cell and all unit cells. As the system is periodic, Bloch's theorem can be applied to find

$$\psi(\mathbf{r}+\mathbf{R}') = \sum_{\alpha,\mathbf{R}} C_{\mathbf{R},\alpha}\varphi_\alpha(\mathbf{r}-\mathbf{R}+\mathbf{R}') = e^{i\mathbf{k}\cdot\mathbf{R}'}\sum_{\alpha,\mathbf{R}} C_{\mathbf{R},\alpha}\varphi_\alpha(\mathbf{r}-\mathbf{R}). \tag{2.6}$$

The fact that the sum runs over all possible positions of unit cells gives that

$$\sum_{\alpha,\mathbf{R}} C_{\mathbf{R}+\mathbf{R}',\alpha}\varphi_\alpha(\mathbf{r}-\mathbf{R}) = e^{i\mathbf{k}\cdot\mathbf{R}'}\sum_{\alpha,\mathbf{R}} C_{\mathbf{R},\alpha}\varphi_\alpha(\mathbf{r}-\mathbf{R}). \tag{2.7}$$

Thus, $C_{\mathbf{R}+\mathbf{R}',\alpha} = e^{i\mathbf{k}\cdot\mathbf{R}'}C_{\mathbf{R},\alpha}$ or, equivalently, $C_{\mathbf{R},\alpha} = e^{i\mathbf{k}\cdot\mathbf{R}}C_{\mathbf{0},\alpha}$. To ensure normalization of the wavefunction, the expansion coefficients are chosen to be $C_{\mathbf{0},\alpha} = C_\alpha/\sqrt{N}$, where N is the number of unit cells. This gives the following expression for the TB wavefunction

$$\psi(\mathbf{r}) = \frac{1}{\sqrt{N}}\sum_{\alpha,\mathbf{R}} C_\alpha e^{i\mathbf{k}\cdot\mathbf{R}}\varphi_\alpha(\mathbf{r}-\mathbf{R}). \tag{2.8}$$

What remains is to determine the energy and the expansion coefficients. These can be found by solving the time-independent Schrödinger equation, which can be expressed as the generalized matrix eigenvalue problem $H\mathbf{C} = ES\mathbf{C}$. Here, $\mathbf{C}$ is the vector with elements C_α, H is the Hamiltonian matrix, and S the overlap matrix. The Hamiltonian matrix-elements are given by

$$\begin{aligned} H_{\alpha,\beta} &= \frac{1}{N}\sum_{\mathbf{R},\mathbf{R}'} e^{i\mathbf{k}\cdot(\mathbf{R}-\mathbf{R}')}\langle\varphi_\beta(\mathbf{r}-\mathbf{R}')|\hat{H}_0|\varphi_\alpha(\mathbf{r}-\mathbf{R})\rangle \\ &= \sum_{\mathbf{R}} e^{i\mathbf{k}\cdot\mathbf{R}}\langle\varphi_\beta(\mathbf{r})|\hat{H}_0|\varphi_\alpha(\mathbf{r}-\mathbf{R})\rangle, \end{aligned} \tag{2.9}$$

where the fact that the sum runs over all possible unit cells have been used again. Similarly, the overlap matrix-elements are found to be

$$S_{\alpha,\beta} = \sum_{\mathbf{R}} e^{i\mathbf{k}\cdot\mathbf{R}}\langle\varphi_\beta(\mathbf{r})|\varphi_\alpha(\mathbf{r}-\mathbf{R})\rangle. \tag{2.10}$$

The transfer integrals $t_{\alpha\beta\mathbf{R}} \equiv \langle\varphi_\beta(\mathbf{r})|\hat{H}_0|\varphi_\alpha(\mathbf{r}-\mathbf{R})\rangle$ and the overlap integrals $s_{\alpha\beta\mathbf{R}} \equiv \langle\varphi_\beta(\mathbf{r})|\varphi_\alpha(\mathbf{r}-\mathbf{R})\rangle$ are parameters, which should be found by fitting

to experiments or to first-principles calculations. In practice, the sum over unit cells in the Hamiltonian and overlap matrix-elements is truncated. This is based on the assumption that only a finite number of different orbitals have non-zero transfer and overlap integrals. Typically, only the nearest or next-nearest neighbours are included in the model. Also, note that the generalized eigenvalue problem $H\mathbf{C} = ES\mathbf{C}$ is dependent on the wavevector $\mathbf{k}$, and for the full energy dispersion relation it should be solved for all value of $\mathbf{k}$ in the Brillouin zone. In the published results of this thesis, TB models have been used for graphene nanoribbons, carbon nanotubes and transition metal dichalcogenides. In the next subsection, the method for including an external magnetic field is discussed.

2.1.1 The Peierls substitution

The main part of the results presented in this thesis deals with systems perturbed by a magnetic field. An external magnetic field is conveniently included in a TB model via the Peierls substitution, which is a transformation of the transfer and overlap integrals. Due to the importance of the Peierls substitution to the work presented in the thesis, a brief derivation of the substitution will be provided in this section. The derivation in this section follows that in [119].

Starting from the Hamiltonian for an electron in a periodic system in Eq. (2.4), an external magnetic field $\mathbf{B}$ can be included by the minimal coupling substitution $\mathbf{p} \mapsto \mathbf{p} + e\mathbf{A}$, to get

$$\hat{H}_B = \frac{(\mathbf{p} + e\mathbf{A})^2}{2m} + U(\mathbf{r}). \tag{2.11}$$

Here, e is the elementary charge and $\mathbf{A} = \nabla \times \mathbf{B}$ is the magnetic vector potential. For simplicity, the magnetic field is assumed to be static and uniform. The same assumption was used to obtain all results relating to magneto-optics and magnetoexcitons in Sec. 3. The main idea when deriving the Peierls substitution is to transform the basis functions in Eq. (2.8) to

$$\tilde{\varphi}_\alpha(\mathbf{r} - \mathbf{R}) = e^{i\phi(\mathbf{r},\mathbf{R}_\alpha)}\varphi_\alpha(\mathbf{r} - \mathbf{R}), \qquad \phi(\mathbf{r}, \mathbf{R}_\alpha) = -\frac{e}{\hbar}\int_{\mathbf{R}_\alpha}^{\mathbf{r}} \mathbf{A} \cdot d\mathbf{l}. \tag{2.12}$$

Here, $\mathbf{R}_\alpha$ denotes the location of the atomic site belonging to α in the unit cell located at $\mathbf{R}$ and $\phi(\mathbf{r}, \mathbf{R}_\alpha)$ is the Peierls phase. Applying the magnetic Hamiltonian on the transformed basis functions gives

$$\begin{aligned}\hat{H}_B|\tilde{\varphi}_\alpha(\mathbf{r} - \mathbf{R})\rangle &= \left[\frac{(\mathbf{p} + e\mathbf{A})^2}{2m} + U(\mathbf{r})\right] e^{i\phi(\mathbf{r},\mathbf{R}_\alpha)}\varphi_\alpha(\mathbf{r} - \mathbf{R}) \\ &= e^{i\phi(\mathbf{r},\mathbf{R}_\alpha)}\hat{H}_0|\varphi_\alpha(\mathbf{r} - \mathbf{R})\rangle.\end{aligned} \tag{2.13}$$

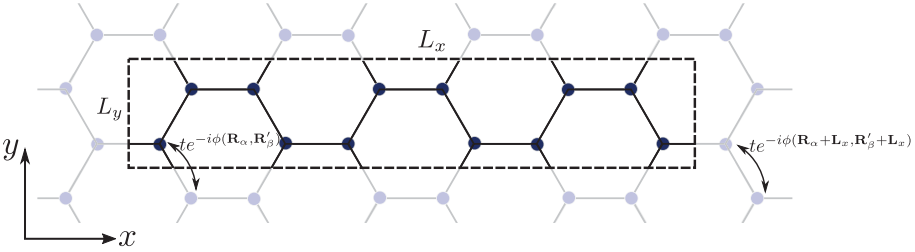

Fig. 2.1: Illustration of the magnetic supercell with length L_x and width L_y. The magnetic vector potential is in the Landau gauge $\mathbf{A} = Bx\hat{y}$.

Then the transfer integral can be found to give

$$\begin{aligned}\langle\tilde{\varphi}_\beta(\mathbf{r}-\mathbf{R}')|\hat{H}_B|\tilde{\varphi}_\alpha(\mathbf{r}-\mathbf{R})\rangle &= \int d\mathbf{r}\; e^{i\phi(\mathbf{r},\mathbf{R}_\alpha)-i\phi(\mathbf{r},\mathbf{R}'_\beta)}\varphi_\alpha(\mathbf{r}-\mathbf{R})\hat{H}_0\varphi_\alpha(\mathbf{r}-\mathbf{R}) \\ &= e^{-i\phi(\mathbf{R}_\alpha,\mathbf{R}'_\beta)}\langle\varphi_\beta(\mathbf{r}-\mathbf{R}')|\hat{H}_0|\varphi_\alpha(\mathbf{r}-\mathbf{R})\rangle.\end{aligned} \tag{2.14}$$

Here, the last equality is found by using

$$\phi(\mathbf{r},\mathbf{R}_\alpha) - \phi(\mathbf{r},\mathbf{R}'_\beta) + \phi(\mathbf{R}'_\beta,\mathbf{R}_\alpha) = 0, \tag{2.15}$$

which holds since the magnetic field is assumed to be static and uniform. A similar expression to Eq. (2.14) is found for the overlap integrals. The expression in Eq. (2.14) shows that the inclusion of a magnetic field in a TB model is done by transforming the transfer and overlap integrals. This is exactly the Peierls substitution.

At first glance, the inclusion of a magnetic field by the Peierls substitution might not seem to complicate the computations of the electronic structure much. However, in general, the additional phase factor in the transfer and overlap integrals breaks the translation symmetry of the Hamiltonian and, consequently, complicates the situation significantly. To see this, consider a system perturbed by a magnetic field in the positive z-direction and with a magnetic vector potential in the Landau gauge $\mathbf{A} = Bx\hat{y}$. Then the Peierls phase is

$$\phi(\mathbf{R}_\alpha,\mathbf{R}'_\beta) \approx -\frac{eB}{2\hbar}(Y'_\beta - Y_\alpha)(X'_\beta + X_\alpha). \tag{2.16}$$

The factor of $(X'_\beta + X_\alpha)$ is the cause of the broken periodicity of the Hamiltonian. If the system is only periodic in a single direction (i.e. quasi-1D systems), the translation symmetry can be retained by orienting the periodic direction of the system with the direction of the magnetic vector potential. Then the situation is no more complicated than for the unperturbed ($B = 0$) system. In contrast, when the system is periodic in more than one direction (i.e. 2D or 3D systems) this possibility no longer exists and another approach is needed. For

such a system, the idea is to introduce a magnetic supercell, which is illustrated in Fig. 2.1. The length of the supercell L_x should be chosen in such a way that the couplings illustrated in Fig. 2.1 obeys the relation

$$\phi(\mathbf{R}_\alpha + \mathbf{L}_x, \mathbf{R}'_\beta + \mathbf{L}_x) = \phi(\mathbf{R}_\alpha, \mathbf{R}'_\beta) + 2\pi, \tag{2.17}$$

where $\mathbf{L}_x = L_x\hat{x}$. Inserting Eq. (2.16) in Eq. (2.17) and isolating for B gives

$$B = 2\pi \frac{\hbar}{eL_x(Y_\alpha - Y'_\beta)}. \tag{2.18}$$

The relation in Eq. (2.18) shows that the magnetic field strength is inversely proportional to the size of the magnetic supercell. Consequently, for experimentally obtainable magnetic fields a very large magnetic supercell is needed. Depending on the material parameters, a magnetic field on the order of 10 T corresponds to a magnetic supercell with many thousand atoms. As each atom corresponds to at least one band in the electronic band structure, the number of bands in a system perturbed by a magnetic field will be huge. These many bands essentially correspond to Landau levels. This is at the core of many of the numerical difficulties related to the treatment of magneto-optics and magnetoexcitons. In the next section, electron-electron interactions are included and the framework for calculating excitonic properties is introduced.

2.2 Excitonic effects

With the single-particle properties described by the tight-binding model in the previous section, it is now time to the include electron-electron interactions, more specifically excitonic effects. First, the Bethe-Salpeter equation (BSE) for an electron-hole pair is derived. The derivation is based on an equation-of-motion (EOM) approach and follows that of [120] and [121]. The outset is the Hamiltonian in Eq. (2.3). However, as excitons are typically generated by absorption of light, a light-matter interaction term is also added to the Hamiltonian. In second-quantization the full Hamiltonian can be expressed as

$$\hat{H} = \hat{H}_0 + \hat{H}_I + \hat{H}_{ee}, \tag{2.19}$$

$$\hat{H}_0 = \sum_k E_k a_k^\dagger a_k, \tag{2.20}$$

$$\hat{H}_I = -\boldsymbol{\mathcal{E}}(t) \cdot \sum_{kl} \mathbf{d}_{kl} a_k^\dagger a_l, \tag{2.21}$$

$$\hat{H}_{ee} = \frac{1}{2} \sum_{klmn} V_{klmn} a_k^\dagger a_l^\dagger a_m a_n. \tag{2.22}$$

Here, the sums run over all single-particle states, E_k is the single-particle energy, $a_i^\dagger$ and a_j are the fermion creation and annihilation operators, respectively,

$\boldsymbol{\mathcal{E}}(t)$ is the electric field, and $\mathbf{d}_{kl}$ is the dipole matrix-elements given by

$$\mathbf{d}_{kl} = -e \int \mathrm{d}\mathbf{r} \psi_k^*(\mathbf{r}) \mathbf{r} \psi_l(\mathbf{r}). \tag{2.23}$$

Here, ψ_k is the single-particle wavefunction corresponding to E_k. Finally, V_{klmn} is given by

$$V_{klmn} = \iint \mathrm{d}\mathbf{r}\mathrm{d}\mathbf{r}' \psi_k^*(\mathbf{r}) \psi_l^*(\mathbf{r}') V(\mathbf{r} - \mathbf{r}') \psi_m(\mathbf{r}') \psi_n(\mathbf{r}), \tag{2.24}$$

where V is the electron-electron interaction potential. For 3D systems, the potential is the usual Coloumb potential. However, for low-dimensional systems the potential should be modified to correctly account for the reduced dimensionality. In quasi-1D systems, an Ohno-type potential has been found to provide accurate predictions of the excitonic properties [122]. Similarly, the Keldysh potential is a suitable a description of Coulomb interactions in monolayers [123, 124]. The Keldysh potential has the following form [123]

$$V(\mathbf{r}) = \frac{\pi}{2r_0} \left[H_0\left(\frac{\kappa|\mathbf{r}|}{r_0}\right) - Y_0\left(\frac{\kappa|\mathbf{r}|}{r_0}\right) \right], \tag{2.25}$$

where r_0 is a material dependent screening length, κ is the average dielectric constant of any potential capping and substrate materials, H_0 is a Struve function, and Y_0 is a Neumann function.

The idea is to try to solve the EOM for the density matrix, which is defined $\rho_{ij} = \langle a_i^\dagger a_j \rangle$. The EOM reads

$$-i\hbar \frac{d}{dt} \rho_{ij} = \left\langle [\hat{H}, \rho_{ij}] \right\rangle. \tag{2.26}$$

The commutator relation on the right-hand side can be computed using the anti-commutator relations for the fermion creation and annihilation operators. Computing the commutators give

$$\begin{aligned} \langle [\hat{H}, \rho_{ij}] \rangle = (E_i - E_j)\rho_{ij} - \boldsymbol{\mathcal{E}}(t) \cdot \sum_l (\mathbf{d}_{li}\rho_{lj} - \mathbf{d}_{jl}\rho_{il}) \\ + \sum_{lmn} \left(V_{lmni} \langle a_l^\dagger a_m^\dagger a_n a_j \rangle - V_{jlmn} \langle a_i^\dagger a_l^\dagger a_m a_n \rangle \right). \end{aligned} \tag{2.27}$$

The next step is to apply the random phase approximation $\langle a_k^\dagger a_l^\dagger a_m a_n \rangle = \rho_{lm}\rho_{kn} - \rho_{km}\rho_{ln}$ and introduce the self-interaction corrected energies

$$\tilde{E}_n = E_n + \sum_l (V_{nlln} - V_{nlnl}) \delta_{l,v}, \tag{2.28}$$

where $\delta_{l,v}$ is one if state k is occupied and zero otherwise. Using the above, the EOM now reads

$$\begin{aligned}-i\hbar\frac{d}{dt}\rho_{ij} =&(E_i - E_j)\rho_{ij} - \boldsymbol{\mathcal{E}}(t)\cdot\sum_l(\mathbf{d}_{li}\rho_{lj} - \mathbf{d}_{jl}\rho_{il})\\ &+\sum_{lmn}(V_{lmni} - V_{mlni})(\rho_{mn} - \delta_{l,i}\delta_{m,n}\delta_{m,v})\rho_{lj}\\ &-\sum_{lmn}(V_{jmnl} - V_{jmln})(\rho_{mn} - \delta_{l,j}\delta_{m,n}\delta_{m,v})\rho_{il}. \end{aligned} \tag{2.29}$$

The first and third electron-electron interaction terms in Eq. (2.29) correspond to exchange terms while the second and fourth terms correspond to direct terms [15]. It is worth noting that in practice the Coulomb interaction in the direct terms is screened by the surrounding electrons, while in the exchange terms it is not. The exchange terms will be neglected in the following.

The rest of the derivation will be restricted to the relevant case where the single-particle states are Bloch states. Then all states are identified by a band index n and a wavevector $\mathbf{k}$. Introducing the bra-ket notation $|n\mathbf{k}\rangle = \psi_{n\mathbf{k}}(\mathbf{r})$, the electron-electron interaction matrix elements in Eq. (2.24) can be rewritten as

$$\begin{aligned}V_{abcd} &= \frac{1}{\Omega}\sum_{\mathbf{q}}\mathcal{V}(\mathbf{q})\langle a\mathbf{k}_a|e^{i\mathbf{q}\cdot\mathbf{r}}|d\mathbf{k}_d\rangle\langle b\mathbf{k}_b|e^{-i\mathbf{q}\cdot\mathbf{r}}|c\mathbf{k}_c\rangle\\ &= \frac{1}{\Omega}\sum_{\mathbf{q}}\mathcal{V}(\mathbf{q})I_{a\mathbf{k}_a,d\mathbf{k}_d}I_{b\mathbf{k}_b,c\mathbf{k}_c}\delta_{\mathbf{k}_d,\mathbf{k}_a-\mathbf{q}}\delta_{\mathbf{k}_c,\mathbf{k}_b+\mathbf{q}}\end{aligned} \tag{2.30}$$

Here, Ω is the system volume, $\mathcal{V}(\mathbf{q})$ is the Fourier transform of $V(\mathbf{r})$, and $I_{m\mathbf{k},n\mathbf{k}'} = \langle m\mathbf{k}|e^{i(\mathbf{k}-\mathbf{k}')\cdot\mathbf{r}}|n\mathbf{k}'\rangle$ are the Bloch overlaps. In addition, the assumption that the density matrix is diagonal with respect to the wave vector is made, i.e. $\rho_{i\mathbf{k}_i,j\mathbf{k}_j} = \rho_{ij\mathbf{k}_i}\delta_{\mathbf{k}_i,\mathbf{k}_j}$. This assumption is based on the fact the dipole approximation allows only vertical transitions. Then the EOM is reduced to

$$\begin{aligned}-i\hbar\frac{d}{dt}\rho_{ij\mathbf{k}} =&\tilde{E}_{ij\mathbf{k}}\rho_{ij\mathbf{k}} - \boldsymbol{\mathcal{E}}(t)\cdot\sum_l(\mathbf{d}_{li\mathbf{k}}\rho_{lj\mathbf{k}} - \mathbf{d}_{jl\mathbf{k}}\rho_{il\mathbf{k}})\\ &-\frac{1}{\Omega}\sum_{lmn\mathbf{k}'}\mathcal{V}(\mathbf{k}'-\mathbf{k})\left[I_{m\mathbf{k}',i\mathbf{k}}I_{l\mathbf{k},n\mathbf{k}'}(\rho_{mn\mathbf{k}'} - \delta_{l,i}\delta_{m,n}\delta_{m,v})\rho_{lj\mathbf{k}}\right.\\ &\left.-I_{j\mathbf{k},n\mathbf{k}'}I_{m\mathbf{k}',l\mathbf{k}}(\rho_{mn\mathbf{k}'} - \delta_{l,j}\delta_{m,n}\delta_{m,v})\rho_{il\mathbf{k}}\right],\end{aligned} \tag{2.31}$$

where $\tilde{E}_{ij\mathbf{k}} = \tilde{E}_{i\mathbf{k}} - \tilde{E}_{j\mathbf{k}}$. The EOM is solved by expanding in orders of the electric field, i.e. $\rho_{ij\mathbf{k}} = \sum_N \rho^{(N)}_{ij\mathbf{k}}$, and solving perturbatively by iteration. The case of interest in this thesis is the first-order equation. Assuming a cold clean semiconductor, the zero'th-order density matrix elements are given by

$\rho^{(0)}_{vv'\mathbf{k}} = \delta_{v,v'}$ and $\rho^{(0)}_{cc'\mathbf{k}} = \rho^{(0)}_{vc\mathbf{k}} = \rho^{(0)}_{cv\mathbf{k}} = 0$. Then, the EOM for $\rho^{(1)}_{cv\mathbf{k}}$ reads

$$-i\hbar\frac{d}{dt}\rho^{(1)}_{cv\mathbf{k}} = \tilde{E}_{cv\mathbf{k}}\rho^{(1)}_{cv\mathbf{k}} - \boldsymbol{\mathcal{E}}(t)\cdot\mathbf{d}_{vc\mathbf{k}} - \frac{1}{\Omega}\sum_{mn\mathbf{k}'}\mathcal{V}(\mathbf{k}'-\mathbf{k})I_{m\mathbf{k}',c\mathbf{k}}I_{v\mathbf{k},n\mathbf{k}'}\rho^{(1)}_{mn\mathbf{k}'}. \tag{2.32}$$

The first order change in band occupation may be assumed to be negligible, i.e. $\rho^{(1)}_{cc'\mathbf{k}}$ and $\rho^{(1)}_{vv'\mathbf{k}}$ can be set to zero. Finally, by applying the Tamm-Dancoff approximation to decouple the resonant and non-resonant part, Eq. (2.32) is simplified to

$$-i\hbar\frac{d}{dt}\rho^{(1)}_{cv\mathbf{k}} = \sum_{c'v'\mathbf{k}'}H_{cv\mathbf{k},c'v'\mathbf{k}'}\rho^{(1)}_{c'v'\mathbf{k}'} - \boldsymbol{\mathcal{E}}(t)\cdot\mathbf{d}_{vc\mathbf{k}}, \tag{2.33}$$

where

$$H_{cv\mathbf{k},c'v'\mathbf{k}'} = \tilde{E}_{cv\mathbf{k}}\delta_{cv\mathbf{k},c'v'\mathbf{k}'} - \frac{1}{\Omega}\sum_{c'v'\mathbf{k}'}\mathcal{V}(\mathbf{k}'-\mathbf{k})I_{c'\mathbf{k}',c\mathbf{k}}I_{v\mathbf{k},v'\mathbf{k}'}. \tag{2.34}$$

The full EOM in Eq. (2.33) will be used to find the optical response with excitonic effects in Sec. 2.3. Finding the solutions to the homogeneous equation, i.e. setting $\boldsymbol{\mathcal{E}}(t) = 0$ in Eq. (2.33), corresponds to solving the eigenvalue problem

$$H_{eh}\Psi_n = E_n\Psi_n, \tag{2.35}$$

where H_{eh} is the matrix with elements given by Eq. (2.34) and Ψ_n is the exciton wavefunction corresponding to the exciton energy E_n. The exciton wavefunction is expressed in a basis of singlet excitations $|v\mathbf{k}\rightarrow c\mathbf{k}\rangle$, i.e. $\Psi_n = \sum_{cv\mathbf{k}}\Psi^{(n)}_{cv\mathbf{k}}|v\mathbf{k}\rightarrow c\mathbf{k}\rangle$. The eigenvalue problem in Eq. (2.35) corresponds to the BSE for the special case of Bloch states.

Note, that the BSE couples pairs of valence and conduction bands at different k-points. Consequently, if the system consists of $N_{v(c)}$ valence (conduction) bands and the Brillouin zone is discretized by N_k points, then the size of the eigenvalue problem is $N_cN_vN_k$. This scaling relation of the problem makes the BSE very computationally demanding to solve for anything more than simple systems. The scaling, combined with the number of bands in a system perturbed by a magnetic field, is at the core of the difficulties related to the computation of excitonic effects on the magneto-optical response of 2D and 3D systems.

2.2.1 The Wannier model

In this section, a brief derivation of the Wannier model will be given. The Wannier model can be expressed as a special case of the BSE and is an extremely

useful model as it provides a clear physical interpretation of the concept of excitons. Besides, the model can easily be generalized to describe magnetoexcitons, trions, or impurity bound excitons.

The derivation of the Wannier model relies on a number of important approximations [15]. The first assumption is that the bands are decoupled, thus, only a single pair of valence and conduction bands are included in the model. Next, the effective mass approximation is applied to write the conduction and valence band energies as

$$\tilde{E}_{c\mathbf{k}} = E_g + \frac{\hbar^2|\mathbf{k}|^2}{2m_e^*}, \quad \tilde{E}_{v\mathbf{k}} = -\frac{\hbar^2|\mathbf{k}|^2}{2m_h^*}, \tag{2.36}$$

where E_g is the band gap energy and $m^*_{e(h)}$ is the electron (hole) effective mass. Finally, the Bloch overlaps are assumed to be diagonal in band-index and independent of $\mathbf{k}$, i.e. $I_{n\mathbf{k},m\mathbf{k}'} = \delta_{n,m}$. Applying these approximations to the BSE in Eq. (2.35), the following equation is found

$$\frac{\hbar^2|\mathbf{k}|^2}{2\mu}\Psi^{(n)}_{cv\mathbf{k}} - \frac{1}{\Omega}\sum_{\mathbf{k}'}\mathcal{V}(\mathbf{k}'-\mathbf{k})\Psi^{(n)}_{cv\mathbf{k}'} = (E_n - E_g)\Psi^{(n)}_{cv\mathbf{k}}, \tag{2.37}$$

where $\mu = 1/(m_e^* + m_h^*)$ is the exciton effective mass. Converting the sum over $\mathbf{k}'$ to an integral and taking the inverse Fourier transform, the following real space differential equation is obtained

$$\left[-\frac{\hbar^2}{2\mu}\nabla^2 - V(\mathbf{r})\right]\Psi^{(n)}(\mathbf{r}) = (E_n - E_g)\Psi^{(n)}(\mathbf{r}), \tag{2.38}$$

where $\mathbf{r}$ is the relative electron-hole coordinate, E_n is the exciton energy shifted by the band gap energy and $\Psi^{(n)}(\mathbf{r})$ is the inverse Fourier transform of $\Psi^{(n)}_{cv\mathbf{k}}$. The differential equation in Eq. (2.38) is the Wannier model for excitons. Upon inspection of Eq. (2.38) it becomes apparent that, in the Wannier model, excitons are mathematically similar to the hydrogen atom. The only difference being the effective mass and the screening of the Coulomb potential. One of the main advantages of the Wannier model is the relative ease in which the model can be generalized to describe more complex systems. In the following, the Wannier model is generalized to include an external magnetic field and to describe three-body systems such as impurity bound excitons. These are the cases of relevance to the work in this thesis.

For the case where the system is perturbed by an external magnetic field, the effect of the field can be included by the minimal coupling substitution $\mathbf{p} \mapsto \mathbf{p} - q\mathbf{A}$, just as in the previous section on the Peierls substitution. However, the Wannier model does not rely on translation symmetry, as the periodic potential due to the atomic nuclei is accounted for in the effective mass. This simplifies the problem of treating magnetoexcitons significantly. The resulting

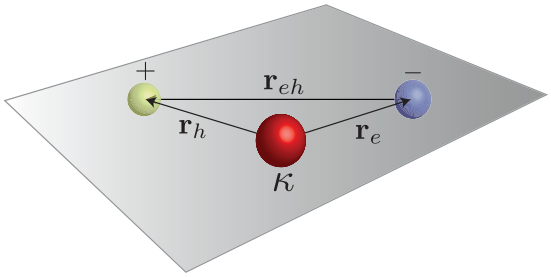

Fig. 2.2: Sketch of a two-dimensional three-body system. The red ball is a particle with charge κ and mass M, the blue ball is an electron, and the yellow ball is a hole. The coordinates $\mathbf{r}_e$ and $\mathbf{r}_h$ are relative to the particle with charge κ. When $M = \infty$ the system corresponds to an impurity localized exciton, and when $M = m^*_{e(h)}$ and $\kappa = \pm e$ it corresponds to either a positively or negatively charged trion.

Schrödinger equation is given by

$$\left[\frac{1}{2m_e^*}(i\hbar\nabla_e + e\mathbf{A})^2 + \frac{1}{2m_h^*}(i\hbar\nabla_h - e\mathbf{A})^2 - V(\mathbf{r})\right]\Psi^{(n)} = E_n\Psi^{(n)}. \quad (2.39)$$

Using the symmetric gauge $\mathbf{A} = \frac{1}{2}\mathbf{B}\times\mathbf{r}$ for the magnetic vector potential, then the Hamiltonian in Eq. (2.39) can be shown to be unitarily equivalent to the following Hamiltonian [125]

$$\hat{H} = -\frac{\hbar^2}{2M}\nabla^2_{\mathbf{R}} - \frac{\hbar^2}{2\mu}\nabla^2_{\mathbf{r}} + \frac{e\hbar}{2\mu}\mathbf{B}\cdot\hat{\boldsymbol{l}} + \frac{e^2}{8\mu}(\mathbf{B}\times\mathbf{r})^2 - V(\mathbf{r}), \quad (2.40)$$

where $M = m_e^* + m_h^*$ and $\mathbf{r}$ and $\mathbf{R}$ are the usual relative and center-of-mass coordinates, respectively. Note, that the relative and the center-of-mass terms in Eq. (2.40) are decoupled. The eigenvalue problem involving $\hat{H}$ can be solved by expanding the exciton wavefunction in a suitable basis and solving it as a matrix eigenvalue problem. This model of magnetoexcitons is very simple and quite useful. However, it also suffers from some shortcomings, which are highlighted in the published results of the thesis, where it is used for comparison with more advanced models.

The Schrödinger equation in Eq. (2.38) can also be generalized to a three-body problem. In this case, the model is capable of modelling both trions and impurity bound excitons. Trions are bound states of either two holes and an electron or two electrons and a hole. Thus, they are related to excitons but have different properties, e.g. they carry charge and have half-integer spin values. The Schrödinger equation for an impurity bound exciton system takes the following form

$$\left[--\frac{\hbar^2}{2m_e^*}\nabla_e^2 - \frac{\hbar^2}{2m_h^*}\nabla_h^2 - V(\mathbf{r}_e - \mathbf{r}_h) - \kappa V(\mathbf{r}_e) + \kappa V(\mathbf{r}_h)\right]\Psi^{(n)} = E_n\Psi^{(n)}, \quad (2.41)$$

where $\mathbf{r}_{e(h)}$ is electron (hole) coordinate relative to the impurity and $\kappa > 0$ is the charge of the impurity. In Eq. (2.41) the impurity has been assumed to have infinite mass. This effectively cancels the kinetic term related to the impurity. The impurity bound exciton system is illustrated in Fig. 2.3. For the case of trions, the third particle would have finite mass and the situation would be slightly more complicated.

2.3 Optical response

In this section, expressions for the linear optical response with and without excitons are derived. In particular, the linear optical conductivity will be determined by solving the EOM derived in Sec. 2.2.

The optical response is determined from the expectation value of the current density $\mathbf{J}(t)$, which can be defined as $\mathbf{J}(t) = \partial\langle\hat{\boldsymbol{P}}(t)\rangle/\partial t$. Here, $\hat{\boldsymbol{P}}(t)$ is the polarization density operator, with expectation value given by

$$\langle\hat{\boldsymbol{P}}(t) = \frac{1}{\Omega}\sum_{cv\mathbf{k}}\left(\mathbf{d}_{cv\mathbf{k}}\rho_{cv\mathbf{k}} + \mathbf{d}_{vc\mathbf{k}}\rho_{vc\mathbf{k}}\right), \tag{2.42}$$

here Ω is either the system volume or area depending on the type of system. Then, up to first-order in the electric field, the current density is given by

$$\mathbf{J}(t) = \frac{1}{\Omega}\sum_{cv\mathbf{k}}\left(\mathbf{d}_{cv\mathbf{k}}\frac{\partial}{\partial t}\rho^{(1)}_{cv\mathbf{k}} + \mathbf{d}_{vc\mathbf{k}}\frac{\partial}{\partial t}\rho^{(1)}_{vc\mathbf{k}}\right), \tag{2.43}$$

The linear optical conductivity tensor elements $\sigma_{ij}(\omega)$ are then defined by the relation

$$J_i(\omega) = \sigma_{ij}(\omega)\mathcal{E}_j(\omega), \tag{2.44}$$

where $i, j \in \{x, y, z\}$, and $J_i(\omega)$ and $\mathcal{E}_j(\omega)$ are elements of the Fourier transform of the current density and the electric field, respectively. Thus, to determine $\sigma_{ij}(\omega)$ the first-order density matrix must be found.

2.3.1 Single-particle response

First, the single-particle optical conductivity is determined. Ignoring the electron-electron interactions in Eq. (2.33), the single-particle EOM for $\rho^{(1)}_{cv\mathbf{k}}$ is

$$-i\hbar\frac{d}{dt}\rho^{(1)}_{cv\mathbf{k}} = E_{cv\mathbf{k}}\rho^{(1)}_{cv\mathbf{k}} - \boldsymbol{\mathcal{E}}(t)\cdot\mathbf{d}_{vc\mathbf{k}}. \tag{2.45}$$

By Fourier transforming from time to frequency domain, isolating for $\rho^{(1)}_{cv\mathbf{k}}$, and transforming back to time domain, the density matrix is found to be

$$\rho^{(1)}_{cv\mathbf{k}} = \frac{1}{2\pi}\int \mathrm{d}\omega e^{-i\omega t}\frac{\boldsymbol{\mathcal{E}}(\omega)\cdot\mathbf{d}_{vc\mathbf{k}}}{E_{cv\mathbf{k}} - \hbar\omega}. \tag{2.46}$$

Inserting this expression in Eq. (2.43) and using the definition of the linear optical conductivity, the tensor elements are found to be

$$\sigma_{ij}(\omega) = -\frac{i\omega}{\Omega}\sum_{cv\mathbf{k}}\left(\frac{d^{(i)}_{cv\mathbf{k}}d^{(j)}_{vc\mathbf{k}}}{E_{cv\mathbf{k}}-\hbar\omega}+\frac{d^{(i)}_{vc\mathbf{k}}d^{(j)}_{cv\mathbf{k}}}{E_{cv\mathbf{k}}+\hbar\omega}\right). \tag{2.47}$$

Here, $d^{(i)}_{cv\mathbf{k}} = -e\langle c\mathbf{k}|x_i|v\mathbf{k}\rangle$ are the dipole-matrix elements in the i direction. Using that dipole- and momentum-matrix elements are related by $-e\hbar p^{(i)}_{cv\mathbf{k}} = im_eE_{cv\mathbf{k}}d^{(i)}_{cv\mathbf{k}}$, the final expression for the optical conductivity is

$$\sigma_{ij}(\omega) = -\frac{ie^2\hbar^2\omega}{m_e^2\Omega}\sum_{cv\mathbf{k}}\left(\frac{p^{(i)}_{cv\mathbf{k}}p^{(j)}_{vc\mathbf{k}}}{E^2_{cv\mathbf{k}}(E_{cv\mathbf{k}}-\hbar\omega)}+\frac{p^{(i)}_{vc\mathbf{k}}p^{(j)}_{cv\mathbf{k}}}{E^2_{cv\mathbf{k}}(E_{cv\mathbf{k}}+\hbar\omega)}\right). \tag{2.48}$$

This expression is used repeatedly to compute the single-particle optical response in the published work of the thesis. It is standard to allow the frequency ω to have a small imaginary part, i.e $\omega \mapsto \omega + i\Gamma$. The imaginary part introduces phenomenological broadening of the spectrum and $\hbar\Gamma$ is typically chosen in the range from a few meV up to 50 meV.

2.3.2 Excitonic response

Turning to the excitonic optical response, the EOM to be solved is exactly the one given in Eq. (2.33). The situation is slightly more complicated than in the case of the single-particle optical response. The solution of the EOM follows that in [120]. As before, the first step is to change from time domain to frequency domain by a Fourier transform. In frequency domain the EOM is

$$\hbar\omega\rho^{(\omega)}_{cv\mathbf{k}} = \sum_{c'v'\mathbf{k}'}H_{cv\mathbf{k},c'v'\mathbf{k}'}\rho^{(\omega)}_{c'v'\mathbf{k}'} - \boldsymbol{\mathcal{E}}(\omega)\cdot\mathbf{d}_{vc\mathbf{k}}, \tag{2.49}$$

where $\rho^{(\omega)}_{cv\mathbf{k}}$ is the Fourier transform of $\rho^{(1)}_{cv\mathbf{k}}$. The exciton Greens function $G^{(\omega)}_{cv\mathbf{k},c'v'\mathbf{k}'}$ in frequency domain is then defined as the solution to

$$-\hbar\omega G^{(\omega)}_{cv\mathbf{k},c'v'\mathbf{k}'} + \sum_{c''v''\mathbf{k}''}H_{cv\mathbf{k},c''v''\mathbf{k}''}G^{(\omega)}_{c''v''\mathbf{k}'',c'v'\mathbf{k}'} = \delta_{cv\mathbf{k},c'v'\mathbf{k}'}. \tag{2.50}$$

In Lehmann representation, the Greens function that solves Eq. (2.50) is given by

$$G^{(\omega)}_{cv\mathbf{k},c'v'\mathbf{k}'} = \sum_n\frac{\Psi^{(n)}_{cv\mathbf{k}}\Psi^{(n)*}_{c'v'\mathbf{k}'}}{E_n-\hbar\omega}, \tag{2.51}$$

where $\Psi^{(n)}_{cv\mathbf{k}}$ are the expansion coefficients of the exciton wavefunction corresponding to E_n and n runs over all exciton states. Applying the Greens function to solve Eq. (2.49) and transforming back to time domain, the density

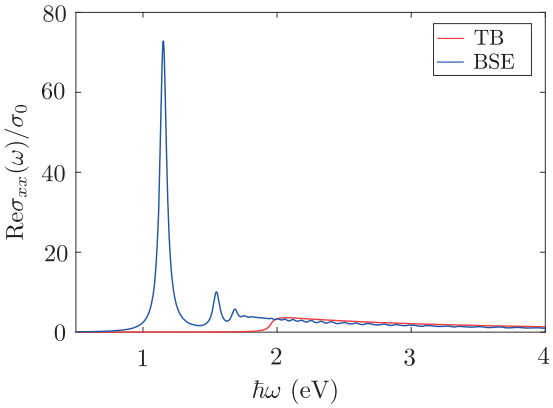

Fig. 2.3: Comparison of optical conductivity with excitons (blue) and without (red) for phosphorene. The spectra are scaled by $\sigma_0 = e^2/4\hbar$. The single-particle properties are described by the TB model of [126]. For the excitonic calculations, the screening parameters in the Keldysh potential were set to $\kappa = 1$ and $r_0 = 23.2$ Å, corresponding to freestanding phosphorene [127].

matrix is given by

$$\rho^{(1)}_{cv\mathbf{k}} = \sum_{n,c'v'\mathbf{k}'} \frac{1}{2\pi} \int \mathrm{d}\omega \frac{\Psi^{(n)}_{cv\mathbf{k}} \Psi^{(n)*}_{c'v'\mathbf{k}'}}{E_n - \hbar\omega} \boldsymbol{\mathcal{E}}(\omega) \cdot \mathbf{d}_{vc\mathbf{k}}. \tag{2.52}$$

By inserting this expression for the density matrix in Eq. (2.43), the optical conductivity tensor with excitonic effects are found to be

$$\sigma_{ij}(\omega) = -\frac{i\omega}{\Omega} \sum_n \left(\frac{D^{(i)}_n D^{(j)*}_n}{E_n - \hbar\omega} + \frac{D^{(i)*}_n D^{(j)}_n}{E_n + \hbar\omega} \right), \tag{2.53}$$

where $D^{(i)}_n = \sum_{cv\mathbf{k}} d^{(i)}_{cv\mathbf{k}} \Psi^{(n)}_{cv\mathbf{k}}$. As in the previous case, the optical conductivity is written in terms of momentum-matrix elements $P^{(i)}_n = \sum_{cv\mathbf{k}} p^{(i)}_{cv\mathbf{k}} \Psi^{(n)}_{cv\mathbf{k}}$. This gives the final expression

$$\sigma_{ij}(\omega) = -\frac{ie^2\hbar^2\omega}{m_e^2\Omega} \sum_n \left(\frac{P^{(i)}_n P^{(j)*}_n}{E^2_n(E_n - \hbar\omega)} + \frac{P^{(i)*}_n P^{(j)}_n}{E^2_n(E_n + \hbar\omega)} \right). \tag{2.54}$$

In Fig. 2.3 the real part of the optical conductivity with and without excitons are shown for phosphorene. The spectra clearly show that the optical response of phosphorene is dominated by excitonic effects. Similar results hold for the materials under consideration in this thesis, as will be seen in Chp. 3.

In some cases, it is only important to know the optical response, and not the actual exciton eigenvalues and eigenvectors. In that case, the Lanczos-Haydock routine can be used to calculate the excitonic optical response without

actually solving the BSE [128]. The Lanczos-Haydock routine is based on a tri-diagonalization of the Hamiltonian matrix. By using the tri-diagonal Hamiltonian, matrix elements of the exciton Green's function can be evaluated by a continued fraction. This process, however, can be truncated when the spectrum is converged. In this manner, the computational complexity can be reduced significantly. In some of the published papers, this approach is used to compute the magneto-optical response.

This concludes the introduction to the theoretical framework used to obtain the results presented in this thesis. A few other models and theoretical approaches are used in the publications, but the theory presented in this chapter is the foundation for most of the work. In the next chapter, a summary of the published results obtained using the models is given.

Chapter 3

Summary of results

This chapter contains a summary of selected results from the published papers. The first section contains a summary of the results related to the existence of impurity bound excitons obtained in paper A and a few previously unpublished results. The next section consists of the results obtained relating to magnetoexcitons and Faraday rotation in quasi-1D systems, including carbon nanotubes and graphene nanoribbons. These results were published in paper B. Finally, in the last section results about magneto-optics in transition metal dichalcogenides are presented. The results present in that section are from papers C, D, and E. Only a selection of details and results are presented here. For a complete and in-depth presentation, the reader is referred to the papers.

3.1 Impurity bound excitons

In paper A, impurity bound excitons in a one-dimensional system are considered. Such a system is modelled by the Wannier model discussed in Sec. 2.2.1. The model Hamiltonian used in paper A is given by

$$H_{\kappa,\sigma} = -\frac{1}{2}\Delta - \sigma\frac{\partial^2}{\partial x \partial y} - \delta(x-y) + \kappa\delta(x) - \kappa\delta(y), \tag{3.1}$$

where $\Delta = \nabla^2$, κ is the charge of the impurity, and $\sigma = m/(M+m)$. Here, M is the mass of the impurity and m is the effective mass of the electron and hole. Impurity bound excitons correspond to discrete eigenvalues of the operator $H_{\kappa,\sigma}$ and, consequently, the paper deals with the existence of such discrete eigenvalues. The two extremes where κ is either sufficiently small or large is studied using a rigorous mathematical approach based on spectral theory for unbounded operators. The validity of the system studied in this paper could be questioned. Obviously zero range interactions modelled by delta distributions are unphysical and one-dimensional systems are not the most

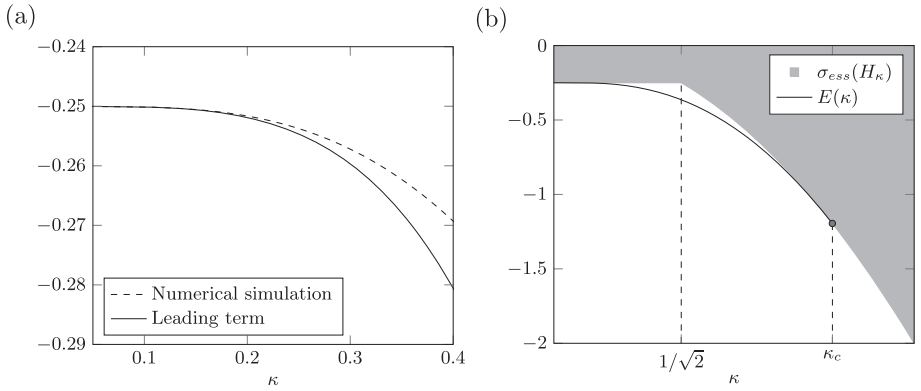

Fig. 3.1: (a) Comparison between the leading term derived in the paper and numerical simulation of the ground state. (b) Illustration of the evolution of the spectrum of the operator $H_{\kappa,0}$ as a function of κ. (From [130])

interesting systems. However, due to the simplicity of such models, they can provide valuable physical insight. This is usually illustrated by the similarities between the one-dimensional hydrogen atom with delta interactions and the true three-dimensional hydrogen atom [129]. Similarly, one of the goals of paper A is to provide physical insights that could prove useful when dealing with impurity bound excitons in more realistic systems.

The two main results obtained in paper A are summarized in Theorem II.1. and Corollary II.3 and are stated for the case where $\sigma = 0$, i.e. where the impurity has infinite mass. Theorem II.1. deals with the case where κ is small. The theorem gives that for $\kappa > 0$ sufficiently small, then the operator $H_{\kappa,0}$ has exactly one discrete eigenvalue. In other words, for κ sufficiently small there exists a single state corresponding to an impurity bound exciton in the system. The leading term of the energy is found to be

$$E(\kappa) = -\frac{1}{4} - 16\left(\frac{4}{\pi} - 1\right)^2 \kappa^4 + \mathcal{O}(\kappa^5). \tag{3.2}$$

In Fig. 3.1 (a), this leading term is compared to a numerical simulation of the ground state energy. This comparison shows that the leading term is an accurate approximation of the energy up to $\kappa \approx 0.2$. The ground state is also found to be non-degenerate and decreasing if $\kappa \in (0, 1/\sqrt{2}]$. This corresponds to what was observed using numerical simulations.

Corollary II.3. deals with the other extreme, i.e. where κ is sufficiently large. The corollary gives the existence of a critical value κ_c, such that the operator $H_{\kappa,0}$ has no discrete eigenvalues for all $\kappa \geq \kappa_c$. This situation is illustrated in Fig. 3.1 (b), where the evolution of the spectrum of the spectrum is shown as a function of κ. The figure shows that, at some value critical value

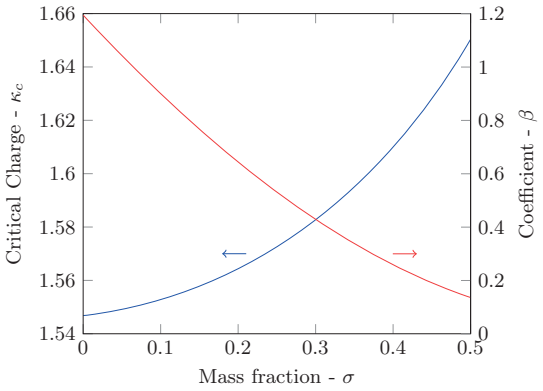

Fig. 3.2: Critical charge κ_c and leading coefficient β as functions of the mass fraction σ. The two extremes $\sigma = 0$ and $\sigma = 0.5$ correspond to an impurity with infinite mass and with mass equal to the effective mass of the other particles, respectively. (From [130])

of κ the discrete eigenvalue disappears in the essential spectrum. Numerical simulations indicate that the true critical value is approximately $\kappa_c \approx 1.546$.

The results are also generalized to the case where $\sigma > 0$, i.e. where the impurity has finite mass. Then, for the case of κ small, the energy of the ground state is equal to

$$E(\kappa) = -\frac{1}{4(1-\sigma)} - \beta(\sigma)\kappa^4 + \mathcal{O}(\kappa^5), \tag{3.3}$$

where the coefficient is

$$\beta(\sigma) := \frac{4\left[6\sigma\sqrt{1-\sigma^2} - (2-\sigma)\sigma\pi - 8\sigma^2\cos^{-1}\left(\frac{\sqrt{1+\sigma}}{\sqrt{2}}\right) + \tan^{-1}\left(\frac{2\sigma(1-\sigma^2)}{1-2\sigma^2}\right)\right]^2}{(1+\sigma)(1-\sigma)^2\pi^2\sigma^2}. \tag{3.4}$$

The coefficient as a function of σ is shown in Fig. 3.2. In the case of κ large, the critical charge κ_c also exhibits dependence on the mass fraction σ. The dependence is found by numerical simulations and is plotted in Fig. 3.1.

The results regarding the existence of a critical charge of the impurity, for which no impurity bound excitons exists, can also be generalized to more complex systems. In the following, the results are generalized to impurity bound excitons in monolayer transition metal dichalcogenides. These results are unpublished. Such a system can be described by the Hamiltonian $\hat{H}$ given in Eq. (2.41), where $\mathbf{r}_e$ and $\mathbf{r}_h$ are taken to be 2D vectors. In a strict 2D system the usual Coulomb potential is replaced by the Keldysh potential. The discrete eigenvalues are then determined by solving $H\Psi(\mathbf{r}_e, \mathbf{r}_h) = E\Psi(\mathbf{r}_e, \mathbf{r}_h)$. The results presented here were obtained by expanding the wavefunction $\Psi(\mathbf{r}_e, \mathbf{r}_h)$ in a basis of the type

$$\phi_{ijk}(\mathbf{r}_e, \mathbf{r}_h) = \exp(-a_i\mathbf{r}_e^2 - b_j\mathbf{r}_h^2 - c_k(\mathbf{r}_e - \mathbf{r}_h)^2). \tag{3.5}$$

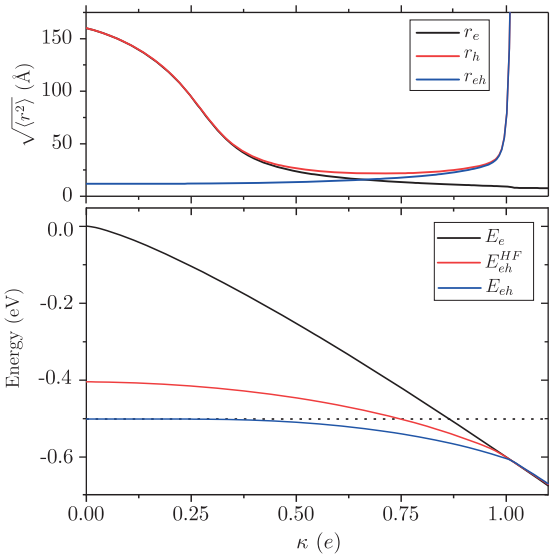

Fig. 3.3: Energies and structure of impurity bound excitons in WSe_2. The top panel shows the root-mean-square of the coordinates for the electron (black), the hole (red), and the electron-hole (blue). The bottom panel shows energies. Here, the black line denotes the energy of the electron-impurity subsystem and the dashed line is the exciton energy. Additionally, the blue and red lines show the ground state energy of the impurity bound exciton calculated with the correlated basis and in the Hartree-Fock approximation, respectively.

The problem can also be solved by Hartree-Fock with a similar type of basis, but in that case there is no correlation in the basis, i.e. $c_k = 0$ for all k.

In the bottom panel of Fig. 3.3, the ground state energy of the impurity localized exciton in free-standing WSe_2 is shown. The energy is calculated using both the correlated basis in Eq. (3.5) and the Hartree-Fock method. The effective masses and the r_0 parameters calculated in [131] are used. Comparing the energies calculated with the correlated basis and the Hartree-Fock method it is apparent that the electron-hole correlation is very important, and that the Hartree-Fock method is not suitable for this type of problem. The critical charge is found by determining the κ value where the energies of the impurity localized exciton and the electron-impurity subsystem crosses, indicated by the crossing of the blue and black lines in Fig. 3.3. The calculations show that $\kappa_c \approx 1.02$ and that the binding energy for an impurity with $\kappa = 1.00$ is approximately 5 meV, which is on the same order as binding energies found in experimental measurements [132]. In the top panel of Fig. 3.3, the root-mean-square (RMS) of the coordinates $\mathbf{r}_e$, $\mathbf{r}_h$, and $\mathbf{r}_{eh}$ is shown as a function of κ. Recall that $\mathbf{r}_{e(h)}$ denotes the position of the electron (hole) relative to the impurity. Initially, the electron-hole system is strongly bound with a RMS of 11.8 Å. Meanwhile, the electron and hole are weakly localized by the impurity. As the charge of

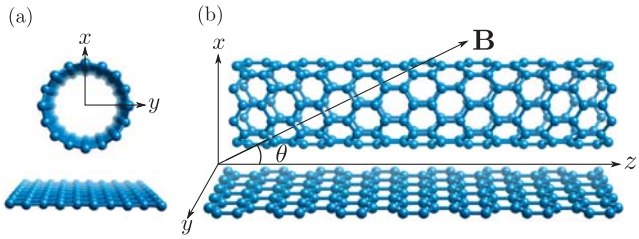

Fig. 3.4: Geometry of CNTs and AGNRs. (a) The structure as seen in the direction of the z-axis. (b) Side view of the structures. The AGNR is in the yz-plane. An external magnetic field at an angle θ to the yz-plane is included. (From [53])

the impurity increases, the electron becomes increasingly localized near the impurity while the hole becomes more delocalized. When the charge of the impurity exceeds the critical charge, the hole is completely delocalized and the electron is strongly localized near the impurity with an RMS of 7.6 Å. This illustrates the structure of impurity localized excitons.

3.2 Magnetoexcitons in quasi-1D systems

In paper B, different aspects of excitonic effects on the magneto-optical response of single-walled carbon nanotubes (CNTs) and armchair graphene nanoribbons (AGNRs) were studied. The study of magneto-optics in quasi-1D systems is interesting for several reasons. First, there are a number of interesting experimental studies of the magneto-optical response of CNTs performed in extremely high magnetic fields (up to 370 T) [75–80]. This allows for experimental observation of interesting physical phenomena, such as the exciton peak splittings caused by brightening of dark exciton states. This splitting is called the Ajiki-Ando splitting. These strong magnetic field measurements also provide the means for verification of theoretical methods. Secondly, some magneto-optical properties of CNTs and AGNRs have previously only been studied in the independent particle approximation and, consequently, lack a theoretical treatment where excitonic effects are included. This includes the Hall conductivities and Faraday rotation. Finally, the study of magnetoexcitons and magneto-optics in CNTs and AGNRs is of interest since the 1D nature of the systems makes the numerical computations less expensive. Consequently, the systems are useful test systems for theoretical methods. This also inspired the use of nanoribbons as a theoretical tool to describe the response of monolayer transition metal dichalcogenides in paper E, as will be discussed in Sec. 3.3.

The geometry of the systems studied in paper B is illustrated in Fig. 3.4. The geometric structure of CNTs is governed by the indices (n, m), which determine the diameter of the tube and the helicity. For AGNRs, the notation N-AGNR is used to denote to describe a specific AGNR with N dimer lines

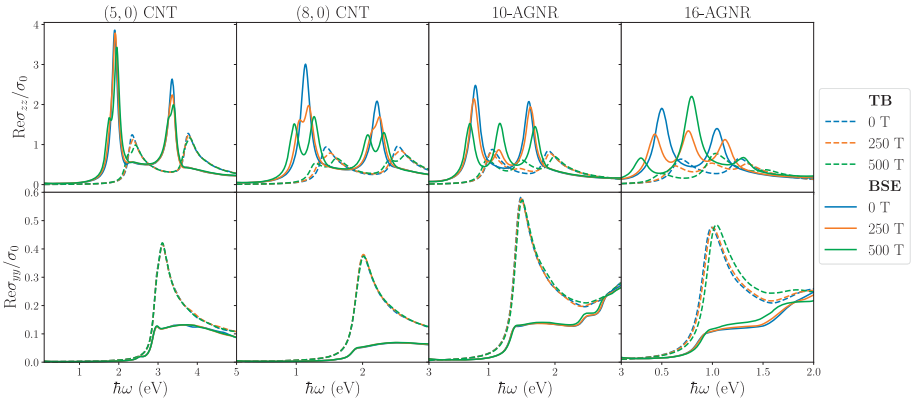

Fig. 3.5: Real part of the optical conductivity tensor. The top and bottom rows show the parallel-polarized and cross-polarized absorption, respectively, of selected CNTs and AGNRs at different magnetic field strengths. The dashed lines correspond to the single-particle response and the solid lines correspond to excitonic response. (From [53])

in the unit cell. The single-particle properties of both materials are described by a non-orthogonal nearest-neighbor tight-binding model. The magnetic field is introduced using the Peierls substitution as described in Sec. 2.1.1 and the excitonic effects are calculated using the BSE. In contrast to the derivation in Sec. 2.2, here the exchange term is included in the BSE, as this is important to obtain the correct ordering of bright and dark exciton states. The optical response of both CNTs and AGNRs is calculated using the Lanczos-Haydock routine mentioned in Sec. 2.3.

In Fig. 3.5, the diagonal optical conductivities of both CNTs and AGNRs are shown for a number of different CNTs, AGNRs, and magnetic fields. Both results with (solid lines) and without excitons (dashed lines) are shown. By inspection of the figure, it is evident that the effect of even very strong magnetic fields on the cross-polarized absorption (Reσ_{yy}) of CNTs and AGNRs is negligible. In contrast, strong magnetic fields significantly alter the parallel-polarized absorption (Reσ_{zz}) of both CNTs and AGNRs. For CNTs both the single-particle and excitonic response exhibit a splitting of the absorption peaks. In the unperturbed case, the valence and conduction bands of CNTs are two-fold degenerate. The degeneracy of the bands is lifted by the magnetic field, and this is exactly the cause of the splitting of the absorption peaks in the single-particle spectra. The size of the split is dependent on the CNT diameter and, as apparent from Fig. 3.5, increases as the nanotube diameter increases. For the excitonic response, the cause of the splitting is more complicated. The inclusion of electron-electron interactions lifts the degeneracy partially and causes three different exciton states. As shown in paper B, only one of these states is optically active at zero field but, as the magnetic field strength is increased, another

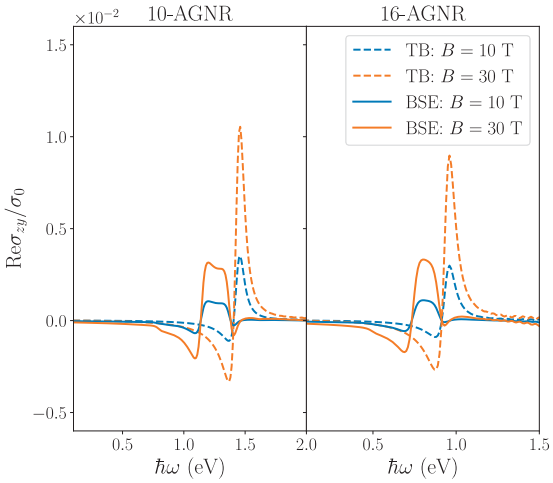

Fig. 3.6: Hall conductivity for 10-AGNR and 16-AGNR at 10 T and 30 T. Both the single-particle response (dashed lines) and the excitonic response (solid lines) are shown. (From [53])

state, which was previously dark, becomes optically active. This is what is observed as splitting of the absorption peaks in the excitonic response of CNTs. The splitting observed in paper B is consistent with the splitting observed in other theoretical studies [70, 71] and in experimental measurements [77–80]. The inclusion of electron-hole interactions also causes a significant decrease in the cross-polarized absorption. This has been shown to be due to strong depolarization effects [72]. Turning to the parallel-polarized absorption of the AGNRs, the spectra exhibit no splitting of the absorption peaks but instead show the emergence of a new absorption. This effect is also dependent on the width of the nanoribbon, for wider nanoribbons the effect increases.

While the effect of an external magnetic field on the diagonal optical conductivities is only observable at very large magnetic fields, the situation is completely different for the off-diagonal conductivities. The off-diagonal conductivities, also called the Hall conductivities, of CNTs and AGNRs, are identically zero when there is no magnetic field. By perturbing with an external magnetic field, the systems obtain finite Hall conductivities. These, in turn, causes the material to exhibit Faraday rotation of the polarization state of incoming light. In Fig. 3.6, the Hall conductivities with and without excitonic effects of both 10-AGNR and 16-AGNR are shown. The spectra clearly show the importance of including excitons when modelling the optical response, since excitonic effects significantly change the Hall conductivities. Additionally, the spectra in Fig. 3.6 also reveal that the Hall conductivities scale linearly with magnetic field strength. It is also clear that this scaling behavior holds for quite strong magnetic fields. This important relation makes it possible to extrapolate the Hall conductivity spectra presented here to various magnetic field strengths.

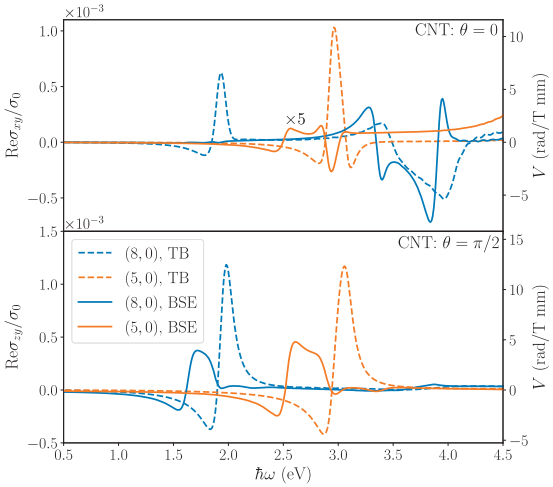

Fig. 3.7: Hall conductivity for $(5,0)$ and $(8,0)$ CNTs in both a parallel and a perpendicular magnetic field. The right y-axis shows the Verdet constant. The dashed lines are the single-particle response and the solid lines are the excitonic response. (From [53])

In Fig. 3.7, the Hall conductivities of CNTs in a perpendicular ($\theta = \pi/2$) and a parallel ($\theta = 0$) magnetic field are shown. The plots again underline the fact that when excitonic effects are included in the calculations the optical response changes drastically. Just as in the case of AGNRs, the magnitude of the excitonic response is smaller than the single-particle response. This in contrast to what is observed for the parallel-polarized absorption where the excitonic response had a larger magnitude than the single-particle response. The explanation for this is found in the strong depolarization effects in the y-direction. As mentioned previously, the finite Hall conductivities of AGNRs and CNTs in a magnetic field causes the system to exhibit Faraday rotation. The Faraday rotation angle ϕ for a weak magnetic field in the z-direction can be computed from

$$\phi = \frac{l}{2c\varepsilon_0} \frac{n\mathrm{Re}\sigma_{xy} - \kappa\mathrm{Im}\sigma_{xy}}{n^2 + \kappa^2}\rho. \tag{3.6}$$

Here, l is the propagation length of the light, c is the speed of light, ε_0 is the vacuum permittivity, $n + i\kappa$ is the complex refractive index (at $B = 0$), and ρ is a volume fraction of either AGNRs or CNTs. Due to the linear scaling of the Hall conductivities with magnetic field, the Faraday rotation angle can be written as $\phi = VlB\rho$, where V is the so-called Verdet constant. The Verdet constant for CNTs in an aqueous solution is also shown in Fig. 3.7.

The final results obtained in paper B relate to the low magnetic field properties of excitons. When the magnetic field is sufficiently weak, the shift in exciton binding energy due to the magnetic field goes like B^2, where B is the magnetic field strength. This quadratic shift in exciton binding energy is called

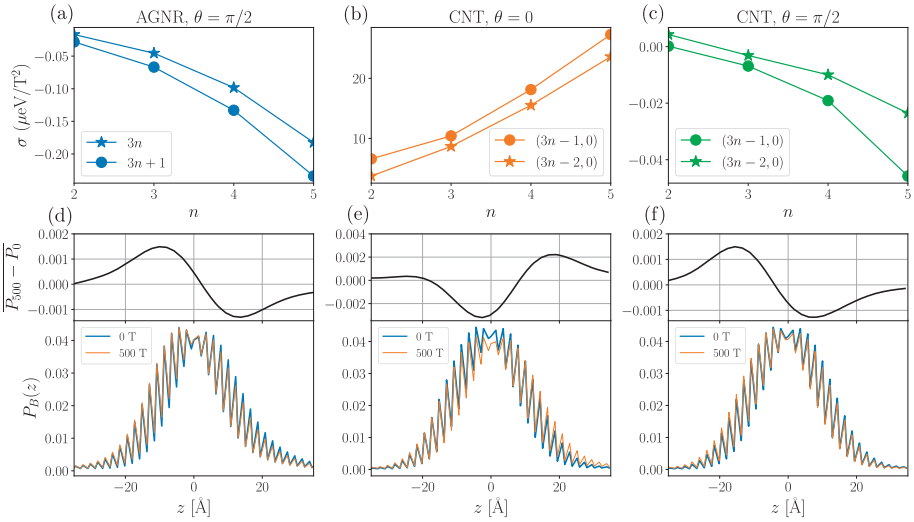

Fig. 3.8: (a-c) Diagmagnetic shift coefficient of the ground state bright exciton as a function of width or chiral indices of (a) AGNRs in perpendicular fields and CNTs in (b) parallel magnetic fields and (c) perpendicular magnetic field. (d-f) Exciton probability distribution with the hole located near the center of the unit cell for (d) 10-AGNR in a perpendicular field, (e) $(8, 0)$ CNT in a parallel field and (f) $(8, 0)$ CNT in a perpendicular field. The top plots in (d-f) show the nearest neighbor averaged change in the exciton probability distribution with magnetic field. (From [53])

the diamagnetic shift and is expressed as $\Delta E_{dia} = \sigma B^2$, where σ is called the diamagnetic shift coefficient. The diamagnetic shift coefficient is an important quantity as it can be used to make an experimental evaluation of the size of excitons. In the top row of Fig. 3.8 the diamagnetic coefficient of a wide number of different CNTs and AGNRs is shown. For CNTs and AGNRs in a perpendicular field, the coefficients are negative and decrease as the systems size increases. This shows that the exciton binding energy increases with magnetic field. In contrast, CNTs in a parallel field have a positive diamagnetic coefficient. Thus, the binding energy of exciton in CNTs perturbed by a parallel magnetic field decrease when the field strength increases. This conclusion is supported by the exciton probability distributions shown in the second row of Fig. 3.8. The probability distribution is computed by fixing the position of the hole on an atomic site near the center of the unit cell and then calculating the probability of the electron being on the different atomic sites of the system. Considering the change in the probability distribution of CNTs in a parallel field, it is clear that the magnetic field causes the exciton to become more delocalized.

The results presented here have served to elucidate the magneto-optical and excitonic properties of AGNRs and CNTs. While the materials share many similarities, the work in paper B also uncovered differences in the magneto-optical

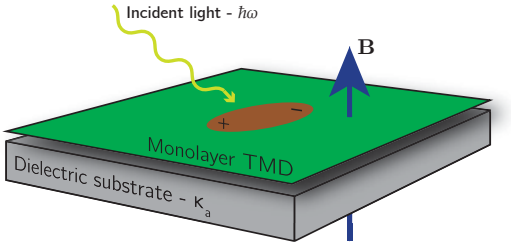

Fig. 3.9: Sketch of the system considered in papers C and D. A monolayer TMD perturbed by an external magnetic field directed perpendicular to the monolayer. The TMD may be encapsulated by dielectric materials. (From [133])

response. In addition, this work also inspired the use of a similar theoretical approach in paper E, where the magneto-optical properties of TMDs were considered.

3.3 Magneto-optics of transition metal dichalcogenides

This section is a review of the results obtained in papers C, D, and E. The focus of these papers are different properties of monolayer TMDs perturbed by an external magnetic field. In paper C the aim is to describe the binding energy of magnetoexcitons using an equation-of-motion (EOM) approach. In paper D, the EOM approach is applied to compute the magneto-optical response of TMDs without excitonic effects. Finally, paper E is an extension of the approach used to compute the magneto-optical response of quasi-1D systems in paper B. Here, a nanoribbon geometry is used to approximate the magneto-optical properties of monolayer TMDs including excitonic effects. By increasing the width of the nanoribbon system, the properties of the nanoribbon system are shown to converge to those of a fully periodic 2D monolayer system.

3.3.1 Equation of motion approach

In this section, the results from papers C and D are presented. The papers deal with magneto-optics and magnetoexcitons in monolayer TMDs. The system under consideration is sketched in Fig. 3.9. Here, a monolayer of TMD is perturbed by an external magnetic field perpendicular to the TMD. In contrast to most of the other work in this thesis, these papers apply a Dirac-type model to describe the single-particle properties of TMDs at the K and K' valleys of the Brillouin zone. If the monolayer is placed in the xy-plane and the magnetic field is in the positive z-direction, then the effective single-particle Hamiltonian

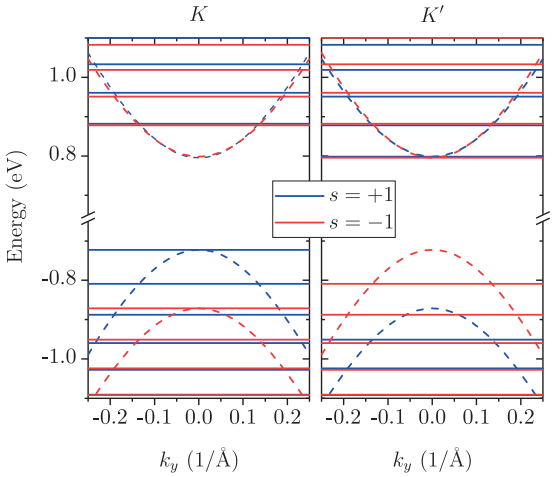

Fig. 3.10: Single-particle energies at the K and K' valleys of MoS_2, calculated for for $B = 0$ T (dashed lines) and $B = 600$ T (solid lines). Blue and red lines indicate spin up and down, respectively. (From [133])

in the Landau gauge can be written as

$$\hat{H}_B = v_F(\tau\sigma_x p_x + \sigma_y(p_y + eBx)) + \Delta_{\tau,s}\sigma_z + \xi_{\tau,s}\mathbb{I}, \tag{3.7}$$

where v_F is the Fermi velocity, $\tau = \pm 1$ is the valley index, σ_i are the Pauli matrices with $i \in \{x, y, z\}$, p_α are the momentum operators with $\alpha \in \{x, y\}$, $\mathbb{I}$ is the 2D identity matrix, and $\Delta_{\tau,s}$ and $\xi_{\tau,s}$ are the mass and on-site energy, respectively.

The wavefunctions and energies of the Hamiltonian $\hat{H}_B$ can be found analytically, both in the perturbed and unperturbed case. Figure 3.10 shows the single-particle energies at the K and K' valleys of MoS_2. When the magnetic field is finite, the energy bands are replaced by discrete Landau levels (LLs), which are given by

$$E_{\tau,s}^{n,\lambda} = \lambda\sqrt{\Delta_{\tau,s}^2 + n(\hbar\omega_c)^2} + \xi_{\tau,s}. \tag{3.8}$$

Here, n is the integer Landau level index, $\lambda = \pm$ indicate conduction $(+)$ or valence band $(-)$ states, and $\hbar\omega_c$ is the cyclotron energy. The Landau level index has to obey the relation $n \geq (1 + \tau\lambda)/2$. This results in the existence of Landau levels with $n = 0$ in the valence band at the K valley and in the conduction bands at the K' valley. This can also be observed in Fig. 3.10.

The aim of paper C is to accurately predict the energy of excitons in TMDs perturbed by a magnetic field. The approach used to compute magnetoexcitonic properties is similar to the approach used to derive the BSE in Sec. 2.2. The main idea is to solve Heisenberg's equation of motion for the density matrix $p_{\alpha,\alpha'}^{\eta} = \langle c_{\alpha,\eta}^{\dagger} c_{\alpha',\eta}\rangle$. Here, $c_{\alpha,\eta}^{\dagger}$ and $c_{\alpha',\eta}$ are the usual fermionic creation

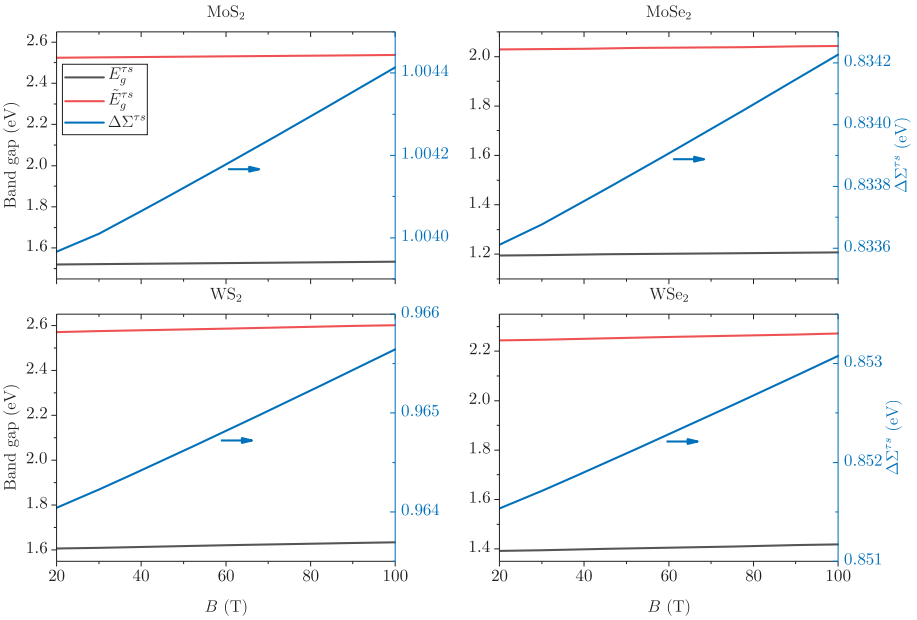

Fig. 3.11: Plot of $\tau s = \pm 1$ band gaps of monolayer TMDs, calculated for $\kappa = 1$. The uncorrected (black) and exchange self-energy corrected (red) band gaps are shown as a function of magnetic field. In addition, the exchange self-energy correction to the band gaps, $\Delta\Sigma^{\tau s} = \tilde{E}_g^{\tau s} - E_g^{\tau s}$, is plotted (blue). The blue lines refer to the blue axes, while the rest refer to the black axes (From [133])

and annihilation operators, respectively. Additionally, α is the set of indices $\{n, \lambda, k_y\}$ and $\eta = \{\tau, s\}$. Then Heisenberg's EOM reads

$$-i\hbar \frac{d}{dt} p^{\eta}_{\alpha,\alpha'} = \left\langle [\hat{H}, c^{\dagger}_{\alpha,\eta} c_{\alpha',\eta}] \right\rangle . \tag{3.9}$$

Here, $\hat{H}$ is the full Hamiltonian, which is given as the sum of the single-particle Hamiltonian, the light-matter interaction Hamiltonian, and the electron-electron interaction Hamiltonian. Computing the commutator on the right-hand side of Eq. (3.9) allows for the derivation of the BSE for magnetoexcitons in TMDs. In paper C, the terms of the commutator in Eq. (3.9) corresponding to excitons and exchange self-energy corrections are included. The exchange self-energy correction results in an increase of the non-interacting band gap and is necessary for accurate theoretical predictions of the exciton transition energy. The corrected and uncorrected band gaps of the four usual TMDs are shown as a function of the magnetic field strength in Fig. 3.11. The plots show that the increase in band gap due to the exchange self-energy correction is on the order of 1 eV for the four typical TMDs. Additionally, the plots also show that the correction to the band gap is approximately linear in magnetic field and that

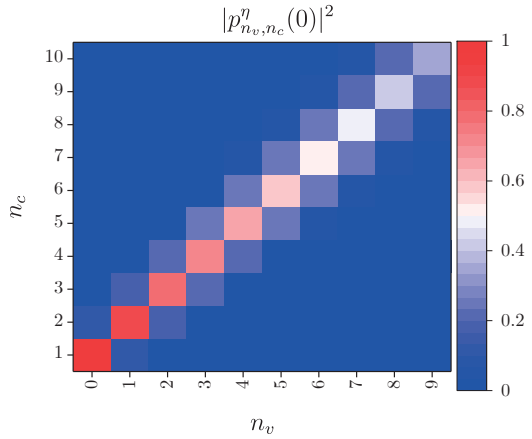

Fig. 3.12: The squared eigenvector elements of the A exciton in MoS_2 in a magnetic field of 100 T. The elements have been normalized such that the largest elements is unity. (From [133])

the magnetic field dependence is minor relative to the corrected band gap.

		Transition energies			Exciton energies	
TMD	κ	EOM	Exp., $B = 0$ T	Exp., $B \approx 65$ T	EOM	Wannier
MoS_2	1.00	1.918			-0.620	-0.617
	1.55	1.907	1.895 [113]	1.896 [113]	-0.491	-0.489
$MoSe_2$	1.00	1.516			-0.526	-0.513
	1.55	1.512	1.660 [109]		-0.419	-0.409
WS_2	1.00	2.042			-0.559	-0.520
	1.55	2.030	2.039 [114]	2.040 [114]	-0.426	-0.392
WSe_2	1.00	1.761			-0.511	-0.468
	1.55	1.755	1.744 [112]		-0.393	-0.357
	3.30	1.721	1.732 [44]	1.733 [44]	-0.229	-0.197
	4.50	1.700	1.723 [115]	1.724 [115]	-0.177	-0.144

Table 3.1: Theoretical and experimental transition and exciton energies for the A exciton in TMDs with different dielectric environments. All theoretical energies are computed at 100 T. The full table is available in [133].

As explained in Sec. 2.2, the computation of magnetoexcitons in a fully periodic 2D system is difficult numerically. The main reason for using the effective Hamiltonian in Eq. (3.7) instead of a tight-binding Hamiltonian is the fact that the analytically derived wavefunctions of $\hat{H}_B$ allow for a reduction in the numerical computations. Some relevant quantities and expressions can be computed or simplified without the use of numerical methods as shown in the paper. This lightens the computational load significantly. However, the

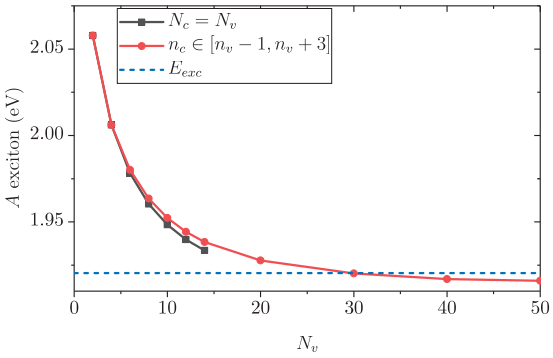

Fig. 3.13: Convergence of the A exciton energy in MoS_2 in a 100 T magnetic field. The dashed blue line correspond to the exciton energy computed from a Wannier model. (From [133])

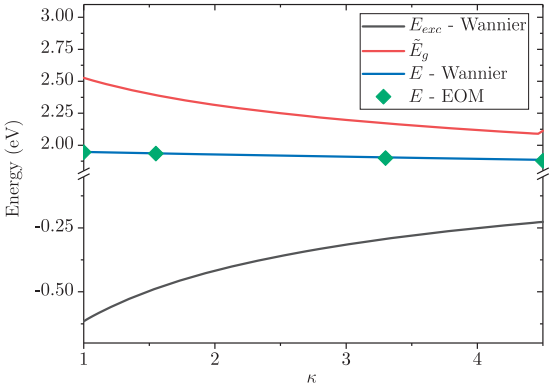

Fig. 3.14: Plot of the corrected band gap (red line), exciton transition energy (blue line and green diamonds), and exciton energy (black line) versus κ for MoS_2 in 100 T magnetic field. The blue line is the sum of the red and black lines. (From [133])

BSE in paper C couples LLs in the valence bands with LLs in the conduction bands. As the single-particle Hamiltonian allows for an infinite number of LLs, it is important to determine which and how many couplings are needed in the BSE to obtain accurate magnetoexcitonic properties. In Fig. 3.12, the squared eigenvector elements of the A exciton of MoS_2 is shown. The plot shows that for each valence-type LL only a few of the couplings to conduction-type LLs are significant. In order to verify this, the convergence of the A exciton transition energy as a function of the number of LLs included in the BSE is also studied. In Fig. 3.13 the convergence is illustrated. The black line corresponds to the case where all couplings are included (up to a cut-off in valence and conduction type LLs of $N_v = N_c$). The red line corresponds to the case where only the most significant couplings are included (with a cutoff in valence type LLs of

N_v). The plot shows that the exciton energy is slightly overestimated when only the most significant couplings are included. However, the computational complexity is decreased to the point where convergence of the exciton transition energy can be obtained.

Using the approach outlined above, the exciton energy and the transition energy of the A and B excitons in TMDs perturbed by a magnetic field are computed. These values are compared to experimentally measured transition energies and to exciton energies found using a Wannier model. The results for the A exciton are summarized in Table 3.1. The results for the B exciton is available in paper C. In general, there is a very good agreement between the experimental measurements and the transition energies computed using the EOM. The largest discrepancy is for $MoSe_2$ where the difference is almost 150 meV. There is also a good agreement between the exciton energies computed using the Wannier model and the EOM approach, with differences ranging from a few meV to 50 meV.

Finally, the effect of the dielectric environment on the exciton transition energy was studied. As mentioned, both excitonic effects and an exchange self-energy correction is included in the computations in paper C. Both of the effects contribute to the transition energy of excitons in TMDs. The exciton transition energy can be found by adding the band gap energy and the exciton energy. The exchange self-energy causes an opening of the band gap. The size of the self-energy correction decreases as the screening from the surroundings increase. This is illustrated by the red line in Fig. 3.14, which shows the corrected band gap versus κ. Recall that κ is the average of the dielectric constant of the encapsulating materials. Similarly, the exciton energy increases when κ increases. This is illustrated by the black line in Fig. 3.14. These two counteracting effects cause the exciton transition energy two exhibit minimal dependence on the dielectric environment as illustrated both by the Wannier results (the blue line) and the EOM results (the green diamonds) in Fig. 3.14. This concludes the summary of the results from paper C.

In paper D, the single-particle magneto-optical response of monolayer TMDs was studied. Using the EOM approach, expressions for the elements of the optical susceptibility tensor were derived. The outset was the same effective Hamiltonian for the single-particle properties as in Eq. (3.7). Using the expressions for the wavefunctions, the dipole matrix elements were computed analytically. The dipole matrix elements showed that the only allowed optical transitions from a LL with index n are those to LLs with index $n \pm 1$. Using these optical selection rules, the expressions for the susceptibility tensor elements were simplified and can be computed numerically for weak magnetic fields with relative ease. In contrast, when using a TB model the calculation of the magneto-optical response is much more expensive computationally and it can be difficult to go to magnetic fields weaker than 50 T. Paper C treats the magneto-optical response of both undoped and doped monolayer TMDs. The

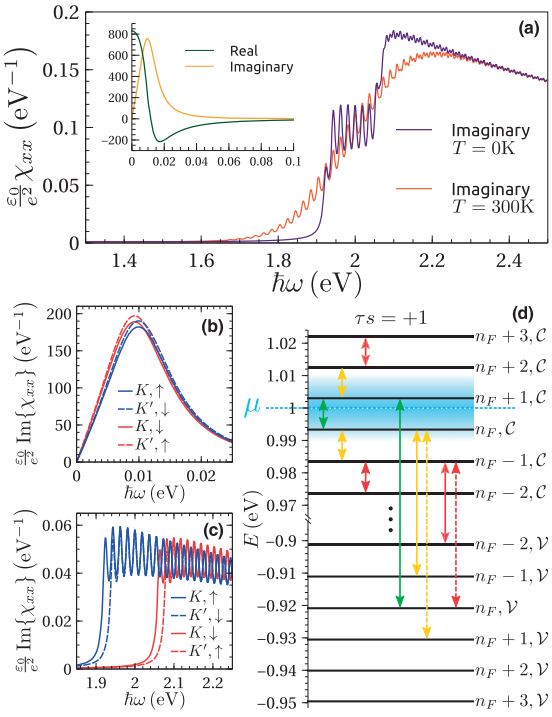

Fig. 3.15: Diagonal magneto-optical response in a doped MoS_2 monolayer ($\mu = 1$ eV) in a 50 T magnetic field. In (a), the tensor element χ_{xx} is plotted as a function of the photon energy (results in the inset are roughly independent of the temperature T); (b) and (c) show the valley and spin breakdown of the absorptive part of χ_{xx} at zero temperature; (d) is a schematic of the optical transitions between LLs. (From [134])

results relating to the undoped regime are at most interesting from a qualitative point of view, since the optical response of undoped TMDs are dominated by excitonic effects. However, as discussed in the paper, if the system is doped sufficiently the excitons are effectively screened. Thus, the single-particle results presented in paper D are expected to hold in the doped regime.

In Fig. 3.15 (a), the diagonal susceptibility element χ_{xx} is plotted for doped ($\mu = 1$ eV) monolayer MoS_2 in a magnetic field of 50 T. This corresponds to the situation where the Fermi level is approximately 0.2 eV above the zero'th LL in K' valley. The diagonal susceptibility of the doped system exhibit a temperature dependence seen in the undoped regime. This temperature dependence can be explained by the schematic in Fig. 3.15 (d). In the schematic, the dashed blue line indicates the Fermi level. For a cold semiconductor ($T = 0$ K), only the transitions corresponding to the green arrows are allowed. In this case, the spectrum features a step structure due to the spin-orbit splitting of the valence bands. However, at room temperature ($T = 300$ K) this step structure

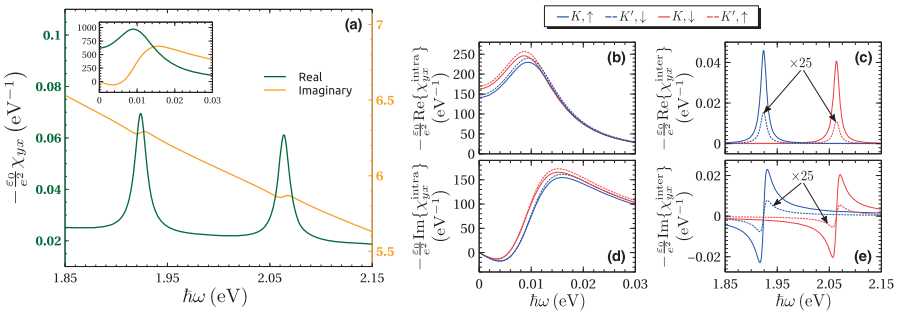

Fig. 3.16: (a) Hall susceptibility χ_{yx} versus photon energy, in a doped ($\mu = 1$ eV) monolayer MoS2 at zero temperature and for a field of 50 T. (b)–(e) Valley and spin breakdown of the real [(b), (c)] and imaginary [(d), (e)] parts of (a), divided in the intraband [(b), (d)] and interband [(c), (e)] transitions. (From [134])

is smeared out. This is due to the fact that the finite temperature allows more optical transitions (illustrated by the yellow arrows in the schematic). This temperature dependence is one of the interesting phenomena found relating to the magneto-optical response of doped TMD monolayers.

Another interesting magneto-optical property of doped monolayer TMDs is the possibility of creating a spin and valley imbalance in TMDs using linearly polarized light. At $T = 0$ K, the lowest energy interband peak is only half the magnitude of the other peaks on the same plateau. In general, each peak is due to four difference transitions. However, in the case of doped TMDs at $T = 0$ K, two of the transitions are not allowed by the Pauli exclusion principle. These transitions are illustrated by the dashed yellow arrow in the schematic in Fig. 3.15 (d). These blocked transitions are the cause of the reduced magnitude of the first interband peak. In paper D, it is shown that the half-height peak is actually due to just a single transition happening for a distinct combination of spin and valley. This is also illustrated in the breakdown of the spin and valley contributions in Fig. 3.15 (c). This provides a method for probing a single combination of valley and spin with linearly polarized light, similar to what can be done using circularly polarized light for undoped and unperturbed monolayer TMDs. Finally, for doped TMDs, a significant contribution from intraband transitions is also present. This is illustrated in the inset of Fig. 3.15 (a) and Fig. 3.15 (b).

In the doped regime, the perturbed monolayer TMDs have finite Hall susceptibility, i.e. $\chi_{yx} \neq 0$. In paper D, analytical expressions for the interband and intraband Hall susceptibility are derived. These expressions hold in the case where the temperature and the Fermi level are such that optical transitions involving the 0 LL are Pauli blocked. In Fig. 3.16 (a), the Hall susceptibility is illustrated for doped MoS_2. Considering the spin and valley breakdown of the Hall susceptibility in Figs. 3.16 (b-e), it is clear that the significant con-

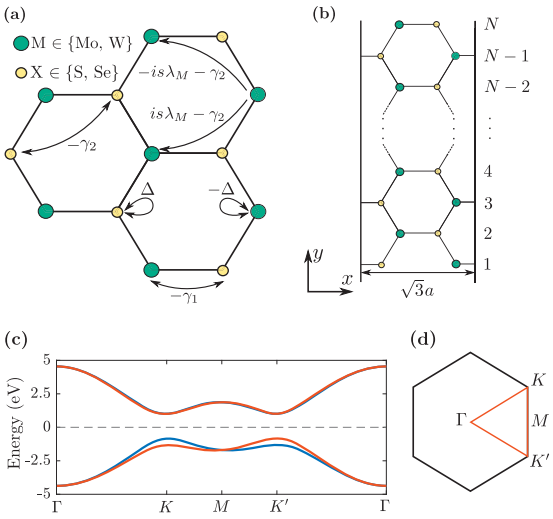

Fig. 3.17: (a) Tight-binding couplings in the NNN-TB model for a monolayer TMD. (b) Unit cell for an armchair TMD nanoribbon, where a is the lattice constant. (c) Band structure of WSe_2. Blue and red lines correspond to spin-up and -down, respectively. (d) Brillouin zone of monolayer TMD. (From [95])

tributions to the interband part of the Hall susceptibility come from the K valley. The explanation for this is the same as for the half-peak in the diagonal susceptibility. In addition to the results presented here, paper D also contains results about the exchange self-energy correction of the LLs and the response to circularly polarized light. In the following subsection, results about the effect of excitons on the magneto-optical properties of monolayer TMDs are presented.

3.3.2 From nanoribbons to 2D response

Paper E aims to include excitonic effects in the magneto-optical response of TMDs. In this sense, the work in paper E is the natural extension of the work presented in papers C and D. However, as have been mentioned previously, the calculation of excitonic effects in the magneto-optical response of a fully periodic 2D system is unfeasible. To circumvent this problem, a nanoribbon geometry is used in paper E. Then, the excitonic effects on the magneto-optical response of the nanoribbon system can be computed using the same methodology as in paper B. By increasing the width of the nanoribbon it is possible to approximate the magneto-optical response with excitonic effects of a fully periodic 2D system.

The TB couplings used to describe monolayer TMDs is illustrated in Fig. 3.17 (a). Using these couplings, both the different spin-splitting of the valence band and the broken electron-hole symmetry is included in the single-particle prop-

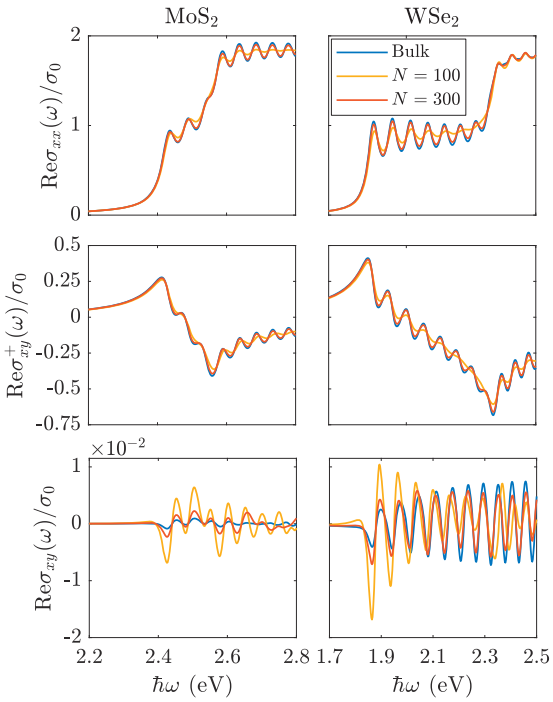

Fig. 3.18: Single-particle linear optical conductivity, calculated for $B = 130$ T and with a broadening of 25 meV. (From [95])

erties. The resulting band structure of a monolayer TMD is shown in Fig. 3.17 (c). The same TB coupling is also used for the nanoribbon. The nanoribbon unit cell is illustrated in Fig. 3.17 (b). The computational load could have been reduced by using a nanoribbon with zigzag edges since the number of atoms in a similarly sized unit cell is less than in the armchair unit cell. However, nanoribbons with zigzag edges proved to have dominant edge effects. Thus, using the armchair nanoribbon geometry was necessary to avoid these effects.

For the 2D TMD system, the optical response can be computed in the two cases: with excitons and without magnetic field, or without excitons and with magnetic field. Before the excitonic magneto-optical response of the nanoribbon system is used to approximate the full 2D response, it is necessary to ensure that convergence can be obtained in these two cases. Using the expression for the optical conductivity derived in Eq. (2.48), the single-particle magneto-optical response of MoS_2 and WSe_2 were computed for both the nanoribbon geometry and a fully periodic 2D geometry. The first row of Fig. 3.18 shows the real part of the diagonal conductivity, corresponding to the absorption of linearly polarized light. The plots clearly illustrate how the optical response of the nanoribbons converge to that of the bulk 2D structure, as the width of

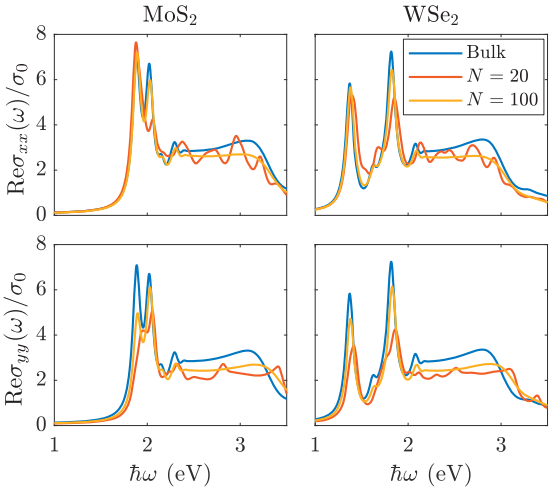

Fig. 3.19: Excitonic diagonal conductivities, calculated for $B = 0$ T, $\kappa = 1$ and a broadening of 50 meV. (From [95])

the ribbons increase. Both the Landau level structure in the spectra and the magnitude of the peaks have converged for the wide nanoribbon. The second row shows the convergence of the spin-dependent Hall conductivities. In this case, the same convergence as for the diagonal conductivity is observed. The final row in Fig. 3.18 shows the Hall conductivity. In this case, the convergence is slightly worse than for the diagonal conductivity.

Turning now to the excitonic properties. In order to ensure that the excitonic properties of the nanoribbons converge to those of the 2D system, it is necessary to consider which electron-electron interaction potential is used for the nanoribbon system. In paper B, an Ohno-type potential was used for the quasi-1D systems. However, if an Ohno-type potential is used for the nanoribbon system here, the excitonic properties will not converge to the excitonic properties of the monolayer TMD. This is due to the fact that in a 2D system, the electron-electron interaction potential is given by the Keldysh potential. Thus, in paper E, an effective 1D potential is derived for the nanoribbon system, such that when the width is increased the excitonic properties of the nanoribbon converge to those of the 2D system with the Keldysh potential. This is done by using an integral form of the Keldysh potential. In this form, a partial one-dimensional Fourier transform can be performed. Using this approach, the interaction matrix-elements are found to be given by

$$W^{s,s}_{cvk,c'v'k'} = \sum_{n,m} I^{n,s}_{ck,c'k'} I^{m,s}_{v'k',vk} U^{k,k'}_{n,m}, \tag{3.10}$$

where the n, m runs over all atomic sites in the unit cell and $I^{n,s}_{\alpha k,\beta k'}$ are the Bloch overlaps given by the product of the TB eigenvector elements correspond-

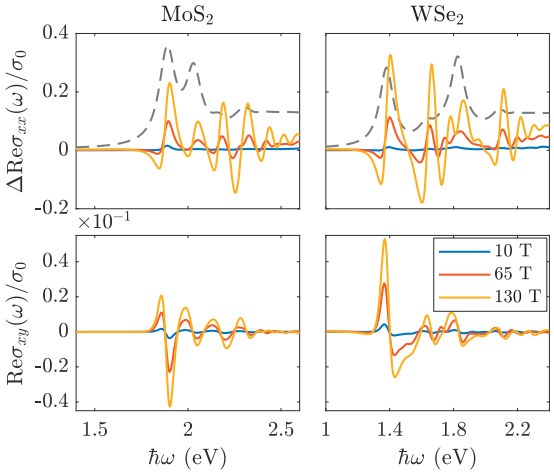

Fig. 3.20: Excitonic optical conductivity versus photon energy, calculated for different magnetic fields. The first row illustrates the difference between the optical conductivity at a finite field strength and at 0 T. The unperturbed spectra is illustrated by the dashed grey line. The second row is the excitonic Hall conductivities. The spectra are for nanoribbons with $N = 100$ and $\kappa = 1$. (From [95])

ing to site n. The integral factors $U_{n,m}^{k,k'}$ are given by

$$U_{n,m}^{k,k'} = -\frac{e^2}{2\pi L \varepsilon_0} \int_0^\infty \mathrm{d}z \; K_0 \left(\sqrt{r_0^2 z^2 + Y_{nm}^2 |k - k'|} \right) e^{-\kappa z}. \tag{3.11}$$

Here, L is the system length, K_0 is a modified Bessel function of the second kind, r_0 and κ are the usual screening parameters, and Y_{nm} is the distance in the y-direction between sites n and m. The integral factors can be computed efficiently numerically.

Just as in paper B, the optical response is computed using the Lanczos-Haydock routine. The convergence of the diagonal conductivity tensor elements is shown in Fig. 3.19. Comparing to the single-particle magneto-optical response, reasonable convergence of the excitonic optical response is obtained for narrower nanoribbons. This is due to the additional localization caused by the electron-hole attraction. The plots also show that the energy of the excitons in the nanoribbons coincide with the 2D exciton energies up to a few meV. This evidently proves the accuracy of the effective 1D potential derived in paper E.

As shown by the previous discussion, the nanoribbon approach is able to accurately describe both the single-particle magneto-optical response and the unperturbed excitonic properties of a monolayer TMD. Consequently, in paper E, the approach is assumed to also provide an accurate description of the excitonic magneto-optical response of monolayer TMDs. In Fig. 3.20 the excitonic

κ	σ - BSE	σ - Wannier	σ - Exper.
1.00	0.22	0.13	
1.55	0.24	0.15	0.18 [44]
2.25	0.27	0.17	0.25 [44]
3.30	0.31	0.19	0.32 [44]
4.50	0.36	0.23	0.24 [45], 0.31 [115]

Table 3.2: Calculated and experimental values of σ in units of $\mu\text{eV}/\text{T}^2$ for the $1s$ state of the A exciton in WSe_2. The first column is the values calculated using the approach presented in paper E, while the second column is values calculated using the Wannier model from paper C.

optical conductivity of MoS_2 and WSe_2 is shown for different magnetic fields. The first row of Fig. 3.20 shows the difference between $\text{Re}\sigma_{xx}(\omega)$ for a finite magnetic field and for $B = 0$ T. The plots illustrate how the exciton peaks experience a small blueshift as the magnetic field increases. This shift corresponds to the diamagnetic shift. In paper E, the diamagnetic shift coefficients are evaluated by fitting this shift to a quadratic function. Additionally, oscillations in the high end of the photon energy range appear for strong magnetic fields. These oscillations are due to transitions between Landau levels.

The second row in Fig. 3.20 shows the Hall conductivities. The plots show that excitonic effects severely change the response. Comparing to the single-particle Hall conductivities in Fig. 3.18, the excitonic effects change both the overall structure of the spectra and increase the magnitude of the response by one order of magnitude. This highlights the importance of a calculation such as the one provided in paper E. Another important aspect relating to the Hall conductivities is the fact that they are identically zero when there is no magnetic field, i.e. $\sigma_{xy}(B = 0) = 0$. When the magnetic field is turned on the Hall conductivities obtain a finite magnitude, which makes the relative change in the Hall conductivities very significant.

The diamagnetic shift coefficient of the A exciton is evaluated in paper E. In Table 3.2 the computed diamagnetic shift of the A exciton of WSe_2 is compared to experimental values and to values obtained using a Wannier model. The diamagnetic shifts are compared for a number of different dielectric environments, corresponding to different values of κ in the Keldysh potential. Table 3.2 shows that values computed using the nanoribbon approach are in general closer to the experimentally measured values than the values computed using the Wannier model.

In addition to providing insight into the effect of excitons on the magneto-optical response of TMDs, the results presented obtained in paper E can also be used to benchmark any future fully periodic 2D descriptions of magnetoexcitons in TMDs.

Chapter 4

Conclusions

With the advancements in synthesis and exfoliation of low-dimensional semiconductor materials, such as carbon nanotubes, graphene nanoribbons, and transition metal dichalcogenides, the study of excitonic effects in such systems has grown increasingly important. In this thesis, the two following aspects of excitons in low-dimensional semiconductors have been studied: Impurity bound excitons and Magnetoexcitons. The excitonic effects have been investigated from a theoretical viewpoint using both mathematical and numerical methods. In the following, the main conclusion obtained in the thesis is summarized.

The first topic of research was impurity bound excitons. Such a system has a simple description in the framework of the Wannier model, and the impurity bound exciton states correspond to the discrete eigenvalues of the Hamilton operator. The existence of such states was studied for a 1D system with zero-range interactions, using a rigorous mathematical approach. The existence of a single bound state, corresponding to an impurity bound exciton, was found in the case where the charge of the impurity was sufficiently small. The leading term of the energy of this bound state was also derived. Considering the case where the charge of the impurity is large, it was proven that as the charge of the impurity surpass some critical value, then the bound state corresponding to an impurity bound exciton cease to exist. These results were initially obtained for a system where the impurity has infinite mass but was also generalized to the case where the impurity has finite mass. The impurity mass dependence of the leading coefficient of the ground state energy and the critical charge was computed. The results for the 1D system motivated a similar study of impurity bound excitons in monolayer transition metal dichalcogenides (TMDs), which is currently unpublished. In this study, the results were obtained using only numerical methods and not rigorous mathematics. In agreement with the 1D case, the existence of a critical charge was also found for monolayer TMDs.

The second topic of research was magnetoexcitons and magneto-optics in

quasi-1D semiconductors, more specifically carbon nanotubes (CNTs) and armchair graphene nanoribbons (AGNRs). This study provided insight into how an external magnetic field affects both the optical response and the properties of excitons. In the case of the diagonal optical conductivity, very strong fields severely change the absorption properties of both CNTs and AGNRs. For CNTs, a splitting of the absorption peaks was observed, while, for AGNRs a new absorption peak emerged in the spectra. The absorption peak splitting computed for CNTs was found to be consistent with experimental measurements performed in very strong magnetic fields. These effects, however, were only found to be observable in very strong magnetic fields (several hundreds of T). At low magnetic field strengths, the most significant effect was found to be the existence of finite Hall conductivities. The finite Hall conductivities causes the systems to exhibit Faraday rotation. Faraday rotation spectra and Hall conductivities were calculated for the systems with and without excitons. These spectra underlined the importance of including excitons in the calculations, as they significantly change the optical response. Finally, the study also focused on the diamagnetic shift of the exciton peaks. Diamagnetic shifts coefficients were computed for a wide range of CNTs and AGNRs.

The final topic was the magneto-optical response of monolayer transition metal dichalcogenides. First, an equation of motion approach was used to compute the transition energy of magnetoexcitons. The computed transition energy of magnetoexcitons in monolayer TMDs was compared to experimental measurements of the exciton peak positions and good agreement between the quantities where found. In addition, the binding energies of the magnetoexcitons were also estimated and compared results based on the Wannier model. In general, these quantities where also in good agreement. Secondly, the single-particle magneto-optical properties of monolayer TMDs were also computed using an EOM approach. In the case of doped monolayer TMDs, a method for inducing a spin and valley imbalance using linear polarized light where described. Finally, by using a tight-binding model and the BSE, the magneto-optical response with excitons were calculated for very wide TMD nanoribbons. The width of the nanoribbons was such that the optical response approximated that of a true monolayer system. Using this approach, the effect of excitons on the Hall conductivity was computed. It was found that excitons increase the magnitude of the Hall conductivity by almost an order of magnitude (compared to the single-particle computations). Also, the diamagnetic shift coefficient of the A exciton in monolayer TMDs were computed for different dielectric environments. This was compared to experimental estimates of the diamagnetic shift and a good agreement was found.

References

[1] Y. Frenkel, Phys. Rev. **37**, 17 (1931).

[2] Y. Frenkel, Physical Review **37**, 1276 (1931).

[3] Y. Frenkel, Phys. Z. Sowjet. **9**, 158 (1936).

[4] R. Peierls, Ann. d. Physik **13**, 905 (1932).

[5] A. S. Davydov, Sov. Phys. Usp. **7**, 145 (1964).

[6] G. H. Wannier, Phys. Rev. **52**, 191 (1937).

[7] N. F. Mott, Proc. R. Soc. London, Ser. A **167**, 384 (1938).

[8] R. Elliott, Phys. Rev. **108**, 1384 (1957).

[9] A. Goi, A. Cantarero, K. Syassen, and M. Cardona, Phys. Rev. B **41**, 10111 (1990).

[10] A. Mang, K. Reimann, M. Steube *et al.*, Phys. Rev. B **53**, 16283 (1996).

[11] W. Shan, B. Little, A. Fischer, J. Song, B. Goldenberg, W. Perry, M. Bremser, and R. Davis, Phys. Rev. B **54**, 16369 (1996).

[12] E. E. Salpeter and H. A. Bethe, Phys. Rev. **84**, 1232 (1951).

[13] L. Sham and T. Rice, Phys. Rev. **144**, 708 (1966).

[14] W. Hanke and L. Sham, Phys. Rev. Lett. **43**, 387 (1979).

[15] I. Egri, Phys. Rep. **119**, 363 (1985).

[16] M. Rohlfing and S. G. Louie, Physical review letters **81**, 2312 (1998).

[17] L. Hedin, Phys. Rev. **139**, A796 (1965).

[18] J.-W. Van der Horst, P. A. Bobbert, M. A. Michels, and H. Bässler, J. Chem. Phys. **114**, 6950 (2001).

[19] C. D. Spataru, S. Ismail-Beigi, L. X. Benedict, and S. G. Louie, Phys. Rev. Lett. **92**, 077402 (2004).

[20] V. Tran, R. Soklaski, Y. Liang, and L. Yang, Phys. Rev. B **89**, 235319 (2014).

[21] M. M. Ugeda, A. J. Bradley, S.-F. Shi, H. Felipe, Y. Zhang, D. Y. Qiu, W. Ruan, S.-K. Mo, Z. Hussain, Z.-X. Shen *et al.*, Nat. Mater. **13**, 1091 (2014).

[22] M. Dvorak, S.-H. Wei, and Z. Wu, Phys. Rev. Lett. **110**, 016402 (2013).

[23] M. H. Degani and O. Hipólito, Phys. Rev. B **35**, 9345 (1987).

[24] T. Takagahara, Phys. Rev. B **47**, 4569 (1993).

[25] C. Riva, F. Peeters, and K. Varga, Phys. Rev. B **61**, 13873 (2000).

[26] T. G. Pedersen, Carbon **42**, 1007 (2004).

[27] L. Yang, M. L. Cohen, and S. G. Louie, Nano Lett. **7**, 3112 (2007).

[28] D. Y. Qiu, H. Felipe, and S. G. Louie, Phys. Rev. Lett. **111**, 216805 (2013).

[29] X. Wang, A. M. Jones, K. L. Seyler, V. Tran, Y. Jia, H. Zhao, H. Wang, L. Yang, X. Xu, and F. Xia, Nat. Nanotech. **10**, 517 (2015).

[30] T. Galvani, F. Paleari, H. P. Miranda, A. Molina-Sánchez, L. Wirtz, S. Latil, H. Amara, and F. Ducastelle, Phys. Rev. B **94**, 125303 (2016).

[31] M. Terrones, A. R. Botello-Méndez, J. Campos-Delgado, F. Lopez-Urias, Y. I. Vega-Cantú, F. J. Rodríguez-Macías, A. L. Elías, E. Munoz-Sandoval, A. G. Cano-Márquez, J.-C. Charlier *et al.*, Nano Today **5**, 351 (2010).

[32] Y. Che, X. Yang, G. Liu, C. Yu, H. Ji, J. Zuo, J. Zhao, and L. Zang, J. Am. Chem. Soc. **132**, 5743 (2010).

[33] R. H. Baughman, A. A. Zakhidov, and W. A. De Heer, Science **297**, 787 (2002).

[34] M. F. De Volder, S. H. Tawfick, R. H. Baughman, and A. J. Hart, Science **339**, 535 (2013).

[35] C. Gong, H. Zhang, W. Wang, L. Colombo, R. M. Wallace, and K. Cho, Appl. Phys. Lett. **103**, 053513 (2013).

[36] D. Jariwala, V. K. Sangwan, L. J. Lauhon, T. J. Marks, and M. C. Hersam, ACS. Nano **8**, 1102 (2014).

[37] L. Kou, C. Chen, and S. C. Smith, J. Phys. Chem. Lett. **6**, 2794 (2015).

[38] A. Carvalho, M. Wang, X. Zhu, A. S. Rodin, H. Su, and A. H. C. Neto, Nat. Rev. Mater. **1**, 16061 (2016).

[39] T. G. Pedersen, Phys. Rev. B **94**, 125424 (2016).

[40] T. G. Pedersen, S. Latini, K. S. Thygesen, H. Mera, and B. K. Nikolić, New J. Phys. **18**, 073043 (2016).

[41] B. Scharf, T. Frank, M. Gmitra, J. Fabian, I. Žutić, and V. Perebeinos, Phys. Rev. B **94**, 245434 (2016).

[42] T. G. Pedersen, New J. Phys. **19**, 043011 (2017).

[43] M. Massicotte, F. Vialla, P. Schmidt, M. B. Lundeberg, S. Latini, S. Haastrup, M. Danovich, D. Davydovskaya, K. Watanabe, T. Taniguchi *et al.*, Nat. Commun. **9**, 1633 (2018).

[44] A. V. Stier, N. P. Wilson, G. Clark, X. Xu, and S. A. Crooker, Nano Lett. **16**, 7054 (2016).

[45] E. Liu, J. van Baren, T. Taniguchi, K. Watanabe, Y.-C. Chang, and C. H. Lui, Phys. Rev. B **99**, 205420 (2019).

[46] M. A. Lampert, Phys. Rev. Lett. **1**, 450 (1958).

[47] W. Dumke, Phys. Rev. **132**, 1998 (1963).

[48] D. S. McClure and C. Pedrini, Phys. Rev. B **32**, 8465 (1985).

[49] R. Sharma and S. Rodriguez, Phys. Rev. **153**, 823 (1967).

[50] B. Meyer, J. Sann, S. Lautenschläger, M. Wagner, and A. Hoffmann, Phys. Rev. B **76**, 184120 (2007).

[51] B. O. Tayo and S. V. Rotkin, Phys. Rev. B **86**, 125431 (2012).

[52] T. Kato and T. Kaneko, ACS. Nano **8**, 12777 (2014).

[53] J. Have and T. G. Pedersen, Phys. Rev. B **97**, 115405 (2018).

[54] J. W. Wilder, L. C. Venema, A. G. Rinzler, R. E. Smalley, and C. Dekker, Nature **391**, 59 (1998).

[55] G. Dresselhaus, S. Riichiro *et al.*, *Physical properties of carbon nanotubes*, (World scientific1998).

[56] S. Iijima, Nature **354**, 56 (1991).

[57] T. Ebbesen and P. Ajayan, Nature **358**, 220 (1992).

[58] Z. Ren, Z. Huang, J. Xu, J. Wang, P. Bush, M. Siegal, and P. Provencio, Science **282**, 1105 (1998).

[59] K. Hata, D. N. Futaba, K. Mizuno, T. Namai, M. Yumura, and S. Iijima, Science **306**, 1362 (2004).

[60] E. T. Thostenson, Z. Ren, and T.-W. Chou, Compos. Sci. Technol. **61**, 1899 (2001).

[61] T. Dürkop, S. Getty, E. Cobas, and M. Fuhrer, Nano Lett. **4**, 35 (2004).

[62] J. M. Schnorr and T. M. Swager, Chem. Mater. **23**, 646 (2010).

[63] D. Zhang, K. Ryu, X. Liu, E. Polikarpov, J. Ly, M. E. Tompson, and C. Zhou, Nano Lett. **6**, 1880 (2006).

[64] M. E. Itkis, D. E. Perea, R. Jung, S. Niyogi, and R. C. Haddon, J. Am. Chem. Soc. **127**, 3439 (2005).

[65] T. Ando, J. Phys. Soc. Jpn. **66**, 1066 (1997).

[66] V. Perebeinos, J. Tersoff, and P. Avouris, Phys. Rev. Lett. **92**, 257402 (2004).

[67] F. Wang, G. Dukovic, L. E. Brus, and T. F. Heinz, Science **308**, 838 (2005).

[68] J. Maultzsch, R. Pomraenke, S. Reich, E. Chang, D. Prezzi, A. Ruini, E. Molinari, M. Strano, C. Thomsen, and C. Lienau, Phys. Rev. B **72**, 241402 (2005).

[69] H. Ajiki and T. Ando, Physica B **201**, 349 (1994).

[70] T. Ando, J. Phys. Soc. Jpn. **73**, 3351 (2004).

[71] T. Ando, J. Phys. Soc. Jpn. **75**, 024707 (2006).

[72] S. Uryu and T. Ando, Phys. Rev. B **74**, 155411 (2006).

[73] A. Zarifi and T. G. Pedersen, Phys. Rev. B **77**, 085409 (2008).

[74] S. Zaric, G. N. Ostojic, J. Kono, J. Shaver, V. C. Moore, M. S. Strano, R. H. Hauge, R. E. Smalley, and X. Wei, Sci. **304**, 1129 (2004).

[75] J. Shaver, J. Kono, O. Portugall, V. Krstić, G. L. Rikken, Y. Miyauchi, S. Maruyama, and V. Perebeinos, Nano Lett. **7**, 1851 (2007).

[76] R. Matsunaga, K. Matsuda, and Y. Kanemitsu, Phys. Rev. Lett. **101**, 147404 (2008).

[77] S. Takeyama, H. Suzuki, H. Yokoi, Y. Murakami, and S. Maruyama, Phys. Rev. B **83**, 235405 (2011).

[78] W. Zhou, T. Sasaki, D. Nakamura, H. Liu, H. Kataura, and S. Takeyama, Phys. Rev. B **87**, 241406 (2013).

[79] W. Zhou, T. Sasaki, D. Nakamura, H. Saito, H. Liu, H. Kataura, and S. Takeyama, Appl. Phys. Lett. **103**, 021117 (2013).

[80] D. Nakamura, T. Sasaki, W. Zhou, H. Liu, H. Kataura, and S. Takeyama, Phys. Rev. B **91**, 235427 (2015).

[81] M. Fujita, K. Wakabayashi, K. Nakada, and K. Kusakabe, J. Phys. Soc. Jpn. **65**, 1920 (1996).

[82] K. Nakada, M. Fujita, G. Dresselhaus, and M. S. Dresselhaus, Phys. Rev. B **54**, 17954 (1996).

[83] K. S. Novoselov, A. K. Geim, S. V. Morozov, D. Jiang, Y. Zhang, S. V. Dubonos, I. V. Grigorieva, and A. A. Firsov, Science **306**, 666 (2004).

[84] M. Y. Han, B. Özyilmaz, Y. Zhang, and P. Kim, Phys. Rev. Lett. **98**, 206805 (2007).

[85] X. Li, X. Wang, L. Zhang, S. Lee, and H. Dai, Science **319**, 1229 (2008).

[86] L. Jiao, X. Wang, G. Diankov, H. Wang, and H. Dai, Nat. Nanotech. **5**, 321 (2010).

[87] D. V. Kosynkin, A. L. Higginbotham, A. Sinitskii, J. R. Lomeda, A. Dimiev, B. K. Price, and J. M. Tour, Nature **458**, 872 (2009).

[88] L. Jiao, L. Zhang, X. Wang, G. Diankov, and H. Dai, Nature **458**, 877 (2009).

[89] L. Liao, J. Bai, Y.-C. Lin, Y. Qu, Y. Huang, and X. Duan, Adv. Mater. **22**, 1941 (2010).

[90] D. Prezzi, D. Varsano, A. Ruini, A. Marini, and E. Molinari, Phys. Rev. B **77**, 041404 (2008).

[91] R. Denk, M. Hohage, P. Zeppenfeld, J. Cai, C. A. Pignedoli, H. Söde, R. Fasel, X. Feng, K. Müllen, S. Wang *et al.*, Nat. Commun. **5**, 4253 (2014).

[92] J. Liu, A. Wright, C. Zhang, and Z. Ma, Appl. Phys. Lett. **93**, 041106 (2008).

[93] J. B. Oostinga, B. Sacépé, M. F. Craciun, and A. F. Morpurgo, Phys. Rev. B **81**, 193408 (2010).

[94] M. Tymchenko, A. Y. Nikitin, and L. Martín-Moreno, ACS. Nano **7**, 9780 (2013).

[95] J. Have, N. M. R. Peres, and T. G. Pedersen, Phys. Rev. B **100**, 045411 (2019).

[96] K. F. Mak, C. Lee, J. Hone, J. Shan, and T. F. Heinz, Phys. Rev. Lett. **105**, 136805 (2010).

[97] J. K. Ellis, M. J. Lucero, and G. E. Scuseria, Appl. Phys. Lett. **99**, 261908 (2011).

[98] Z. Y. Zhu, Y. C. Cheng, and U. Schwingenschlögl, Phys. Rev. B **84**, 153402 (2011).

[99] A. Kormányos, V. Zólyomi, N. D. Drummond, P. Rakyta, G. Burkard, and V. I. Fal'ko, Phys. Rev. B **88**, 045416 (2013).

[100] T. Cheiwchanchamnangij and W. R. L. Lambrecht, Phys. Rev. B **85**, 205302 (2012).

[101] D. Xiao, G.-B. Liu, W. Feng, X. Xu, and W. Yao, Phys. Rev. Lett. **108**, 196802 (2012).

[102] T. Cao, G. Wang, W. Han, H. Ye, C. Zhu, J. Shi, Q. Niu, P. Tan, E. Wang, B. Liu *et al.*, Nature communications **3**, 887 (2012).

[103] H. Zeng, J. Dai, W. Yao, D. Xiao, and X. Cui, Nat. Nanotech. **7**, 490 (2012).

[104] T. C. Berkelbach, M. S. Hybertsen, and D. R. Reichman, Phys. Rev. B **88**, 045318 (2013).

[105] A. Chaves, R. Ribeiro, T. Frederico, and N. Peres, 2D Mater. **4**, 025086 (2017).

[106] Z. Wang, J. Shan, and K. F. Mak, Nat. Nanotechnol. **12**, 144 (2017).

[107] F. Rose, M. O. Goerbig, and F. Piéchon, Phys. Rev. B **88**, 125438 (2013).

[108] Y. Li, J. Ludwig, T. Low, A. Chernikov, X. Cui, G. Arefe, Y. D. Kim, A. M. van der Zande, A. Rigosi, H. M. Hill *et al.*, Phys. Rev. Lett. **113**, 266804 (2014).

[109] D. MacNeill, C. Heikes, K. F. Mak, Z. Anderson, A. Kormányos, V. Zólyomi, J. Park, and D. C. Ralph, Phys. Rev. Lett. **114**, 037401 (2015).

[110] G. Wang, L. Bouet, M. Glazov, T. Amand, E. Ivchenko, E. Palleau, X. Marie, and B. Urbaszek, 2D Mater. **2**, 034002 (2015).

[111] A. Srivastava, M. Sidler, A. V. Allain, D. S. Lembke, A. Kis, and A. Imamoğlu, Nat. Phys. **11**, 141 (2015).

[112] G. Aivazian, Z. Gong, A. M. Jones, R.-L. Chu, J. Yan, D. G. Mandrus, C. Zhang, D. Cobden, W. Yao, and X. Xu, Nat. Phys. **11**, 148 (2015).

[113] A. V. Stier, K. M. McCreary, B. T. Jonker, J. Kono, and S. A. Crooker, Nat. Commun. **7**, 10643 (2016).

[114] A. V. Stier, K. M. McCreary, B. T. Jonker, J. Kono, and S. A. Crooker, J. Vac. Sci. Technol. **34**, 04J102 (2016).

[115] A. V. Stier, N. P. Wilson, K. A. Velizhanin, J. Kono, X. Xu, and S. A. Crooker, Phys. Rev. Lett. **120**, 057405 (2018).

[116] M. Van der Donck, M. Zarenia, and F. Peeters, Phys. Rev. B **97**, 195408 (2018).

[117] F. Bechstedt, *Many-Body Approach to Electronic Excitations*, (Springer2016).

[118] R. Peierls, Z. Phys. **80**, 763 (1933).

[119] J. Luttinger, Phys. Rev. **84**, 814 (1951).

[120] T. G. Pedersen, Phys. Rev. B **92**, 235432 (2015).

[121] A. Taghizadeh and T. G. Pedersen, Phys. Rev. B **97**, 205432 (2018).

[122] T. G. Pedersen, Phys. Rev. B **69**, 075207 (2004).

[123] L. V. Keldysh, Sov. Phys. JETP **29**, 658 (1979).

[124] M. L. Trolle, T. G. Pedersen, and V. Véniard, Sci. Rep. **7**, 39844 (2017).

[125] C. Stafford, S. Schmitt-Rink, and W. Schaefer, Phys. Rev. B **41**, 10000 (1990).

[126] T. G. Pedersen, Phys. Rev. B **95**, 235419 (2017).

[127] E. Prada, J. Alvarez, K. Narasimha-Acharya, F. Bailen, and J. Palacios, Phys. Rev. B **91**, 245421 (2015).

[128] R. Haydock, in *Solid state physics*, volume 35, 215–294, (Elsevier1980).

[129] A. A. Frost, J. Chem. Phys. **25**, 1150 (1956).

[130] J. Have, H. Kovařík, T. G. Pedersen, and H. D. Cornean, J. Math. Phys. **58**, 052106 (2017).

[131] F. A. Rasmussen and K. S. Thygesen, J. Phys. Chem. C **119**, 13169 (2015).

[132] G. Wang, L. Bouet, D. Lagarde, M. Vidal, A. Balocchi, T. Amand, X. Marie, and B. Urbaszek, Phys. Rev. B **90**, 075413 (2014).

[133] J. Have, G. Catarina, T. G. Pedersen, and N. Peres, Physical Review B **99**, 035416 (2019).

[134] G. Catarina, J. Have, J. Fernández-Rossier, and N. Peres, Physical Review B **99**, 125405 (2019).

Publications

(**A**). **J. Have**, H. Kovařík, T. G. Pedersen, and H. D. Cornean, "On the existence of impurity bound excitons in one-dimensional systems with zero range interactions", J. Math. Phys. **58**, 052106 (2017).

(**B**). **J. Have** and T. G. Pedersen, "Magnetoexcitons and Farday rotation in single-walled carbon nanotubes and graphene nanoribbons", Phys. Rev. B. **97**, 115405 (2018).

(**C**). **J. Have**, G. Catarina, T. G. Pedersen, and N. M. R. Peres, "Monolayer transition metal dichalcogenides in strong magnetic fields", Phys. Rev. B **99**, 035416 (2019).

(**D**). G. Catarina, **J. Have**, J. Fernández-Rossier, and N. M. R. Peres, "Optical orientation with linearly polarized light in transition metal dichalcogenides", Phys. Rev. B **99**, 125405 (2019).

(**E**). **J. Have**, N. M. R. Peres and T. G. Pedersen, "Excitonic magneto-optics in monolayer transition metal dichalcogenides: From nanoribbons to two-dimensional response", Phys. Rev. B **100** 045411 (2019).

Paper A

On the existence of impurity bound excitons in one-dimensional systems with zero range interactions

J. Have, H. Kovařík, T. G. Pedersen, and H. D. Cornean

Published in
Journal of Mathematical Physics **58**, 052106 (2017).

JOURNAL OF MATHEMATICAL PHYSICS **58**, 052106 (2017)

On the existence of impurity bound excitons in one-dimensional systems with zero range interactions

Jonas Have,[1,2,a)] Hynek Kovařík,[3] Thomas G. Pedersen,[2] and Horia D. Cornean[1]
[1]*Department of Mathematical Sciences, Aalborg University, Aalborg, Denmark*
[2]*Department of Physics and Nanotechnology, Aalborg University, Aalborg, Denmark*
[3]*DICATAM, Sezione di Matematica, Università degli Studi di Brescia, Brescia, Italy*

(Received 16 January 2017; accepted 8 May 2017; published online 25 May 2017)

We consider a three-body one-dimensional Schrödinger operator with zero range potentials, which models a positive impurity with charge $\kappa > 0$ interacting with an exciton. We study the existence of discrete eigenvalues as κ is varied. On one hand, we show that for sufficiently small κ there exists a unique bound state whose binding energy behaves like κ^4, and we explicitly compute its leading coefficient. On the other hand, if κ is larger than some critical value, then the system has no bound states. *Published by AIP Publishing.* [http://dx.doi.org/10.1063/1.4983921]

I. INTRODUCTION

In this paper, we consider a system of three one-dimensional non-relativistic quantum particles with zero range interactions. The system models an impurity interacting with an exciton, which is a pair made of an electron and a hole in either a semiconductor or an insulator. We want to give a rigorous description of the existence of bound states in the cases where the impurity has either a small or a large charge. In the small charge case, we prove the existence of a non-degenerate ground state, and we explicitly compute its leading order behavior and compare it to numerical calculations. In the case of a large impurity charge, we prove the existence of a critical charge above which the discrete spectrum is absent, and we compute it numerically. The proofs of our main results are based on a combined application of the Feshbach inversion formula and the Birman-Schwinger principle.

The bound states of a helium-like system with two negatively charged particles and a positively charged nucleus interaction through zero range potentials were previously examined in Ref. 1 and in Ref. 2, while the bound states of a system with a negatively charged particle and two positively charged particles with infinite mass were examined in Ref. 3. Also, the spectral properties of the similar, but more realistic, three-body Coulomb systems in three dimensions have been examined in Refs. 4–6.

The choice of Coulomb interaction potential in one-dimensional systems is a non-trivial one. The Schrödinger operator for the one-dimensional hydrogen atom with the $1/|x|$ Coulomb potential is not essentially self-adjoint but has an infinite number of self-adjoint extensions, and the choice of extension and corresponding spectral properties are still the subject of active research.[7–9] Other options are to modify the Coulomb potential to get rid of the singularity[10] or use zero range interactions, as used in the present paper. One-dimensional systems and zero range interactions might seem unphysical, but in many cases they can be used as toy models in order to avoid complicated numerical computations. In fact some three-dimensional Coulomb systems and one-dimensional systems with zero range interactions share important spectral properties. A classical example is the analogy between the one-dimensional hydrogen atom and the true three-dimensional hydrogen atom as described in Ref. 11.

a)E-mail: jh@math.aau.dk

Also, such simplified models naturally emerge as effective models for higher-dimensional systems submitted to various forms of confinement, for example, the one-dimensional effective models for excitons in carbon nanotubes in Refs. 12 and 13, one-dimensional models of optical response in one-dimensional semiconductors in Ref. 14, and the effective model for atoms in strong magnetic fields in Refs. 15 and 16. In a similar fashion, the system we consider in this paper can be interpreted as a model for impurity bound excitons in a one-dimensional semiconductor using the Wannier model. Excitonic effects are known to have a significant impact on the optical properties of semiconductors,[17] especially in one- and two-dimensional semiconductors where the reduced screening leads to large exciton binding energies compared to the bandgap. For a thorough introduction to systems with zero range potentials we refer to the book in Ref. 18.

The paper is structured as follows. In Sec. II, we present the model and comment on the main results of the paper. In Sec. III, we specify the framework and introduce some important notation. In Sec. IV we prove our first main result, namely, that there exists a single discrete eigenvalue for sufficiently small impurity charge. In Secs. V and VI we prove our second main result about the disappearance of the discrete spectrum if κ becomes supercritical.

II. THE MODEL AND THE MAIN RESULTS

Consider the system of two equal but oppositely charged particles with charge ± 1 and mass m, and an impurity with charge κ and mass M. Let $\sigma = m/(m+M)$ denote the mass fraction, $0 \le \sigma < 1$. Using relative atomic coordinates and removing its center of the mass, the system is formally described by the Schrödinger operator

$$H_{\kappa,\sigma} = -\frac{1}{2}\Delta - \sigma\partial_x\partial_y - \delta(x-y) + \kappa\delta(x) - \kappa\delta(y), \tag{2.1}$$

on $L^2(\mathbb{R}^2)$, where Δ is the two-dimensional Laplace operator and δ is the Dirac delta distribution.

The discrete spectrum of $H_{\kappa,\sigma}$ corresponds to impurity localized excitons. In the following we state our results regarding the discrete spectrum of $H_{\kappa,\sigma}$ and prove them in Secs. IV, V, and VI. The situation is sketched in Fig. 1(a) where we see the ground state energy and the essential spectrum for $\sigma = 0$. The essential spectrum of $H_{\kappa,0}$ will be derived in Sec. III, but as illustrated by the shaded area in the figure, its bottom stays equal to $-1/4$ on the closed interval $[0, 1/\sqrt{2}]$, while for larger κ, it equals $-\kappa^2/2$.

The first result concerns the existence and behaviour of a discrete eigenvalue of $H_{\kappa,0} =: H_\kappa$ when $\kappa \in (0, 1/\sqrt{2}]$.

Theorem II.1. *If $\kappa > 0$ is sufficiently small, the operator H_κ has precisely one discrete eigenvalue and its leading order behaviour is*

$$E(\kappa) = -\frac{1}{4} - 16\left(\frac{4}{\pi} - 1\right)^2\kappa^4 + \mathcal{O}(\kappa^5). \tag{2.2}$$

Furthermore, the energy $E(\kappa)$ is non-degenerate and decreasing if $\kappa \in (0, 1/\sqrt{2}]$; hence, the operator H_κ has at least one discrete eigenvalue on this interval.

The behaviour κ^4 of the leading order of $E(\kappa)$ (for κ sufficiently small) equals the weak coupling asymptotic of the ground state energy of one-dimensional Schrödinger operators with zero-mean potentials as was shown in Ref. 19. Also, the binding requirement (that κ should be sufficiently small) is similar to one of the two binding requirements that were found in Ref. 5 for the three-dimensional Coulomb system.

In Fig. 1(b) the leading behavior of the discrete eigenvalue given in Theorem II.1 is compared to a numerical calculation of the smallest discrete eigenvalue of H_κ. The numerical calculations are done using a similar method to what was presented in Ref. 1. The figure shows that they agree well for κ below 0.25.

The results can be generalized to hold for $0 < \sigma < 1$ as well. If κ is sufficiently small, the operator $H_{\kappa,\sigma}$ has a single discrete eigenvalue, and the leading behavior of this discrete eigenvalue E is

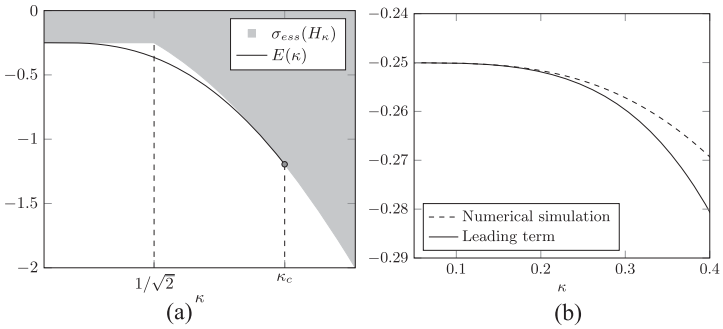

FIG. 1. In (a), a plot of the ground state energy is given as a function of the impurity charge κ. (b) is a comparison of the leading term of the discrete eigenvalue and the numerically calculated discrete eigenvalue.

calculated to be

$$E(\kappa) = -\frac{1}{4(1-\sigma)} - \beta(\sigma)\kappa^4 + \mathcal{O}(\kappa^5),$$

where

$$\beta(\sigma) := 4\frac{\left[6\sigma\sqrt{1-\sigma^2} - (2-\sigma)\sigma\pi - 8\sigma^2\cos^{-1}\left(\frac{\sqrt{1+\sigma}}{\sqrt{2}}\right) + \tan^{-1}\left(\frac{2\sigma(1-\sigma^2)}{1-2\sigma^2}\right)\right]^2}{(1+\sigma)(1-\sigma)^2\pi^2\sigma^2} \tag{2.3}$$

when $0 < \sigma < 1/\sqrt{2}$. The solution can be extended to the range $1/\sqrt{2} \le \sigma < 1$ by choosing another branch of $\tan^{-1}$.

For $\kappa \ge 1/\sqrt{2}$ we have the following results.

Theorem II.2. *Let $H_{\kappa,\tilde{\kappa}}$ be the self-adjoint operator formally described by*

$$H_{\kappa,\tilde{\kappa}} = -\frac{1}{2}\Delta - \delta(x-y) + \tilde{\kappa}\delta(x) - \kappa\delta(y) \tag{2.4}$$

on $L^2(\mathbb{R}^2)$. Given any $\tilde{\kappa} > 1$, there exists κ_M such that $H_{\kappa,\tilde{\kappa}}$ has no discrete eigenvalues for all $\kappa \ge \kappa_M$. Furthermore, given any $0 < \tilde{\kappa} < 1$, there exists some κ_M such that $H_{\kappa,\tilde{\kappa}}$ has at least one discrete eigenvalue for all $\kappa \ge \kappa_M$.

As a consequence of the previous two theorems, we will also prove the following corollary.

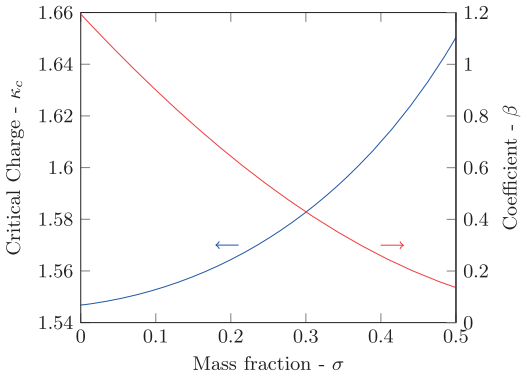

FIG. 2. Plot of the critical charge and the κ^4 coefficient of the discrete eigenvalue against the mass fraction σ.

Corollary II.3. Let H_κ be the operator in (2.1). Then there exists a critical charge of the impurity, which we will denote κ_c, such that the discrete spectrum of H_κ is non-empty for all $0 < \kappa < \kappa_c$ and empty for $\kappa \geq \kappa_c$.

Using numerical simulations to calculate the smallest discrete eigenvalue of H_κ, we see that at $\kappa \approx 1.546$ the ground state energy hits the essential spectrum. Thus, we expect that the true κ_c is close to 1.546. In Fig. 2 a numerical calculation of the critical charge κ_c is plotted against the mass fraction σ. We see that as the mass of the impurity decreases, the critical charge is increased, and thus bound states exists for impurities with larger charges. We have also plotted the coefficient β in (2.3) against the mass fraction, and we see that the coefficient decreases as the mass of the impurity decreases.

III. THE FRAMEWORK

In this section, we introduce the framework we use to study the discrete spectrum of $H_{\kappa,\sigma}$. This framework has been used in Refs. 2 and 20, and we refer to those papers for more details.

We define $H_{\kappa,\sigma}$ as the unique self-adjoint operator associated to the sesquilinear form

$$\begin{aligned} Q(f,g) = \frac{1}{2}\langle \nabla f, A\nabla g\rangle_{L^2(\mathbb{R}^2)} - \langle f(x,x), g(x,x)\rangle_{L^2(\mathbb{R})} \\ + \kappa\langle f(0,y), g(0,y)\rangle_{L^2(\mathbb{R})} - \kappa\langle f(x,0), g(x,0)\rangle_{L^2(\mathbb{R})}, \end{aligned} \tag{3.1}$$

on $H^1(\mathbb{R}^2) \times H^1(\mathbb{R}^2)$, where $H^1(\mathbb{R}^2)$ is the Sobolev space of first order and $A \in \mathbb{R}^{2\times 2}$ is the matrix

$$A = \begin{bmatrix} 1 & \sigma \\ \sigma & 1 \end{bmatrix}. \tag{3.2}$$

Let $\psi \in H^1(\mathbb{R}^2)$ and let $e \in \mathbb{R}^2$ be a unit vector. We define the trace operator $\tau_e : H^1(\mathbb{R}^2) \to L^2(\mathbb{R})$ by $(\tau_e\psi)(s) := \psi(se)$. Let us write $\tau := (\tau_{e_1}, \tau_{e_2}, \tau_{e_{12}})$ as an operator defined on $H^1(\mathbb{R}^2)$ with values in $[L^2(\mathbb{R})]^3 := \oplus_{i=1}^3 L^2(\mathbb{R})$, where $\{e_1, e_2\}$ is the canonical basis in $\mathbb{R}^2$ and $e_{12} = 1/\sqrt{2}(e_1 + e_2)$. Then $H_{\kappa,\sigma}$ is

$$H_{\kappa,\sigma} = -\frac{1}{2}\Delta - \sigma\frac{\partial^2}{\partial x \partial y} + \tau^* g \tau, \tag{3.3}$$

where $g := \operatorname{diag}\{-\kappa, \kappa, -1\} \in \mathbb{R}^{3\times 3}$.

As a direct application of the Hunziker-Van Winter Zhislin (HVZ) theorem[21] and a consequence of the signs of the potential terms in (2.1) the following lemma holds.

Lemma III.1. The essential spectrum of $H_{\kappa,\sigma}$ is

$$\left[\min\left\{-\frac{1}{4(1-\sigma)}, -\frac{\kappa^2}{2}\right\}, \infty\right).$$

The essential spectrum of $H_{\kappa,0}$ is illustrated by the shaded area in Fig. 1(a). Write the operator in (2.1) as $H_{\kappa,\sigma} = H_{0,\sigma} - V_\kappa$, where

$$H_{0,\sigma} := -\frac{1}{2}\Delta - \sigma\frac{\partial^2}{\partial x \partial y}, \qquad V_\kappa := \delta(x-y) - \kappa\delta(x) + \kappa\delta(y).$$

If $R(z)$ denotes the full resolvent operator $(H_{\kappa,\sigma} - z)^{-1}$ and $R_0(z)$ denotes the resolvent $(H_{0,\sigma} - z)^{-1}$, then by Krein's formula,

$$R(z) = R_0(z) - R_0(z)\tau^*(g^{-1} + \tau R_0(z)\tau^*)^{-1}\tau R_0(z), \quad z \in \rho(H_{0,\sigma}) \cap \rho(H_{\kappa,\sigma}). \tag{3.4}$$

Define

$$G_{\kappa,\sigma}(z) := g^{-1} + \tau R_0(z)\tau^*. \tag{3.5}$$

It can be shown that $E < \inf \sigma_{ess}(H_{\kappa,\sigma})$ belongs to the discrete spectrum of H_κ if and only if $G_{\kappa,\sigma}(E)$ is not invertible. Note that $G_{\kappa,\sigma}(z)$ is a 3×3 operator valued matrix which acts on $[L^2(\mathbb{R})]^3$ and its entries are z dependent. We will denote the elements of $\tau R_0(z)\tau^*$ by

$$\tau R_0(z)\tau^* = \begin{bmatrix} T_{0,\sigma} & T_{1,\sigma} & T^*_{2,\sigma} \\ T_{1,\sigma} & T_{0,\sigma} & T^*_{2,\sigma} \\ T_{2,\sigma} & T_{2,\sigma} & T_{3,\sigma} \end{bmatrix}. \tag{3.6}$$

The integral kernel of $R_0(z)$ is

$$R_0(\mathbf{x},\mathbf{y},z) = \frac{1}{2\pi^2}\int_{\mathbb{R}^2} \frac{e^{i\mathbf{k}\cdot(\mathbf{x}-\mathbf{y})}}{|\mathbf{k}|^2 + 2\sigma k_1 k_2 - 2z}\,\mathrm{d}k_1\,\mathrm{d}k_2. \tag{3.7}$$

Using the integral kernel of $R_0(z)$ in the Fourier representation, we can explicitly calculate the integral kernels of the elements in $\tau R_0(z)\tau^*$ (the first and the last operators are multiplication operators in Fourier space),

$$\hat{T}_{0,\sigma}(s) = \frac{1}{\sqrt{(1-\sigma^2)s^2 - 2z}}, \tag{3.8}$$

$$\hat{T}_{1,\sigma}(s,t) = \frac{1}{\pi}\frac{1}{s^2 + t^2 + 2\sigma st - 2z}, \tag{3.9}$$

$$\hat{T}_{2,\sigma}(s,t) = \frac{1}{\pi}\frac{1}{t^2 + (s-t)^2 + 2\sigma t(s-t) - 2z}, \tag{3.10}$$

$$\hat{T}_{3,\sigma}(s) = \frac{1}{\sqrt{(1-\sigma^2)s^2 - (1-\sigma)4z}}. \tag{3.11}$$

From these expressions, it is easy to see that the operators in (3.6) are bounded if $\mathrm{Re}(z) < 0$, and their norms go to zero when $\mathrm{Re}(z) \to -\infty$.

IV. PROOF OF THEOREM II.1

We are now ready to prove the first of our main results, i.e., the existence of a single discrete eigenvalue of $H_\kappa = H_{\kappa,0}$ when κ becomes sufficiently small. In the following we will also denote $T_{i,0}$ by T_i.

Assume that $\kappa < 1/\sqrt{2}$. In that case, it follows from Lemma III.1 that any discrete eigenvalues $E \in \mathbb{R}$ must satisfy $E < -1/4$. Moreover, E is a discrete eigenvalue of H_κ if and only if the operator $G_\kappa(E)$ is not invertible. Define $\tilde{G}_\kappa(E) := \kappa^{-1}G_\kappa(E)$ for $\kappa > 0$, then $\tilde{G}_\kappa(E)$ is invertible when $G_\kappa(E)$ is invertible. In matrix representation we can write $\tilde{G}_\kappa(E)$ as

$$\tilde{G}_\kappa(E) = \begin{bmatrix} -\mathbb{1} & 0 & 0 \\ 0 & \mathbb{1} & 0 \\ 0 & 0 & 0 \end{bmatrix} + \kappa \begin{bmatrix} T_0 & T_1 & T_2^* \\ T_1 & T_0 & T_2^* \\ T_2 & T_2 & -\mathbb{1} + T_3 \end{bmatrix}, \tag{4.1}$$

where $\mathbb{1}$ denotes the identity operator on $L^2(\mathbb{R})$. In order to find the values E where the inverse of $\tilde{G}_\kappa(E)$ does not exist, we use Feshbach's formula (see Equations (6.1) and (6.2) in Ref. 22) to reduce the dimension of the operator pencil we are trying to invert.

Let Π be the orthogonal projection such that $\Pi[L^2(\mathbb{R})]^3$ is isomorphic to $L^2(\mathbb{R})$, and $\Pi\tilde{G}_\kappa(E)\Pi \cong -\kappa + \kappa T_3$. The congruence symbol simply means that $\Pi\tilde{G}_\kappa(E)\Pi$ can be identified with $-\kappa + \kappa T_3$ on $L^2(\mathbb{R})$. Let $\Pi^\perp := \mathbb{1} - \Pi$ correspond to the orthogonal subspace $\Pi^\perp[L^2(\mathbb{R})]^3$ which is isomorphic to $[L^2(\mathbb{R})]^2$. Then, we get

$$\Pi^\perp\tilde{G}_\kappa(E)\Pi^\perp \cong \begin{bmatrix} -\mathbb{1} & 0 \\ 0 & \mathbb{1} \end{bmatrix} + \kappa \begin{bmatrix} T_0 & T_1 \\ T_1 & T_0 \end{bmatrix}. \tag{4.2}$$

The next lemma gives conditions under which the inverse of $\Pi^\perp\tilde{G}_\kappa(E)\Pi^\perp$ exists as an operator on $\Pi^\perp[L^2(\mathbb{R})]^3$.

Lemma IV.1. There exists $K > 0$ such that $R(E) := [\Pi^\perp\tilde{G}_\kappa(E)\Pi^\perp]^{-1}$ exists in $\Pi^\perp[L^2(\mathbb{R})]^3$ for all $E < -1/4$ and $0 < \kappa < K$.

Proof. We rewrite $\Pi^{\perp}\tilde{G}_{\kappa}(E)\Pi^{\perp}$ as

$$\Pi^{\perp}\tilde{G}_{\kappa}(E)\Pi^{\perp} \cong \left(\begin{bmatrix} \mathbb{1} & 0 \\ 0 & \mathbb{1} \end{bmatrix} + \kappa \begin{bmatrix} T_0 & T_1 \\ T_1 & T_0 \end{bmatrix} \begin{bmatrix} -\mathbb{1} & 0 \\ 0 & \mathbb{1} \end{bmatrix}\right) \begin{bmatrix} -\mathbb{1} & 0 \\ 0 & \mathbb{1} \end{bmatrix}. \tag{4.3}$$

The operators T_0 and T_1 are uniformly bounded on $L^2(\mathbb{R})$ for $E < -1/4$. Thus, we can choose a constant $K > 0$ such that

$$\left\| \kappa \begin{bmatrix} T_0 & T_1 \\ T_1 & T_0 \end{bmatrix} \right\| < 1, \tag{4.4}$$

for all $E < -1/4$ and $0 < \kappa < K$. Then the inverse $\Pi^{\perp}\tilde{G}_{\kappa}(E)\Pi^{\perp}$ exists for all $0 < \kappa < K$ and $E < -1/4$.

Additionally, we can write $R(E)$ as a Neumann series

$$R(E) \cong \begin{bmatrix} -\mathbb{1} & 0 \\ 0 & \mathbb{1} \end{bmatrix} + \sum_{j=1}^{\infty} (-1)^j \kappa^j \begin{bmatrix} -\mathbb{1} & 0 \\ 0 & \mathbb{1} \end{bmatrix} \left(\begin{bmatrix} T_0 & T_1 \\ T_1 & T_0 \end{bmatrix} \begin{bmatrix} -\mathbb{1} & 0 \\ 0 & \mathbb{1} \end{bmatrix} \right)^j, \tag{4.5}$$

for all $0 < \kappa < K$. □

By Feshbach's formula and Lemma IV.1, there exists K sufficiently small such that if $0 < \kappa < K$ and $E < -1/4$, the inverse of $\tilde{G}_{\kappa}(E)$ exists if and only if the inverse of

$$S_W(E) = \Pi\tilde{G}_{\kappa}(E)\Pi - \Pi\tilde{G}_{\kappa}(E)\Pi^{\perp}R(E)\Pi^{\perp}\tilde{G}_{\kappa}(E)\Pi, \tag{4.6}$$

exists as an operator restricted to the proper subspace. Using the matrix representation we can write $S_W(E)$ as

$$S_W(E) \cong \mathbb{1} - T_3 - \kappa \begin{bmatrix} T_2 & T_2 \end{bmatrix} R(E) \begin{bmatrix} T_2^* \\ T_2^* \end{bmatrix}, \quad \text{on } L^2(\mathbb{R}). \tag{4.7}$$

Note that the contribution to $S_W(E)$ from the first term of $R(E)$ in (4.5) is zero. To find the values where the inverse of $S_W(E)$ does not exist on $L^2(\mathbb{R})$, we use the following version of the Birman-Schwinger[23] principle.

Proposition IV.2. Let $E < -1/4$ and let $S_W(E)$ be given by (4.7). There exist two bounded operators $V_1 : [L^2(\mathbb{R})]^2 \to L^2(\mathbb{R})$ and $V_2 : L^2(\mathbb{R}) \to [L^2(\mathbb{R})]^2$ such that $S_W(E)^{-1}$ exists if and only if the inverse of

$$\mathbb{1}_2 - \kappa V_2(\mathbb{1} - T_3)^{-1}V_1 \tag{4.8}$$

exists on $[L^2(\mathbb{R})]^2$, where $\mathbb{1}_2$ is the identity operator on $[L^2(\mathbb{R})]^2$. We call the operator in (4.8) for the Birman-Schwinger operator.

Proof. Let $\Psi \in L^2(\mathbb{R})$ and define $V_2 : L^2(\mathbb{R}) \to [L^2(\mathbb{R})]^2$ as

$$V_2\Psi = R(E) \begin{bmatrix} T_2^*\Psi \\ T_2^*\Psi \end{bmatrix}. \tag{4.9}$$

By the boundedness of $R(E)$ and T_2^*, it follows that V_2 is a bounded operator. Furthermore, let $\Psi = [\Psi_1, \Psi_2] \in [L^2(\mathbb{R})]^2$ and define the operator $V_1 : [L^2(\mathbb{R})]^2 \to L^2(\mathbb{R})$ by

$$V_1\Psi = T_2\Psi_1 + T_2\Psi_2. \tag{4.10}$$

The operator V_1 is bounded since T_2 is bounded. Using V_1 and V_2 it is possible to rewrite the operator $S_W(E)$ on $L^2(\mathbb{R})$ as

$$S_W(E) = \mathbb{1} - T_3 - \kappa V_1V_2 = (\mathbb{1} - \kappa V_1V_2(\mathbb{1} - T_3)^{-1})(\mathbb{1} - T_3),$$

since the bounded inverse of $\mathbb{1} - T_3$ exists on $L^2(\mathbb{R})$ for all $E < -1/4$. Consequently $S_W(E)$ exists if and only if $(\mathbb{1} - \kappa V_1V_2(1 - T_3)^{-1})^{-1}$ exists on $L^2(\mathbb{R})$. But for any fixed κ we can choose E sufficiently

negative such that $\|\kappa V_1 V_2(\mathbb{1} - T_3)^{-1}\| < 1$ and we can expand in a Neumann series

$$(\mathbb{1} - \kappa V_1 V_2(\mathbb{1} - T_3)^{-1})^{-1} = \sum_{j=0} \kappa^j [V_1 V_2(\mathbb{1} - T_3)^{-1}]^j.$$

Using resummation, we obtain that if E is sufficiently negative we have

$$S_W(E)^{-1} = (\mathbb{1} - T_3)^{-1} + \kappa(\mathbb{1} - T_3)^{-1} V_1 \left(\mathbb{1}_2 - \kappa V_2(\mathbb{1} - T_3)^{-1} V_1\right)^{-1} V_2(\mathbb{1} - T_3)^{-1}. \tag{4.11}$$

Both the left-hand and the right-hand sides define meromorphic functions for $\mathrm{Re}(E) < -1/4$; hence, we can use the right-hand side to extend $S_W(E)^{-1}$ everywhere where the Birman-Schwinger operator exists. This proves one implication.

Conversely, if we define

$$A := \kappa V_2(\mathbb{1} - T_3)^{-1} V_1,$$

Equation (4.11) implies

$$\kappa V_2 S_W(E)^{-1} V_1 = A + A(\mathbb{1} - A)^{-1} A = -\mathbb{1} + (\mathbb{1} - A)^{-1}$$

or

$$(\mathbb{1} - A)^{-1} = \mathbb{1} + \kappa V_2 S_W(E)^{-1} V_1. \tag{4.12}$$

Now we can extend $(\mathbb{1} - A)^{-1}$ using the right-hand side. This concludes the proof. □

Let V_1 and V_2 be as in the above proof. Then the discrete eigenvalues E of H_κ for $0 < \kappa < K$ are those $E < -1/4$ for which the inverse of the Birman-Schwinger operator (4.8) does not exist on $[L^2(\mathbb{R})]^2$. In Fourier representation, the operator $(\mathbb{1} - T_3)^{-1}$ is given by multiplication with

$$\frac{1}{\sqrt{2\pi}}\left(1 - \frac{1}{\sqrt{s^2 - 4E}}\right)^{-1} = \frac{1}{\sqrt{2\pi}} \frac{2}{s^2 - 4E - 1} + \frac{1}{\sqrt{2\pi}} + \frac{1}{\sqrt{2\pi}} \frac{1}{\sqrt{s^2 - 4E} + 1}. \tag{4.13}$$

The first term on the right hand side has a singularity at $E = -1/4$. As κ becomes small, any possible discrete eigenvalues will be close to $-1/4$, and thus we expect the singular term to be the significant contribution. To simplify notation we define $\varepsilon := -4E - 1 > 0$. Taking the Fourier transform of each term on the right-hand side of (4.13), we get the integral kernel of $(\mathbb{1} - T_3)^{-1}$,

$$\begin{aligned}(\mathbb{1} - T_3)^{-1}(x, y) &= \frac{1}{\sqrt{\varepsilon}} e^{-\sqrt{\varepsilon}|x-y|} + \delta(x - y) + \frac{1}{2\pi} \int_{\mathbb{R}} \frac{e^{is(x-y)}}{\sqrt{s^2 + \varepsilon + 1} + 1}\, \mathrm{d}s \\ &= \frac{1}{\sqrt{\varepsilon}} - \int_0^{|x-y|} e^{-\sqrt{\varepsilon}s}\, \mathrm{d}s + \delta(x - y) + \frac{1}{2\pi} \int_{\mathbb{R}} \frac{e^{is(x-y)}}{\sqrt{s^2 + \varepsilon + 1} + 1}\, \mathrm{d}s. \end{aligned} \tag{4.14}$$

From (4.14) we see that there are four contributions to $V_2(\mathbb{1} - T_3)^{-1} V_1$. We will show that the operators that we get from the three last terms in (4.14) are uniformly bounded for $\varepsilon > 0$. Only the second term may pose problems due to its linear growth, while the third term is the distribution kernel of the identity operator and the fourth term is multiplication by a uniformly bounded function in Fourier space for $\varepsilon > 0$.

We show that the operator corresponding to the second term is uniformly bounded. By the construction of V_1 and V_2, the contribution that might be problematic is the operator with the integral kernel

$$0 \le C(x, y) = \int_{\mathbb{R}^2} T_2^*(x, t) \left(\int_0^{|t-t'|} e^{-\sqrt{\varepsilon}s}\, \mathrm{d}s \right) T_2(t', y)\, \mathrm{d}t\, \mathrm{d}t', \tag{4.15}$$

since the other factors from V_1 and V_2 are bounded. We will show that $C(x, y)$ is the integral kernel of a Hilbert-Schmidt operator. To do that, we need the following result which is based on the Paley-Wiener theorem.[24]

Lemma IV.3. There exists $\alpha > 0$ sufficiently small such that the kernels $T_2(x,y)e^{\alpha|x|}$, $T_2^*(x,y)e^{\alpha|y|}$, $T_1(x,y)e^{\alpha|y|}$, and $T_1(x,y)e^{\alpha|x|}$ are in $L^2(\mathbb{R}^2)$ uniformly in $\varepsilon > 0$.

Proof. We will show that $T_2(x,y)e^{\alpha|x|} \in L^2(\mathbb{R}^2)$ using the Paley-Wiener theorem. The proofs for the other integral kernels are similar and therefore not included. To apply the Paley-Wiener theorem, we must show that $\hat{T}_2(s,t)$ can be analytically continued to a subset of the type

$$\{\xi \in \mathbb{C}^2 : |\mathrm{Im}(\xi)| < a\} \subset \mathbb{C}^2,$$

for some $a > 0$. Write $s = s_1 + is_2$ and $t = t_1 + it_2$, with $s_1, s_2, t_1, t_2 \in \mathbb{R}$, then

$$\hat{T}_2(s,t) = \frac{1}{\pi} \frac{1}{t_1^2 - t_2^2 + 2it_1t_2 + (s_1 - t_1)^2 - (s_2 - t_2)^2 + 2i(s_1 - t_1)(s_2 - t_2) + \varepsilon + 1}.$$

This function has no poles for t_2 and s_2 satisfying $t_2^2 + (s_2 - t_2)^2 < 1$, and is analytic on the subset

$$\left\{\xi \in \mathbb{C}^2 : |\mathrm{Im}(\xi)| < \frac{1}{2}\right\} \subset \mathbb{C}^2.$$

Take $\eta = (s_2, t_2) \in \mathbb{R}^2$ such that $|\eta| < 1/2$ and define $\delta := \varepsilon + 1 - t_2^2 - (s_2 - t_2)^2$. By the choice of η, we get $\delta > 0$, and the norm

$$\|\hat{T}_2(\cdot + i\eta)\|^2_{L^2(\mathbb{R}^2)} \le \frac{1}{\pi^2} \int_{\mathbb{R}^2} \frac{1}{\left(t_1^2 + (s_1 - t_1)^2 + \delta\right)^2} \,\mathrm{d}s_1 \,\mathrm{d}t_1 = \frac{1}{\pi\delta} < \infty.$$

Thus, $\|\hat{T}_{2,0}(\cdot + i\eta)\|_{L^2(\mathbb{R}^2)} < \infty$ for all such $\eta \in \mathbb{R}^2$. Then the Paley-Wiener theorem implies that $e^{\alpha\sqrt{x^2+y^2}} T_2(x,y) \in L^2(\mathbb{R}^2)$ for all $\alpha < 1/2$. This concludes the proof of $T_2(x,y)e^{\alpha|x|} \in L^2(\mathbb{R}^2)$. □

We are now ready to show that $C(x,y)$ is an integral kernel of a Hilbert-Schmidt operator. To do that, we use the following inequality:

$$C(x,y) \le \int_{\mathbb{R}^2} T_2^*(x,t)|t|T_2(t',y)\,\mathrm{d}t\,\mathrm{d}t' + \int_{\mathbb{R}^2} T_2^*(x,t)|t'|T_2(t',y)\,\mathrm{d}t\,\mathrm{d}t', \tag{4.16}$$

which follows from the definition of $C(x,y)$ and the inequality

$$\int_0^{|t-t'|} e^{-\sqrt{\varepsilon}s}\,\mathrm{d}s \le |t - t'| \le |t| + |t'|.$$

We will show that the last the term in (4.16) is in $L^2(\mathbb{R}^2)$ (the proof that the first term is also in $L^2(\mathbb{R}^2)$ is identical). Note that the integral is separable and

$$\int_{\mathbb{R}^2} T_2^*(x,t)|t'|T_2(t',y)\,\mathrm{d}t\,\mathrm{d}t' =: F(x)G(y).$$

We will show that $F, G \in L^2(\mathbb{R})$. Applying the Cauchy-Schwarz inequality with respect to the t-integral and using Lemma IV.3, we find

$$\begin{aligned}\|F\|^2_{L^2(\mathbb{R})} &= \int_{\mathbb{R}} \left|\int_{\mathbb{R}} T_2^*(x,t)\,\mathrm{d}t\right|^2 \mathrm{d}x = \int_{\mathbb{R}} \left|\int_{\mathbb{R}} T_2^*(x,t)e^{\alpha|t|}e^{-\alpha|t|}\,\mathrm{d}t\right|^2 \mathrm{d}x \\ &\le C_\alpha \int_{\mathbb{R}^2} |T_2^*(x,t)|^2 e^{2\alpha|t|}\,\mathrm{d}t\,\mathrm{d}x < \infty,\end{aligned} \tag{4.17}$$

for $\alpha > 0$ sufficiently small. Similarly

$$\begin{aligned}\|G\|^2_{L^2(\mathbb{R})} &= \int_{\mathbb{R}} \left|\int_{\mathbb{R}} |t'|T_2(t',y)\,\mathrm{d}t'\right|^2 \mathrm{d}y \le C_\alpha \int_{\mathbb{R}} \left|\int_{\mathbb{R}} e^{\frac{\alpha}{2}|t'|}T_2(t',y)\,\mathrm{d}t'\right|^2 \mathrm{d}y \\ &= C_\alpha \int_{\mathbb{R}} \left|\int_{\mathbb{R}} e^{-\frac{\alpha}{2}|t'|}e^{\alpha|t'|}T_2(t',y)\,\mathrm{d}t'\right|^2 \mathrm{d}y \le \tilde{C}_\alpha \int_{\mathbb{R}^2} e^{2\alpha|t'|}|T_2(t',y)|^2\,\mathrm{d}t'\,\mathrm{d}y < \infty,\end{aligned}$$

again for $\alpha > 0$ sufficiently small. We conclude that $C(x,y) \in L^2(\mathbb{R}^2)$ uniformly in $\varepsilon > 0$.

Using the expansion in (4.14), the integral kernel of the Birman-Schwinger operator is

$$\mathbb{1}_2 - \kappa \int_{\mathbb{R}^2} V_2(x,t)[(\mathbb{1}-T_3)^{-1}](t,t')V_1(t',y)\,\mathrm{d}t\,\mathrm{d}t' = \mathbb{1}_2 - \frac{\kappa}{\sqrt{\varepsilon}}|\Psi\rangle\langle\Phi| + \kappa B_\varepsilon(x,y), \tag{4.18}$$

where $B_\varepsilon(x,y)$ is the integral kernel of the uniformly bounded operator for $\varepsilon > 0$ that comes from the non-singular terms of (4.14). Also

$$\overline{\Phi(y)} := \int_{\mathbb{R}} V_1(x,y)\,\mathrm{d}x, \quad \Psi(x) := \int_{\mathbb{R}} V_2(x,y)\,\mathrm{d}y. \tag{4.19}$$

The functions Ψ and Φ are in $L^2(\mathbb{R})$ and let us prove this for Ψ. From the above definition and from (4.9), we see that it is enough to prove that $\int_{\mathbb{R}} T_2^*(x,t)dt$ belongs to $L^2(\mathbb{R})$. But this is exactly what we did in (4.17).

By the usual factorization trick, the operator in (4.18) is invertible if and only if

$$\mathbb{1}_2 - \frac{\kappa}{\sqrt{\varepsilon}}|\Psi\rangle\langle\Phi|(\mathbb{1}_2 + \kappa B_\varepsilon)^{-1}$$

is invertible. The later operator is not invertible if and only if ε is a zero of the following function:

$$(0,\infty) \ni \varepsilon \mapsto 1 - \frac{\kappa}{\sqrt{\varepsilon}}\langle\Phi|(\mathbb{1}_2 + \kappa B_\varepsilon)^{-1}|\Psi\rangle \in \mathbb{R}.$$

Introduce the new variable $r^2 = \varepsilon$. The above function has a positive root ε_0 if and only if the map

$$[-1,1] \ni r \mapsto f_\kappa(r) := \kappa\langle\Phi|(\mathbb{1}_2 + \kappa B_{r^2})^{-1}|\Psi\rangle \in [-1,1]$$

has a positive fixed point $r_0 > 0$ and $r_0 = \sqrt{\varepsilon_0}$.

It is not difficult to extend the methods we used for proving that B_ε was uniformly bounded in $\varepsilon > 0$ in order to show that actually all the ε dependent quantities are norm differentiable with globally bounded derivatives on $\varepsilon > 0$. Thus f_κ becomes a contraction if κ is small enough and its unique fixed point r_0 can be computed by iteration starting from $r = 0$.

Using the definitions of V_1 and V_2 (in which we put $\varepsilon = 0$ or equivalently $E = -1/4$) we can calculate the inner product $\langle\Phi,\Psi\rangle$ to get

$$\langle\Phi,\Psi\rangle|_{\varepsilon=0} = 8\kappa\left(\frac{4}{\pi} - 1\right) + \mathcal{O}(\kappa^2) > 0.$$

Thus $r_0 \sim \kappa\langle\Phi,\Psi\rangle \sim \kappa^2 > 0$ if κ is small enough which leads to $\varepsilon_0 = r_0^2 \sim \kappa^2\langle\Phi,\Psi\rangle^2 \sim \kappa^4$. Consequently, the leading order behaviour of the discrete eigenvalue $E(\kappa)$ of H_κ for κ sufficiently small is

$$E(\kappa) = -\frac{1}{4} - 16\left(\frac{4}{\pi} - 1\right)^2\kappa^4 + \mathcal{O}(\kappa^5),$$

where we used the formula $\varepsilon = -4E - 1 > 0$. This concludes the first part of the proof of Theorem II.1.

We will now prove that the ground state energy is always non-degenerate (when it exists) by first showing that the heat semigroup e^{-tH_κ} is positivity improving. Some key formulas from Ref. 25 give the explicit expression of the heat kernel of $-\mathrm{d}^2/\mathrm{d}y^2 + \kappa\delta(y)$ from which we conclude that the integral kernel of

$$e^{-t(-\frac{1}{2}\Delta+\kappa\delta(y))}(x,y;x',y') = e^{t\frac{1}{2}\frac{\mathrm{d}^2}{\mathrm{d}x^2}}(x,x')e^{-t(-\frac{1}{2}\frac{\mathrm{d}^2}{\mathrm{d}y^2}+\kappa\delta(y))}(y,y'), \quad t > 0$$

is positive and point-wise smaller than $e^{t\frac{1}{2}\Delta}(x,y;x',y')$. Applying the analogue of the Dyson formula between e^{-tH_κ} and $e^{-t(-\frac{1}{2}\Delta+\kappa\delta(y))}$ (one has to be careful when deriving it due to the singularity of the delta "potentials"), we see that the integral kernel of e^{-tH_κ} is larger than or equal to that of $e^{-t(-\Delta+\kappa\delta(y))}$; hence, it is also positivity improving. The Perron-Frobenius theorem[26] then guarantees the non-degeneracy of the lowest eigenvalue of H_κ, provided that such an eigenvalue exists.

In order to prove that a discrete eigenvalue exists for all $\kappa \in (0, 1/\sqrt{2})$, we first need to extend our previous analysis to negative κ's. It is not difficult to see from the expression of H_κ that the previous existence result also holds for small negative $\kappa \neq 0$ as well. The family H_κ is analytic of type B in the sense of Kato. The regular analytic perturbation theory allows one to extend the construction of a real analytic ground state energy $E(\kappa)$ from a neighborhood of $\kappa \neq 0$ to some maximal open intervals $I_\pm$, respectively, included in $(0, 1/\sqrt{2})$ and $(-1/\sqrt{2}, 0)$. The only reason for which the right endpoint of I_+ might not go all the way to $1/\sqrt{2}$ is that $E(\kappa)$ might start increasing and eventually hit the bottom of the essential spectrum (i.e., $-1/4$) at some $\kappa_+ < 1/\sqrt{2}$. We will show that this is not possible.

Fix $\epsilon > 0$ small enough for which we know that $E(\pm\epsilon)$ exist. Then we can construct two families of real analytic normalized eigenvectors Ψ_κ on $I_\pm$, starting from some given eigenvectors at $\kappa = \pm\epsilon$.

The operator which implements the interchange of x with y is denoted by U and acts as $(Uf)(x, y) = f(y, x)$. It is unitary and $U = U^{-1}$. Moreover, we have

$$UH_\kappa U^{-1} = H_{-\kappa}, \quad H_\kappa U^{-1}\Psi_{-\kappa} = E(-\kappa)U^{-1}\Psi_{-\kappa}.$$

This shows that $E(-\kappa)$ is also an eigenvalue for H_κ, hence $E(\kappa) \leq E(-\kappa)$. By a similar argument we also obtain that $E(-\kappa) \leq E(\kappa)$; hence, $E(\kappa) = E(-\kappa)$ as long as they exist. Moreover, there must exist a unimodular complex number $e^{i\phi(k)}$ (the phase can be chosen to be smooth on $|\kappa| > \epsilon$) such that

$$\Psi_\kappa(x, y) = e^{i\phi(k)}\Psi_{-\kappa}(y, x), \quad \kappa \in I_\pm. \tag{4.20}$$

All the quantities defined above are smooth if $\kappa \neq 0$, but the eigenvectors are not *a priori* κ-differentiable in the $H^1(\mathbb{R}^2)$ norm, only in $L^2(\mathbb{R}^2)$. We can formally apply the Feynman-Hellmann formula to the quadratic form and get

$$E'(\kappa) = \int_{\mathbb{R}} (|\Psi_\kappa(x, 0)|^2 - |\Psi_\kappa(0, x)|^2)dx. \tag{4.21}$$

The rigorous proof of this identity is based on the following identity:

$$\frac{1}{1 + \alpha E(\kappa)} = \langle \Psi_\kappa, (1 + \alpha H_\kappa)^{-1}\Psi_\kappa \rangle, \quad 0 < \alpha \ll 1,$$

in which we now can differentiate with respect to κ in the norm topology and after that take the limit $\alpha \downarrow 0$.

We will now show that there cannot exist a $\kappa \in I_+$ such that $E'(\kappa) > 0$. Assume the contrary and consider such a κ. Define the vector $\Phi(x, y) = \Psi_{-\kappa}(y, x)$ and choose $\kappa' \in I_+$ with $\kappa' > \kappa$. Φ is a normalized vector which belongs to the form domain of $H_{\kappa'}$. First using the min-max principle and second (4.20), we have

$$E(\kappa') \leq \langle \Phi, H_{\kappa'}\Phi \rangle = E(\kappa) + (\kappa' - \kappa) \int_{\mathbb{R}} (|\Phi(t, 0)|^2 - |\Phi(0, t)|^2)dt.$$

Taking the limit $\kappa' \downarrow \kappa$ in $(E(\kappa') - E(\kappa))/(\kappa' - \kappa)$ leads to

$$E'(\kappa) \leq \int_{\mathbb{R}} (|\Phi(t, 0)|^2 - |\Phi(0, t)|^2)dt. \tag{4.22}$$

Due to (4.20) we have $|\Phi(t, 0)|^2 = |\Psi_\kappa(0, t)|^2$ and $|\Phi(0, t)|^2 = |\Psi_\kappa(t, 0)|^2$; hence, (4.21) implies that

$$\int_{\mathbb{R}} (|\Phi(t, 0)|^2 - |\Phi(0, t)|^2)dt = -\int_{\mathbb{R}} (|\Psi_\kappa(t, 0)|^2 - |\Psi_\kappa(0, t)|^2)dt = -E'(\kappa). \tag{4.23}$$

Introducing this identity back into (4.22), we obtain $E'(\kappa) \leq 0$. We conclude that $E'(\kappa) \leq 0$ for all $\kappa \in I_+$, hence $E(\kappa) \leq E(\epsilon) < -1/4$ for $\kappa \in I_+$ which insures the existence of a positive minimal distance between $E(\kappa)$ and the essential spectrum. Consequently, the right endpoint κ_+ of I_+ cannot be smaller than $1/\sqrt{2}$ because in that case $E(\kappa_+) := \lim_{\kappa \uparrow \kappa_+} E(\kappa)$ would be an eigenvalue, thus I_+ could be extended a bit to the right of κ_+ by analytic perturbation theory. Hence the operator H_κ must have at least one eigenvalue for $0 < \kappa \leq 1/\sqrt{2}$. This concludes the proof of Theorem II.1.

V. PROOF OF THEOREM II.2

In this section we prove the second main result, namely, that if $\tilde{\kappa} > 1$ is fixed, then $H_{\kappa,\tilde{\kappa}}$ has no discrete eigenvalues for κ in a connected neighborhood of $+\infty$. The proof is based on a similar method as used in Sec. IV.

Since H_κ and $H_{\kappa,\tilde{\kappa}}$ only differ in the positive interaction term while the bottom of the essential spectrum is given by the negative interaction terms, we have that $\sigma_{ess}(H_{\kappa,\tilde{\kappa}}) = \sigma_{ess}(H_\kappa)$. We assume that $\kappa \geq 1/\sqrt{2}$. Then Lemma III.1 implies that

$$\sigma_{ess}(H_{\kappa,\tilde{\kappa}}) = \left[-\frac{\kappa^2}{2}, \infty\right).$$

The framework described in Sec. III is easily generalized to the operator $H_{\kappa,\tilde{\kappa}}$. Consequently, $E < -\kappa^2/2$ is a discrete eigenvalue of $H_{\kappa,\tilde{\kappa}}$ if and only if the inverse of the operator $\mathcal{G}_{\kappa,\tilde{\kappa}}(E)$ does not exist on $[L^2(\mathbb{R})]^3$, where $\mathcal{G}_{\kappa,\tilde{\kappa}}(E)$ is given by

$$\mathcal{G}_{\kappa,\tilde{\kappa}}(E) = g^{-1} + \tau R_0(E)\tau^*,$$

and $\tau R_0(E)\tau^*$ is as before but g is changed to $\mathrm{diag}\{-\kappa, \tilde{\kappa}, -1\}$. To study when the operator $\mathcal{G}_{\kappa,\tilde{\kappa}}(z)$ is invertible, we scale it using the unitary operator U_κ which acts on $L^2(\mathbb{R})$ by $[U_\kappa f](x) = \sqrt{\kappa} f(\kappa x)$. We have

$$[U_\kappa \hat{T}_1(E) U_\kappa^* f](x) = \frac{1}{\pi\kappa} \int_{\mathbb{R}} \frac{1}{x^2 + y^2 - \frac{2E}{\kappa^2}} f(y)\, \mathrm{d}y.$$

Define a rescaled energy $\varepsilon := -2E/\kappa^2 > 1$. Thus $U_\kappa \hat{T}_1(E) U_\kappa^* = \frac{1}{\kappa}\hat{T}_1(-\varepsilon)$. Equivalent results hold for $\hat{T}_0, \hat{T}_2, \hat{T}_2^*$ and $\hat{T}_3$. Consequently, the operator $\mathcal{G}_{\kappa,\tilde{\kappa}}(E)$ is unitarily equivalent to the operator,

$$G_{\kappa,\tilde{\kappa}}(-\varepsilon) := \begin{bmatrix} -\frac{1}{\kappa} & 0 & 0 \\ 0 & \frac{1}{\tilde{\kappa}} & 0 \\ 0 & 0 & -\mathbb{1} \end{bmatrix} + \frac{1}{\kappa} \begin{bmatrix} T_0(-\varepsilon) & T_1(-\varepsilon) & T_2^*(-\varepsilon) \\ T_1(-\varepsilon) & T_0(-\varepsilon) & T_2^*(-\varepsilon) \\ T_2(-\varepsilon) & T_2(-\varepsilon) & T_3(-\varepsilon) \end{bmatrix}. \tag{5.1}$$

As mentioned the strategy, we apply to show the absence of discrete eigenvalues is basically the same as in Sec. IV, i.e., some applications of Feshbach's formula and the Birman-Schwinger principle. So we begin by choosing the orthogonal projection Π on $[L^2(\mathbb{R})]^3$ which satisfies

$$\Pi G_{\kappa,\tilde{\kappa}}(-\varepsilon)\Pi \cong \frac{1}{\kappa} \begin{bmatrix} -\mathbb{1} + T_0(-\varepsilon) & T_1(-\varepsilon) \\ T_1(-\varepsilon) & \frac{\kappa}{\tilde{\kappa}} + T_0(-\varepsilon) \end{bmatrix}, \tag{5.2}$$

on $\Pi[L^2(\mathbb{R})]^3$. We will also need the projection on the orthogonal subspace of $\Pi[L^2(\mathbb{R})]^3$, which is defined by $\Pi^\perp := \mathbb{1} - \Pi$.

Lemma V.1. Let $G_{\kappa,\tilde{\kappa}}(-\varepsilon)$ be given by (5.1). Then $R(\varepsilon) := [\Pi^\perp G_{\kappa,\tilde{\kappa}}(-\varepsilon)\Pi^\perp]^{-1}$ exists as a bounded operator on the proper subspace for all $\varepsilon > 1$ and $\kappa > 1/\sqrt{2}$.

Proof. By the definition of $\Pi^\perp$ we have $\Pi^\perp G_{\kappa,\tilde{\kappa}}(-\varepsilon)\Pi^\perp \cong -\mathbb{1} + \kappa^{-1} T_3(-\varepsilon)$. We need to check the invertibility of $\mathbb{1} - \kappa^{-1} T_3(-\varepsilon)$ on $L^2(\mathbb{R})$. In the Fourier representation, this operator is a multiplication operator with the function

$$\left(1 - \frac{1}{\kappa} \frac{1}{\sqrt{s^2 + 2\varepsilon}}\right)^{-1}. \tag{5.3}$$

Thus, the norm $\|\kappa^{-1} T_3\| < 1/(\kappa\sqrt{2}) \leq 1$ for all $\kappa \geq 1/\sqrt{2}$ and $\varepsilon > 1$. Consequently, $\Pi^\perp G_\kappa(-\varepsilon)\Pi^\perp$ is invertible on $L^2(\mathbb{R})$ for all $\kappa > 1/\sqrt{2}$ and $\varepsilon > 1$. □

By Feshbach's formula and Lemma V.1, the inverse of $G_{\kappa,\tilde{\kappa}}(-\varepsilon)$ exists if the inverse of

$$S_W(\varepsilon) := \Pi G_{\kappa,\tilde{\kappa}}(-\varepsilon)\Pi - \Pi G_{\kappa,\tilde{\kappa}}(-\varepsilon)\Pi^\perp R(\varepsilon)\Pi^\perp G_{\kappa,\tilde{\kappa}}(-\varepsilon)\Pi \tag{5.4}$$

exists as an operator on $[L^2(\mathbb{R})]^2$. In order to simplify notation, we stop writing the explicit dependence on ε of the various T-operators. We get the following expression for $S_W(\varepsilon)$:

$$S_W(\varepsilon) \cong \begin{bmatrix} -\mathbb{1} + T_0 & T_1 \\ T_1 & \frac{\kappa}{\tilde{\kappa}} + T_0 \end{bmatrix} + \frac{1}{\kappa} \begin{bmatrix} T_2^* \\ T_2^* \end{bmatrix} \left(\mathbb{1} - \frac{1}{\kappa} T_3 \right)^{-1} \begin{bmatrix} T_2 & T_2 \end{bmatrix}. \tag{5.5}$$

To find the conditions for the inverse of $S_W(\varepsilon)$ to exist on $[L^2(\mathbb{R})]^2$, we apply Feshbach's formula again. Consequently, we need to define another pair of orthogonal projections $\tilde{\Pi}$ and $\tilde{\Pi}^\perp := \mathbb{1} - \tilde{\Pi}$ on $[L^2(\mathbb{R})]^2$ such that

$$\tilde{\Pi} S_W(\varepsilon) \tilde{\Pi} \cong -\mathbb{1} + T_0 + \frac{1}{\kappa} T_2^* (\mathbb{1} - \kappa^{-1} T_3)^{-1} T_2 \quad \text{on} \quad L^2(\mathbb{R}). \tag{5.6}$$

Lemma V.2. Let $S_W(\varepsilon)$ be given by (5.5), and let $\tilde{\Pi}^\perp$ be the orthogonal projection on $[L^2(\mathbb{R})]^2$ such that

$$\tilde{\Pi}^\perp S_W(\varepsilon) \tilde{\Pi}^\perp \cong \frac{\kappa}{\tilde{\kappa}} + T_0 + \frac{1}{\kappa} T_2^* (\mathbb{1} - \kappa^{-1} T_3)^{-1} T_2, \tag{5.7}$$

on $L^2(\mathbb{R})$. Then $\tilde{R}(\varepsilon) := [\tilde{\Pi}^\perp S_W(\varepsilon) \tilde{\Pi}^\perp]^{-1}$ exists on the proper subspace for all $\kappa \geq 1/\sqrt{2}$ and $\varepsilon > 1$.

Proof. The proof follows from the fact that T_0 and $\kappa^{-1} T_2^* (\mathbb{1} - \kappa^{-1} T_3)^{-1} T_2$ are bounded and positive for all $\kappa \geq 1/\sqrt{2}$ and $\varepsilon > 1$. □

Lemma V.2 and Feshbach's formula implies that the inverse of $G_{\kappa,\tilde{\kappa}}(\varepsilon)$ exists if the inverse of

$$\tilde{S}_W(\varepsilon) \cong \mathbb{1} - T_0 - \frac{1}{\kappa} T_2^* (\mathbb{1} - \kappa^{-1} T_3)^{-1} T_2 + W_{\kappa,\tilde{\kappa}}(\varepsilon) \tag{5.8}$$

exists as an operator on $L^2(\mathbb{R})$, where

$$W_{\kappa,\tilde{\kappa}}(\varepsilon) := D \left(\frac{\kappa}{\tilde{\kappa}} + T_0 + \frac{1}{\kappa} T_2^* \left(\mathbb{1} - \frac{1}{\kappa} T_3 \right)^{-1} T_2 \right)^{-1} D, \tag{5.9}$$

$$D := T_1 + \frac{1}{\kappa} T_2^* \left(\mathbb{1} - \frac{1}{\kappa} T_3 \right)^{-1} T_2. \tag{5.10}$$

The idea is to apply the Birman-Schwinger principle to study for which values of $\varepsilon > 1$ and $\kappa \geq 1/\sqrt{2}$ the inverse of $\tilde{S}_W(\varepsilon)$ does not exist on $L^2(\mathbb{R})$. Before we do that we rewrite $\tilde{S}_W(\varepsilon)$ a bit. Factorizing $\kappa/\tilde{\kappa}$ in $W_{\kappa,\tilde{\kappa}}(\varepsilon)$ we can write

$$\tilde{S}_W(\varepsilon) \cong \mathbb{1} - T_0 + \frac{1}{\kappa} \widetilde{W}_{\kappa,\tilde{\kappa}}, \tag{5.11}$$

where

$$\widetilde{W}_{\kappa,\tilde{\kappa}} = -T_2^* \left(\mathbb{1} - \frac{1}{\kappa} T_3 \right)^{-1} T_2 + \tilde{\kappa} D \left(\mathbb{1} + \frac{\tilde{\kappa}}{\kappa} T_0 + \frac{\tilde{\kappa}}{\kappa^2} T_2^* \left(\mathbb{1} - \frac{1}{\kappa} T_3 \right)^{-1} T_2 \right)^{-1} D. \tag{5.12}$$

We are now ready to construct the Birman-Schwinger operator for $\tilde{S}_W(\varepsilon)$ given by (5.11).

Proposition V.3. Let $\tilde{S}_W(\varepsilon)$ be as in (5.11), and let $\tilde{\kappa} > 0$ be fixed, $\kappa \geq 1/\sqrt{2}$ and $\varepsilon > 1$. Then there exists bounded operators $V_1 : [L^2(\mathbb{R})]^2 \to L^2(\mathbb{R})$ and $V_2 : L^2(\mathbb{R}) \to [L^2(\mathbb{R})]^2$ such that $\tilde{S}_W(\varepsilon)$ is invertible if and only if

$$\mathbb{1}_2 + \frac{1}{\kappa} V_2 (\mathbb{1} - T_0)^{-1} V_1 \tag{5.13}$$

is invertible on $[L^2(\mathbb{R})]^2$.

Proof. The proof is almost identical to the proof of Theorem IV.2, so we will only describe the construction of $V_1 : [L^2(\mathbb{R})]^2 \to L^2(\mathbb{R})$ and $V_2 : L^2(\mathbb{R}) \to [L^2(\mathbb{R})]^2$. We need V_1 and V_2 to have the property that

$$V_1 V_2 = \tilde{W}_{\kappa,\tilde{\kappa}}.$$

Let $\Psi \in L^2(\mathbb{R})$ and let D be as in (5.10). Define the operator $V_2 : L^2(\mathbb{R}) \to [L^2(\mathbb{R})]^2$ by

$$V_2\Psi = \begin{bmatrix} -\left(\mathbb{1} - \frac{1}{\kappa}T_3\right)^{-\frac{1}{2}} T_2\Psi \\ \left(\mathbb{1} + \frac{\tilde{\kappa}}{\kappa}T_0 + \frac{\tilde{\kappa}}{\kappa^2}T_2^*\left(\mathbb{1} - \frac{1}{\kappa}T_3\right)^{-1}T_2\right)^{-1/2} D\Psi \end{bmatrix}. \tag{5.14}$$

Similarly, let $\Phi = [\Phi_1, \Phi_2]^T \in [L^2(\mathbb{R})]^2$. We define the operator $V_1 : [L^2(\mathbb{R})]^2 \to L^2(\mathbb{R})$ by

$$\begin{aligned} V_1\Phi &= \begin{bmatrix} T_2^*\left(\mathbb{1} - \frac{1}{\kappa}T_3\right)^{-\frac{1}{2}}, & \tilde{\kappa}D\left(\mathbb{1} + \frac{\tilde{\kappa}}{\kappa}T_0 + \frac{\tilde{\kappa}}{\kappa^2}T_2^*\left(\mathbb{1} - \frac{1}{\kappa}T_3\right)^{-1}T_2\right)^{-1/2} \end{bmatrix} \begin{bmatrix} \Phi_1 \\ \Phi_2 \end{bmatrix} \\ &= T_2^*\left(\mathbb{1} - \frac{1}{\kappa}T_3\right)^{-\frac{1}{2}}\Phi_1 + \tilde{\kappa}D\left(\mathbb{1} + \frac{\tilde{\kappa}}{\kappa}T_0 + \frac{\tilde{\kappa}}{\kappa^2}T_2^*\left(\mathbb{1} - \frac{1}{\kappa}T_3\right)^{-1}T_2\right)^{-1/2}\Phi_2. \end{aligned} \tag{5.15}$$

For $\Psi \in L^2(\mathbb{R})$ we find that $V_1V_2\Psi$ is given by

$$V_1V_2\Psi = \tilde{W}_{\kappa,\tilde{\kappa}}\Psi$$

and we have our factorization. □

The strategy to show an absence of discrete eigenvalues is to find a necessary condition which any eigenvalue must satisfy, and then show that for every fixed $\tilde{\kappa} > 1$ and for any κ larger than some value κ_M (depending on $\tilde{\kappa}$) the above necessary condition cannot be satisfied.

The first important remark is that both V_1 and V_2 have finite limits when $\kappa \to \infty$, uniformly in $\epsilon > 1$. Thus the operator in (5.13) is always invertible if ϵ is larger than some value $\varepsilon_\kappa > 1$. Moreover, this ε_κ converges to 1 when κ goes to infinity. Therefore we know *a priori* that the points where (5.13) might not be invertible on $[L^2(\mathbb{R})]^2$ must obey $\varepsilon \in (1, 2)$ if κ is larger than some value κ_1. Let us expand the integral kernel of $(\mathbb{1} - T_0)^{-1}$ around the threshold $\varepsilon = 1$ and introduce the variable λ (see below) to find the following:

$$(\mathbb{1} - T_0)^{-1}(x, y) = \frac{1}{\lambda} - |x - y| + \delta(x - y) + \frac{1}{2\pi}\int_{\mathbb{R}} \frac{e^{is(x-y)}}{\sqrt{s^2 + 1} + 1}\,\mathrm{d}s + \mathcal{O}(\lambda), \quad \lambda := \sqrt{\varepsilon - 1}. \tag{5.16}$$

Using this expansion of the integral kernel, the Birman-Schwinger operator (5.13) can be written as

$$\mathbb{1}_2 + \frac{1}{\kappa}\frac{|\Psi\rangle\langle\Phi|}{\lambda} + \frac{1}{\kappa}B, \tag{5.17}$$

where the operator B is given by the product of V_2, the non-singular terms of (5.16) and V_1. Using the same approach as in Sec. IV, we can show that B is uniformly bounded for $\lambda > 0$ and $\kappa \geq 1/\sqrt{2}$. Furthermore, $|\Psi\rangle$ and $\langle\Phi|$ in (5.17) is given by

$$|\Psi\rangle := \int_{\mathbb{R}} V_2(x, x')\,\mathrm{d}x', \quad \langle\Phi| := \int_{\mathbb{R}} V_2(y', y)\,\mathrm{d}y', \tag{5.18}$$

and Ψ and Φ can be shown to be in $L^2(\mathbb{R}^2)$ using Lemma IV.3. Let us rewrite the Birman-Schwinger operator in (5.17),

$$\mathbb{1}_2 + \frac{1}{\kappa}\frac{|\Psi\rangle\langle\Phi|}{\lambda} + \frac{1}{\kappa}B = \left(\mathbb{1}_2 + \frac{1}{\kappa}\frac{|\Psi\rangle\langle\Phi|}{\lambda}\left[\mathbb{1}_2 + \frac{1}{\kappa}B\right]^{-1}\right)\left(\mathbb{1}_2 + \frac{1}{\kappa}B\right). \tag{5.19}$$

But since B is uniformly bounded in both $\lambda > 0$ and $\kappa > 1/\sqrt{2}$, there exists some $\kappa_2 \geq \kappa_1 > 1/\sqrt{2}$ such that if $\kappa > \kappa_2$ we have that $\left(\mathbb{1}_2 + \kappa^{-1}B\right)^{-1}$ exists on $[L^2(\mathbb{R})]^2$ for all $\lambda > 0$. Consequently, for $\kappa > \kappa_2$ the inverse of the Birman-Schwinger operators exists at $\lambda \in (0, 1)$ if and only if

$$\left(\mathbb{1}_2 + \frac{1}{\kappa}\frac{|\Psi\rangle\langle\Phi|}{\lambda}\left[\mathbb{1}_2 + \frac{1}{\kappa}B\right]^{-1}\right)^{-1}, \quad \kappa > \kappa_2 \tag{5.20}$$

exists. Using Feshbach's formula with a rank-1 projection constructed from $|\Psi\rangle$ we get the only values of $0<\lambda<1$ where (5.20) might not exist are those which solve

$$\lambda+\frac{1}{\kappa}\left\langle\Phi,\left[\mathbb{1}_2+\frac{1}{\kappa}B\right]^{-1}\Psi\right\rangle=0,\quad \kappa>\kappa_2. \tag{5.21}$$

Thus if $\kappa>\kappa_2$, any discrete eigenvalue of $H_{\kappa,\tilde{\kappa}}$ has to have a corresponding $\lambda\in(0,1)$ which is a solution to (5.21).

Let us define the function

$$f(\lambda,\kappa):=\left\langle\Phi,\left[\mathbb{1}_2+\frac{1}{\kappa}B\right]^{-1}\Psi\right\rangle,\quad \lambda\in[0,1],\quad \kappa\geq\kappa_2.$$

We are interested in finding possible values of $\lambda\in(0,1)$ where the graphs of $f(\lambda,\kappa)$ and $-\kappa\lambda$ cross each other. The function f is jointly uniformly continuous. Moreover, by explicit computation we obtain

$$\lim_{\kappa\to\infty}f(0,\kappa)=2\pi\left(\tilde{\kappa}\int_{\mathbb{R}}\hat{T}_1(0,s)^2\,\mathrm{d}s-\int_{\mathbb{R}}\hat{T}_2^*(0,s)\hat{T}_2(s,0)\,\mathrm{d}s\right)\Big|_{\lambda=0}=\tilde{\kappa}-1. \tag{5.22}$$

Thus there exists $\kappa_3>\kappa_2$ such that

$$f(0,\kappa)\geq(\tilde{\kappa}-1)/2,\quad \kappa>\kappa_3.$$

From the uniform continuity of f, we obtain the existence of some $\delta\in(0,1)$ such that

$$f(\lambda,\kappa)\geq(\tilde{\kappa}-1)/4>0,\quad \lambda\in(0,\delta),\quad \kappa>\kappa_3. \tag{5.23}$$

Moreover, $|f(\lambda,\kappa)|$ is bounded by some constant K for all λ and κ. This implies that if $\kappa>\kappa_3$, the value of $f(\cdot,\kappa)$ is positive on $(0,\delta)$ and is larger than $-K$ on $[\delta,1)$. At the same time, $-\lambda\kappa$ is negative on $(0,\delta)$ and less than $-\kappa\delta$ on $[\delta,1)$. Define $\kappa_M=\max\{\kappa_3,K/\delta\}$. Then the two graphs cannot intersect each other if $\kappa>\kappa_M$ and this completes the proof of absence of eigenvalues.

Now let us consider the case $0<\tilde{\kappa}<1$. All our previous considerations remain true up to and including the identity (5.22) where now $\tilde{\kappa}-1<0$, hence

$$f(0,\kappa)\leq(\tilde{\kappa}-1)/2<0,\quad \kappa>\kappa_3. \tag{5.24}$$

Also, as before, $f(\lambda,\kappa)\geq-K$ for all λ and κ.

Consider the function $g(\lambda,\kappa)=\lambda\kappa+f(\lambda,\kappa)$ with $\lambda\in[0,1]$. We have $g(0,\kappa)=f(0,\kappa)<0$ while $g(1,\kappa)=\kappa+f(1,\kappa)\geq\kappa-K>0$ provided $\kappa>K$. Thus $g(\cdot,\kappa)$ must have a zero in $(0,1)$, and this proves the existence of discrete spectrum for all $\kappa>K$.

VI. PROOF OF COROLLARY II.3

We can now prove the final result, i.e., the existence of a critical charge κ_c which has the property that for every $0<\kappa<\kappa_c$, the operator H_κ has at least one discrete eigenvalue, while if $\kappa\geq\kappa_c$ the discrete spectrum is empty.

The proof has three steps. First, we show that there exists some $\kappa_1\geq1/\sqrt{2}$ such that H_{κ_1} has no discrete spectrum. Second, we show that given such a κ_1, the operator H_κ has empty discrete spectrum for all $\kappa\geq\kappa_1$. Third, we show that κ_c is the smallest of all such κ_1.

Step 1. Let $\kappa>1/\sqrt{2}$ and consider the operator $H_{\kappa,2}$, i.e., with $\tilde{\kappa}=2>1$. Theorem II.2 implies the existence of a $\kappa_M>1/\sqrt{2}$ such that $H_{\kappa,2}$ has no discrete eigenvalues if $\kappa>\kappa_M$.

We know that the operators H_κ and $H_{\kappa,2}$ have the same essential spectrum. Additionally, we have that

$$H_\kappa\geq H_{\kappa,2}\quad\text{if }\kappa\geq2, \tag{6.1}$$

where the inequality should be understood in the sense of quadratic forms. If $\kappa_1=\kappa_M+1$, the operator $H_{\kappa_1,2}$ has no discrete spectrum, hence (6.1) and the min-max principle imply that the discrete spectrum of H_{κ_1} is empty.

Step 2. We will now show that the discrete spectrum of H_κ with $\kappa \geq \kappa_1$ is also empty. Define the unitary operator $U_\kappa : L^2(\mathbb{R}^2) \to L^2(\mathbb{R}^2)$ by $(U_\kappa \Psi)(x, y) = \kappa \Psi(\kappa x, \kappa y)$. Then by direct calculation

$$U_\kappa^{-1} H_\kappa U_\kappa = \kappa^2 \widetilde{H}_\kappa, \quad \tilde{H}_\kappa := -\frac{1}{2}\Delta - \delta(y) + \delta(x) - \frac{1}{\kappa}\delta(x - y).$$

Using the HVZ theorem we can prove that for $\kappa \geq 1/\sqrt{2}$ the essential spectrum of $\tilde{H}_\kappa$ is $[-1/2, \infty)$. Additionally, due to the sign of the κ-dependent term we have

$$\widetilde{H}_\kappa \geq \widetilde{H}_{\kappa_1}, \quad \text{if } \kappa \geq \kappa_1.$$

The operator $\widetilde{H}_{\kappa_1} = \kappa_1^{-2} U_{\kappa_1}^{-1} H_{\kappa_1} U_{\kappa_1}$ has no discrete spectrum. Since the bottom of the essential spectrum of $\widetilde{H}_\kappa$ is constant in κ and equals $-1/2$, the min-max principle implies that $\widetilde{H}_\kappa$ has no discrete spectrum and the same holds true for H_κ.

Step 3. The set S consisting of all the κ_1's considered in the previous two steps is bounded from below by $1/\sqrt{2}$ due to Theorem II.1. Let $\kappa' \geq 1/\sqrt{2}$ be the infimum of S. Assume that κ' does not belong to S. Then there would exist a ground state with energy $E(\kappa') < -\kappa'^2/2$. Using the analytic perturbation theory, we could extend this ground state energy to a small interval centered at κ'; thus, κ' would not belong to the closure of S, contradiction.

Thus $S = [\kappa', \infty)$ and $\kappa_c = \kappa'$. In fact, this proof provides us with an alternative characterisation of κ_c, i.e. κ_c is the right endpoint of the open interval of κ's for which a ground state exists.

VII. CONCLUSIONS

In this paper, we considered the discrete spectrum of the Schrödinger operator for a one-dimensional three-body system with Dirac delta potentials, which models an impurity interacting with an exciton. We have proven that for κ close to zero, there exists a single non-degenerate bound state which behaves like κ^4, and we have explicitly calculated the coefficient of the leading term. The ground state survives when $\kappa \in (0, 1/\sqrt{2})$, but for some charge $\kappa_c > 1/\sqrt{2}$, the ground state energy hits the essential spectrum, and no bound states of the system exists for $\kappa \geq \kappa_c$. We cannot give an explicit value for κ_c, but numerical calculations indicate that $\kappa_c \approx 1.546$.

A future project is to study a related system of an impurity and two oppositely charged particles with multiplicative potentials in both one and two dimensions. While the results are expected to be somehow similar, the technical tools one needs to use are quite different.

ACKNOWLEDGMENTS

J.H. and T.G.P. are supported by the QUSCOPE Center, which is funded by the Villum Foundation. H.C. was partially supported by the Danish Council of Independent Research | Natural Sciences, Grant No. DFF-4181-00042. H.K. was partially supported by the No. MIUR-PRIN2010-11 grant for the project "Calcolo delle variazioni."

[1] C. Rosenthal, J. Chem. Phys. **55**, 2474 (1971).
[2] H. Cornean, P. Duclos, and B. Ricaud, Few-Body Syst. **38**, 125 (2006).
[3] H. Hogreve, Int. J. Quantum Chem. **109**, 1430 (2009).
[4] A. Martin, J.-M. Richard, and T. T. Wu, Phys. Rev. A **52**, 2557 (1995).
[5] A. Martin, *Multiscale Methods in Quantum Mechanics* (Springer, 2004), pp. 69–81.
[6] D. Gridnev, C. Greiner, and W. Greiner, J. Math. Phys. **46**, 052104 (2005).
[7] C. R. de Oliveira and A. A. Verri, J. Math. Phys. **53**, 052104 (2012).
[8] C. R. De Oliveira and A. A. Verri, Ann. Phys. **324**, 251 (2009).
[9] H. Hogreve, J. Phys. A: Math. Theor. **47**, 125302 (2014).
[10] W. Fischer, H. Leschke, and P. Müller, J. Math. Phys. **36**, 2313 (1995).
[11] A. Frost, J. Chem. Phys. **25**, 1150 (1956).
[12] H. Cornean, P. Duclos, and T. Pedersen, Few-Body Syst. **34**, 155 (2004).
[13] T. F. Rønnow, T. G. Pedersen, and H. D. Cornean, Phys. Lett. A **373**, 1478 (2009).
[14] T. G. Pedersen, Phys. Lett. A **379**, 1785 (2015).
[15] R. Brummelhuis and P. Duclos, Few-Body Syst. **31**, 119 (2002).
[16] M. Beau, R. Benguria, R. Brummelhuis, and P. Duclos, J. Phys. A: Math. Theor. **43**, 474005 (2010).
[17] S. Albrecht, L. Reining, R. Del Sole, and G. Onida, Phys. Rev. Lett. **80**, 4510 (1998).

[18] S. Albeverio, F. Gesztesy, R. Hoegh-Krohn, and H. Holden, *Solvable Models in Quantum Mechanics* (Springer Science & Business Media, 1988).
[19] B. Simon, Ann. Phys. **97**, 279 (1976).
[20] H. Cornean, P. Duclos, and B. Ricaud, in *Proceedings of Symposia in Pure Mathematics: Analysis on Graphs and its Applications*, edited by P. Exner, J. Keating, P. Kuchment, T. Sunada, and A. Teplyaev (American Mathematical Society (AMS), 2008), Vol. 77, p. 657.
[21] B. Simon, "Quantum mechanics for Hamiltonians defined as quadratic forms," in *Princeton Series in Physics* (Princeton University Press, 1971).
[22] G. Nenciu, Rev. Mod. Phys. **63**, 91 (1991).
[23] B. Simon, *Functional Integration and Quantum Physics* (Academic Press, 1979), Vol. 86.
[24] M. Reed and B. Simon, *Fourier Analysis, Self-Adjointness* (Elsevier, 1975), Vol. 2.
[25] S. Albeverio, Z. Brzezniak, and L. Dabrowski, J. Funct. Anal. **130**, 220 (1995).
[26] M. Reed and B. Simon, *Analysis of Operators* (Elsevier, 1978), Vol. 4.

Paper B

Magnetoexcitons and Faraday rotation in single-walled carbon nanotubes and graphene nanoribbons

J. Have and T. G. Pedersen

Published in
Physical Review B **97**, 115405 (2018).

Magnetoexcitons and Faraday rotation in single-walled carbon nanotubes and graphene nanoribbons

Jonas Have[1,2,*] and Thomas G. Pedersen[1,3]

[1]*Department of Materials and Production, Aalborg University, DK-9220 Aalborg East, Denmark*
[2]*Department of Mathematical Sciences, Aalborg University, DK-9220 Aalborg East, Denmark*
[3]*Center for Nanostructured Graphene (CNG), DK-9220 Aalborg East, Denmark*

(Received 4 December 2017; published 5 March 2018)

The magneto-optical response of single-walled carbon nanotubes (CNTs) and graphene nanoribbons (GNRs) is studied theoretically, including excitonic effects. Both diagonal and nondiagonal response functions are obtained and employed to compute Faraday rotation spectra. For single-walled CNTs in a parallel field, the results show field-dependent splitting of the exciton absorption peaks caused by brightening a dark exciton state. Similarly, for GNRs in a perpendicular magnetic field, we observe a field-dependent shift of the exciton peaks and the emergence of an absorption peak above the energy gap. Results show that excitonic effects play a significant role in the optical response of both materials, particularly for the off-diagonal tensor elements.

DOI: 10.1103/PhysRevB.97.115405

I. INTRODUCTION

Single-walled carbon nanotubes (CNTs) and graphene nanoribbons (GNRs) are prominent quasi-one-dimensional carbon-based structures defined geometrically as cylindrical tubes and thin strips of graphene, respectively. The two materials are intimately related, since GNRs can be regarded as (and produced from) unrolled CNTs [1,2]. Moreover, both materials have a large number of potential applications in various areas of electronics and optoelectronics [3–6]. The reduced dimensionality and screening of narrow GNRs and small radius CNTs lead to excitons with binding energy on the order of a few hundred meV [7–10]. Therefore, excitons have a strong impact on the optical response of both CNTs [9] and GNRs [11,12] and must be accounted for in models of the optical response.

Excitons are sensitive to a number of external perturbations, such as electric and magnetic fields. For instance, magnetic fields can be used as an effective tool to probe various properties of excitons, including their transport [13] and spatial extent [14]. Additionally, an accurate understanding of the dynamics of magnetoexcitons reveals details of the role played by magnetic fields in optoelectronic devices [15,16]. The electronic and optical properties of CNTs in the presence of a static magnetic field were considered theoretically in a series of papers by Ando [17–19], and the results were later verified experimentally [20–26]. However, the off-diagonal elements of the conductivity tensor were not evaluated in these papers. The presence of an external magnetic field breaks time-reversal symmetry and results in finite off-diagonal conductivity elements [27], also called the Hall conductivities. Calculating the off-diagonal conductivity for CNTs and GNRs is one of the objectives in the present paper. The Hall conductivity gives rise to the optical Hall effect manifesting itself as Faraday rotation [28] of the electromagnetic field, which is important for several electro-optic applications [29,30]. The Faraday rotation for CNTs [28] and GNRs [31] has been calculated in the independent-particle approximation. But, as discussed above, this approximation is not well suited to describe the optical response of CNTs and GNRs. The solution is to include excitonic effects, which we do in the present work.

With respect to GNRs, the amount of theoretical work is rather limited compared to the case of CNTs. The available works either focus on GNRs in the presence of a magnetic field without excitons [32,33] or the converse [11,12] (i.e., including excitons but not an external magnetic field). In the present work, we improve upon this by calculating the magnetoexcitonic response for a range of GNRs.

An additional interesting aspect of quasi-one-dimensional systems, including CNTs, GNRs, and conjugated polymers, is that these can serve as convenient test systems for theoretical methods. Recent years have seen an increase in experimental work on magnetoexcitonic effects in two-dimensional semiconductors such as transition metal dichalcogenides [34–37]. In this class of materials, a number of challenges limit theoretical models of magnetoexcitons to effective-mass models [38]. In comparison, quasi-one-dimensional systems are much less computationally demanding. As a consequence, it is possible to obtain an accurate description of magnetoexcitons in these systems. Thus, we will present calculations of all the elements of the linear optical conductivity tensor for a number of different CNTs and GNRs. Our calculations are based on a tight-binding model that provides the independent-particle properties, while the excitonic properties are obtained from the Bethe-Salpeter equation.

II. THEORETICAL MODELS

In this section, we will briefly describe the applied theoretical models and computational tools. The GNR and CNT structures are illustrated in Fig. 1. In general, both GNRs

*jh@nano.aau.dk

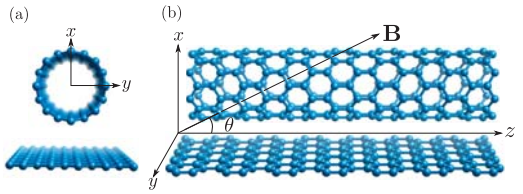

FIG. 1. (a) CNT and GNR structures as seen in the direction of the z axis. (b) Side view of the CNT and GNR structures. The GNR structure is parallel to the yz plane, with a magnetic field at an angle θ to the yz plane and in the xz plane.

and CNTs exist in a variety of geometries. Hence, GNRs are characterized by their width and edge type, whereas CNTs are defined by their chiral index (n,m) that, in turn, determines diameter and chirality [39]. However, in the present work, we limit ourselves to zigzag CNTs with chiral indices $(n,0)$ for $n \in \mathbb{N}_+$, and armchair GNRs characterized by the number of dimer lines N across the ribbon, which we denote by N-AGNRs. We ignore any effects of geometrical relaxation of edge atoms. For calculation of the independent-particle energies and wave functions, we apply a nonorthogonal π-electron nearest-neighbor tight-binding (TB) model. Studies have shown that the single-particle properties of carbon-based materials, e.g., graphene, CNTs, and GNRs, are well described by π-electron TB models [39,40]. The choice of a nonorthogonal (in contrast to the usual orthogonal) TB model is made to break the electron-hole symmetry, as electron-hole symmetry results in Hall conductivities that are identically zero [27,28].

The external magnetic field is introduced via the minimal substitution of the momentum operator $\hat{\mathbf{p}} \mapsto \hat{\boldsymbol{\pi}} = \hat{\mathbf{p}} + e\mathbf{A}$, where $\mathbf{A}$ denotes the magnetic vector potential, related to the magnetic field $\mathbf{B}$ via $\mathbf{B} = \nabla \times \mathbf{A}$. In a TB model, the substitution gives rise to a Peierls phase factor in the hopping integrals t such that $t \mapsto t_{ij} = te^{i\phi_{ij}}$, with the Peierls phase given by [41]

$$\phi_{ij} = \frac{e}{\hbar}\int_{\mathbf{R}_i}^{\mathbf{R}_j} \mathbf{A}\cdot d\mathbf{l}, \tag{1}$$

where $\mathbf{R}_i$ and $\mathbf{R}_j$ denote the location of atoms at site i and j, respectively. For periodic systems in more than one dimension, the phase factor necessarily breaks the translation symmetry. However, given an appropriate choice of gauge, the translation symmetry can be preserved in one-dimensional (1D) systems. This fact is responsible for the relative tractability of 1D magnetoexcitons, in contrast to two and three dimensions (2D, 3D). The appropriate gauge depends on the direction of the magnetic field. As illustrated in Fig. 1, we take the long axis along z and consider a magnetic field $\mathbf{B} = B(\sin\theta\hat{\mathbf{x}} + \cos\theta\hat{\mathbf{z}})$, where θ is the angle between field and long axis, and $B = |\mathbf{B}|$ is the magnetic field strength. For this geometry, the symmetry-preserving gauge is

$$\mathbf{A} = -By(\cos\theta\hat{\mathbf{x}} - \sin\theta\hat{\mathbf{z}}). \tag{2}$$

Below, however, we only consider parallel ($\theta = 0$) and perpendicular ($\theta = \pi/2$) magnetic fields. Moreover, for GNRs we only consider perpendicular fields, since the electronic structure and optical response of GNRs are unaffected by a parallel field.

A. Excited states

Using the independent-particle energies and wave functions, the exciton states of the systems can be found by solving the Bethe-Salpeter equation (BSE) [7,42,43]. The excited states $|\text{exc}\rangle$ can be expanded as

$$|\text{exc}\rangle = \sum_{cvk} \Psi_{cvk}|vk \to ck\rangle, \tag{3}$$

where Ψ_{cvk} are the expansion coefficients, and $|vk \to ck\rangle$ are the singlets of singly excited states between the valence (v) and conduction (c) bands at k. Using the expansion of the excited states in Eq. (3), the BSE is expressed as

$$E_{cvk}\Psi_{cvk} + \sum_{c'v'k'} K_{cvk,c'v'k'}\Psi_{c'v'k'} = E_{\text{exc}}\Psi_{cvk}, \tag{4}$$

$$K_{cvk,c'v'k'} := W_{cvk,c'v'k'} - 2V_{cvk,c'v'k'},$$

where E_{exc} is the exciton energy, $E_{cvk} = E_{ck} - E_{vk}$, $V_{cvk,c'v'k'}$ is the exchange matrix element, and $W_{cvk,c'v'k'}$ is the Coulomb interaction matrix element. We follow Ref. [44] and calculate the exchange and Coulomb interaction matrix elements using an Ohno-type potential, which has been shown to produce results that compare well with more advanced models and experiments for quasi-1D systems [44]. In this approximation, the bare electron-hole interaction takes the form

$$v(\mathbf{r}_e - \mathbf{r}_h) = -U\left[1 + \left(\frac{4\pi\epsilon_0 U}{e^2}\right)^2 |\mathbf{r}_e - \mathbf{r}_h|^2\right]^{-\frac{1}{2}}, \tag{5}$$

where $\mathbf{r}_e$ and $\mathbf{r}_h$ are the position of the electron and hole, respectively, and $U = 11.3$ eV is the Hubbard energy [45]. The screened Coulomb interaction matrix elements are then calculated using $W(\mathbf{r}_e - \mathbf{r}_h) = v(\mathbf{r}_e - \mathbf{r}_h)/\epsilon$, where ϵ is the screening parameter. The Coulomb term is screened by both the self-screening and the screening from the surrounding media. Similarly, the exchange matrix elements can be calculated using $W(\mathbf{r}_e - \mathbf{r}_h) = v(\mathbf{r}_e - \mathbf{r}_h)/\epsilon_{exc}$, where ϵ_{exc} denotes the screening of the exchange term. According to Ref. [46], the exchange term should only be screened by the surrounding media; thus we have that $\epsilon_{exc} < \epsilon$.

It is worth noting that the dimension of the eigenvalue problem in Eq. (4) is given by $N_c \times N_v \times N_k$, where N_c,N_v, and N_k are the number of conduction bands, valence bands, and k points, respectively. Even for a reasonably small system such as the (8,0) CNT, which has 32 atoms in the unit cell and a k grid with 150 points, the Bethe-Salpeter matrix (BSM) has dimension 38 400 × 38 400. Thus, using this method for typical chiral CNTs such as (6,5) CNTs with unit cells containing several hundred atoms is computationally unfeasible.

B. Optical response

The evaluation of the optical conductivity tensor, in the presence of electron-hole interactions, follows that of Ref. [47]. The many-body momentum operator acting on the many-body

ground state is

$$|P_i\rangle := \hat{P}_i|0\rangle = \sqrt{2}\sum_{cvk} p^i_{cvk}\Psi_{cvk}, \tag{6}$$

where $|0\rangle$ is the many-body ground state and $\hat{P}_i$ and p^i_{cvk} are the many-body momentum operator and the single-particle momentum matrix elements in direction $i \in \{x,y,z\}$, respectively. Ignoring the nonresonant terms of the optical conductivity tensor, the real part of the tensor elements can be expressed as [47]

$$\mathrm{Re}\sigma_{ij} = -\frac{e^2}{m^2\omega A}\mathrm{Im}\langle P_i|\hat{G}(\hbar\omega)|P_j\rangle, \tag{7}$$

where $\hbar\omega$ is the photon energy, $\hat{G}(\hbar\omega)$ is the many-body Green's function, and A is the cross-sectional area of the system, where the height of the ribbon and the wall thickness of the tubes is taken to be $d = 3.35$ Å [48]. In terms of the many-body Hamiltonian $\hat{H}$, the Green's function $\hat{G}(\hbar\omega)$ is defined by

$$\hat{G}(\hbar\omega) := \lim_{\eta\to 0^+}\frac{1}{\hbar\omega - \hat{H} + i\eta}. \tag{8}$$

To increase the numerical stability, we use a finite $\eta \approx 1$ meV in Eq. (8), and to add additional broadening to the spectra obtained by Eq. (7), we convolute with a Lorentzian line-shape function having a width Γ.

The off-diagonal tensor elements, i.e., σ_{ij} for $i \neq j$, are the so-called Hall conductivities. This notation stems from the fact that, if the off-diagonal tensor elements are finite, the system exhibits the optical Hall effect, in analogy to the electric Hall effect in the static case. The optical Hall effect is closely related to the Faraday rotation of a material [27,28], whereby the polarization plane of light rotates as the wave propagates in the material under the influence of a magnetic field. The Faraday rotation for a weak magnetic field in the z direction reads [27]

$$\phi = \frac{l}{2c\epsilon_0}\frac{n\mathrm{Re}\sigma_{xy} - \kappa\mathrm{Im}\sigma_{xy}}{n^2+\kappa^2}\rho, \tag{9}$$

where l is the propagation distance of the light, c is the speed of light, ϵ_0 is the vacuum permittivity, ρ is an effective volume fraction of either AGNRs or CNTs in space, and $n + i\kappa$ is the complex refractive index at $B = 0$. In the idealized situation, where either CNTs or AGNRs are packed tightly in space, the volume fraction is $\rho = 1$ and otherwise $0 \leqslant \rho < 1$. For weak magnetic fields the Hall conductivities are linear in B [27], and the Faraday rotation can be expressed $\phi = VlB\rho$, where V is the Verdet constant. Measurements of the Faraday rotation provide a convenient experimental method for determining the optical Hall conductivity, even at low magnetic field strengths [49].

With regards to the diagonalization of the BSM, a significant reduction in computation time can be obtained if one does not need the eigenvalues and eigenstates of the BSE but only the matrix elements of the Green's function, which can be calculated effectively using the Lanczos-Haydock routine [50]. The routine allows for efficient evaluation of matrix elements of the type $\langle u|\hat{G}|u\rangle$ by a recursive tridiagonalization of the Hamiltonian and subsequent evaluation of the matrix element using continued fractions. When convergence of the continued fractions is obtained, the calculations can be truncated. For evaluation of the Hall conductivities involving off-diagonal matrix elements of the type $\langle v|\hat{G}|u\rangle$, one can make use of the relation

$$\langle v+iu|\hat{G}|v+iu\rangle = \langle v|\hat{G}|v\rangle + \langle u|\hat{G}|u\rangle + i2\mathrm{Im}\langle v|\hat{G}|u\rangle \tag{10}$$

and the similar relation for $\langle v+u|\hat{G}|v+u\rangle$ to find the real part of $\langle v|\hat{G}|u\rangle$.

III. RESULTS AND DISCUSSION

In this section, we present and discuss binding energies and optical response of magnetoexcitons for a range of CNT and GNR geometries. All results have been obtained using $t = -3.0$ eV for the hopping integral and $s = 0.1$ for the overlap in the TB model. The spectra are normalized by a factor $\sigma_0 = e^2/d\hbar$ and convoluted with a Lorentzian line-shape function with a broadening of 0.08 eV. Convergence of the Lanczos-Haydock routine was obtained after 2000 iterations. The screening of the Coulomb matrix elements is set to $\epsilon = 3.5$, corresponding to CNTs in an aqueous solution [9]. For the exchange term, we find that a value of $\epsilon_{exc} = 2.5$ is appropriate, similarly to what was used in Ref. [44]. As our primary interest is a qualitative description of the effect of an external magnetic field on the excitonic response, we have used the same screening for the GNR calculations. So far, experimental absorption spectra for AGNRs are only available for AGNRs deposited on some type of metal [51,52]. Metal substrates strongly screen the Coulomb interaction and, hence, suppress the excitonic effects significantly.

We begin our presentation of the results by focusing on the real part of the diagonal optical conductivity elements σ_{zz} and σ_{yy}, denoting the parallel-polarized and cross-polarized absorption, respectively. The first and second column in Fig. 2 show the absorption spectra for (8,0) and (5,0) CNTs, respectively. In the considered photon energy range, there are two dominant peaks in the parallel-polarized exciton absorption of CNTs in the absence of magnetic fields. The peaks correspond to the first and second subband transitions and are typically denoted E_{11} and E_{22}. These spectra show the same features as spectra obtained using more advanced *ab initio* methods [42].

When the magnetic field becomes sufficiently strong, the Ajiki-Ando (AA) [18,19] splitting of the excitonic peaks in the σ_{zz} spectra can be observed. Without Coulomb effects (the dashed lines in Fig. 2), the splitting of the absorption peaks is caused by a field-assisted lifting of the twofold degenerate valence and conduction bands. Coulomb effects, i.e., excitons, lift the degeneracy partially and result in three exciton states: two nondegenerate (one dark and one bright) and a dark state, which is twofold degenerate [45]. The zero-field energy difference between the nondegenerate bright and dark exciton states is denoted Δ_{bd}. The observed splitting of the exciton absorption peak is then caused by the magnetic field brightening the nondegenerate dark exciton state and increasing the energy separation. The energy difference Δ_{bd} was reported in Refs. [19,43] to be proportional to $1/d_t^2$, where d_t is the CNT diameter. Similarly, both the field-dependent

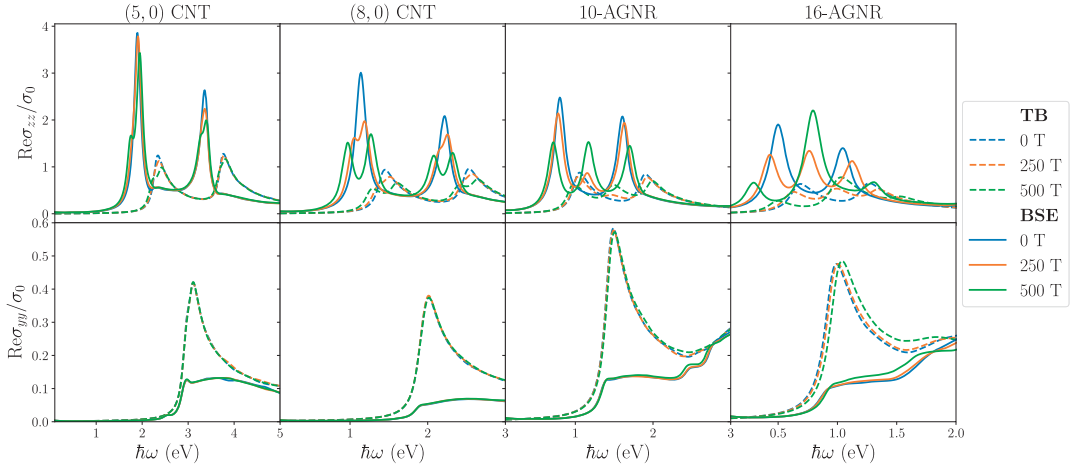

FIG. 2. Real part of the independent-particle (dashed lines) and excitonic (solid lines) diagonal conductivities σ_{zz} and σ_{yy} of (5,0) and (8,0) CNTs, and 10- and 16-AGNRs. The colors of the spectra correspond to the same magnetic field strengths in all plots. For the CNTs, the magnetic field is oriented in the parallel direction, while for GNRs it is oriented in the perpendicular direction.

increase in the energy splitting and the field-dependent change in oscillator strength of the bright and dark excitons depend on the CNT diameter [18,19]. The field-dependent increase in the energy splitting is proportional to d_t, while the changes in oscillator strength of the bright and dark excitons are dampened when Δ_{bd} is increasing[18]. Consequently, the observed splitting is not as clear for the (5,0) CNTs as for the (8,0) CNTs. For experimental observation of the AA splitting, one would need to use either large-diameter CNTs [20–22] or very strong fields [26], as illustrated here. The splitting we observe in the BSE results is comparable to what was reported in Refs. [18] and [19] using the $\mathbf{k}\cdot\mathbf{p}$ model, and what was observed experimentally for (6,5) CNTs in Ref. [26]. The AA splitting is only observed in parallel fields. The diagonal conductivities of CNTs in the presence of a perpendicular field do not show any significant change in fields up to 500 T and are therefore not shown.

Turning now to the diagonal conductivity tensor elements of AGNRs in perpendicular fields, the parallel- and cross-polarized absorption spectra are shown in the third and the fourth column of Fig. 2. The unperturbed spectra show two dominant exciton peaks similar to what was obtained using *ab initio* methods [7,12]. We reuse notation and denote the peaks by E_{11} and E_{22}. As the magnetic field strength is increased, the E_{11} peak is shifted to lower energies, and the shift of the peak is accompanied by a decrease in oscillator strength. Similarly, the E_{22} peak is shifted to higher energies and the oscillator strength of that peak is also decreased. Simultaneously, a new peak between the E_{11} and E_{22} peaks emerges for strong magnetic fields. We also observe that the effect is stronger for the wider AGNR, which is caused by the increased magnetic flux through the wider unit cell. Since there exists no experimental results regarding the optical response of magnetoexcitons in AGNRs yet, we cannot validate these changes in the spectra. But we expect that if AGNRs could be deposited on a nonmetallic material and aligned, the change in the absorption spectrum could be measured in an experimental setup similar to that described in Ref. [26]. A common feature of both CNTs and AGNRs is that the effect of the magnetic field on the cross-polarized absorption is negligible and only causes small changes in the spectra. In addition, the inclusion of electron-hole interaction effects dampens the cross-polarized absorption due to strong depolarization [53].

The changes in the parallel-polarized absorption spectra are further elucidated in Fig. 3, which shows the smallest eigenvalues of the BSE for (8,0) CNTs and 10-AGNRs. The line color illustrates the optical intensity (oscillator strength) of the state associated with the eigenvalue. Figure 3(a) shows the lowest eigenvalues as a function of field strength for (8,0) CNTs in a parallel field. When there is no magnetic field, all but two of the exciton states are degenerate and only a single state is optically active. But, as the field strength is increased, the energies are altered and one of the dark excitons becomes optically active. This is what we observed as the splitting of the absorption peaks in Fig. 2. The field also lifts the degeneracy of the exciton states, and some eigenvalues are raised above the band-gap energy. We also see that the band gap of CNTs is affected by the external magnetic field and, e.g., in the case of (8,0) CNTs it decreases linearly. Whether the band gap increases or decreases with magnetic field depends on the family of CNTs considered [54]. Our results show a value of $\Delta_{bd} \approx 41$ meV at $B = 0$ T and a linear increase at high fields with a slope of approximately 0.54 meV/T. Comparing our results to the experimental results in Refs. [20–26], we see a larger value of Δ_{bd} and a smaller field-dependent increase in the splitting. As mentioned, this is due to the smaller diameter of the CNTs under consideration in this paper. If we compare to (6,5) CNTs and use the $1/d_t^2$ and d_t scaling on our results, we find $\Delta_{bd} \approx 28$ meV and a linear increase in the splitting of 0.65 meV/T at high fields. These values agree reasonably with experimental values [20–26]. Figure 3(b) shows the eigenvalues for 10-AGNR in

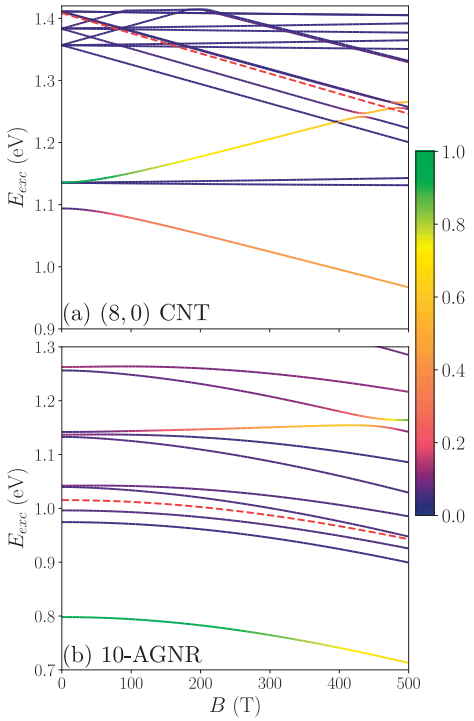

FIG. 3. Exciton energies as a function of magnetic field strength. The color of the lines in both plots corresponds to the relative optical intensity in the z direction, and the dashed red line is the band-gap energy. (a) Exciton energies of an (8,0) CNT in a parallel field. (b) Exciton energies of a 10-AGNR in a perpendicular field.

a perpendicular field. When the magnetic field strength is increased, the state associated with the E_{11} transition decreases in oscillator strength. Simultaneously, the oscillator strength of a state above the gap (at about 1.14 eV) is increased. Similar to what was observed for CNTs, the band gap of AGNRs is also altered by the magnetic field but not in a linear manner.

We now consider the Faraday rotation and Hall conductivities. In Figs. 4 and 5, the off-diagonal conductivities of CNTs and AGNRs, respectively, are shown. Generally, the off-diagonal optical conductivities are identically zero if there is no magnetic field to break time-reversal symmetry. Additionally, the electron-hole symmetry must be broken as clarified in Ref. [27], which is why a small overlap was included in the TB model. This could also have been achieved by including interactions beyond nearest neighbors in the TB model. Assuming that the complex refractive index in Eq. (9) is dominated by the surrounding media, the expression for the Faraday rotation of CNTs in an aqueous solution can be simplified to $\phi \approx l\mathrm{Re}\sigma_{xy}\rho/(2nc\epsilon_0)$. This holds, since $n \gg \kappa$ for water in the photon energy range where CNTs show absorption [55]. Consequently, the contribution of the CNTs to the Faraday rotation is proportional to the real part of the Hall conductivities. In Fig. 4, the real part of σ_{xy} for CNTs

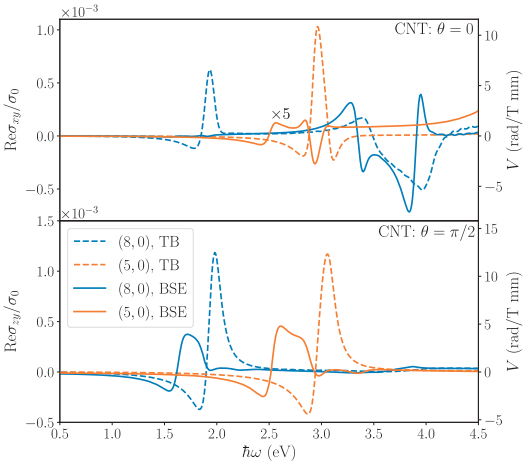

FIG. 4. Independent-particle and excitonic results for the dispersions of the Verdet constant and the real part of the off-diagonal conductivities of (5,0) and (8,0) CNTs for different directions of the magnetic field and $B = 10$ T.

in a parallel field and the real part of σ_{zy} for CNTs in a perpendicular field are shown, as well as the dispersion of the Verdet constant. The nonexcitonic results for $\mathrm{Re}\sigma_{xy}$ and the Verdet constant agree with Ref. [28]. But, in line with expectations, the excitonic effects significantly alter the Hall conductivities and the Faraday rotation. The plots clearly show that excitons must be included in a correct description of the Faraday rotation in CNTs. The other off-diagonal parts of the conductivity tensor are zero except for σ_{xy} in a perpendicular field, but this contribution is 3 orders of magnitude smaller than σ_{xy} in a parallel field. Thus, even for magnetic fields that

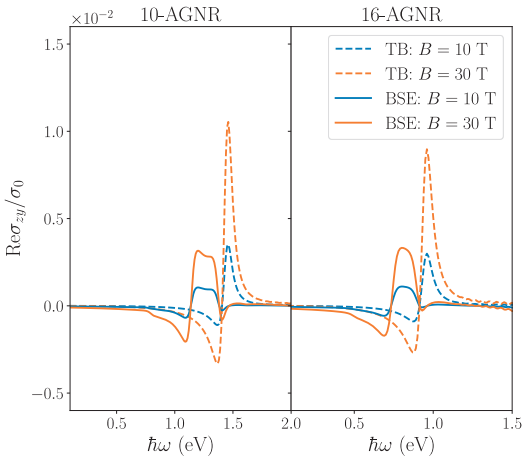

FIG. 5. Real part of the independent-particle and excitonic off-diagonal conductivities of 10- and 16-AGNRs in a perpendicular magnetic field.

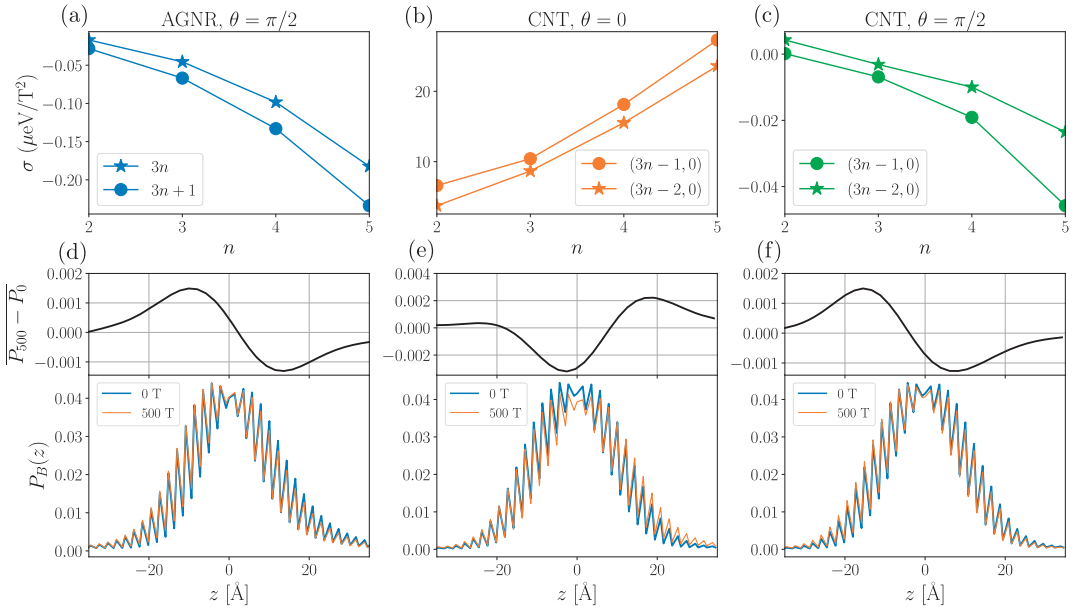

FIG. 6. (a–c) Diamagnetic coefficient of the low-energy bright exciton as a function of width or chiral indices for semiconducting families of (a) AGNRs in perpendicular fields and CNT in (b) parallel magnetic fields and (c) perpendicular magnetic field. (d–f) Exciton probability distribution with the hole located near the center of the unit cell for (d) 10-AGNR in a perpendicular field, (e) (8,0) CNT in a parallel field, and (f) (8,0) CNT in a perpendicular field. The top plots in (d–f) show the nearest-neighbor averaged change in the exciton probability distribution with magnetic field.

are not perfectly aligned with the axis of the CNT, the σ_{xy} conductivity is going to be dominated by the part related to the parallel field.

For AGNRs in a perpendicular field, the only finite Hall conductivity is σ_{zy}, which is shown in Fig. 5. The AGNR off-diagonal spectra underline the fact that the inclusion of excitonic effects is necessary for an accurate theoretical description of the optical response of AGNRs. For the magnetic field strengths considered in this paper, the off-diagonal conductivity scales linearly with field strength and the overall shape of the off-diagonal conductivity remains unchanged. This scaling holds true for both CNTs and AGNRs when the direction of the magnetic field is perpendicular to the directions of the off-diagonal element.

Finally, for the low-energy bright exciton we have evaluated both the diamagnetic coefficient and the exciton probability distribution. In real space, the exciton wave function can be written in the form $\Psi_{exc}(\mathbf{r}_e, \mathbf{r}_h)$. We fix the position of the hole $\mathbf{r}_h$ at an atom in the middle unit cell, and so the exciton probability distribution can be expressed as $P_B(z) = \sum |\Psi_{exc}(\mathbf{r}, \mathbf{r}_h)|^2$, where we sum over contributions with identical z coordinates and the subscript B denotes the magnetic field dependence. The diamagnetic shift ΔE_{dia} is the second-order change in exciton binding energy [56], i.e., $\Delta E_{\text{dia}} = \sigma B^2$, where σ is the diamagnetic coefficient. In Fig. 6, the diamagnetic coefficient for different semiconducting families of AGNRs and zigzag CNTs, the exciton probability distributions and the nearest-neighbor averaged change in exciton probability distributions are shown. Figure 6(a) shows the diamagnetic coefficient of AGNRs in the presence of a perpendicular field. The negative coefficient $\sigma < 0$ shows that the binding energy of the ground-state exciton will increase as a function of field strength. In contrast, Fig. 6(b) shows that CNTs in a parallel magnetic field see a decrease in the binding energy for increasing field strength. The explanation for this observation is found in the geometries: The electron and hole in CNTs are restricted to the tube, and the parallel magnetic field increases the delocalization of the exciton wave function as illustrated by Fig. 6(e), where we see a decrease in the electron concentration around the hole. Consequently, the binding energy is decreased. On the other hand, the magnetic field increases the localization of the exciton wave function in AGNRs in a perpendicular field [see Fig. 6(d)] and the binding energy is increased. The increase in binding energy for AGNRs is in line with what is observed for monolayer materials [34]. Figure 6(c) shows the diamagnetic coefficient for CNTs in a perpendicular field. The results show that the shift changes from positive to negative as the tube radius increases. When the tube radius is large, the effect of the perpendicular magnetic field on the excitons will resemble that of AGNRs in a perpendicular field.

IV. SUMMARY

To summarize the work presented in this paper, we used a TB model and subsequently solved the BSE to study the optical properties of CNTs and AGNRs in the presence of a static

magnetic field. In both cases, pronounced excitonic effects are observed. We have shown that the optical absorption of AGNRs is significantly altered by a strong perpendicular field, while a strong parallel field alters the optical absorption of CNTs. For CNTs we see a field-dependent splitting of the exciton absorption peaks, caused by brightening of a dark exciton state, while a perpendicular field gives rise to a new absorption peak in AGNRs. We also calculated the different nonzero Hall conductivities, including excitonic effects for both CNTs and AGNRs. The calculations show that excitonic effects are essential for a correct evaluation of the off-diagonal conductivities and, hence, for the Faraday rotation. Finally, we have illustrated how the magnetic field changes the band gap, the exciton eigenvalues, and the localization of the exciton.

ACKNOWLEDGMENTS

The authors gratefully acknowledges financial support by the QUSCOPE Center, sponsored by the Villum Foundation. Additionally, T.G.P. is supported by the Center for Nanostructured Graphene (CNG), which is sponsored by the Danish National Research Foundation, Project No. DNRF103.

[1] D. V. Kosynkin, A. L. Higginbotham, A. Sinitskii, J. R. Lomeda, A. Dimiev, B. K. Price, and J. M. Tour, Nature (London) **458**, 872 (2009).
[2] L. Jiao, L. Zhang, X. Wang, G. Diankov, and H. Dai, Nature (London) **458**, 877 (2009).
[3] L. Liao, J. Bai, Y.-C. Lin, Y. Qu, Y. Huang, and X. Duan, Adv. Mater. **22**, 1941 (2010).
[4] J. Liu, A. Wright, C. Zhang, and Z. Ma, Appl. Phys. Lett. **93**, 041106 (2008).
[5] M. Terrones, A. R. Botello-Méndez, J. Campos-Delgado, F. López-Urías, Y. I. Vega-Cantú, F. J. Rodríguez-Macías, A. L. Elías, E. Munoz-Sandoval, A. G. Cano-Márquez, J.-C. Charlier *et al.*, Nano Today **5**, 351 (2010).
[6] J. M. Schnorr and T. M. Swager, Chem. Mater. **23**, 646 (2010).
[7] L. Yang, M. L. Cohen, and S. G. Louie, Nano Lett. **7**, 3112 (2007).
[8] T. G. Pedersen, Phys. Rev. B **67**, 073401 (2003).
[9] T. G. Pedersen, Carbon **42**, 1007 (2004).
[10] T. F. Rønnow, T. G. Pedersen, and H. D. Cornean, Phys. Lett. A **373**, 1478 (2009).
[11] B. Monozon and P. Schmelcher, Physica B **500**, 89 (2016).
[12] D. Prezzi, D. Varsano, A. Ruini, A. Marini, and E. Molinari, Phys. Rev. B **77**, 041404 (2008).
[13] J. A. Alexander-Webber, C. Faugeras, P. Kossacki, M. Potemski, X. Wang, H. D. Kim, S. D. Stranks, R. A. Taylor, and R. J. Nicholas, Nano Lett. **14**, 5194 (2014).
[14] A. V. Stier, N. P. Wilson, G. Clark, X. Xu, and S. A. Crooker, Nano Lett. **16**, 7054 (2016).
[15] B. A. Gregg, J. Phys. Chem. B **107**, 4688 (2003).
[16] J. Kalinowski, M. Cocchi, D. Virgili, P. Di Marco, and V. Fattori, Chem. Phys. Lett. **380**, 710 (2003).
[17] H. Ajiki and T. Ando, Physica B **201**, 349 (1994).
[18] T. Ando, J. Phys. Soc. Jpn. **73**, 3351 (2004).
[19] T. Ando, J. Phys. Soc. Jpn. **75**, 024707 (2006).
[20] S. Zaric, G. N. Ostojic, J. Kono, J. Shaver, V. C. Moore, M. S. Strano, R. H. Hauge, R. E. Smalley, and X. Wei, Science **304**, 1129 (2004).
[21] J. Shaver, J. Kono, O. Portugall, V. Krstić, G. L. Rikken, Y. Miyauchi, S. Maruyama, and V. Perebeinos, Nano Lett. **7**, 1851 (2007).
[22] R. Matsunaga, K. Matsuda, and Y. Kanemitsu, Phys. Rev. Lett. **101**, 147404 (2008).
[23] S. Takeyama, H. Suzuki, H. Yokoi, Y. Murakami, and S. Maruyama, Phys. Rev. B **83**, 235405 (2011).
[24] W. Zhou, T. Sasaki, D. Nakamura, H. Liu, H. Kataura, and S. Takeyama, Phys. Rev. B **87**, 241406 (2013).
[25] W. Zhou, T. Sasaki, D. Nakamura, H. Saito, H. Liu, H. Kataura, and S. Takeyama, Appl. Phys. Lett. **103**, 021117 (2013).
[26] D. Nakamura, T. Sasaki, W. Zhou, H. Liu, H. Kataura, and S. Takeyama, Phys. Rev. B **91**, 235427 (2015).
[27] T. G. Pedersen, Phys. Rev. B **68**, 245104 (2003).
[28] A. Zarifi and T. G. Pedersen, Phys. Rev. B **77**, 085409 (2008).
[29] L. Sun, S. Jiang, and J. Marciante, Opt. Express **18**, 5407 (2010).
[30] M. A. Schmidt, L. Wondraczek, H. W. Lee, N. Granzow, N. Da, and P. S. J. Russell, Adv. Mater. **23**, 2681 (2011).
[31] M. Tymchenko, A. Y. Nikitin, and L. Martin-Moreno, ACS Nano **7**, 9780 (2013).
[32] C. Ritter, S. S. Makler, and A. Latgé, Phys. Rev. B **77**, 195443 (2008).
[33] Y. Huang, C. Chang, and M.-F. Lin, Nanotechnology **18**, 495401 (2007).
[34] A. V. Stier, K. M. McCreary, B. T. Jonker, J. Kono, and S. A. Crooker, Nat. Commun. **7**, 10643 (2016).
[35] A. Mitioglu, P. Plochocka, A. Granados del Aguila, P. Christianen, G. Deligeorgis, S. Anghel, L. Kulyuk, and D. Maude, Nano Lett. **15**, 4387 (2015).
[36] A. A. Mitioglu, K. Galkowski, A. Surrente, L. Klopotowski, D. Dumcenco, A. Kis, D. K. Maude, and P. Plochocka, Phys. Rev. B **93**, 165412 (2016).
[37] G. Plechinger, P. Nagler, A. Arora, A. Granados del Aguila, M. V. Ballottin, T. Frank, P. Steinleitner, M. Gmitra, J. Fabian, P. C. Christianen *et al.*, Nano Lett. **16**, 7899 (2016).
[38] A. V. Stier, N. P. Wilson, K. A. Velizhanin, J. Kono, X. Xu, and S. A. Crooker, Phys. Rev. Lett. **120**, 057405 (2017).
[39] R. Saito, G. Dresselhaus, and M. S. Dresselhaus, *Physical Properties of Carbon Nanotubes* (World Scientific, Singapore, 1998).
[40] S. Reich, J. Maultzsch, C. Thomsen, and P. Ordejon, Phys. Rev. B **66**, 035412 (2002).
[41] W. Kohn, Phys. Rev. **115**, 1460 (1959).
[42] C. D. Spataru, S. Ismail-Beigi, L. X. Benedict, and S. G. Louie, Phys. Rev. Lett. **92**, 077402 (2004).
[43] C. D. Spataru, S. Ismail-Beigi, R. B. Capaz, and S. G. Louie, Phys. Rev. Lett. **95**, 247402 (2005).
[44] T. G. Pedersen, Phys. Rev. B **69**, 075207 (2004).
[45] V. Perebeinos, J. Tersoff, and P. Avouris, Phys. Rev. Lett. **92**, 257402 (2004).
[46] L. X. Benedict, Phys. Rev. B **66**, 193105 (2002).

[47] M. L. Trolle, G. Seifert, and T. G. Pedersen, Phys. Rev. B **89**, 235410 (2014).
[48] T. G. Pedersen and K. Pedersen, Phys. Rev. B **79**, 035422 (2009).
[49] I. Crassee, J. Levallois, A. L. Walter, M. Ostler, A. Bostwick, E. Rotenberg, T. Seyller, D. Van Der Marel, and A. B. Kuzmenko, Nat. Phys. **7**, 48 (2011).
[50] R. Haydock, Comput. Phys. Commun. **20**, 11 (1980).
[51] S. Linden, D. Zhong, A. Timmer, N. Aghdassi, J. Franke, H. Zhang, X. Feng, K. Müllen, H. Fuchs, L. Chi *et al.*, Phys. Rev. Lett. **108**, 216801 (2012).
[52] R. Denk, M. Hohage, P. Zeppenfeld, J. Cai, C. A. Pignedoli, H. Söde, R. Fasel, X. Feng, K. Müllen, S. Wang *et al.*, Nat. Commun. **5**, 5253 (2014).
[53] S. Uryu and T. Ando, Phys. Rev. B **74**, 155411 (2006).
[54] J. P. Lu, Phys. Rev. Lett. **74**, 1123 (1995).
[55] G. M. Hale and M. R. Querry, Appl. Opt. **12**, 555 (1973).
[56] S. N. Walck and T. L. Reinecke, Phys. Rev. B **57**, 9088 (1998).

Paper C

Monolayer transition metal dichalcogenides in strong magnetic fields: Validating the Wannier model using a microscopic calculation

J. Have, G. Catarina, T. G. Pedersen, and N. M. R. Peres

Published in
Physical Review B **99**, 035416 (2019).

Monolayer transition metal dichalcogenides in strong magnetic fields: Validating the Wannier model using a microscopic calculation

J. Have,[1,2,*] G. Catarina,[3] T. G. Pedersen,[1,4] and N. M. R. Peres[5,6]

[1]*Department of Materials and Production, Aalborg University, DK-9220 Aalborg East, Denmark*
[2]*Department of Mathematical Sciences, Aalborg University, DK-9220 Aalborg East, Denmark*
[3]*QuantaLab, International Iberian Nanotechnology Laboratory (INL), 4715-330 Braga, Portugal*
[4]*Center for Nanostructured Graphene (CNG), DK-9220 Aalborg East, Denmark*
[5]*International Iberian Nanotechnology Laboratory (INL), 4715-330 Braga, Portugal*
[6]*Center and Department of Physics, and QuantaLab, University of Minho, Campus de Gualtar, 4710-057 Braga, Portugal*

(Received 16 October 2018; revised manuscript received 27 November 2018; published 9 January 2019)

Using an equation of motion (EOM) approach, we calculate excitonic properties of monolayer transition metal dichalcogenides perturbed by an external magnetic field. We compare our findings to the widely used Wannier model for excitons in two-dimensional materials and to recent experimental results. We find good agreement between the calculated excitonic transition energies and the experimental results. In addition, we find that the exciton energies calculated using the EOM approach are slightly lower than the ones calculated using the Wannier model. Finally, we also show that the effect of the dielectric environment on the magnetoexciton transition energy is minimal due to counteracting changes in the exciton energy and the exchange self-energy correction.

DOI: 10.1103/PhysRevB.99.035416

I. INTRODUCTION

The first use of an external magnetic field to study excitons and the electronic structure in thin-film transition metal dichalcogenides (TMDs) was published in 1978 [1]. Since then, the study of magnetoexcitons has been an active field of research. With the recent emergence of monolayer TMDs, research in this area has undergone a rapid development, due in part to the interesting electronic and optical properties of monolayer TMDs [2–4], including large exciton binding energies on the order of 0.5–1 eV [5–7]. Additionally, exciting magneto-optical phenomena of monolayer TMDs [8–10] have inspired novel applications, for which a detailed understanding of the effect of a magnetic field on the excitons is necessary. These phenomena include the valley Zeeman effect, a magnetic field assisted lifting of the degeneracy of the inequivalent K and K' valleys [11–13]. This control of the degeneracy could prove useful in the area of valleytronics [14]. Another phenomenon lending itself to possible optical applications is Faraday rotation [15], which has also been observed in monolayer TMDs perturbed by a magnetic field [16,17].

In addition to potential applications, perturbation by an external magnetic field provides experimental insight into the properties of excitons, such as their spatial extent [18,19] and the effect of the dielectric environment [20]. Using strong magnetic fields of up to 65 T, the Zeeman valley effect and diamagnetic shift of the excitonic states have been measured for the four most common monolayer TMDs: MoS_2 [21,22], $MoSe_2$ [19,21,23], WS_2 [24,25], and WSe_2 [20,26]. The analysis of such experimental results would benefit from a thorough theoretical study of the effect of an external magnetic field on excitons. But while there is a plethora of experimental results on magnetoexcitons, there have been fewer theoretical studies. The difficulties related to a theoretical description of magnetoexcitons in two-dimensional materials is, in part, due to the magnetic field breaking the translation symmetry. In one-dimensional systems, translation symmetry can be retained by choosing a suitable gauge for the magnetic vector potential [27], but in two- and three-dimensional systems that option is not available.

The standard theoretical approach has been to use an effective mass model such as the Wannier model [28], where the effective mass is calculated from the band structure of the unperturbed system. Using this approach, results regarding the binding energy of excitons, trions, and biexcitons in monolayer TMDs perturbed by a magnetic field were recently published in Ref. [29]. But with no other theoretical models for magnetoexcitons in 2D materials, it can be difficult to validate the effective mass model. In addition, the effective mass model does not take into account the unique Landau level structure of monolayer TMDs [8,10], which affects the magneto-optical response. In this paper, we provide an alternative approach for describing magnetoexcitons, which does not depend on the effective mass approximation. The approach is an extension of the equation of motion (EOM) method in Ref. [7] to the case in which the TMDs are perturbed by an external magnetic field. This model has several advantages, which include accounting for the Landau level structure of TMDs, allowing coupling between distinct bands and valleys, and providing a more self-contained theoretical

*jh@nano.aau.dk

framework. The EOM approach can also be used to calculate the optical response and was previously used to include second-order effects in the electric field in Ref. [30].

The present paper is structured as follows: In Sec. II, we introduce the single-particle Hamiltonian, which will serve as the outset for our study. In Sec. III, the EOM approach is briefly introduced. Section IV contains the definition of the electron-electron interaction Hamiltonian, as well as the derivation of the EOM for the excitonic problem. Section V serves to introduce the Wannier model, which we will use for comparison with the results obtained in the EOM approach. Finally, in Sec. VI our results are presented and compared to recent experiments.

II. SINGLE-PARTICLE HAMILTONIAN

In this section, we present the system and the single-particle Hamiltonian, which is the outset for our study of magnetoexcitons. The system is illustrated in Fig. 1. A monolayer TMD material, possibly deposited on some dielectric substrate with relative dielectric constant κ_a and capped by a dielectric with relative dielectric constant κ_b, is perturbed by a uniform static magnetic field perpendicular to the TMD. Under absorption of an incident photon with energy $\hbar\omega$ an exciton is generated. The properties of the exciton, i.e., size and energy, are affected by the magnetic field.

To describe magnetoexcitons in monolayer TMDs, we need an accurate description of the single-particle properties of unperturbed TMDs. For that purpose, we apply the effective Hamiltonian from Ref. [3]. This effective Hamiltonian describes a massive Dirac system, and has been found to reproduce the band structure of monolayer TMDs in the low-energy range around the direct band gaps in the K and K' valleys, including the spin-orbit splitting of the bands. For a monolayer in the xy plane the Hamiltonian is given by

$$\hat{H}_0 = v_F(\tau\sigma_x p_x + \sigma_y p_y) + \Delta_{\tau,s}\sigma_z + \xi_{\tau,s}\mathbb{I}, \tag{1}$$

where v_F is the Fermi velocity, $\tau = \pm 1$ is the valley index ($+1$ for the K valley and -1 for the K' valley), σ_i are the Pauli matrices with $i \in \{x, y, z\}$, p_x and p_y are the canonical momentum operators, $\mathbb{I}$ is the 2×2 identity matrix, and $\Delta_{\tau,s}$ and $\xi_{\tau,s}$ are the valley- and spin-dependent mass and on-site

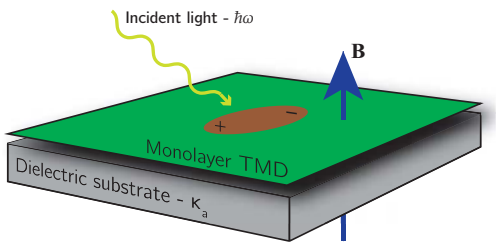

FIG. 1. Sketch of the system under consideration: Excitons in a monolayer TMD material perturbed by a uniform static magnetic field perpendicular to the monolayer. The monolayer may be encapsulated between a dielectric substrate and a capping material.

TABLE I. Parameters of the effective Hamiltonian for the four common types of TMDs. The mass parameters and the Fermi velocities are taken from Ref. [2] and the spin-orbit couplings are from Ref. [31]; both sets of parameters were calculated from first principles. An alternative set of parameters is provided in Ref. [4].

	Δ (eV)	$\hbar v_F$ (eV Å^{-1})	$\Delta_{\text{soc}}^{\mathcal{V}}$ (eV)	$\Delta_{\text{soc}}^{\mathcal{C}}$ (eV)
MoS_2	0.797	2.76	0.149	−0.003
$MoSe_2$	0.648	2.53	0.186	−0.022
WS_2	0.90	4.38	0.430	0.029
WSe_2	0.80	3.94	0.466	0.036

energy, respectively. The mass and on-site energy are given by

$$\Delta_{\tau,s} = \Delta - \tau s\frac{\Lambda_1}{2}, \quad \xi_{\tau,s} = \tau s\frac{\Lambda_2}{2}, \tag{2}$$

where $s = \pm 1$ ($+1$ for the spin up and -1 for spin down), $\Lambda_1 = (\Delta_{\text{soc}}^{\mathcal{V}} - \Delta_{\text{soc}}^{\mathcal{C}})/2$, and $\Lambda_2 = (\Delta_{\text{soc}}^{\mathcal{V}} + \Delta_{\text{soc}}^{\mathcal{C}})/2$. The parameters v_F, Δ, $\Delta_{\text{soc}}^{\mathcal{V}}$, and $\Delta_{\text{soc}}^{\mathcal{C}}$ are material dependent, and found by fitting to first-principles band structure calculation [2,31]. The material parameters used in this paper are provided in Table I. The single-particle energy bands are the eigenvalues $\varepsilon_{\tau,s}$ of $\hat{H}_0$, which are given by

$$\varepsilon_{\tau,s} = \pm\sqrt{\hbar^2 v_F^2|\mathbf{k}|^2 + \Delta_{\tau,s}^2} + \xi_{\tau,s}. \tag{3}$$

Note that the eigenvalues only depend on the product $\tau s = \pm 1$, and not on τ and s as individual parameters. The eigenvalues of MoS_2 are plotted as dashed lines in Fig. 2. We observe that the energy dispersion shows spin-orbit splitting of both valence and conduction bands and that the K and K' valleys are inequivalent due to spin.

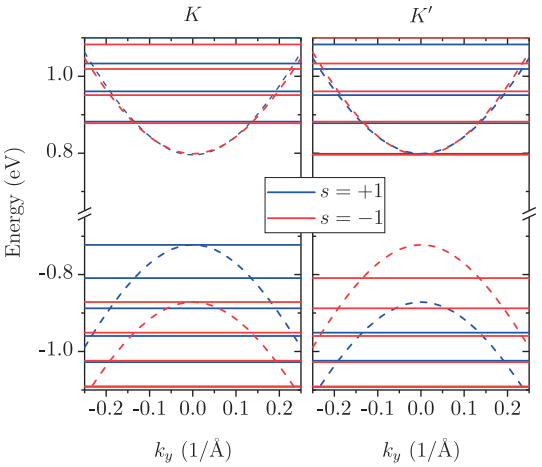

FIG. 2. Single-particle spectrum at the K and K' valleys of MoS_2 with (solid lines) and without (dashed lines) magnetic field. Red and blue indicate spin up and spin down, respectively. The Landau level spectrum is plotted for a very high magnetic field (600 T) to make it possible to distinguish the individual Landau levels. Qualitatively similar features are found at lower magnetic field strengths.

The next step is the inclusion of a perpendicular magnetic field **B**. The magnetic field is introduced using the minimal coupling substitution $\mathbf{p} \mapsto \mathbf{p} + e\mathbf{A}$, where $\mathbf{p}$ is the momentum operator, $-e$ is the electron charge, and $\mathbf{A}$ is the magnetic vector potential, related to the magnetic field by $\nabla \times \mathbf{A} = \mathbf{B}$. Using the Landau gauge, $\mathbf{A} = Bx\hat{\mathbf{y}}$, the effective perturbed Hamiltonian is

$$\hat{H}_B = v_F[\tau\sigma_x p_x + \sigma_y(p_y + eBx)] + \Delta_{\tau,s}\sigma_z + \xi_{\tau,s}\mathbb{I}. \quad (4)$$

The eigenvalues and eigenfunctions of $\hat{H}_B$ can be found by expressing $\hat{H}_B$ in terms of creation and annihilation operators [8,32], and then expanding the eigenfunctions in a basis of harmonic oscillator eigenfunctions. We find that the eigenvalues and the normalized eigenfunctions are given by

$$E^{n,\lambda}_{\tau,s} = \lambda\sqrt{\Delta^2_{\tau,s} + n(\hbar\omega_c)^2} + \xi_{\tau,s}, \quad (5)$$

$$\Psi^{n,\lambda}_{\tau,s,k_y}(\mathbf{r}) = \frac{e^{ik_y y}}{\sqrt{L_y}}\Phi^{n,\lambda}_{\tau,s}(\tilde{x}). \quad (6)$$

Here, $n \geqslant (1+\tau\lambda)/2$ is the integer Landau level (LL) index, $\lambda = \pm$ indicates the type of LLs (+ for conduction type LLs and − for valence type LLs), $\hbar\omega_c = \sqrt{2}\hbar v_F/l_B$ is the cyclotron energy, $l_B = \sqrt{\hbar/(eB)}$ is the magnetic length, L_y is the length of the system in the y direction, and the spinor wave function is

$$\Phi^{n,\lambda}_{\tau,s}(\tilde{x}) = \frac{1}{\sqrt{2}}\begin{pmatrix} B^{n,\lambda}_{\tau,s}\phi_{n-(\tau+1)/2}(\tilde{x}) \\ C^{n,\lambda}_{\tau,s}\phi_{n+(\tau-1)/2}(\tilde{x}) \end{pmatrix}. \quad (7)$$

Here, $\tilde{x} = x + l_B^2 k_y$, $\phi_n(\tilde{x})$ are the usual harmonic oscillator eigenstates, and $B^{n,\lambda}_{\tau,s}$ and $C^{n,\lambda}_{\tau,s}$ are normalization constants given by

$$B^{n,\lambda}_{\tau,s} = \lambda\sqrt{1+\lambda\alpha^n_{\tau,s}}, \quad C^{n,\lambda}_{\tau,s} = \sqrt{1-\lambda\alpha^n_{\tau,s}}, \quad (8)$$

where $\alpha^n_{\tau,s} = \Delta_{\tau,s}/\sqrt{\Delta^2_{\tau,s} + n(\hbar\omega_c)^2}$. The harmonic oscillator eigenstates are given by

$$\phi_n(\tilde{x}) = \frac{1}{\sqrt{2^n n!}}\left(\frac{1}{\pi l_B^2}\right)^{\frac{1}{4}} e^{-\frac{\tilde{x}^2}{2l_B^2}} H_n\left(\frac{\tilde{x}}{l_B}\right), \quad (9)$$

where H_n are the physicist's Hermite polynomials, which are defined by

$$H_n(x) = (-1)^n e^{x^2}\frac{d^n}{dx^n}e^{-x^2}. \quad (10)$$

Note that the energies $E^{n,\lambda}_{\tau,s}$ define a discrete set of LLs that have a degeneracy corresponding to the number of distinct k_y values. The Landau level spectrum of MoS_2 is plotted (solid lines) in Fig. 2. From Fig. 2 and the allowed values of n, we see that a LL with $n = 0$ is only allowed when $\tau \neq \lambda$. This gives rise to a magnetic-field-dependent increase of the band gap. Finally, the valley Zeeman splitting [12] is not included in the effective Hamiltonian $\hat{H}_B$. It could have been by adding additional terms to $\hat{H}_B$ [33], but since the focus of the present paper is on the excitonic effects, it is ignored for simplicity.

A. Dipole matrix elements

In this section, the dipole matrix elements for the single-particle wave functions are calculated. In addition to being necessary for calculating the optical response, the dipole matrix elements provide information about the optical selection rules, which can be used to exclude some dark transitions from our excitonic calculations. This speeds up the numerical studies performed below by a significant factor. The interaction of the system with the incident light is included, within the dipole approximation, via the interaction Hamiltonian

$$H_I = -\mathbf{d}\cdot\boldsymbol{\mathcal{E}}(t) = e\mathbf{r}\cdot\boldsymbol{\mathcal{E}}(t). \quad (11)$$

Here, $\mathbf{d} = -e\mathbf{r}$ is the dipole moment operator and $\boldsymbol{\mathcal{E}}(t)$ the time-dependent electric field of the light. By construction, transitions between different valleys and different spins are not allowed. We introduce some notation to simplify the expressions. Let α be shorthand for $\{n, \lambda, k_y\}$ and η for $\{\tau, s\}$; then the dipole matrix elements are written as $\mathbf{d}^{\alpha\to\alpha'}_{\eta} = \langle\Psi^{n,\lambda}_{\tau,s,k_y}|\mathbf{d}|\Psi^{n',\lambda'}_{\tau's',k'_y}\rangle$, where $\Psi^{n,\lambda}_{\tau,s,k_y}$ are the single-particle eigenstates of $\hat{H}_B$. For the dipole matrix elements in the x direction, we find

$$\begin{aligned} d^{\alpha\to\alpha'}_{\eta,x} &= -e\delta_{k_y,k'_y}\langle\Phi^{n,\lambda}_{\tau,s}|x|\Phi^{n',\lambda'}_{\tau,s}\rangle \\ &= -e\delta_{k_y,k'_y}\frac{\langle\Phi^{n,\lambda}_{\tau,s}|[\hat{H}_B, x]|\Phi^{n',\lambda'}_{\tau,s}\rangle}{E^{n,\lambda}_{\tau,s} - E^{n',\lambda'}_{\tau,s}}. \end{aligned} \quad (12)$$

The commutator is simply $[\hat{H}_B, x] = -i\hbar v_F\tau\sigma_x$. A similar expression holds for the commutator with y. Consequently, the dipole matrix elements are found to be

$$\begin{aligned} \mathbf{d}^{\alpha\to\alpha'}_{\eta} = \frac{e\hbar v_F\delta_{k_y,k'_y}}{2\Delta E^{n,\lambda}_{n',\lambda'}}\Bigg[& B^{\lambda,n}_{\tau,s}C^{n',\lambda'}_{\tau,s}\begin{pmatrix} -i\tau \\ 1 \end{pmatrix}\delta_{n-\tau,n'} \\ & - B^{n',\lambda'}_{\tau,s}C^{n,\lambda}_{\tau,s}\begin{pmatrix} i\tau \\ 1 \end{pmatrix}\delta_{n+\tau,n'}\Bigg]. \end{aligned} \quad (13)$$

Here, $\Delta E^{n,\lambda}_{n',\lambda'} := E^{n,\lambda}_{\tau,s} - E^{n',\lambda'}_{\tau,s}$. The nonzero dipole matrix elements correspond to the bright interband transitions. Equation (13) shows that the allowed interband transitions from a LL with index n are to LLs with index $n' = n \pm 1$ and at the same k_y points.

III. EQUATION OF MOTION APPROACH

The excitonic properties will be calculated using an EOM approach similar to that of Ref. [7], which is an extension of the method introduced to describe the magneto-optics of graphene in a cavity in Ref. [34]. The approach relies primarily on writing and solving Heisenberg's equation of motion, which is given by

$$-i\hbar\frac{\partial\hat{\rho}}{\partial t} = [\hat{H}, \hat{\rho}]. \quad (14)$$

Here $\hat{H}$, is the full Hamiltonian including $\hat{H}_I$, and $\hat{\rho}$ is the density matrix for the states of $\hat{H}_B$.

To compute the density matrix, we introduce the creation and annihilation operators $\hat{c}^\dagger_{\alpha,\eta}(t)$ and $\hat{c}_{\alpha,\eta}(t)$, which, respectively, create or annihilate an electron in state $\Psi^\eta_\alpha \equiv \Psi^{n,\lambda}_{\tau,s,k_y}$ (recall that α is short for $\{n, \lambda, k_y\}$ and η is short

for $\{\tau, s\}$). The creation and annihilation operators obey the usual anticommutator relations. Using these operators, we can express the single-particle Hamiltonian and the light-matter interaction Hamiltonian as

$$\hat{H}_B(t) = \sum_{\alpha,\eta} E^{\eta}_{\alpha} \hat{\rho}^{\eta}_{\alpha,\alpha}(t), \tag{15}$$

$$\hat{H}_I(t) = -\boldsymbol{\mathcal{E}}(t) \cdot \sum_{\alpha,\alpha',\eta} \mathbf{d}^{\alpha\to\alpha'}_{\eta} \hat{\rho}^{\eta}_{\alpha,\alpha'}(t), \tag{16}$$

where $\hat{\rho}^{\eta}_{\alpha,\alpha'}(t) = \hat{c}^{\dagger}_{\alpha,\eta}(t)\hat{c}_{\alpha',\eta}(t)$ are elements of the density matrix in a basis of the eigenstates of $\hat{H}_B$. Note that only a few of the terms in the sum over α' give nonzero contributions to $\hat{H}_I$ due to the optical selection rules from Sec. II.

Solving Heisenberg's EOM exactly as expressed in Eq. (14) is not possible. Consequently, we take the expectation value on both sides of Eq. (14) with respect to the equilibrium state, and get the following EOM for the expectation value:

$$-i\hbar \frac{\partial}{\partial t} p^{\eta}_{\alpha,\alpha'} = \langle [\hat{H}, \hat{\rho}^{\eta}_{\alpha,\alpha'}] \rangle, \tag{17}$$

with $p^{\eta}_{\alpha,\alpha'} = \langle \rho^{\eta}_{\alpha,\alpha'} \rangle$. Note that the diagonal elements $\alpha = \alpha'$ define a new electron distribution. The commutators of $\hat{H}_B$ and $\hat{H}_I$ with the density matrix are calculated in Appendix A and can be used to calculate the single-particle optical response as in Ref. [35]. We now turn to the problem of including electron-electron interactions in the Hamiltonian and then find the excitonic states by solving Eq. (17).

IV. ELECTRON-ELECTRON INTERACTIONS

From this point on, we consider the full Hamiltonian given by $\hat{H} = \hat{H}_B + \hat{H}_I + \hat{H}_{ee}$, where the electron-electron interaction Hamiltonian is defined by

$$\hat{H}_{ee} = \frac{1}{2} \int d\mathbf{r}_1 d\mathbf{r}_2 \hat{\psi}^{\dagger}(\mathbf{r}_1)\hat{\psi}^{\dagger}(\mathbf{r}_2) U(\mathbf{r}_1 - \mathbf{r}_2)\hat{\psi}(\mathbf{r}_2)\hat{\psi}(\mathbf{r}_1). \tag{18}$$

Here, the integrals also cover spin, $U(\mathbf{r})$ is the electron-electron interaction potential defined below, and $\hat{\psi}(\mathbf{r})$ is the field operator, given by

$$\hat{\psi}(\mathbf{r}) = \sum_{\alpha,\eta} \hat{c}_{\alpha,\eta} \Psi^{\eta}_{\alpha}(\mathbf{r}). \tag{19}$$

Here and in the following, we drop the explicit time dependence of $\hat{c}_{\alpha,\eta}(t)$ and $\hat{\rho}^{\eta}_{\alpha,\alpha'}(t)$ to simplify notation.

Although monolayer TMDs are not strictly 2D materials, the electrons are effectively confined to move in two dimensions by the negligible thickness of the layer [6,7]. Consequently, instead of the usual Coulomb potential, we model the electron-electron interaction $U(\mathbf{r})$ by the Keldysh potential [36], which is valid for strict 2D systems. In momentum space the Keldysh potential has the following simple form [36–38]:

$$U(\mathbf{q}) = \frac{e^2}{2\varepsilon_0} \frac{1}{q(\kappa + r_0 q)}, \tag{20}$$

where $q = |\mathbf{q}|$, ε_0 is the vacuum permittivity, r_0 is a material-dependent in-plane screening length, and $\kappa = (\kappa_a + \kappa_b)/2$ is the average of the relative dielectric constant of the substrate and the capping material. The in-plane screening lengths are related to the in-plane polarizability, and can be calculated from a first-principles band structure. The parameters used in this paper were calculated in Ref. [6] and are listed in Table II. It is worth mentioning that the Keldysh potential previously has been used successfully to describe various excitonic properties of TMDs [6,7,46,47].

TABLE II. Parameters used in the calculation of the excitonic properties for the four common types of TMDs. The first and second columns contain the reduced exciton masses for the spin-up and spin-down bands, respectively. The third column is the in-plane screening length, and is taken from Ref. [6].

	$\mu_{\tau,+1}$ (m_e)	$\mu_{\tau,-1}$ (m_e)	r_0 (Å)
MoS_2	0.380	0.418	41.4
$MoSe_2$	0.355	0.417	51.7
WS_2	0.159	0.199	37.9
WSe_2	0.170	0.223	45.1

Before calculating the commutator of $\hat{H}_{ee}$ with the density matrix and solving the Heisenberg EOM, we will rewrite $\hat{H}_{ee}$ slightly. Assuming that the electron-electron coupling between different valleys is negligible, the $\hat{H}_{ee}$ can be written as

$$\hat{H}_{ee} = \frac{1}{2} \sum_{\substack{\tau,\, s,\, s' \\ \alpha_1,\, \alpha_2 \\ \alpha_3,\, \alpha_4}} U^{\tau,s,s'}_{\alpha_1\alpha_4,\alpha_2\alpha_3} \hat{c}^{\dagger}_{\alpha_1,\tau,s} \hat{c}^{\dagger}_{\alpha_2,\tau,s'} \hat{c}_{\alpha_3,\tau,s'} \hat{c}_{\alpha_4,\tau,s}, \tag{21}$$

where two of the summations over spin cancel because of the spin integrals in Eq. (18), and the so-called Coulomb integrals are

$$U^{\tau,s,s'}_{\alpha_1\alpha_4,\alpha_2\alpha_3} = \frac{1}{4\pi^2} \int d^2\mathbf{q} U(\mathbf{q}) F^{\tau,s}_{\alpha_1,\alpha_4}(\mathbf{q}) F^{\tau,s'}_{\alpha_2,\alpha_3}(-\mathbf{q}). \tag{22}$$

Here, $F^{\tau,s}_{\alpha,\alpha'}(\mathbf{q})$ are structure factors defined as

$$F^{\tau,s}_{\alpha,\alpha'}(\mathbf{q}) = \int d^2\mathbf{r} e^{i\mathbf{q}\cdot\mathbf{r}} \left[\Psi^{\alpha}_{\tau,s}(\mathbf{r})\right]^* \Psi^{\alpha'}_{\tau,s}(\mathbf{r}). \tag{23}$$

An explicit expression for the structure factors is provided in Appendix B. Using Eq. (21), we calculate the commutator of the full Hamiltonian with the density matrix in Appendix A and find that the EOM in Eq. (17) can be written as

$$\left(E^{\eta}_{\alpha'} - E^{\eta}_{\alpha} - i\hbar\frac{\partial}{\partial t}\right) p^{\eta}_{\alpha,\alpha'} = \sum_{\substack{\alpha_1,\, \alpha_2 \\ \alpha_3}} p^{\eta}_{\alpha_1,\alpha_3} \left(U^{\tau,s,s}_{\alpha'\alpha_3,\alpha_1\alpha_2} p^{\eta}_{\alpha,\alpha_2} - U^{\tau,s,s}_{\alpha_1\alpha,\alpha_2\alpha_3} p^{\eta}_{\alpha_2,\alpha'}\right) - \boldsymbol{\mathcal{E}}(t) \cdot \sum_{\alpha''} \left(\mathbf{d}^{\alpha''\to\alpha}_{\eta} p^{\eta}_{\alpha'',\alpha'} - \mathbf{d}^{\alpha'\to\alpha''}_{\eta} p^{\eta}_{\alpha,\alpha''}\right). \tag{24}$$

Here, $E^{\eta}_{\alpha} \equiv E^{\tau,s}_{n,\lambda}$ and the expectation value of the four-body operator in $\hat{H}_{ee}$ has been truncated at the random phase approximation (RPA) level [39]. Comparing the EOM to what was found in Ref. [7], we see that the general form of the equation is equivalent to the expression for a system with an arbitrary number of bands. In the following subsections, we keep only the terms of Eq. (24), which are of first order in the electric field and collect the terms corresponding to the exchange self-energy corrections and electron-hole interactions.

A. Exchange self-energy corrections

In this section, we briefly touch upon the exchange self-energy corrections caused by the electron-electron interactions. The term exchange should be understood in the sense of the Hartree-Fock approximation, where there are two corrections to self-energy: the Hartree correction, which is canceled by the interaction with the positive background (see Appendix A), and the exchange correction.

Although exchange self-energy corrections are not the main focus of this work, it is still important to include them if we hope to accurately describe the transition energy of the excitons. This is because the self-energy correction has a strong impact on the value of the single-particle gap. In Appendix A, the first-order terms that result in a renormalization of the LLs are collected. It is found that the self-energy-renormalized LLs, $\tilde{E}^{\eta}_{\alpha}$, are given by

$$\tilde{E}^{\eta}_{\alpha} = E^{\eta}_{\alpha} - \Sigma^{\eta}_{\alpha}, \quad \Sigma^{\eta}_{\alpha} = \sum_{\alpha'} f\left(E^{\eta}_{\alpha'}\right) U^{\tau,s,s}_{\alpha'\alpha,\alpha\alpha'}. \tag{25}$$

Here, Σ^{η}_{α} is the exchange self-energy correction and $f(E)$ is the Fermi-Dirac distribution. We calculate the exchange self-energy correction using the structure factors from Appendix B. Converting the sum over k_y to an integral, the exchange self-energy can be written as

$$\sum_{\alpha'} U^{\tau,s,s}_{\alpha'\alpha,\alpha\alpha'} f\left(E^{\eta}_{\alpha'}\right) = \sum_{n',\lambda'} f\left(E^{\eta}_{n',\lambda'}\right) I^{\eta}_{\lambda' n',\lambda n}, \tag{26}$$

where the integrals are defined as

$$I^{\eta}_{\lambda n,\lambda' n'} = \frac{1}{16\pi^2} \int d^2\mathbf{q} U(\mathbf{q}) e^{-\frac{l_B^2 q^2}{2}} \left| J^{\eta}_{\lambda n,\lambda' n'}(\mathbf{q}) \right|^2. \tag{27}$$

Here, $J^{\eta}_{\lambda n,\lambda' n'}$ is the function defined in Eq. (B4). The integral in Eq. (27) is simplified by the fact that $U(\mathbf{q})$ and $|J^{\eta}_{\lambda n,\lambda' n'}(\mathbf{q})|^2$ only depend on $q = |\mathbf{q}|$, meaning that the angular integral simply gives a factor of 2π. In the remainder of the paper, we assume that the system is undoped, i.e., the Fermi level is in the band gap, and that $T = 0$ K. This implies that the sum in Eq. (26) only runs over the valence-type LLs, which simplifies the numerical calculations.

For graphene described in the Dirac approximation, the exchange self-energy correction has been found to diverge logarithmically when summing over an infinite number of valence LLs [40]. We have observed the same type of divergence numerically for the expression in Eq. (26). Consequently, a cutoff N_{cut} of the summation over LLs has to be introduced. In Ref. [41] (see also Ref. [42]), the cutoff was calculated for graphene by equating the concentration of electrons in N_{cut} LLs to that in the filled valence band. The same approach can be used for TMDs and we find a cutoff equal to

$$N_{\text{cut}} = \frac{\pi l_B^2}{\Omega_0}, \tag{28}$$

with $\Omega_0 = \sqrt{3}a^2/2$ the area of the primitive unit cell of the TMD. Taking $a = 3.2$ Å for all four TMDs [43], we get a cutoff equal to $N_{\text{cut}} \approx 2.33 \times 10^4/B$ T.

B. Excitonic effects

Finally, using the exchange self-energy corrected LLs, we proceed to calculating the excitonic effects of TMDs perturbed by an external magnetic field. As shown in Appendix A, the excitonic states can be found by solving the first-order equation

$$\left(\tilde{E}^{\eta}_{\alpha'} - \tilde{E}^{\eta}_{\alpha} - i\hbar\frac{\partial}{\partial t}\right) p^{\eta,1}_{\alpha,\alpha'} = \left(\sum_{\alpha_1,\alpha_2} U^{\tau,s,s}_{\alpha'\alpha_2,\alpha_1\alpha} p^{\eta,1}_{\alpha_1,\alpha_2} - \boldsymbol{\mathcal{E}}(t)\cdot\mathbf{d}^{\alpha'\to\alpha}_{\eta}\right)\Delta f^{\eta}_{\alpha',\alpha}, \tag{29}$$

where $\Delta f^{\eta}_{\alpha',\alpha} = f(E^{\eta}_{\alpha'}) - f(E^{\eta}_{\alpha})$. As in Ref. [7] the excitonic transition energies can be calculated by solving the homogeneous equation, i.e., setting $\boldsymbol{\mathcal{E}}(t) = \mathbf{0}$. Changing from time to frequency domain, we get the homogeneous equation

$$\left(\tilde{E}^{\eta}_{\alpha'} - \tilde{E}^{\eta}_{\alpha} - E\right) p^{\eta}_{\alpha,\alpha'} = \sum_{\alpha_1,\alpha_2} U^{\tau,s,s}_{\alpha'\alpha_2,\alpha_1\alpha} p^{\eta}_{\alpha_1,\alpha_2} \Delta f^{\eta}_{\alpha',\alpha}. \tag{30}$$

Here, $p^{\eta}_{\alpha,\alpha'}$ should be understood as the Fourier transform of $p^{\eta,1}_{\alpha,\alpha'}$ and E is the exciton transition energy for a fixed combination of spin and valley. The excitonic states are the interband solutions of Eq. (30), i.e., where α and α' correspond to valence and conduction states, respectively. Thus, we assume that to be the case. Additionally, the sum over α_1 and α_2 can be split into two contributions: one where α_1 and α_2 are valence and conduction states, respectively, and one where the converse holds. We denote these cases the resonant contribution and the nonresonant contribution, respectively. In the following, we keep only the resonant contribution. It has been shown in Ref. [7] that this is a valid approximation.

To clearly distinguish the valence and conduction states, we write α_v and α_c for α_1 and α_2 in Eq. (30), respectively. Setting $k_y = k'_y$ (which corresponds to ignoring the dark nonvertical transitions; see Sec. II A), we simplify the right-hand side of Eq. (30) by writing

$$\sum_{\alpha_v,\alpha_c} U^{\tau,s,s}_{\alpha'\alpha_c,\alpha_v\alpha} p^{\eta}_{\alpha_v,\alpha_c} \approx \sum_{n_v,n_c} \int_{-\infty}^{\infty} dq_y \mathcal{K}^{\tau,s,s}_{n'n_c,n_v n}(q_y - k_y) \times p^{\eta}_{n_v,n_c}(q_y). \tag{31}$$

Here, we write the approximate sign to indicate the approximations discussed above, and we denote $p^{\eta}_{\alpha_v,\alpha_c}$ by $p^{\eta}_{n_v,n_c}(k_y)$ for the case in which the k_y values associated with α_c and α_v are equal. The different λ parameters are fixed by the previous assumptions and are not written explicitly. The electron-hole interaction kernel $\mathcal{K}^{\tau,s,s}_{n'n_c,n_v n}$ is calculated using the structure

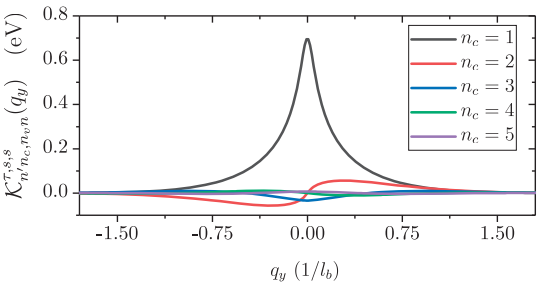

FIG. 3. Electron-hole interaction kernels plotted for MoS_2 in a magnetic field of 100 T. The kernels are plotted for the K valley, spin up, and $(n, n', n_v) = (0, 1, 0)$.

factors and is found to be

$$\mathcal{K}^{\tau,s,s}_{n'n_c,n_vn}(q_y) = \frac{1}{16\pi^2}\int_{-\infty}^{\infty} dq_x U(\mathbf{q}) e^{-\frac{l_B^2|\mathbf{q}|^2}{2}} \times J^{\tau,s}_{+n',+n_c}(\mathbf{q}) J^{\tau,s}_{-n_v,-n}(-\mathbf{q}), \tag{32}$$

where the integral over q_x must be performed numerically. This finally implies a homogeneous first-order equation given by

$$\left(\tilde{E}^{\eta}_{\alpha'} - \tilde{E}^{\eta}_{\alpha} - E\right) p^{\eta}_{n,n'}(k_y) = \sum_{n_v,n_c}\int_{-\infty}^{\infty} dq_y \mathcal{K}^{\tau,s,s}_{n'n_c,n_vn}(q_y - k_y) p^{\eta}_{n_v,n_c}(q_y). \tag{33}$$

Equation (33) corresponds to the Bethe-Salpeter equation for electron-hole pairs [44], and it can be written as an eigenvalue problem with eigenvalues E by discretizing the integral over q_y. The size of the eigenvalue problem scales as $N_k N_c N_v$, where N_k is the number of points used to discretize the integral, and where N_c and N_v are the number of conduction and valence LLs, respectively. It is clear that only if the electron-hole kernel decays sufficiently fast with increasing n_c and n_v can we hope to solve Eq. (33), since that would imply that the sums over n_c and n_v can be truncated. Fortunately, the kernel does decay quite fast in n_c and n_v, as illustrated for n_c in Fig. 3. In the next section, we turn our attention to an alternative (and nonmicroscopic) description of the excitonic properties of TMDs.

V. WANNIER MODEL

In this section, we briefly introduce the Wannier model [28] for excitons. The Wannier model is based on the effective mass approximation for a single pair of valence and conduction bands. For a two-dimensional semiconductor in a perpendicular magnetic field (using the symmetric gauge for the magnetic vector potential), the operator describing zero angular momentum excitons, i.e., s-type states, is [45]

$$\hat{H}_{\text{ex}} = -\frac{\hbar^2}{2\mu}\nabla^2 + \frac{e^2B^2}{8\mu}r^2 - U(\mathbf{r}). \tag{34}$$

Here, μ is the reduced effective mass, ∇^2 is the 2D Laplace operator, r is the relative electron-hole distance, and $U(\mathbf{r})$ is the electron-hole interaction potential given as the real-space representation of Eq. (20). Taking the inverse Fourier transform of Eq. (20), we find

$$U(\mathbf{r}) = \frac{e^2}{8\varepsilon_0 r_0}\left[H_0\left(\frac{\kappa r}{r_0}\right) - Y_0\left(\frac{\kappa r}{r_0}\right)\right], \tag{35}$$

with $r = |\mathbf{r}|$, H_0 the Struve function, and Y_0 a Bessel function of the second kind.

For a direct comparison of the Wannier model with the solutions to Eq. (33), we want to use the same parameters in both models. Thus, we calculate the effective mass from the eigenvalues of the unperturbed single-particle operator $\hat{H}_0$. Expanding the eigenvalues in Eq. (3) around $|\mathbf{k}| = 0$, we find that the effective mass of an electron or hole in the τ valley and with spin s is

$$m^*_{\tau,s} = \frac{|\Delta_{\tau,s}|}{v_F^2}. \tag{36}$$

The effective masses of electrons and holes are equal due to the symmetric conduction and valence bands. The reduced effective mass is then $\mu_{\tau,s} = m^*_{\tau,s}/2$, for which the values for the four common TMDs are given in Table II.

The s-type excitons, corresponding to bright excitons [46], can be found by solving the eigenvalue problem $\hat{H}_{\text{ex}}\psi(r) = E_{\text{exc}}\psi(r)$, where E_{exc} is the exciton energy. We solve it by expanding $\psi(r)$ in a basis of Bessel functions, more specifically the basis $\phi_i(r) = J_0(\lambda_i r/R)$, where λ_i is the ith zero of the Bessel J_0 function and $r \leqslant R$. This basis corresponds to introducing an infinite barrier at $r = R$, but this should not affect the results as long as R is sufficiently large. The same basis was recently used to describe the Stark shift of excitons in monolayer TMDs [46,47].

VI. RESULTS

In this section, our results are presented and discussed. In addition, we devote some attention to the computational approaches applied. All results were obtained using the parameters in Tables I and II. Evaluating the integrals in the exchange self-energy correction, i.e., Eq. (27), is done using an adaptive quadrature and a numerical high-precision library [48]. This approach, although computationally expensive, is found to provide accurate results for the rapidly oscillating integrands that occur when n and n' are large. In contrast, since the sum in Eq. (33) can be truncated at reasonably low values of n_c and n_v, as illustrated by Fig. 3, the integral in the electron-hole kernel can be evaluated using the Gauss-Hermite quadrature. For the calculation of excitonic energies using the Wannier model, we use 400 basis functions and fix R at $R = 20$ nm. The kinetic and magnetic matrix elements can be calculated analytically in this basis, while the potential matrix elements are computed numerically using a Gauss-Legendre quadrature.

First, we consider the exchange corrections. We denote the exchange self-energy corrected and the uncorrected band gaps as $\tilde{E}_g^{\tau s}$ and $E_g^{\tau s}$, respectively. The $\tilde{E}_g^{\tau s}$ and $E_g^{\tau s}$ band gaps are plotted in Fig. 4 as a function of magnetic field for $\tau s = +1$, i.e., spin up at the K valley or spin down at the K' valley. The results show that the self-energy correction gives rise to an opening of the band gap on the order of 0.8 to 1.0 eV. Similar values hold for the $\tau s = -1$ gaps. We find smaller

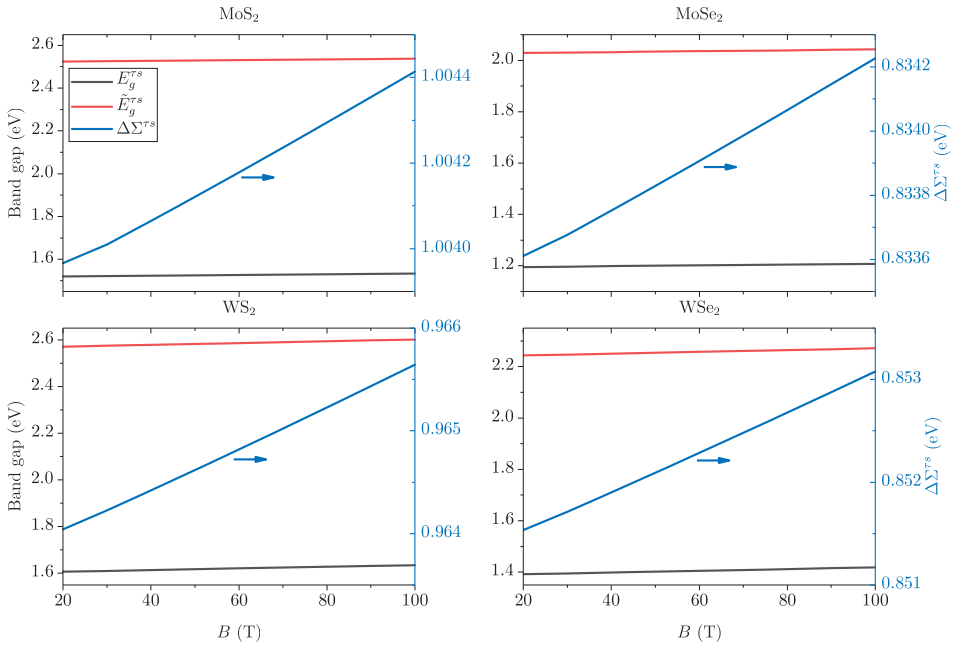

FIG. 4. Plot of $\tau s = +1$ band gaps of suspended monolayer TMDs, i.e., taking $\kappa = 1$. The uncorrected (black) and exchange self-energy corrected (red) band gaps are shown as a function of magnetic field. In addition, the exchange self-energy correction to the band gaps, $\Delta\Sigma^{\tau s} \equiv \tilde{E}_g^{\tau s} - E_g^{\tau s}$, is plotted (blue). The blue lines refer to the blue axes, while the rest refer to the black axes.

exchange self-energy corrections than those of Ref. [7] for the case of unperturbed monolayer TMDs. The explanation for this discrepancy is twofold: First, we use a different parameter set. Second, the cutoffs that are used are different. But, as will be shown later, our approach results in exciton transition energies that match experiments quite well.

Considering the magnetic field dependence of the band gaps, we see that the uncorrected band gaps calculated using the LL energies in Eq. (5) vary linearly with magnetic field for the field range in Fig. 4. We also find a linear magnetic field dependence of the exchange self-energy correction to the band gap with slopes of 5.57 μeV/T for MoS_2, 7.76 μeV/T for $MoSe_2$, 20.0 μeV/T for WS_2, and 19.3 μeV/T for WSe_2. The slopes are for $\tau s = +1$ states, but similar slopes hold for the $\tau s = -1$ states. This apparent linear behavior of $\Delta\Sigma^{\tau s} = \tilde{E}_g^{\tau s} - E_g^{\tau s}$ can be explained by studying the expression in Eq. (26). For small B, it can be shown using Eqs. (27) and (B4) that the integrals $I^{\eta}_{\lambda n,\lambda' n'}$ are proportional to $\sqrt{B}$, for all λ, λ', n, and n'. If we can show that $I^{\eta}_{-0,-n'} - I^{\eta}_{+1,-n'}$ is proportional to $(n'+1)^{-3/2}$ as a function of n', the result is a linear behavior of $\Delta\Sigma^{\tau s}$ since

$$\Delta\Sigma^{\tau s} \propto \sqrt{B}\sum_{n'}^{N_{\rm cut}}(n'+1)^{-\frac{3}{2}} \approx \sqrt{B}\int_1^{N_{\rm cut}+1} dn' n'^{-\frac{3}{2}}$$
$$\approx 2\sqrt{K}B. \qquad (37)$$

Here, the last approximation holds for a cutoff of the type $N_{\rm cut} = K/B$, with K some constant, and for small B. The inset in Fig. 5 shows $I^{\eta}_{-0,-n'} - I^{\eta}_{+1,-n'}$ on a log-log scale for MoS_2, with $B = 100$ T and $\tau s = +1$. Fitting with a linear function, we find a power of $q = -1.33 \pm 0.03$ covering the range from 20 T to 100 T. Thus, an approximately linear behavior of the exchange self-energy correction is expected.

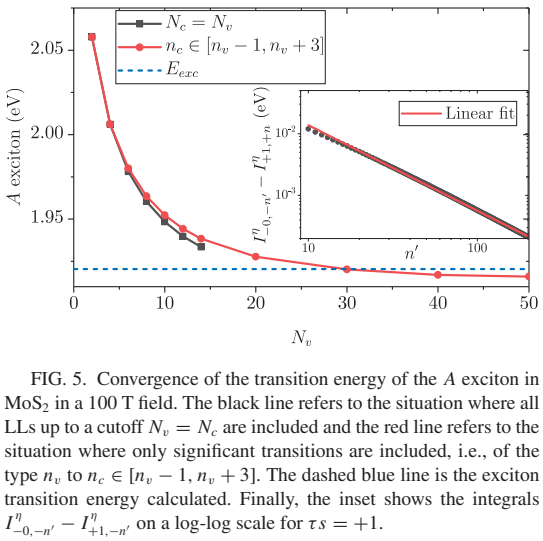

FIG. 5. Convergence of the transition energy of the A exciton in MoS_2 in a 100 T field. The black line refers to the situation where all LLs up to a cutoff $N_v = N_c$ are included and the red line refers to the situation where only significant transitions are included, i.e., of the type n_v to $n_c \in [n_v - 1, n_v + 3]$. The dashed blue line is the exciton transition energy calculated. Finally, the inset shows the integrals $I^{\eta}_{-0,-n'} - I^{\eta}_{+1,-n'}$ on a log-log scale for $\tau s = +1$.

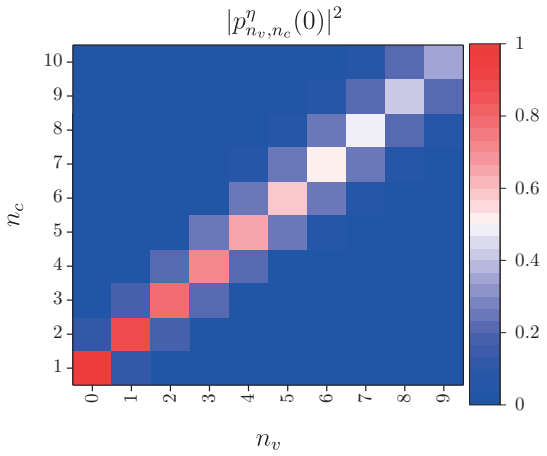

FIG. 6. Plot of the squared eigenvector of the A exciton in MoS_2 in an external field of 100 T at $k_y = 0$. The elements of the eigenvector have been normalized, such that the largest norm is unity. The plot shows that only a few transitions are significant, and that they are centered around transitions allowed by the optical selection rules.

In photoluminescence and spectroscopy experiments, it is typically the exciton transition energy and not the exchange self-energy corrected band gap that is measured. But demonstrating that the exchange self-energy correction is approximately linearly in the magnetic field is important if the diamagnetic shift of the exciton transition energy is used to estimate the exciton size, as was done in Refs. [18,20,22]. Any finite quadratic dependence of the exchange self-energy correction would result in errors in the estimates of the exciton sizes. Although the results presented here do not exclude finite quadratic terms in the exchange self-energy correction, they appear to be small enough that any error in the estimation of the exciton size should be negligible.

Turning our attention to the exciton states, we note that it is difficult to separate the bright and dark exciton states calculated in the EOM approach, since Eq. (33) mixes dark and bright transitions. This difficulty might be resolved by writing the magnetic vector potential in the symmetric gauge in $\hat{H}_B$ and repeating the derivations in Sec. IV, but this study is left for future work. At the present time, we will instead focus on the exciton with the lowest transition energy, also called the ground state exciton. We follow convention and denote the spin up and down ground state excitons at the K valley as A and B, respectively. Similarly, we have A' and B' excitons in the K' valley. In the absence of valley Zeeman splitting, the A and A' excitons are energetically degenerate and the same holds for the B and B' excitons. Consequently, in the following, only the A and B excitons are considered. In Fig. 6, the squared eigenvector of the A exciton in MoS_2 is plotted for $k_y = 0$. The plot shows that the significant transitions between LLs are where n_v couples to $n_c = n_v + 1$, which coincides exactly the bright transitions according to Sec. II A. We also find that the same holds for the B exciton. Consequently, the A and B excitons must be bright.

When solving Eq. (33), discretizing the integral over q_y using a Gauss-Hermite quadrature with $N_k = 300$ nodes has been found to result in good convergence. If we then include the first 15 valence and conduction LLs in the summation in Eq. (33), the resulting matrix has size $67\,500 \times 67\,500$ and is at the limit of what we can handle numerically. But for these values the exciton transition energy has not yet converged, as illustrated for the A exciton in MoS_2 by the black line in Fig. 5. Alternatively, we can utilize that only a few transitions are significant in the exciton ground state, as was demonstrated in Fig. 6. In fact, calculating the norm of the eigenvector where only transitions of the type n_v to $n_c \in [n_v - 1, n_v + 3]$ have been included, we find that the squared overlap is only 2% less than unity. Including only these significant transitions allows us to include more valence LLs and, as illustrated by the red line in Fig. 5, obtain a better convergence. The cost is a small error on the order of a few meV. The numerical difficulties associated with including a high number of LLs in the excitonic calculations result in a restriction on the magnetic field strength used hence: as the magnetic field strength decreases, more LLs need to be included in the calculations to secure sufficiently converged results. Eventually, the current computational restrictions limit us to magnetic fields above 100 T.

Turning to the exciton transition energies, it has been shown in Refs. [19,22] that for magnetic fields in the range considered here the transition energies E_τ can be approximated by

$$E_\tau = E_0 + \mu_g B + \tau \mu_Z B + \sigma_{\text{dia}} B^2, \tag{38}$$

with τ the valley index, E_0 the zero-field exciton transition energy, $\mu_g B$ the field-dependent change in band gap, $\tau \mu_Z B$ the valley Zeeman shift, and finally $\sigma_{\text{dia}} B^2$ the diamagnetic shift. Since the valley Zeeman shift is not included in our single-particle Hamiltonian, the transition energies found by solving Eq. (33) can be approximated by $E = E_0 + \mu_g B + \sigma_{\text{dia}} B^2$. To allow for comparisons between the theoretical and the experimentally measured exciton transition energies, we average the experimentally measured exciton transition energies from the K and K' valleys to remove the valley Zeeman splitting, i.e., use $E = (E_{+1} + E_{-1})/2$.

The exciton transition energies of the A and B excitons are presented in Table III. In columns three and four, we show the theoretical transition energies, which were calculated by solving Eq. (33). Columns five and six contain the experimental exciton transition energies when there is no external magnetic field. In columns seven and eight, we show the experimental exciton transition energies at approximately 65 T. Comparing the zero-field transition energies with the experimental transition energies in columns seven and eight, we see that the exciton transition energies exhibit a minimal dependence on the magnetic field. In fact, experiments predict that the quadratic diamagnetic shift is on the order of only a few meV [18,22] for a magnetic field of 100 T. Consequently, we can compare the calculated transition energies to the measured transition energies in a system with no magnetic field. Table III shows that the transition energies of MoS_2, WS_2, and WSe_2 are very well captured by our model, with differences on the order of 10 meV. The calculated results for $MoSe_2$ differ more from the experimental results, with

TABLE III. Theoretical and experimental transition and exciton energies for A and B excitons in TMDs with different dielectric environments. All theoretical energies are computed at 100 T.

		Transition energies						Exciton energies			
		EOM		Experimental, $B = 0$ T		Experimental, $B \approx 65$ T		EOM		Wannier	
TMD	κ	A	B	A	B	A	B	A	B	A	B
MoS_2	1.00	1.918	2.076					−0.620	−0.632	−0.617	−0.632
	1.55	1.907	2.066	1.895 [22], 1.948 [21]	2.042 [22], 2.092 [21]	1.896 [22], 1.948 [21]	2.044 [22], 2.094 [21]	−0.491	−0.504	−0.489	−0.503
$MoSe_2$	1.00	1.516	1.735					−0.526	−0.542	−0.513	−0.533
	1.55	1.512	1.730	1.660 [13]				−0.419	−0.434	−0.409	−0.428
WS_2	1.00	2.042	2.467					−0.559	−0.584	−0.520	−0.555
	1.55	2.030	2.453	2.039 [25], 2.045 [22]	2.442 [25], 2.453 [22]	2.040 [25], 2.046 [22]	2.442 [25], 2.454 [22]	−0.426	−0.450	−0.392	−0.424
WSe_2	1.00	1.761	2.216					−0.511	−0.535	−0.468	−0.505
	1.55	1.755	2.209	1.744 [12]				−0.393	−0.417	−0.357	−0.391
	3.30	1.721	2.173	1.732 [20]		1.733 [20]		−0.229	−0.247	−0.197	−0.224
	4.50	1.700	2.152	1.723 [18]		1.724 [18]		−0.177	−0.192	−0.144	−0.168

the calculated transition energy being approximately 150 meV below the experimental transition energy. This discrepancy indicates a problem with the material parameters used and not the method, as the results agree well for the three other types of materials.

In the final four columns of Table III, the exciton energies calculated using the EOM approach and the Wannier model are presented. For the EOM method, the exciton energies are found from $E_{\text{exc}} = E - \tilde{E}_g$, where E is the exciton transition energy found by solving Eq. (33) and $\tilde{E}_g$ is the exchange self-energy corrected band gap. Comparing the results, we see that all the exciton energies calculated using the EOM approach are below the Wannier results. That is to be expected since the EOM approach relies on less strict approximations. The differences between the calculated energies are quite small and vary from a few meV to 50 meV. Thus, if errors in this range are acceptable, the Wannier model provides a useful model for excitons in monolayer TMDs.

Finally, we also consider the effect of changing the dielectric environment of the TMDs, i.e., varying the screening parameter κ in the potentials in Eqs. (20) and (35). The effect is illustrated in Fig. 7 for MoS_2 in a magnetic field of 100 T. The figure shows that the exchange self-energy corrected band gap decreases while the exciton energy increases as a function of κ. These two counteracting effects result in exciton transition energies, which only exhibit minimal dependence on the dielectric environment, as illustrated by the blue line and green squares in Fig. 7. This effect has previously been demonstrated in TMDs with no external magnetic field [49], but Fig. 7 illustrates that it still holds for systems in the presence of a perpendicular magnetic field. This phenomenon further underlines the importance of including the exchange self-energy corrections in a self-contained model. We find that similar results hold for the other TMDs.

Comparing the EOM method and the Wannier model, we see that both have advantages and disadvantages. The EOM method provides a self-contained framework, including the unique LL structure and a higher accuracy of the exciton energies. The disadvantage is that the numerical computations are demanding and, as a consequence, small magnetic fields cannot be considered. For the Wannier method, the numerical calculations are relatively simple and arbitrary magnetic field strengths can be considered. The disadvantages are that for some systems the accuracy is lower than the EOM method and that only the excitonic properties are described. The Wannier model provides no information about the unique LL structure, the band gap, or the field-dependent change of the band gap. Consequently, the choice between the EOM method and the Wannier method depends on the application, and which aspects are deemed important.

VII. SUMMARY

In summary, starting from a Dirac-type Hamiltonian describing the band structure of monolayer TMDs around the K and K' points, we have introduced an external magnetic field and then included electron-electron interactions to account for the exchange self-energy corrections and excitons. In this

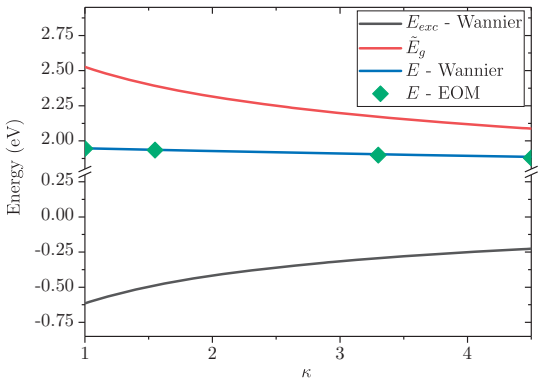

FIG. 7. Plot of the corrected band gap (red line), the exciton transition energy (blue line and green diamonds), and the exciton energy (black line) as a function of the relative dielectric constant of the surrounding medium for MoS_2, with $B = 100$ T and $\tau s = +1$. The exciton transition energy calculated from the Wannier results (blue line) is the sum of exciton energy (black line) and the corrected band gap (red line), i.e., $E = \tilde{E}_g + E_{\text{exc}}$.

setup, we used the EOM approach to find the low-energy A and B excitons. Our results were compared to the popular Wannier model for excitons and recent experimental results.

When comparing with the Wannier model, we found that the A and B exciton energies match quite well. Consequently, the EOM method validates the Wannier model in this case. The exciton energies only exhibit a small dependence on the magnetic field (up to a few meV for realistic field strengths), but the optical properties are expected to change significantly. These changes include optical transitions between discrete LLs, which depend strongly on the magnetic field, and a finite optical Hall conductivity giving rise to Faraday rotation in TMDs. Thus, we will focus on the optical properties of magnetoexcitons in future projects. We also expect to see more pronounced differences between the optical response calculated using the EOM approach and the Wannier model.

Comparing the calculated transition energies with the experimental values, we also found a very good agreement. This shows that the exchange self-energy correction is central if accurate theoretical calculations of the exciton transition energies are needed. Finally, we considered the effect of the dielectric environment on the exciton transition energy. We found that increasing the dielectric constant of the environment causes a decrease in the corrected band gap and an increase in the exciton energy. These two counteracting effects cause a minimal dependence of the exciton transition energies on the dielectric environment. This holds for both the EOM method results and transition energies calculated from the Wannier model results.

ACKNOWLEDGMENTS

J.H. and T.G.P. gratefully acknowledge financial support by the QUSCOPE Center, sponsored by the Villum Foundation. Additionally, T.G.P. is supported by the Center for Nanostructured Graphene (CNG), which is sponsored by the Danish National Research Foundation, Project No. DNRF103. G.C. acknowledges financial support from FCT for the P2020-PTDC/FIS-NAN/4662/2014 project. N.M.R.P. acknowledges support from the European Commission through the project "Graphene-Driven Revolutions in ICT and Beyond" (Ref. No. 785219), and the Portuguese Foundation for Science and Technology (FCT) in the framework of the Strategic Financing UID/FIS/04650/2013. Additionally, N.M.R.P. acknowledges COMPETE2020, PORTUGAL2020, FEDER, and the Portuguese Foundation for Science and Technology (FCT) through Project No. PTDC/FIS-NAN/3668/201.

APPENDIX A: COMMUTATOR RELATIONS AND THE EQUATION OF MOTION

In this section, we present the commutator relations between $\hat{H} = \hat{H}_B + \hat{H}_I + \hat{H}_{ee}$ and the density matrix, as well as the relevant equation of motion. First, we calculate the commutator relations using the following relation:

$$\left[\hat{\rho}^{\eta}_{\alpha_1,\alpha_2}, \hat{\rho}^{\eta'}_{\alpha_3,\alpha_4}\right] = \hat{\rho}^{\eta}_{\alpha_1,\alpha_4}\delta_{\alpha_2,\alpha_3}\delta_{\eta,\eta'} - \hat{\rho}^{\eta}_{\alpha_3,\alpha_2}\delta_{\alpha_1,\alpha_4}\delta_{\eta,\eta'}. \tag{A1}$$

Applying this relation to the first two terms of the commutator $[\hat{H}, \rho^{\eta}_{\alpha,\alpha'}]$, we find

$$\left[\hat{H}_B, \hat{\rho}^{\eta}_{\alpha,\alpha'}\right] = \sum_{\alpha'',\eta'} E^{\eta'}_{\alpha''}\left[\hat{\rho}^{\eta'}_{\alpha'',\alpha''}, \hat{\rho}^{\eta}_{\alpha,\alpha'}\right] \tag{A2}$$

$$= \left(E^{\eta}_{\alpha} - E^{\eta}_{\alpha'}\right)\hat{\rho}^{\eta}_{\alpha,\alpha'} \tag{A3}$$

and

$$\left[\hat{H}_I, \hat{\rho}^{\eta}_{\alpha,\alpha'}\right] = -\boldsymbol{\mathcal{E}}(t)\cdot\sum_{\alpha_1,\alpha_2,\eta'}\mathbf{d}^{\alpha_1\to\alpha_2}_{\eta'}\left[\hat{\rho}^{\eta'}_{\alpha_1,\alpha_2}, \hat{\rho}^{\eta}_{\alpha,\alpha'}\right] \tag{A4}$$

$$= -\boldsymbol{\mathcal{E}}(t)\cdot\sum_{\alpha''}\left(\mathbf{d}^{\alpha''\to\alpha}_{\eta}\hat{\rho}^{\eta}_{\alpha'',\alpha'} - \mathbf{d}^{\alpha'\to\alpha''}_{\eta}\hat{\rho}^{\eta}_{\alpha,\alpha''}\right). \tag{A5}$$

In the commutator relation between the electron-electron interaction Hamiltonian and the density matrix, the following commutator relation is useful:

$$\left[\hat{c}^{\dagger}_{\alpha_1,\tau,s'}\hat{c}^{\dagger}_{\alpha_2,\tau,s''}\hat{c}_{\alpha_3,\tau,s''}\hat{c}_{\alpha_4,\tau,s'}, \hat{c}^{\dagger}_{\alpha,\tau',s}\hat{c}_{\alpha',\tau',s}\right] = \delta_{\tau,\tau'}\big(\hat{c}^{\dagger}_{\alpha_1,\tau,s}\hat{c}^{\dagger}_{\alpha_2,\tau,s''}\hat{c}_{\alpha_3,\tau,s''}\hat{c}_{\alpha',\tau,s}\delta_{\alpha,\alpha_4}\delta_{s,s'} + \hat{c}^{\dagger}_{\alpha_1,\tau,s'}\hat{c}^{\dagger}_{\alpha_2,\tau,s}\hat{c}_{\alpha',\tau,s}\hat{c}_{\alpha_4,\tau,s'}\delta_{\alpha,\alpha_3}\delta_{s,s''}$$
$$- \hat{c}^{\dagger}_{\alpha,\tau,s}\hat{c}^{\dagger}_{\alpha_2,\tau,s''}\hat{c}_{\alpha_3,\tau,s''}\hat{c}_{\alpha_4,\tau,s}\delta_{\alpha',\alpha_1}\delta_{s,s'} - \hat{c}^{\dagger}_{\alpha_1,\tau,s'}\hat{c}^{\dagger}_{\alpha,\tau,s}\hat{c}_{\alpha_3,\tau,s}\hat{c}_{\alpha_4,\tau,s'}\delta_{\alpha',\alpha_2}\delta_{s,s''}\big). \tag{A6}$$

Applying Eq. (A6) to the $[\hat{H}_{ee}, \hat{\rho}^{\eta}_{\alpha,\alpha'}]$ commutator, we find

$$\left[H_{ee}, \hat{\rho}^{\eta}_{\alpha,\alpha'}\right] = \sum_{\substack{s',\,\alpha_1\\ \alpha_2,\,\alpha_3}}\left\{U^{\tau,s,s'}_{\alpha_1\alpha,\alpha_2\alpha_3}\hat{c}^{\dagger}_{\alpha_1,\tau,s}\hat{c}^{\dagger}_{\alpha_2,\tau,s'}\hat{c}_{\alpha_3,\tau,s'}\hat{c}_{\alpha',\tau,s} - U^{\tau,s,s'}_{\alpha'\alpha_1,\alpha_2\alpha_3}\hat{c}^{\dagger}_{\alpha,\tau,s}\hat{c}^{\dagger}_{\alpha_2,\tau,s'}\hat{c}_{\alpha_3,\tau,s'}\hat{c}_{\alpha_1,\tau,s}\right\}, \tag{A7}$$

where we also used the relation

$$U^{\tau,s,s'}_{\alpha_1\alpha_4,\alpha_2\alpha_3} = U^{\tau,s',s}_{\alpha_2\alpha_3,\alpha_1\alpha_4}. \tag{A8}$$

Collecting the terms in Eqs. (A3), (A5), and (A7), we can now write Heisenberg's equation of motion for the full Hamiltonian including electron-electron interactions. To write Eq. (17), we compute the expectation value of the commutator relations keeping terms that are of first order in the electric field. While the expectation values of Eqs. (A3) and (A5) are found by straightforward calculation, we apply the random phase approximation (RPA) [39] to find

$$\left\langle\left[H_{ee}, \hat{\rho}^{\tau,s}_{\alpha,\alpha'}\right]\right\rangle = \sum_{\substack{s',\,\alpha_1\\ \alpha_2,\,\alpha_3}}\left\{U^{\tau,s,s'}_{\alpha_1\alpha,\alpha_2\alpha_3}\left(p^{\tau,s'}_{\alpha_2,\alpha_3}p^{\tau,s}_{\alpha_1,\alpha'} - \delta_{s,s'}p^{\tau,s}_{\alpha_1,\alpha_3}p^{\tau,s}_{\alpha_2,\alpha'}\right) - U^{\tau,s,s'}_{\alpha'\alpha_1,\alpha_2\alpha_3}\left(p^{\tau,s'}_{\alpha_2,\alpha_3}p^{\tau,s}_{\alpha,\alpha_1} - \delta_{s,s'}p^{\tau,s}_{\alpha_2,\alpha_1}p^{\tau,s}_{\alpha,\alpha_3}\right)\right\}, \tag{A9}$$

where $p^{\tau,s}_{\alpha,\alpha'} = \langle \hat{\rho}^{\tau,s}_{\alpha,\alpha'} \rangle$. Terms allowing mixing of spins correspond to the Hartree terms in Hartree-Fock theory. They are canceled by the interaction with the positive background [50] and, as a result, the expectation value has the following form:

$$\langle [H_{ee}, \hat{\rho}^{\tau,s}_{\alpha,\alpha'}] \rangle = \sum_{\alpha_1,\alpha_3} p_{\alpha_1,\alpha_3} \sum_{\alpha_2} \left(U^{\tau,s,s}_{\alpha'\alpha_3,\alpha_1\alpha_2} p^{\tau,s}_{\alpha,\alpha_2} - U^{\tau,s,s}_{\alpha_1\alpha,\alpha_2\alpha_3} p^{\tau,s}_{\alpha_2,\alpha'} \right). \tag{A10}$$

This gives the following EOM for the expectation value:

$$\left(E^{\eta}_{\alpha'} - E^{\eta}_{\alpha} - i\hbar \frac{\partial}{\partial t} \right) p^{\eta}_{\alpha,\alpha'} = \sum_{\substack{\alpha_1,\alpha_2 \\ \alpha_3}} p^{\eta}_{\alpha_1,\alpha_3} \left(U^{\tau,s,s}_{\alpha'\alpha_3,\alpha_1\alpha_2} p^{\eta}_{\alpha,\alpha_2} - U^{\tau,s,s}_{\alpha_1\alpha,\alpha_2\alpha_3} p^{\eta}_{\alpha_2,\alpha'} \right) - \boldsymbol{\mathcal{E}}(t) \cdot \sum_{\alpha''} \left(\mathbf{d}^{\alpha''\to\alpha}_{\eta} p^{\eta}_{\alpha'',\alpha'} - \mathbf{d}^{\alpha'\to\alpha''}_{\eta} p^{\eta}_{\alpha,\alpha''} \right). \tag{A11}$$

The final step is to expand the expectation values in orders of the electric field and collect first-order terms in Eq. (A11). The zeroth order of the expectation value can be expressed using the Fermi-Dirac distribution

$$p^{\eta,0}_{\alpha,\alpha'} = f\left(E^{\eta}_{\alpha}\right) \delta_{\alpha,\alpha'}, \tag{A12}$$

where $f(E)$ is the Fermi-Dirac distribution. Consequently, the first-order equation is

$$\left(E^{\eta}_{\alpha'} - E^{\eta}_{\alpha} - i\hbar \frac{\partial}{\partial t} \right) p^{\eta,1}_{\alpha,\alpha'} = \left(\sum_{\alpha_1,\alpha_2} U^{\tau,s,s}_{\alpha'\alpha_2,\alpha_1\alpha} p^{\eta,1}_{\alpha_1,\alpha_2} - \boldsymbol{\mathcal{E}}(t) \cdot \mathbf{d}^{\alpha'\to\alpha}_{\eta} \right) \Delta f^{\eta}_{\alpha',\alpha} + \sum_{\alpha_1,\alpha_2} f\left(E^{\eta}_{\alpha_1}\right) \left(U^{\tau,s,s}_{\alpha'\alpha_1,\alpha_1,\alpha_2} p^{\eta,1}_{\alpha,\alpha_2} - U^{\tau,s,s}_{\alpha_1\alpha,\alpha_2\alpha_1} p^{\eta,1}_{\alpha_2,\alpha'} \right), \tag{A13}$$

where $\Delta f^{\eta}_{\alpha',\alpha} = f(E^{\eta}_{\alpha'}) - f(E^{\eta}_{\alpha})$ and $p^{\eta,1}_{\alpha,\alpha'}$ is the first-order term of the expectation value. We rewrite the last term on the right-hand side to isolate the exchange self-energy correction

$$\sum_{\alpha_1,\alpha_2} f\left(E^{\eta}_{\alpha_1}\right) \left(U^{\tau,s,s}_{\alpha'\alpha_1,\alpha_1,\alpha_2} p^{\eta,1}_{\alpha,\alpha_2} - U^{\tau,s,s}_{\alpha_1\alpha,\alpha_2\alpha_1} p^{\eta,1}_{\alpha_2,\alpha'} \right) = \Sigma^{\eta}_{\alpha'} - \Sigma^{\eta}_{\alpha} + \sum_{\alpha_1} f\left(E^{\eta}_{\alpha_1}\right) \left(\sum_{\alpha_2 \neq \alpha'} U^{\tau,s,s}_{\alpha'\alpha_1,\alpha_1\alpha_2} p^{\eta,1}_{\alpha,\alpha_2} - \sum_{\alpha_2 \neq \alpha} U^{\tau,s,s}_{\alpha_1\alpha,\alpha_2\alpha_1} p^{\eta,1}_{\alpha_2,\alpha'} \right), \tag{A14}$$

where Σ^{η}_{α} is the exchange self-energy correction given by

$$\Sigma^{\eta}_{\alpha} = \sum_{\alpha_1} f\left(E^{\eta}_{\alpha_1}\right) U^{\tau,s,s}_{\alpha_1\alpha,\alpha\alpha_1}. \tag{A15}$$

The remaining terms in Eq. (A14) correspond to density terms and will be disregarded in this work. Thus, the first-order EOM for the expectation value of the density matrix reads

$$\left(\tilde{E}^{\eta}_{\alpha'} - \tilde{E}^{\eta}_{\alpha} - i\hbar \frac{\partial}{\partial t} \right) p^{\eta,1}_{\alpha,\alpha'} = \left(\sum_{\alpha_1,\alpha_2} U^{\tau,s,s}_{\alpha'\alpha_2,\alpha_1\alpha} p^{\eta,1}_{\alpha_1,\alpha_2} - \boldsymbol{\mathcal{E}}(t) \cdot \mathbf{d}^{\alpha'\to\alpha}_{\eta} \right) \Delta f^{\eta}_{\alpha',\alpha}, \tag{A16}$$

with $\tilde{E}^{\eta}_{\alpha} = E^{\eta}_{\alpha} - \Sigma^{\eta}_{\alpha}$. The interband solutions to the system of first-order differential equations in Eq. (A16) give the excitonic states.

APPENDIX B: STRUCTURE FACTORS

In this section, we find an explicit expression for the structure factors $F^{\tau,s}_{\alpha,\alpha'}$ defined in Eq. (23). The explicit expression allows for a numerical evaluation of the Coulomb integrals in Eq. (22). Inserting the expression for the single-particle wave function, Eq. (6), in the structure factors, we find

$$F^{\tau,s}_{\alpha,\alpha'} = \int d^2\mathbf{r} \frac{e^{i(q_y - k_y + k'_y)y}}{L_y} e^{iq_x x} \left[B^{n,\lambda}_{\tau,s} B^{n',\lambda'}_{\tau,s} \phi_{n_{\tau,-}}(\tilde{x}) \phi_{n'_{\tau,-}}(\tilde{x}') + C^{n,\lambda}_{\tau,s} C^{n',\lambda'}_{\tau,s} \phi_{n_{\tau,+}}(\tilde{x}) \phi_{n'_{\tau,+}}(\tilde{x}') \right], \tag{B1}$$

where the notation is $\tilde{x} = x + l_B^2 k_y$, $\tilde{x}' = x + l_B^2 k'_y$, $n_{\tau,-} = n - (\tau+1)/2$, and $n_{\tau,+} = n + (\tau-1)/2$. For each term of Eq. (B1), we calculate an integral of the type

$$\int dx e^{iq_x x} \phi_n(\tilde{x}) \phi_{n'}(\tilde{x}') = \exp\left(-\frac{l_B^2 (k_y - k'_y)^2 + l_B^2 q_x^2}{4} + i q_x \frac{l_B^2}{2} (k_y + k'_y) \right) \sqrt{\frac{n_<!}{n_>!}} \left(\frac{i l_B q_x + l_B \, \mathrm{sgn}(n - n')(k_y - k'_y)}{\sqrt{2}} \right)^{n_> - n_<}$$
$$\times L^{n_> - n_<}_{n_<} \left(\frac{l_B^2 q_x^2 + l_B^2 (k_y - k'_y)^2}{2} \right), \tag{B2}$$

where $n_> = \max\{n, n'\}$, $n_< = \min\{n, n'\}$, and L_n^m are associated Laguerre polynomials. The detailed calculation of the integral in Eq. (B2) was provided in Ref. [51]. The previous expression allows us to write the structure factors as

$$F^{\tau,s}_{\alpha,\alpha'}(\mathbf{q}) = \frac{\pi\delta(q_y - k_y + k'_y)}{L_y} \exp\left(-\frac{l_B^2|\mathbf{q}|^2}{4} + iq_x\frac{l_B^2}{2}(k_y + k'_y)\right) J^{\tau,s}_{\lambda n,\lambda' n'}(\mathbf{q}), \tag{B3}$$

where the function $J^{\eta}_{\lambda n,\lambda' n'}$ is defined as

$$J^{\tau,s}_{\lambda n,\lambda' n'}(\mathbf{q}) = \left(\frac{il_B q_x + l_B\,\mathrm{sgn}(n-n')q_y}{\sqrt{2}}\right)^{n_>-n_<}\left[\sqrt{\frac{[n_< - (\tau+1)/2]!}{[n_> - (\tau+1)/2]!}} B^{n,\lambda}_{\tau,s} B^{n',\lambda'}_{\tau,s} L^{n_>-n_<}_{n_<-(\tau+1)/2}\left(\frac{l_B^2|\mathbf{q}|^2}{2}\right)\right.$$
$$\left. + \sqrt{\frac{[n_< + (\tau-1)/2]!}{[n_> + (\tau-1)/2]!}} C^{n,\lambda}_{\tau,s} C^{n',\lambda'}_{\tau,s} L^{n_>-n_<}_{n_<+(\tau-1)/2}\left(\frac{l_B^2|\mathbf{q}|^2}{2}\right)\right]. \tag{B4}$$

The expression for the structure factors in Eq. (B3) is used to calculate both the excitonic properties and the exchange self-energy corrections.

[1] M. Tanaka, H. Fukutani, and G. Kuwabara, J. Phys. Soc. Jpn. **45**, 1899 (1978).
[2] D. Xiao, G.-B. Liu, W. Feng, X. Xu, and W. Yao, Phys. Rev. Lett. **108**, 196802 (2012).
[3] A. Kormányos, V. Zólyomi, N. D. Drummond, P. Rakyta, G. Burkard, and V. I. Fal'ko, Phys. Rev. B **88**, 045416 (2013).
[4] A. Kormányos, G. Burkard, M. Gmitra, J. Fabian, V. Zólyomi, N. D. Drummond, and V. Fal'ko, 2D Mater. **2**, 022001 (2015).
[5] A. Ramasubramaniam, Phys. Rev. B **86**, 115409 (2012).
[6] T. C. Berkelbach, M. S. Hybertsen, and D. R. Reichman, Phys. Rev. B **88**, 045318 (2013).
[7] A. Chaves, R. Ribeiro, T. Frederico, and N. Peres, 2D Mater. **4**, 025086 (2017).
[8] F. Rose, M. O. Goerbig, and F. Piéchon, Phys. Rev. B **88**, 125438 (2013).
[9] R.-L. Chu, X. Li, S. Wu, Q. Niu, W. Yao, X. Xu, and C. Zhang, Phys. Rev. B **90**, 045427 (2014).
[10] Z. Wang, J. Shan, and K. F. Mak, Nat. Nanotechnol. **12**, 144 (2017).
[11] A. Srivastava, M. Sidler, A. V. Allain, D. S. Lembke, A. Kis, and A. Imamoğlu, Nat. Phys. **11**, 141 (2015).
[12] G. Aivazian, Z. Gong, A. M. Jones, R.-L. Chu, J. Yan, D. G. Mandrus, C. Zhang, D. Cobden, W. Yao, and X. Xu, Nat. Phys. **11**, 148 (2015).
[13] D. MacNeill, C. Heikes, K. F. Mak, Z. Anderson, A. Kormányos, V. Zólyomi, J. Park, and D. C. Ralph, Phys. Rev. Lett. **114**, 037401 (2015).
[14] J. R. Schaibley, H. Yu, G. Clark, P. Rivera, J. S. Ross, K. L. Seyler, W. Yao, and X. Xu, Nat. Rev. Mater. **1**, 16055 (2016).
[15] M. A. Schmidt, L. Wondraczek, H. W. Lee, N. Granzow, N. Da, and P. S. J. Russell, Adv. Mater. **23**, 2681 (2011).
[16] R. Schmidt, A. Arora, G. Plechinger, P. Nagler, A. G. del Águila, M. V. Ballottin, P. C. Christianen, S. M. de Vasconcellos, C. Schüller, T. Korn *et al.*, Phys. Rev. Lett. **117**, 077402 (2016).
[17] H. Da, L. Gao, Y. An, H. Zhang, and X. Yan, Adv. Opt. Mater. **6**, 1701175 (2018).
[18] A. V. Stier, N. P. Wilson, K. A. Velizhanin, J. Kono, X. Xu, and S. A. Crooker, Phys. Rev. Lett. **120**, 057405 (2018).
[19] J. Zipfel, J. Holler, A. A. Mitioglu, M. V. Ballottin, P. Nagler, A. V. Stier, T. Taniguchi, K. Watanabe, S. A. Crooker, P. C. Christianen *et al.*, Phys. Rev. B **98**, 075438 (2018).
[20] A. V. Stier, N. P. Wilson, G. Clark, X. Xu, and S. A. Crooker, Nano Lett. **16**, 7054 (2016).
[21] A. A. Mitioglu, K. Galkowski, A. Surrente, L. Klopotowski, D. Dumcenco, A. Kis, D. K. Maude, and P. Plochocka, Phys. Rev. B **93**, 165412 (2016).
[22] A. V. Stier, K. M. McCreary, B. T. Jonker, J. Kono, and S. A. Crooker, Nat. Commun. **7**, 10643 (2016).
[23] Y. Li, J. Ludwig, T. Low, A. Chernikov, X. Cui, G. Arefe, Y. D. Kim, A. M. van der Zande, A. Rigosi, H. M. Hill *et al.*, Phys. Rev. Lett. **113**, 266804 (2014).
[24] G. Plechinger, P. Nagler, A. Arora, A. Granados del Aguila, M. V. Ballottin, T. Frank, P. Steinleitner, M. Gmitra, J. Fabian, P. C. Christianen *et al.*, Nano Lett. **16**, 7899 (2016).
[25] A. V. Stier, K. M. McCreary, B. T. Jonker, J. Kono, and S. A. Crooker, J. Vac. Sci. Technol. **34**, 04J102 (2016).
[26] A. A. Mitioglu, P. Plochocka, A. Granados del Aguila, P. Christianen, G. Deligeorgis, S. Anghel, L. Kulyuk, and D. Maude, Nano Lett. **15**, 4387 (2015).
[27] J. Have and T. G. Pedersen, Phys. Rev. B **97**, 115405 (2018).
[28] G. H. Wannier, Phys. Rev. **52**, 191 (1937).
[29] M. Van der Donck, M. Zarenia, and F. M. Peeters, Phys. Rev. B **97**, 195408 (2018).
[30] T. G. Pedersen, Phys. Rev. B **92**, 235432 (2015).
[31] G.-B. Liu, W.-Y. Shan, Y. Yao, W. Yao, and D. Xiao, Phys. Rev. B **88**, 085433 (2013).
[32] J. L. Cheng and C. Guo, Phys. Rev. B **97**, 125417 (2018).
[33] D. V. Rybkovskiy, I. C. Gerber, and M. V. Durnev, Phys. Rev. B **95**, 155406 (2017).
[34] A. Ferreira, J. Viana-Gomes, Y. V. Bludov, V. Pereira, N. M. R. Peres, and A. H. Castro Neto, Phys. Rev. B **84**, 235410 (2011).
[35] G. Catarina, J. Have, J. Fernández-Rossier, and N. M. R. Peres, arXiv:1811.04003.
[36] L. V. Keldysh, Pis'ma Zh. Eksp. Teor. Fiz. **29**, 716 (1979) [Sov. Phys. JETP **29**, 658 (1979)].
[37] P. Cudazzo, I. V. Tokatly, and A. Rubio, Phys. Rev. B **84**, 085406 (2011).
[38] M. L. Trolle, T. G. Pedersen, and V. Véniard, Sci. Rep. **7**, 39844 (2017).

[39] H. Ehrenreich and M. H. Cohen, Phys. Rev. **115**, 786 (1959).
[40] K. Shizuya, Phys. Rev. B **81**, 075407 (2010).
[41] A. A. Sokolik, A. D. Zabolotskiy, and Y. E. Lozovik, Phys. Rev. B **95**, 125402 (2017).
[42] J. Nilsson, A. H. Castro Neto, F. Guinea, and N. M. R. Peres, Phys. Rev. Lett. **97**, 266801 (2006).
[43] F. A. Rasmussen and K. S. Thygesen, J. Phys. Chem. C **119**, 13169 (2015).
[44] M. Rohlfing and S. G. Louie, Phys. Rev. B **62**, 4927 (2000).
[45] C. Stafford, S. Schmitt-Rink, and W. Schaefer, Phys. Rev. B **41**, 10000 (1990).
[46] T. G. Pedersen, Phys. Rev. B **94**, 125424 (2016).
[47] M. Massicotte, F. Vialla, P. Schmidt, M. B. Lundeberg, S. Latini, S. Haastrup, M. Danovich, D. Davydovskaya, K. Watanabe, T. Taniguchi *et al.*, Nat. Commun. **9**, 1633 (2018).
[48] F. Johansson *et al.*, mpmath: A Python library for arbitrary-precision floating-point arithmetic (version 0.18), http://mpmath.org.
[49] Y. Lin, X. Ling, L. Yu, S. Huang, A. L. Hsu, Y.-H. Lee, J. Kong, M. S. Dresselhaus, and T. Palacios, Nano Lett. **14**, 5569 (2014).
[50] G. D. Mahan, *Many-Particle Physics* (Springer Science & Business Media, New York, 2013).
[51] Y. A. Bychkov and E. I. Rashba, Zh. Eksp. Teor. Fiz. **85**, 1826 (1983) [Sov. Phys. JETP **58**, 1062 (1983)].

Paper D

Optical orientation with linearly polarized light in transition metal dichalcogenides

G. Catarina, J. Have, J. Fernández-Rossier, and N. M. R. Peres

Published in
Physical Review B **99**, 125405 (2019).

Optical orientation with linearly polarized light in transition metal dichalcogenides

G. Catarina,[1,*] J. Have,[2,3] J. Fernández-Rossier,[1,†] and N. M. R. Peres[1,4]

[1]*QuantaLab, International Iberian Nanotechnology Laboratory, 4715-330 Braga, Portugal*

[2]*Department of Materials and Production, Aalborg University, DK-9220 Aalborg East, Denmark*

[3]*Department of Mathematical Sciences, Aalborg University, DK-9220 Aalborg East, Denmark*

[4]*Centro de Física das Universidades do Minho e Porto and Departamento de Física and QuantaLab, Universidade do Minho, Campus de Gualtar, 4710-057 Braga, Portugal*

(Received 13 November 2018; published 5 March 2019)

We study the optical properties of semiconducting transition metal dichalcogenide monolayers under the influence of strong out-of-plane magnetic fields, using the effective massive Dirac model. We pay attention to the role of spin-orbit-coupling effects, doping level, and electron-electron interactions, treated at the Hartree-Fock level. We find that optically induced valley and spin imbalance, commonly attained with circularly polarized light, can also be obtained with linearly polarized light in the doped regime. Additionally, we explore an exchange-driven mechanism to enhance the spin-orbit splitting of the conduction band, in *n*-doped systems, controlling both the carrier density and the intensity of the applied magnetic field.

DOI: 10.1103/PhysRevB.99.125405

I. INTRODUCTION

The discovery of two-dimensional (2D) systems whose quasiparticles are described in terms of a Dirac theory [1] has been one of the major breakthroughs over the last two decades in condensed matter physics and has fueled research in the area of 2D materials [2,3]. Graphene, that features gapless Dirac cones in the neighborhood of the Fermi energy [4], is a paradigmatic example. Interestingly, there are also 2D semiconductors that require a description through a massive Dirac equation [5,6], instead of a Schrödinger-type model. Whereas both Dirac and Schrödinger theories would yield similar energy bands, their wave functions and linear response are distinct. The massive Dirac Hamiltonian comprises a finite Berry curvature that entails an unconventional Hall response [7]. The Landau level spectrum of massive Dirac electrons features valley-dependent zeroth Landau levels aligned with either the valence or the conduction bands [8]. These properties are absent for Schrödinger quasiparticles.

The effective picture in terms of a gapped Dirac Hamiltonian provides a unifying description of materials that, from the chemical point of view, are quite different. For instance, whereas for graphene the Dirac states are made of p_z orbitals [4], for transition metal dichalcogenides they are made of $d_{x^2-y^2}$ and d_{xy} orbitals in the valence band and d_{z^2} in the conduction band [5,9].

In this work, we study the optical response of massive Dirac systems under the influence of applied out-of-plane magnetic fields. We focus on the case of transition metal dichalcogenide (TMD) monolayers MX_2, where $M =$ Mo,W and $X =$ S,Se, whose magneto-optical properties have attracted considerable interest both from the experimental [10–13] and theoretical [14,15] sides. These direct-band-gap semiconductors are the object of intense scrutiny because of their strong light-matter coupling [16,17], strong spin-orbit interactions [5,9], rich excitonic effects [18–21], and potential applications in the emergent field of valleytronics [22,23]. Nevertheless, our results can be easily adapted to other systems described by a massive Dirac equation, such as gapped graphene [24,25], silicene and related materials [26], or antiferromagnetic honeycomb semiconductors [27].

The effects of orbital coupling to an external out-of-plane magnetic field, as well as spin-orbit interactions, are explicitly taken into account. Electron-electron interactions are considered at the Hartree-Fock level, but electron-hole attraction and corresponding excitonic effects are left for a companion publication [28].

The rest of this paper is organized as follows. In Sec. II, we introduce the physical system and its model Hamiltonian, which forms the basis for the whole work. Section III contains the formalism used to calculate the magneto-optical properties, in particular the derivation of the electric susceptibility response function. The analysis of the results is presented in Sec. IV for the longitudinal susceptibility, in Sec. V for the transverse susceptibility, and in Sec. VI for the response to circularly polarized light. Section VII is devoted to the calculation of the exchange self-energy corrections. Additional technical details are provided in the Appendices.

II. MODEL HAMILTONIAN

We consider a single-layer TMD in the xy plane with a perpendicular uniform magnetic field pointing in the z direction. The crystal structure consists of a hexagonal lattice of trigonal prismatic unit cells, each of them containing one transition metal atom and two chalcogens. The resulting hexagonal Brillouin zone has two inequivalent sets of three equivalent

*goncalo.catarina@inl.int

†On leave from Departamento de Física Aplicada, Universidad de Alicante, 03690 San Vicente del Raspeig, Spain.

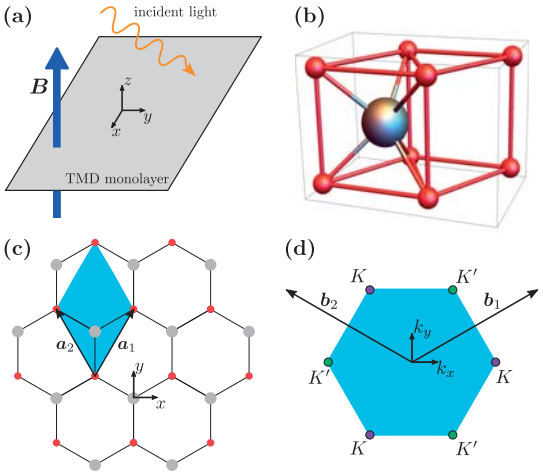

FIG. 1. Representation of the physical system. (a) Light is shinned into a transition metal dichalcogenide (TMD) monolayer subject to a perpendicular magnetic field $\boldsymbol{B}$, uniform in space and time. (b), (c) The TMD crystal structure consists of a hexagonal lattice [top view shown in (c)] of trigonal prismatic unit cells (b), each of them containing one transition metal atom (big gray spheres) and two chalcogens (small red spheres); in (c), the blue region marks the unit cell of the crystal, defined by the primitive vectors $\boldsymbol{a}_1$ and $\boldsymbol{a}_2$. (d) Corresponding (hexagonal) Brillouin zone, defined in reciprocal space by the primitive vectors $\boldsymbol{b}_1$ and $\boldsymbol{b}_2$, with the Dirac points K and K' indicated.

corners, the so-called K and K' valleys (or Dirac points). Due to the absence of an inversion center, the valley index provides an additional discrete degree of freedom for carriers in this system. The physical system is depicted in Fig. 1.

In the low-energy regime, the electronic properties of TMD monolayers are often described by a massive Dirac Hamiltonian around the valleys [5,14,29,30]. Spin-orbit coupling (SOC) splits both the valence and conduction bands, with opposite spin splittings at the two valleys, preserving time-reversal symmetry thereby and leading to the so-called spin-valley coupling [5]. The magnitude of SOC splitting in the valence and conduction bands is different, on account of their different atomic orbital breakdown. The spin splitting of the valence band is of the order of hundreds of meV whereas, in the conduction band, it is smaller than few tens of meV [29]. Moreover, different TMD materials yield different relative signs of spin splitting in the conduction and valence bands at a given valley [29]. In these systems, SOC commutes with the spin operator S_z. As a result, it can be introduced in a phenomenological manner [20,31] by redefining the Dirac mass, including a valley (τ) and spin (s) dependency $\Delta \to \Delta_{\tau s}$, and adding an offset energy term $\xi_{\tau s}$, defined below.

In the presence of a uniform out-of-plane magnetic field $\boldsymbol{B} = B_0\hat{\boldsymbol{z}}$, the single-particle Hamiltonian for each valley and spin subspace is thus written, in the Landau gauge, as

$$H_0^{\tau,s} = v_F(\tau\sigma_x p_x + \sigma_y p_y + eB_0 x\sigma_y) + \Delta_{\tau s}\sigma_z + \xi_{\tau s}\mathbb{1}_2, \quad (1)$$

where $\tau = \pm$ (+ for the K valley and − for the K'), $s = \uparrow(+), \downarrow(-)$, v_F is the Fermi velocity, σ_i ($i = x, y, z$) are the Pauli matrices with eigenvalues ± 1, $\boldsymbol{p} = (p_x, p_y) = -i\hbar\boldsymbol{\nabla}$ is the canonical electron momentum ($\hbar$ is the reduced Planck constant), $-e < 0$ is the electron charge and $\mathbb{1}_2$ is the 2×2 identity matrix. The Pauli matrices and the identity matrix act on the space of the highest-energy valence and lowest-energy conduction states [5]. The explicit forms of the valley- and spin-dependent Dirac mass $\Delta_{\tau s}$ and offset energy $\xi_{\tau s}$ read as [20,31]

$$\Delta_{\tau s} = \Delta - \tau s\frac{\Delta_{\rm SOC}^{\mathcal{V}} - \Delta_{\rm SOC}^{\mathcal{C}}}{4}, \quad \xi_{\tau s} = \tau s\frac{\Delta_{\rm SOC}^{\mathcal{V}} + \Delta_{\rm SOC}^{\mathcal{C}}}{4}, \quad (2)$$

where $\Delta_{\rm SOC}^{\mathcal{V}}$ ($\Delta_{\rm SOC}^{\mathcal{C}}$) is the spin splitting in the valence (conduction) band. For $B_0 = 0$, the band gap is given by $2\Delta_{\tau s}$.

The effective Hamiltonian (1) shows that the dependency of the mass term on the valley and spin indices is encoded in the product τs. In addition, the valley index appears on its own in the kinetic term, leading to valley-selective circular dichroism (introduced in Sec. III C), as we discuss in Sec. VI. We neglect Zeeman splitting, that could be easily added as an additional term $g\mu_B B_0 \frac{s}{2}\mathbb{1}_2$, where g is the g factor and μ_B the Bohr magneton. This term would split the energy bands of the two spin channels by $|g|\mu_B B_0 \simeq 0.12 B_0$ [T] meV. Compared to the spin splitting driven by the strong SOC, this effect is, for any reasonable scenario, negligible in the valence bands of TMDs. As for the conduction bands, even though Zeeman and SOC can yield comparable magnitudes for strong applied fields, the results discussed in this paper are not substantially affected by the absence of Zeeman splitting in the model. The effect of higher than first order $\boldsymbol{k}\cdot\boldsymbol{p}$ terms in the Hamiltonian [30] has also been ignored.

Closed analytical expressions for the eigenstates of $H_0^{\tau,s}$ can be obtained in terms of Landau levels that fall into two categories: the zeroth Landau level and the $n \neq 0$ Landau levels [8,24,32]. The eigenvalues read as

$$E_{n,\lambda}^{\tau,s} = \lambda\sqrt{\Delta_{\tau s}^2 + \tfrac{1}{2}(\hbar\omega_0)^2 n} + \xi_{\tau s}, \quad (3)$$

where $\frac{\omega_0}{2} = \frac{v_F}{l_B}$ is the characteristic angular frequency ($l_B = \sqrt{\frac{\hbar}{eB_0}}$ is the magnetic length) and $\{n;\lambda\}$ is the set of quantum numbers that describes the energy levels of this system, in which n is the Landau level (LL) index and λ the conduction ($\mathcal{C}$) or valence ($\mathcal{V}$) band index. For the $n \neq 0$ LLs, $n = 1, 2, \ldots$, and $\lambda = +(\mathcal{C}), -(\mathcal{V})$; the zeroth Landau level (0LL) is obtained setting $n = 0$ and $\lambda = -\tau$. The corresponding wave functions yield

$$\psi_{n,\lambda,k_y}^{\tau,s}(u,y) = \frac{e^{ik_y y}}{\sqrt{L_y}}\frac{e^{-u^2/2}}{\sqrt{\sqrt{\pi}l_B}}C_{n,\lambda}^{\tau,s}\begin{pmatrix}\tilde{H}_{n_\tau}(u)\\ iB_{n,\lambda}^{\tau,s}\tilde{H}_{n_\tau+\tau}(u)\end{pmatrix}, \quad (4)$$

where k_y stands for the wave vector in the y direction, which is quantized as $k_y = \frac{2\pi n_y}{L_y}$, $n_y \in \mathbb{Z}$ by applying periodic boundary conditions along the y direction to a sample of length L_y. We have also defined $u \equiv \frac{x}{l_B} + l_B k_y$, $n_\tau \equiv n - \frac{1+\tau}{2}$, $\tilde{H}_n \equiv \frac{1}{\sqrt{2^n n!}}H_n$ for $n \geqslant 0$ (where H_n are the Hermite polynomials) and $\tilde{H}_{-1} \equiv 0$. The normalization constants $C_{n,\lambda}^{\tau,s}$ and $B_{n,\lambda}^{\tau,s}$ are

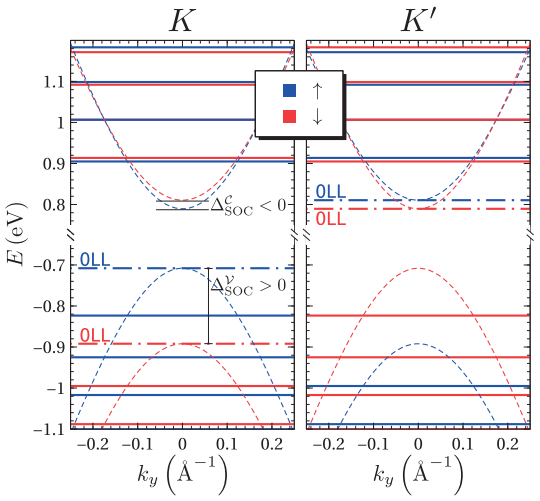

FIG. 2. Energy bands of monolayer $MoSe_2$ in the Dirac approximation. Different colors represent different spin projections: blue for spin up and red for spin down. Dashed lines describe the solutions without external fields; band crossing exists in the conduction bands because $\Delta^{\mathcal{C}}_{\rm SOC} < 0$. The application of an out-of-plane magnetic field ($B_0 = 500$ T in this figure) leads to the quantization of these bands into the Landau levels (horizontal lines); the unfeasible magnitude of B_0 is set only for readability purposes, as the observed features do not change qualitatively when working with practical values. Comparing the energy bands of both K and K' valleys, only the spin projection is interchanged, except for the zeroth Landau levels (dashed-dotted lines).

given by

$$C^{\tau,s}_{n,\lambda} = \sqrt{\frac{\bar{\Delta}_{\tau s}\left(\bar{\Delta}_{\tau s} + \check{E}^{\tau,s}_{n,\lambda}\right) + n}{\bar{\Delta}_{\tau s}\left(\bar{\Delta}_{\tau s} + \check{E}^{\tau,s}_{n,\lambda}\right) + 2n}} \in \mathbb{R} \tag{5}$$

and

$$B^{\tau,s}_{0\rm LL} = -i, \quad B^{\tau,s}_{n\neq 0,\lambda} = \frac{\sqrt{2n}}{\bar{\Delta}_{\tau s} + \check{E}^{\tau,s}_{n,\lambda}} \in \mathbb{R}, \tag{6}$$

in which $\bar{\Delta}_{\tau s} \equiv \frac{2\Delta_{\tau s}}{\hbar\omega_0}$, $\check{E}^{\tau,s}_{n,\lambda} \equiv \bar{E}^{\tau,s}_{n,\lambda} - \bar{\xi}_{\tau s}$, $\bar{E}^{\tau,s}_{n,\lambda} \equiv \frac{2E^{\tau,s}_{n,\lambda}}{\hbar\omega_0}$, and $\bar{\xi}_{\tau s} \equiv \frac{2\xi_{\tau s}}{\hbar\omega_0}$.

The band structure implied by Eq. (3) is depicted in Fig. 2 for the case of $MoSe_2$. Except for Sec. VII, typical general values $\hbar v_F = 3.5$ eV Å and $\Delta = 0.8$ eV [5] are fixed throughout the paper. Regarding the SOC parameters, each TMD is treated in separate as there are significant differences among different materials, for instance, on the sign of $\Delta^{\mathcal{C}}_{\rm SOC}$. The SOC values used in this work are listed in Table I.

The properties of the 0LL eigenstates are quite different from those of the $n \neq 0$ LLs. The energy levels of the $n \neq 0$ LLs depend on the product τs, meaning that we can correspond K to K' bands by interchanging the spin projections. However, this does not hold for the $n = 0$ LLs, whose energy is given by $E^{\tau,s}_{0\rm LL} = -\tau\Delta_{\tau s} + \xi_{\tau s}$. In fact, we see that the K (K') valley hosts a valencelike (conductionlike) 0LL spin doublet. This doublet is split exclusively by SOC, as the 0LLs do not disperse with the applied magnetic field, which also contrasts with the $n \neq 0$ LLs.

TABLE I. List of spin-orbit-coupling (SOC) parameters $\Delta^{\mathcal{V}/\mathcal{C}}_{\rm SOC}$ and effective Bohr magnetons $\tilde{\mu}^{(\tau s)}_B$ (in units of Bohr magneton μ_B) for different transition metal dichalcogenide materials. The SOC parameters are taken from Ref. [29]. The effective Bohr magnetons are calculated through the expression defined in the text. By definition, $\tilde{\mu}^{(\tau s)}_B$ depends on the product of valley (τ) and spin (s).

	$\Delta^{\mathcal{V}}_{\rm SOC}$(eV)	$\Delta^{\mathcal{C}}_{\rm SOC}$(eV)	$\tilde{\mu}^{(\tau s=+)}_B(\mu_B)$	$\tilde{\mu}^{(\tau s=-)}_B(\mu_B)$
MoS_2	0.148	−0.003	2.11	1.92
WS_2	0.430	+0.029	2.30	1.79
$MoSe_2$	0.184	−0.021	2.15	1.89
WSe_2	0.466	+0.036	2.32	1.77

It must be noted, however, that more elaborate calculations [15,33] reveal a valley-dependent spectrum that contrasts with the Dirac model. Although the valley-dependent physics of the 0LL is captured in the same manner, these first-principles calculations show $n \neq 0$ LLs that are also different for both valleys, even when SOC is ignored [33].

For most practical values of $n \neq 0$ and B_0, it is true that $\Delta^2_{\tau s} \gg \frac{1}{2}(\hbar\omega_0)^2 n$. Therefore, we can expand Eq. (3) in Taylor series and obtain

$$E^{\tau s}_{n\neq 0,\mathcal{C}} \simeq \Delta + 2\tilde{\mu}^{(\tau s)}_B n B_0 + \tau s\frac{\Delta^{\mathcal{C}}_{\rm SOC}}{2} \tag{7}$$

and

$$E^{\tau s}_{n\neq 0,\mathcal{V}} \simeq -\left(\Delta + 2\tilde{\mu}^{(\tau s)}_B n B_0 - \tau s\frac{\Delta^{\mathcal{V}}_{\rm SOC}}{2}\right), \tag{8}$$

where we have defined the effective Bohr magneton as $\tilde{\mu}^{(\tau s)}_B = \frac{e\hbar}{2m_{\tau s}}$, in which $m_{\tau s} = \frac{\Delta_{\tau s}}{v_F^2}$ is the effective electron rest mass. From these equations, it is clear that the $n \neq 0$ LLs disperse linearly with n and B_0, but with a slope that is controlled by $\tilde{\mu}^{(\tau s)}_B$ and thus yields different values for $\tau s = +$ or $\tau s = -$ (see Table I). As a result, at a given valley, the sign of the spin splitting between two LLs with the same $n \neq 0$ and different spin s can be reversed as we ramp either n or B_0. This is apparent in the conduction bands of Fig. 2 and is a direct consequence of the fact that SOC leads to a spin-dependent nonrelativistic mass in the Dirac theory, which in turn controls LL dispersion.

III. MAGNETO-OPTICAL RESPONSE: FORMALISM

In this section, we introduce a general formalism to calculate the magneto-optical response in metals and semiconductors: the equation of motion (EOM) method [34], a technique based on Ref. [35] and generalized to include the effect of external magnetic fields. The EOM method permits to derive analytical expressions of response functions that are fully equivalent to the Kubo formula when linear response theory is employed and electron-electron interactions are not taken into account. Here, we apply this formalism to the Hamiltonian described in Sec. II and derive, within the linear response regime, analytical expressions for the electric susceptibility

tensor in the Cartesian basis, which are then manipulated to explicitly address the case in which the incident light is circularly polarized. Free carrier transitions are considered in a first approximation, disregarding all the Coulomb interactions and thus treating electrons and holes as quasifree particles. Compared to the Kubo formula, the advantage of the EOM method is that, by treating Coulomb effects at the same level of the interaction with light, further corrections can be introduced within the same formalism. In Sec. VII, we account for Coulomb interactions at the self-energy level. The role of excitonic effects is the main subject of a forthcoming publication [28].

A. Dipole matrix elements

The interaction with light is included, within the dipole approximation, via the following Hamiltonian:

$$H_I = -\boldsymbol{d}\cdot\boldsymbol{\mathcal{E}} = e\boldsymbol{r}\cdot\boldsymbol{\mathcal{E}}(t), \tag{9}$$

where $\boldsymbol{r}=(x,y)$ is the 2D position vector, $\boldsymbol{d}=-e\boldsymbol{r}$ is the electric dipole moment, and $\boldsymbol{\mathcal{E}}=\boldsymbol{\mathcal{E}}(t)$ is the electric field of the incident light, which is assumed homogeneous and dependent of the time t.

The method used in this paper relies on the calculation of the expectation value of the electric polarization density operator with regard to the unperturbed Hamiltonian, whose (complete) basis is $\alpha=\{n;\lambda;k_y\}$. Therefore, the matrix elements of the polarization density created by the dipole $\boldsymbol{P}=\frac{\boldsymbol{d}}{A}$ (A is the area of the system) are relevant quantities that define optical selection rules.

The computation of the dipole matrix elements in each one of the $\eta=\{\tau;s\}$ subspaces, $\boldsymbol{d}^{\eta}_{\alpha\to\alpha'}=\langle\alpha'|\boldsymbol{d}|\alpha\rangle_{\eta}=(\boldsymbol{d}^{\eta}_{\alpha'\to\alpha})^{*}$, shows that only transitions between the same k_y are coupled, i.e., $\boldsymbol{d}^{\eta}_{\alpha\to\alpha'}=\delta_{k_y,k_y}\boldsymbol{d}^{\eta\{n';\lambda'\}}_{\{n;\lambda\}}$ [36]. In addition, it also reveals that the only nonzero terms are

$$\boldsymbol{d}^{\eta\{n+\tau;\lambda'\}}_{\{n;\lambda\}}=\frac{-e\hbar v_F}{E^{\eta}_{n,\lambda}-E^{\eta}_{n+\tau,\lambda'}}C^{\eta}_{n+\tau,\lambda'}C^{\eta}_{n,\lambda}B^{\eta}_{n,\lambda}(-\tau,i) \tag{10}$$

for $n+\tau\geqslant 0$, and

$$\boldsymbol{d}^{\eta\{n-\tau;\lambda'\}}_{\{n;\lambda\}}=\frac{-e\hbar v_F}{E^{\eta}_{n,\lambda}-E^{\eta}_{n-\tau,\lambda'}}C^{\eta}_{n-\tau,\lambda'}C^{\eta}_{n,\lambda}\left(B^{\eta}_{n-\tau,\lambda'}\right)^{*}(\tau,i) \tag{11}$$

for $n-\tau\geqslant 0$. The former relations embody the following optical selection rule: for an electron with wave vector k_y and in a given LL with index n, the absorption of a photon can only induce a transition, which can be intraband or interband, to a state with the same wave vector and with a LL index given by $n'=n\pm 1\geqslant 0$. This well-known selection rule [25,26,34,37] adds up to the ones imposed by construction: the decoupling of the valleys, which is consistent with the dipole approximation, and the decoupling of the spins, which is consistent with the lack of spin-flip terms in the Hamiltonian.

B. Electric susceptibility

Moving to the Heisenberg picture, and introducing the (time-dependent) creation/annihilation fermionic operators in this representation, $\hat{c}^{\dagger}_{\alpha,\eta}(t)/\hat{c}_{\alpha,\eta}(t)$, the total Hamiltonian can be written as

$$\hat{H}(t)=\hat{H}_0(t)+\hat{H}_I(t), \tag{12}$$

where

$$\hat{H}_0(t)=\sum_{\eta,\alpha}E^{\eta}_{\alpha}\hat{c}^{\dagger}_{\alpha,\eta}(t)\hat{c}_{\alpha,\eta}(t) \tag{13}$$

is the unperturbed Hamiltonian and

$$\hat{H}_I(t)=-\boldsymbol{\mathcal{E}}(t)\cdot\sum_{\eta,\alpha,\alpha'}\boldsymbol{d}^{\eta}_{\alpha\to\alpha'}\hat{c}^{\dagger}_{\alpha',\eta}(t)\hat{c}_{\alpha,\eta}(t) \tag{14}$$

is the Hamiltonian that describes the dipole interaction with light. Repeating the same procedure for the polarization density, we get

$$\hat{\boldsymbol{P}}(t)=\frac{1}{A}\sum_{\eta,\alpha,\alpha'}\boldsymbol{d}^{\eta}_{\alpha\to\alpha'}\hat{c}^{\dagger}_{\alpha',\eta}(t)\hat{c}_{\alpha,\eta}(t) \tag{15}$$

and, defining the general operator $\hat{T}^{\eta}_{\alpha,\alpha'}(t)\equiv\hat{c}^{\dagger}_{\alpha',\eta}(t)\hat{c}_{\alpha,\eta}(t)$, whose EOM reads as

$$-i\hbar\frac{d}{dt}\hat{T}^{\eta}_{\alpha,\alpha'}(t)=\left[\hat{H}(t),\hat{T}^{\eta}_{\alpha,\alpha'}(t)\right], \tag{16}$$

it is apparent that the time evolution of the polarization density operator can be achieved by solving Eq. (16).

The details regarding the technical step of solving the above-mentioned EOM are provided in Appendix A. In short, we start by calculating the commutator, so we can explicitly write the differential equation. Then, we solve for its expectation value within the linear response approximation and in the adiabatic regime. The outcome is the expression for $\langle\hat{\boldsymbol{P}}(t)\rangle\equiv\boldsymbol{P}(t)$ within the former approximations.

Expressing $\boldsymbol{P}(t)$ through its Fourier transform $\boldsymbol{P}(\omega)$, we are then able to recognize the (homogeneous and dynamical) electric susceptibility tensor

$$\chi(\omega)=\begin{pmatrix}\chi_{xx}(\omega) & \chi_{xy}(\omega)\\ \chi_{yx}(\omega) & \chi_{yy}(\omega)\end{pmatrix} \tag{17}$$

via the constitutive relation $\boldsymbol{P}(\omega)=\varepsilon_0\chi(\omega)\boldsymbol{\mathcal{E}}(\omega)$, where ε_0 is the vacuum permittivity, ω is the angular frequency, and $\boldsymbol{\mathcal{E}}(\omega)$ is the Fourier transform of $\boldsymbol{\mathcal{E}}(t)$. Putting it all together, we conclude that $\chi_{xx}=\chi_{yy}$ and $\chi_{xy}=-\chi_{yx}$, which is an expected result for systems with C_6 symmetry [38]. The final expressions for the longitudinal and transverse susceptibilities χ_{xx} and χ_{yx}, respectively, read as

$$\chi_{xx}(\omega)=\mathcal{S}_{+}(\omega),\qquad \chi_{yx}(\omega)=i\mathcal{S}_{-}(\omega), \tag{18}$$

where $\mathcal{S}_{\pm}(\omega)$ are auxiliary functions defined as

$$\mathcal{S}_{\pm}(\omega)\equiv\sum_{\eta}\sum_{\{n;\lambda\},\lambda'}\frac{f\left(E^{\eta}_{n+1,\lambda'}\right)-f\left(E^{\eta}_{n,\lambda}\right)}{2\pi l_B^2\varepsilon_0}\left|d_x^{\eta\{n+1;\lambda'\}}_{\{n;\lambda\}}\right|^2\times\left(\frac{1}{E^{\eta}_{n,\lambda}-E^{\eta}_{n+1,\lambda'}+\hbar\omega+i\Gamma}\pm\frac{1}{E^{\eta}_{n,\lambda}-E^{\eta}_{n+1,\lambda'}-\hbar\omega-i\Gamma}\right), \tag{19}$$

in which Γ is a phenomenological parameter that accounts for disorder within the adiabatic approximation and f stands for the Fermi-Dirac distribution at Fermi level μ and absolute temperature T (see Appendix A for details). Throughout this

work, we have set $\Gamma = 7$ meV, which is a rather low but feasible value that corresponds to samples of TMDs encapsulated in hexagonal boron nitride and with little impurity [39,40]. The disorder parameter does not influence the results presented in this paper if the full-width at half-maximum of the Lorentzian implicit in Eq. (19), 2Γ, is smaller (or at least of the same order of magnitude) than the LL splitting, which is roughly given by $2\tilde{\mu}_B^{(\tau s)}B_0 \sim 0.2B_0$ [T] meV. This explains why we have set such strong (but still feasible) out-of-plane magnetic fields in the optical response results. For clarity purposes, we stress that, to write $\chi_{yx}(\omega)$ in its final form, we have used that $(d_{y\,\{n;\lambda\}}^{\eta\,\{n+1;\lambda'\}})^* d_{x\,\{n;\lambda\}}^{\eta\,\{n+1;\lambda'\}} = i|d_{x\,\{n;\lambda\}}^{\eta\,\{n+1;\lambda'\}}|^2$.

C. Circularly polarized light

Associated with the will of exploring valley-based optoelectronic applications, many studies deal with circularly polarized light [41,42]. The underlying mechanism is valley-selective circular dichroism, i.e., differential absorption of left- and right-handed photons when comparing the contributions from inequivalent valleys. This contrasts with the usual circular dichroism, for which there is a difference in the (overall) absorption of left-handed (σ^-) and right-handed (σ^+) light. At $\boldsymbol{B} = \boldsymbol{0}$, the massive Dirac Hamiltonian breaks time-reversal symmetry in each valley, leading to a circular dichroism that is valley dependent [41,43,44]. In this case, the total circular dichroism vanishes when summing over valleys, as time-reversal symmetry is restored. However, illumination with circularly polarized light results in populations of excited carriers with valley polarization. Conceptually, this permits to access the valley pseudospin degree of freedom, the key idea of valleytronics. In addition, because of the strong SOC, the same mechanism also leads to an optically induced spin imbalance in TMD materials [44]. In this work, we propose a complementary route to induce both valley and spin polarization in TMDs with linearly polarized light. Nevertheless, for completeness, we discuss here the case of incident circularly polarized light, which is relevant for Sec. VI.

Assuming incident light with circular polarization, i.e., $\boldsymbol{\mathcal{E}}(\omega) = \boldsymbol{\mathcal{E}}^{\pm}(\omega) \equiv \frac{\mathcal{E}_0(\omega)}{\sqrt{2}}(1, e^{\pm i\pi/2})$, where $\mathcal{E}_0(\omega)$ is the (equal) amplitude of the two plane waves and $\pm$ stands, in the point of view of the source, for right and left polarization, respectively, the electric susceptibility tensor is shown to be diagonal in the circular basis, with the diagonal elements given by

$$\chi_{\pm}(\omega) = \chi_{xx}(\omega) \pm i\chi_{yx}(\omega). \tag{20}$$

This relation lays on symmetry foundations as it is valid as long as $\chi_{xx} = \chi_{yy}$ and $\chi_{xy} = -\chi_{yx}$ are satisfied. Moreover, it shows that circular dichroism is encoded in the real part of χ_{yx}.

IV. LONGITUDINAL SUSCEPTIBILITY

We now move onto the discussion of the main features that characterize the low-energy noninteracting magneto-optical response in TMDs. Although Coulomb interactions are known to be significant [10,13,21], the study of the noninteracting limit provides reference for further analyses.

In this section, we discuss the results for the dynamical longitudinal susceptibility $\chi_{xx}(\omega)$. This quantity is directly relevant in modeling experiments where TMDs are excited with linearly polarized light. In addition, $\chi_{xx}(\omega)$ contributes to $\chi_{\pm}(\omega)$, as seen in Eq. (20). Therefore, it is also important to interpret the response to circularly polarized light (Sec. VI).

The evaluation of Eq. (19) requires a cutoff, as usual when dealing with low-energy effective models. For this matter, we establish a range of frequencies that are consistent with the underlying $\boldsymbol{k}\cdot\boldsymbol{p}$ theory that leads to the Dirac Hamiltonian. By construction, this theory is only valid in the neighborhood of the high-symmetry K and K' points, which sets an energy window out of which the model does not work. Taking an energy window of $[-1.5, 1.5]$ eV, for which the upper bound lies $\sim$0.7 eV above the bottom of the conduction band, and bearing in mind the optical selection rules, plus the Pauli exclusion principle, we see that $\hbar\omega \lesssim 3$ eV is a suitable criterion, as it contemplates all and only the transitions between bands within the energy window. This provides an intrinsic cutoff for the imaginary part of $\chi_{xx}(\omega)$, given that the only bands that contribute satisfy $|E_{n,\lambda}^{\eta} - E_{n+1,\lambda'}^{\eta}| \simeq \hbar\omega$. For the real part, we have found that numerical convergence is attained with a cutoff energy of $|E_{\text{cut}}| \sim 4$ eV, which corresponds to a cutoff in the LLs, n_{cut}, that varies roughly as $4 \times 10^4 (B_0\ [\text{T}])^{-1}$.

The analysis of the results in this section is divided into three main categories that depend on the doping level. We first consider the case of an intrinsic TMD, with μ lying inside the gap. Then, we focus on the doped regime and separate two distinct scenarios. First, we take a system on which the 0LLs do not participate in the optical transitions. Second, we discuss the case of a TMD n-doped (p-doped) up to the first 0LL in the conduction (valence) band, for which the optical transitions that involve the 0LLs take a predominant role.

A. Undoped regime: Fermi level in the gap

As we discuss in Sec. V, χ_{yx} vanishes for arbitrary ω in the undoped regime. Thus, for intrinsic TMDs, the magneto-optical response is governed exclusively by χ_{xx}. When μ lies in the gap, intraband transitions are Pauli blocked, as thermal activations are negligible compared to the band gap, even at room temperature ($k_BT \simeq 26$ meV for $T = 300$ K, compared to gaps in the order of $2\Delta = 1.6$ eV). Therefore, in the undoped regime, the magneto-optical response is independent of the temperature and fully driven by interband transitions. Figure 3 shows a plot of $\chi_{xx}(\omega)$ in a neutral MoS_2 for $B_0 = 30$ T, whose discussion follows.

The imaginary part of $\chi_{xx}(\omega)$ describes photon absorption processes, induced when the photon energy matches the energy difference between an occupied and an empty state. The resulting curve features a structure of peaks that correspond to interband transitions satisfying the optical selection rules, which are summarized in Table II. It must be noted that, although spin-valley coupling is not manifest in the LL spectrum due to the valley-dependent 0LLs (see Fig. 2), τs is still a relevant quantity to characterize transition energies, as all of them are maintained when we change valley and spin at the same time, even if the 0LLs are involved.

Within the frequency range $\mathcal{T}_0^{(\tau s=+)} < \hbar\omega < \mathcal{T}_0^{(\tau s=-)}$, where $\mathcal{T}_0^{(\tau s=\pm)} = E_{1,\mathcal{C}}^{K,\pm} - E_{0\text{LL}}^{K,\pm} = E_{0\text{LL}}^{K',\mp} - E_{1,\mathcal{V}}^{K',\mp}$ are the transition energies that correspond to the vertical blue and red

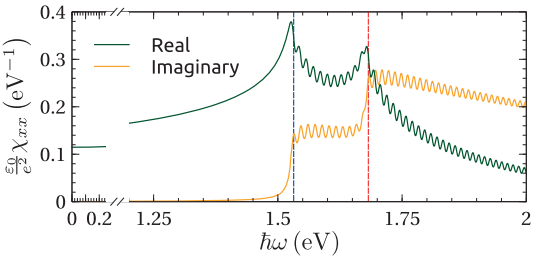

FIG. 3. Longitudinal susceptibility χ_{xx}, as a function of the photon energy, in monolayer MoS_2 at the charge neutrality point and for a magnetic field of 30 T (results independent of the temperature). The imaginary part, which is directly related with optical absorption, shows a sequence of peaks that correspond to the allowed optical transitions. The vertical dashed lines mark the energy of the less energetic transition for each spin-valley product: for the K (K') valley, blue is for spin up (down) and red for spin down (up). The presence of a plateau between the vertical lines is the signature of spin-orbit-coupling effects.

lines in Fig. 3 (respectively), only two (out of four) flavors of τ and s contribute to the absorption, namely, the ones that respect $\tau s = +$. For $\hbar\omega > \mathcal{T}_0^{(\tau s=-)}$, the absorption curve features a second step that marks the entrance of transitions with $\tau s = -$. The energy splitting of the two thresholds, given by $\mathcal{T}_0^{(\tau s=-)} - \mathcal{T}_0^{(\tau s=+)}$, depends explicitly on the SOC parameters and is easily shown to vanish if and only if $\Delta_{\mathrm{SOC}}^{\mathcal{V}} = \Delta_{\mathrm{SOC}}^{\mathcal{C}} = 0$. Thus, the presence of a plateau in $\mathrm{Im}\{\chi_{xx}(\omega)\}$ is a direct consequence of SOC interactions.

We now discuss the intensity of the degenerate transitions, which come in doublets for $\mathcal{T}_0^{(\tau s)}$ and in quadruplets for all the other transition energies, as depicted in Table II. The height of the transitions is governed by the dipole matrix elements in Eq. (19), which satisfy the identity

$$\left|d_x^{\tau,s\{n+1;\lambda'\}}_{\{n;\lambda\}}\right|^2 = \left|d_x^{-\tau,-s\{n+1;-\lambda'\}}_{\{n;-\lambda\}}\right|^2. \tag{21}$$

This relation shows that "counterpart transitions," i.e., transitions with the same energy and equal contributions to the optical response, are obtained by changing valley, spin, and also the band indexes at the same time. In Table II, we present the counterpart transitions in the same line. It is therefore clear that every absorption peak in Fig. 3 (which is characterized by a given τs product) has equal contributions from the two possible τ and s combinations. For instance, using the notation of Table II, this means that a peak with energy $\mathcal{T}_n^{(\tau s=+)}$ has equal contributions from $\tau = K, s = \uparrow$ and $\tau = K', s = \downarrow$.

TABLE II. List of the allowed optical transitions in intrinsic transition metal dichalcogenides, organized by their energies $(\mathcal{T}_0^{(\tau s)}, \mathcal{T}_1^{(\tau s)}, \ldots)$. The representation of the transitions that correspond to each energy is separated by valley τ, for a fixed spin-valley product (in this case given by $\tau s = s$, where s is the spin index). There are four degenerate transitions for every energy, except for $\mathcal{T}_0^{(\tau s)}$, for which there are two. Transitions with equal contributions to the optical response are presented in the same line.

	K, s	$K', -s$
$\mathcal{T}_0^{(\tau s)}$	$\{0;\mathcal{V}\} \to \{1;\mathcal{C}\}$	$\{1;\mathcal{V}\} \to \{0;\mathcal{C}\}$
$\mathcal{T}_1^{(\tau s)}$	$\{1;\mathcal{V}\} \to \{2;\mathcal{C}\}$	$\{2;\mathcal{V}\} \to \{1;\mathcal{C}\}$
	$\{2;\mathcal{V}\} \to \{1;\mathcal{C}\}$	$\{1;\mathcal{V}\} \to \{2;\mathcal{C}\}$
$\mathcal{T}_2^{(\tau s)}$	$\{2;\mathcal{V}\} \to \{3;\mathcal{C}\}$	$\{3;\mathcal{V}\} \to \{2;\mathcal{C}\}$
	$\{3;\mathcal{V}\} \to \{2;\mathcal{C}\}$	$\{2;\mathcal{V}\} \to \{3;\mathcal{C}\}$
$\mathcal{T}_{n>0}^{(\tau s)}$	$\{n;\mathcal{V}\} \to \{n+1;\mathcal{C}\}$	$\{n+1;\mathcal{V}\} \to \{n;\mathcal{C}\}$
	$\{n+1;\mathcal{V}\} \to \{n;\mathcal{C}\}$	$\{n;\mathcal{V}\} \to \{n+1;\mathcal{C}\}$

Interestingly, in the case of the quadruplets, the two pairs of counterpart transitions are not equivalent in intensities. In fact, the computation of the dipole matrix elements shows that one pair of transitions is overwhelmingly stronger than the other. This feature cannot be observed through the spin and valley breakdown of the absorption curve because both the weak and strong pairs of transitions are allowed in the undoped regime. However, as we discuss in Sec. IV B, doping allows to explore this property.

The real part of $\chi_{xx}(\omega)$, which describes the reactive dielectric response of the TMD, is also shown in Fig. 3. Expectedly, for in-gap frequencies, it decays smoothly as we decrease $\hbar\omega$ below the absorption threshold. Above the absorption threshold, it oscillates as a function of the frequency, due to the presence of many resonant peaks in absorption.

B. Doped system with optical transitions to zeroth Landau levels Pauli blocked

Away from charge neutrality, we find two fundamental differences with the undoped regime. First, intraband transitions enter into play, while some of the interband ones become Pauli blocked. Second, the ac Hall response, given by $\chi_{yx}(\omega)$, is no longer null, as we explore in Sec. V. The carrier density implied to get to this regime can arise either from gating or chemical doping.

We start with the case where the 0LLs cannot participate in the optical transitions, neither as initial nor final states. Due to the optical selection rules, it suffices to have μ lying above (below) both $n = 1$ LLs in the conduction (valence) band. In this regime, the system is a quantum Hall insulator and the ground state has no spin nor valley polarization. Without loss of generality, we take the example of an n-doped MoS_2, with $\mu = 1$ eV ($\sim$0.2 eV above the bottom of the conduction band), for a magnetic field of 50 T. The overview of the results is presented in Fig. 4, and its analysis follows.

Intraband and interband absorptions occur at very different frequencies, as observed in Fig. 4(a). The energy scale of the intraband absorption peak is controlled by the energy difference between two adjacent LLs in the same band, which, using Eqs. (7) and (8), can be estimated as $2\tilde{\mu}_B^{(\tau s)}B_0 \sim 0.2B_0$ [T] meV. Even for a very large field of 50 T, we see that the intraband peak occurs around $\hbar\omega = 10$ meV $\ll 2\Delta$. Thus, the discussion of the intra and interband parts of the magneto-optical spectrum can be separated.

At $T = 0$, the intraband peak in absorption has contributions from a total of four transitions. These intraband transitions connect the last occupied LL, $\{n;\lambda\} = \{n_F; \mathrm{sign}(\mu)\}$, and the first empty one, $\{n;\lambda\} = \{n_F + \mathrm{sign}(\mu); \mathrm{sign}(\mu)\}$, for the four channels of τ and s. Due to spin-valley coupling, the four transitions are divided into two nondegenerate pairs of degenerate transitions. The valley and spin breakdown of

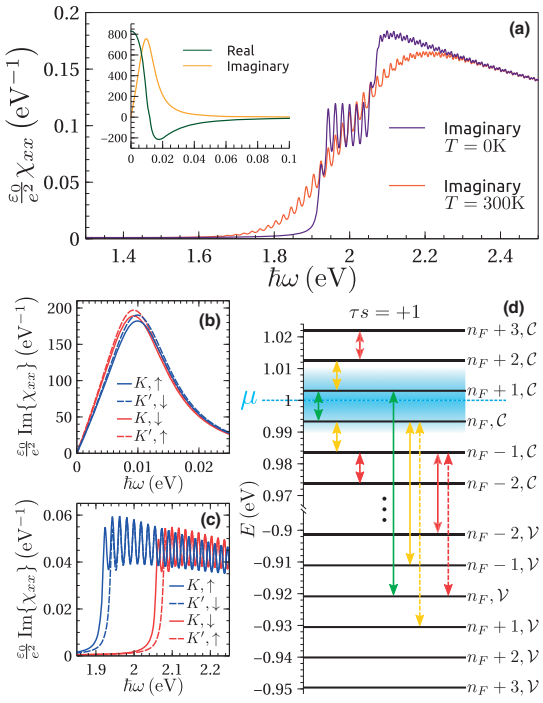

FIG. 4. Longitudinal magneto-optical response in a doped (Fermi level $\mu = 1$ eV) monolayer MoS_2, for a magnetic field of 50 T: in (a), the longitudinal susceptibility χ_{xx} is plotted as a function of the photon energy (results in the inset are roughly independent of the temperature T); (b) and (c) show the valley and spin breakdown of the absorptive part of χ_{xx} at zero absolute temperature; in (d), a scheme of the optical transitions between the energy bands is presented. Discussion is provided in the text.

the intraband absorption peak, presented in Fig. 4(b), shows that the degenerate transitions yield different but comparable intensities. In addition, it also shows that the nondegenerate transitions cannot be resolved in energy. This is explained by the presence of a broadening parameter $\Gamma = 7$ meV, which blurs the small energy splitting between the peaks.

The broadening parameter also makes the intraband optical spectrum robust with respect to variations in the temperature. The small temperature dependency can be understood with the help of the scheme in Fig. 4(d). Looking at the short arrows, which represent intraband transitions that respect the optical selection rules, we see that the green one marks the only allowed transition at $T = 0$. At finite temperatures, other LLs are thermally activated (blue region) and enable more transitions (yellow arrows). The absence of a noticeable temperature dependency is then obtained because, up to the first Pauli blocked transitions (red arrows), the variation in energy of these transitions is small compared to Γ. This is a consequence of the highly linear dispersion of the LLs with n in the regime $\Delta_{\tau s}^2 \gg \frac{1}{2}(\hbar\omega_0)^2 n$.

Doping introduces new features in the interband contributions to $\chi_{xx}(\omega)$. First, we observe a blue-shift of the absorption threshold, associated with the filling of LLs in the conduction band, for the case of an n-doped system, or the depletion of LLs in the valence band, in the case of p doping. Second, we obtain a line shape that carries a significant temperature dependency, as seen in Fig. 4(a). At $T = 0$, the line shape features a similar double-step structure that reflects the strong SOC. However, at room temperature, this feature is smoothed out and the explanation is self-evident in the scheme of Fig. 4(d). Looking at the long arrows, which mark the less energetic interband transitions in play due to thermal activation (within the same color code as before), it is clear that, in contrast with the intraband optical spectrum, the increase of the temperature induces transitions that can be resolved in energy, which in turn leads to the disappearance of a clear double-step structure. It must be noted that our analysis does not include the reduction of the band gap with the increase of the temperature, expected due to thermal expansion of the lattice that widens the bands [45].

The most intriguing difference between the doped and undoped interband optical spectra is observed in the limit of $T = 0$, whose validity is discussed below. In the doped case, the height of the lowest-energy interband peak in absorption is half of the others within the SOC plateau. The origin of this "half-peak" is explained through the Pauli exclusion principle. For a given τs, and since 0LLs are not in play, there are in general four degenerate interband transitions contributing to the absorption peaks, as depicted in Table II. However, for the half-peak, two out of the four transitions are Pauli blocked, leading to a reduction of the intensity by half. In Fig. 4(d), the two blocked transitions are represented by the yellow dashed arrow, while the two allowed ones are represented by the long green arrow [46]. In practice, the limit $T = 0$ is valid as long as the thermal activation does not change considerably the occupation of the LLs that are immediately above or below the Fermi level. This is realized for $T \lesssim 0.5B_0$ [T] K.

Interestingly, the elimination of two out of four transitions that results in the half-peak also provides a way to induce both a valley and spin imbalance in TMDs using linearly polarized light. The intensity of the four degenerate transitions is controlled by the matrix elements, in such a way that there are two equally strong and two equally weak oscillator strengths, as previously mentioned in Sec. IV A. For instance, Eq. (21) imposes that if some transition $\{n;\mathcal{V}\} \to \{n+1;\mathcal{C}\}$ is strong in the channel $\{\tau;s\}$, so it is the (counterpart) transition $\{n+1;\mathcal{V}\} \to \{n;\mathcal{C}\}$ in the channel $\{-\tau;-s\}$. Now, in the case of the half-peak, Pauli blocking occurs for transitions that are not counterpart of each other, which results on having only one of the two strong transitions active. Therefore, the resulting absorption is overwhelmingly dominated by just one valley and one spin, as observed in Fig. 4(c). In fact, the intensities are so different that the contribution of the weak transition cannot be detected.

Our findings imply that driving a doped TMD with linearly polarized light can induce a nearly perfect spin and valley imbalance at some specific range of frequencies of the longitudinal magneto-optical absorption. As we shall see in Sec. V, the same imbalance is also verified in the transverse response. These findings permit to envision a mechanism for optical orientation and add value to the field of valleytronics.

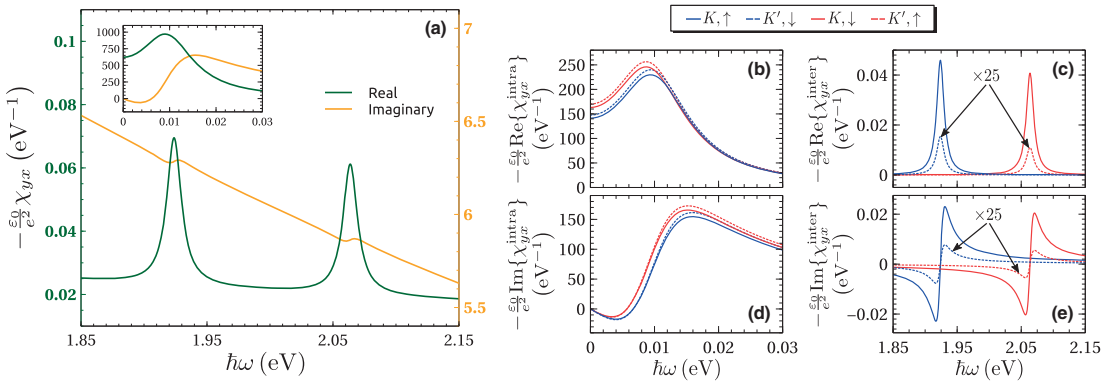

FIG. 5. (a) Hall susceptibility χ_{yx}, as a function of the photon energy, in a doped (Fermi level $\mu = 1$ eV) monolayer MoS_2 at zero absolute temperature and for a magnetic field of 50 T. (b)–(e) Valley and spin breakdown of the real [(b), (c)] and imaginary [(d), (e)] parts of (a), divided in the (noncanceling) contributions that come from intraband [(b), (d)] and interband [(c), (e)] optical transitions. The valley and spin breakdown of the interband optical spectrum reveals a dominant contribution of transitions within the K valley.

C. Doped system with a single Landau level polarized

We now briefly comment on the regime where the TMD is doped with electrons or holes up to the first 0LL in the conduction or valence band, respectively. In this case, the system has a spin-polarized ground state.

It is straightforward to check that, at sufficiently low temperatures, a single valley and spin control can be achieved either at the intraband part of the longitudinal absorption spectrum or at the frequency of the less energetic transition in the interband part. In this situation, the spin and valley selectiveness is not nearly perfect as a consequence of extremely unbalanced dipole matrix elements (as in Sec. IV B) but exact and based entirely on the optical selection rules. This is strongly connected with the findings from Ref. [26].

The carrier density needed to polarize a single LL is given by $|\rho| \simeq 2.4 \times 10^{10} B_0$ [T] cm^{-2}. Thus, the right combination of carrier density and magnetic field that leads to this regime seems within experimental reach.

V. TRANSVERSE SUSCEPTIBILITY

In this section, we undertake the analysis of the dynamical transverse susceptibility $\chi_{yx}(\omega)$, also known as Hall susceptibility. As seen in Eq. (20), this quantity determines circular dichroism. Therefore, it is relevant to model experiments that explore the magneto-optical Kerr effect and the Faraday rotation, for example.

At half-filling, the contributions to $\chi_{yx}(\omega)$ coming from opposite valleys have opposite signs. As a result, the total $\chi_{yx}(\omega)$ vanishes, although each valley yields a finite ac Hall response, as demonstrated in Appendix B. Thus, the application of an out-of-plane magnetic field, which breaks time-reversal symmetry, is not sufficient to induce a Hall response in intrinsic TMDs.

For doped TMDs, the transverse susceptibility is no longer null and can be split into two terms $\chi_{yx}(\omega) = \chi_{yx}^{\text{intra}}(\omega) + \chi_{yx}^{\text{inter}}(\omega)$, which are determined by intraband and interband types of optical transitions, respectively. For simplicity, we take $T = 0$ and consider a system in which the 0LLs cannot participate in the optical transitions. This regime is realized for $T \lesssim 0.5 B_0$ [T] K and $\mu > \max(E^{\eta}_{1,c})$ or $\mu < \min(E^{\eta}_{1,v})$. Within these considerations, we obtain largely simplified analytical expressions for $\chi_{yx}^{\text{intra}}(\omega)$ and $\chi_{yx}^{\text{inter}}(\omega)$, given by

$$\chi_{yx}^{\text{intra}}(\omega) = i\frac{\text{sign}(\mu)(\hbar\omega + i\Gamma)}{\pi l_B^2 \varepsilon_0} \sum_{\eta} \frac{\left|d_x^{\eta\,\{n_\mu+1;\text{sign}(\mu)\}}_{\{n_\mu;\text{sign}(\mu)\}}\right|^2}{\left(\hbar\omega^{\eta}_{n_\mu}\right)^2 - (\hbar\omega + i\Gamma)^2}, \tag{22}$$

$$\chi_{yx}^{\text{inter}}(\omega) = i\frac{\text{sign}(\mu)(\hbar\omega + i\Gamma)}{\pi l_B^2 \varepsilon_0} \sum_{\eta} \frac{\left|d_x^{\eta\,\{n_\mu+1;\text{sign}(\mu)\}}_{\{n_\mu;-\text{sign}(\mu)\}}\right|^2}{\left(\hbar\Omega^{\eta}_{n_\mu}\right)^2 - (\hbar\omega + i\Gamma)^2}, \tag{23}$$

where $n_\mu = n_F - \frac{1-\text{sign}(\mu)}{2}$ is introduced for convenience and corresponds to the last occupied LL if $\mu > 0$ or to the first empty one if $\mu < 0$, while

$$\hbar\omega^{\eta}_{n_\mu} = \left|E^{\eta}_{n_\mu+1,\text{sign}(\mu)} - E^{\eta}_{n_\mu,\text{sign}(\mu)}\right| \tag{24}$$

and

$$\hbar\Omega^{\eta}_{n_\mu} = \left|E^{\eta}_{n_\mu+1,\text{sign}(\mu)} - E^{\eta}_{n_\mu,-\text{sign}(\mu)}\right| \tag{25}$$

are the energies of the intraband and interband transitions contributing to the Hall response, respectively. For clarity purposes, we note that the sum over LLs, present in the general expression for $\chi_{yx}(\omega)$, is taken care of by the fact that all the (canceling) contributions that lead to a null ac Hall response in the undoped regime can be removed.

In Fig. 5, we present typical results in the regime for which Eqs. (22) and (23) are valid. The doping case is the same as the one considered in Sec. IV B. Additionally, the choice of the parameters allows for a direct comparison of these results with the ones obtained in Fig. 4.

In contrast to the longitudinal response, resonance peaks are observed in the real part of the Hall susceptibility. This

is justified by the fact that absorption is described by the susceptibility tensor in its diagonal form [Eq. (20)], i.e., in the circular basis. In this basis, the contribution to the imaginary part of $\chi_{\pm}(\omega)$ comes from the real part of $\chi_{yx}(\omega)$. Analytically, this is also verified through Eq. (18) by the presence of an extra overall imaginary unit when comparing the expressions for $\chi_{xx}(\omega)$ and $\chi_{yx}(\omega)$.

The results shown in Fig. 5(a) imply genuine (as opposed to valley-resolved) circular dichroism. Through Eq. (20), we see that $\mathrm{Re}\{\chi_{yx}\} \neq 0$ leads to a differential absorption of σ^+ and σ^- photons. This effect is stronger at the resonant frequencies.

The spin and valley breakdown of the Hall response, shown in Figs. 5(b)–5(e), reveals that interband absorption is dominated by the K valley. Due to SOC, this also implies a spin imbalance, given that transition energies are related by spin-valley coupling. The origin of this result is completely analogous to the discussion of the half-peak in Sec. IV B.

As in Sec. IV C, it is straightforward to verify that, at sufficiently low temperatures, a TMD with a single LL polarized induces a (perfect) spin and valley imbalance in the Hall response, which is based entirely on the optical selection rules. Evidently, the transitions responsible for this phenomenon involve the 0LLs.

VI. RESPONSE TO CIRCULARLY POLARIZED LIGHT

The thorough study of χ_{xx} and χ_{yx} presented in the last two sections permits to address the magneto-optical response of TMDs to circularly polarized light. Here, we focus on the absorptive part of $\chi_{\pm}(\omega) = \chi_{xx}(\omega) \pm i\chi_{yx}(\omega)$ at half-filling. In Fig. 6, we show representative results, obtained for undoped MoS_2 and $B_0 = 30$ T. The analysis follows.

It is apparent that the absorption of σ^- (σ^+) photons is dominated by the K (K') valley. Thus, the well-known [41,43,44] valley-resolved circular dichroism at $B_0 = 0$ is preserved at finite field. Given that $\chi_{xx}(\omega)$ has equal contributions from both valleys, the valley imbalance is fully controlled by $\chi_{yx}(\omega)$. This is made possible by the fact that, in the intrinsic case, $\chi_{yx}(\omega)$ is nonzero for each valley, even though the sum over valleys yields a vanishing ac Hall response.

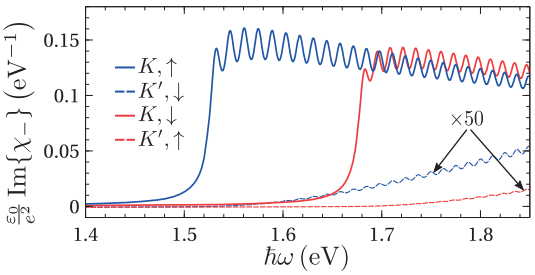

FIG. 6. Imaginary part of the susceptibility to left-handed circularly polarized light χ_-, as a function of the photon energy, in monolayer MoS_2 and for a magnetic field of 30 T (results independent of the temperature and resolved in the valley and spin contributions). The peaks in Im$\{\chi_-\}$, which are directly related with absorption of left-handed photons, reveal a valley-selective circular dichroism towards the K valley. Results for right polarization are the same with opposite spin and valley.

To gain insight about the origin of the valley-selective circular dichroism, we make the limit of no impurities $\Gamma \to 0^+$, and use the Sokhotski-Plemelj theorem to write

$$\mathrm{Im}\{\chi_{\pm}(\omega)\} = \pm \sum_{\eta} \sum_{\{n;\lambda\}} \frac{\lambda}{l_B^2 \varepsilon_0} \left| d_x^{\eta\{n+1;-\lambda\}}_{\{n;\lambda\}} \right|^2 \times \delta\left(E^{\eta}_{n,\lambda} - E^{\eta}_{n+1,-\lambda} \mp \hbar\omega\right), \quad (26)$$

where we have also used that, in the undoped regime,

$$f\left(E^{\eta}_{n+1,\lambda'}\right) - f\left(E^{\eta}_{n,\lambda}\right) = \lambda \delta_{\lambda',-\lambda}. \quad (27)$$

Looking at Eq. (26), we observe that the Dirac Delta implies $\lambda = \mathcal{C}/\mathcal{V}$ for right/left polarization. This relation blocks counterpart transitions for the whole interband optical spectrum, in the same way that doping blocks a specific set of counterpart interband transitions that contribute to χ_{xx} and χ_{yx}. As a result, we get highly unbalanced valley contributions at any ω of the interband absorption, which are determined exclusively by the magnitude of the dipole matrix elements.

The presence of SOC interactions is only reflected by the splitting of the line shapes that correspond to different spin contributions within the same valley. Thus, the valley-selective circular dichroism is independent of SOC and only determined by the τ dependency of the kinetic term in the Hamiltonian.

These results show that the well-established optically induced valley polarization for intrinsic TMDs [42] remains upon application of an out-of-plane magnetic field. In addition, the analytical approach to this problem unveils that the valley-selective circular dichroism is not a selection rule that completely cancels absorption in one valley, but a consequence of extremely unbalanced dipole matrix elements.

VII. EXCHANGE SELF-ENERGY CORRECTIONS

We now turn our attention to how the electronic and optical properties discussed before are modified due to Coulomb interactions. In particular, we keep track of corrections up to the self-energy (SE) level, which lead to the renormalization of the electronic band structure and thus affect the optical response by changing the frequency of the transitions in play. Since the dipole matrix elements remain identical, the main features of the magneto-optical response of TMD monolayers are maintained at this level of approximation. The inclusion of these effects is carried out within the same EOM formalism.

A. Keldysh potential

In order to account for electron-electron repulsions in a 2D landscape, we replace the typical Coulomb potential by the Keldysh potential [47]. In the direct space, the Keldysh energy potential between two electrons in $\boldsymbol{r}$ and $\boldsymbol{r}'$, $U(\boldsymbol{r} - \boldsymbol{r}')$, has a rather intricate form. In contrast, its Fourier transform yields a more transparent expression, given by

$$U(\boldsymbol{q}) = \frac{e^2}{2\varepsilon_0} \frac{1}{q(r_0 q + 1)}, \quad (28)$$

where $\boldsymbol{q} = (q_x, q_y)$ is the transferred momentum and r_0 is a material-dependent constant that measures the deviation from the 2D Coulomb energy potential, which is recovered making $r_0 = 0$.

When in presence of a dielectric medium with relative permittivity ε_r, Eq. (28) is modified by the transformation $r_0 q + 1 \to r_0 q + \varepsilon_r$. For simplicity, we assume TMDs in vacuum or suspended in air ($\varepsilon_r \simeq 1$), thus ignoring screening effects due to the presence of dielectric media. The magnitude of the band renormalization so obtained is therefore an upper limit.

B. Exchange self-energy: Analytical expressions

Disregarding coupling between different valleys, we write the (two-particle) Hamiltonian that accounts for electron-electron interactions as

$$\hat{H}_{ee}(t) = \frac{1}{2} \sum_{\substack{\tau \\ s,\, s'}} \sum_{\substack{\alpha_1,\, \alpha_2 \\ \alpha_3,\, \alpha_4}} U^{\tau,s,s'}_{\substack{\alpha_1,\, \alpha_2 \\ \alpha_3,\, \alpha_4}} \hat{c}^{\dagger}_{\alpha_1,\tau,s} \hat{c}^{\dagger}_{\alpha_2,\tau,s'} \hat{c}_{\alpha_3,\tau,s'} \hat{c}_{\alpha_4,\tau,s}, \quad (29)$$

where

$$U^{\tau,s,s'}_{\substack{\alpha_1,\, \alpha_2 \\ \alpha_3,\, \alpha_4}} = \int_{\mathbb{R}^2} \frac{d\boldsymbol{q}}{(2\pi)^2}\, U(q) F^{\tau,s}_{\alpha_1,\alpha_4}(\boldsymbol{q}) F^{\tau,s'}_{\alpha_2,\alpha_3}(-\boldsymbol{q}) \quad (30)$$

are the Coulomb integrals and

$$F^{\tau,s}_{\alpha,\alpha'}(\boldsymbol{q}) = \int_A d\boldsymbol{r}\, e^{i\boldsymbol{q}\cdot\boldsymbol{r}} \left[\psi^{\tau,s}_{\alpha}(\boldsymbol{r})\right]^{\dagger} \psi^{\tau,s}_{\alpha'}(\boldsymbol{r}) \quad (31)$$

the structure factors. In Eq. (29), the time dependency of the fermionic operators is omitted to shorten notation. The exclusion of intervalley contributions is justified by the large momentum difference between K and K', which implies a large transferred momentum that in turn suppresses $U(q)$ and, consequently, the intervalley Coulomb integrals.

The following task is to include $\hat{H}_{ee}(t)$ in the total Hamiltonian (12), and obtain the new (interacting) EOM. This task boils down to the calculation of the commutator $[\hat{H}_{ee}(t), \hat{T}^{\eta}_{\alpha,\alpha'}(t)]$, whose result is shown in Appendix C 1. Among the new terms, we then identify and keep the ones that lead to a band renormalization. Random phase approximation and linear response regime are implied in this last step and the details regarding this manipulation can be found in Appendix C 2. As a final result, we find that the energy bands are renormalized as

$$\left(E^{\eta}_{\alpha}\right)_{\text{renorm}} = E^{\eta}_{\alpha} + \Sigma^{\eta}_{\alpha}, \quad (32)$$

where

$$\Sigma^{\eta}_{\alpha} = -\sum_{\alpha'} f\left(E^{\eta}_{\alpha'}\right) U^{\tau,s,s}_{\substack{\alpha',\, \alpha \\ \alpha',\, \alpha}} \quad (33)$$

are the exchange SE corrections. As usual, we observe that the exchange corrections to energy bands with a given spin come from electrons in bands with the same spin.

The Coulomb integrals can be reduced to one-dimensional quadratures (see Appendix C 3 for details). At $T = 0$, Eq. (33) is simplified into

$$\Sigma^{\eta}_{\alpha} = -\sum_{\{n',\lambda'\} \in \text{occ.}} D^{\eta}_{\substack{\{n,\,\lambda\} \\ \{n',\,\lambda'\}}} I^{\eta}_{\substack{\{n,\,\lambda\} \\ \{n',\,\lambda'\}}}, \quad (34)$$

where $D^{\eta}_{\substack{\{n,\,\lambda\} \\ \{n',\,\lambda'\}}}$ are real constants defined as

$$D^{\eta}_{\substack{\{n,\,\lambda\} \\ \{n',\,\lambda'\}}} = \frac{1}{2^{|n-n'|}} \left(C^{\eta}_{n,\lambda} C^{\eta}_{n',\lambda'}\right)^2, \quad (35)$$

$I^{\eta}_{\substack{\{n,\,\lambda\} \\ \{n',\,\lambda'\}}}$ are integrals given by

$$I^{\eta}_{\substack{\{n,\,\lambda\} \\ \{n',\,\lambda'\}}} = \frac{1}{l_B^2} \int_0^{+\infty} \frac{d\bar{q}}{2\pi}\, \bar{q}^{2|n-n'|+1} U\left(\frac{\bar{q}}{l_B}\right) e^{-\bar{q}^2/2} \times \left| \tilde{L}^{|n-n'|}_{(n_\tau,n'_\tau)}\left(\frac{\bar{q}^2}{2}\right) + B^{\eta}_{n,\lambda} B^{\eta}_{n',\lambda'} \tilde{L}^{|n-n'|}_{(n_\tau+\tau,n'_\tau+\tau)}\left(\frac{\bar{q}^2}{2}\right) \right|^2, \quad (36)$$

and the notation $\{n', \lambda'\} \in$ occ. means that the sum runs over occupied states only. In Eq. (36), we have defined $\bar{q} \equiv l_B q$, $\tilde{L}^{|n-n'|}_{(b,c)} \equiv \sqrt{\frac{\min(b,c)!}{\max(b,c)!}} L^{|n-n'|}_{\min(b,c)}$ for $\min(b, c) \in \mathbb{N}^0$ ($L^{|n-n'|}_{\min(b,c)}$ are the associated Laguerre polynomials) and $\tilde{L}^{|n-n'|}_{(b,c)} \equiv 0$ for $\min(b, c) = -1$. Moreover, we remind that $n_\tau \equiv n - \frac{1+\tau}{2}$.

In order to evaluate Eq. (34), it is clear that a cutoff is again required, as the summation implied extends over an infinity of valence states. Furthermore, we have verified numerically that the summation diverges logarithmically with the LL cutoff n_{cut}. Even when dealing with energy differences, this was checked to lead to corrections that are, to some extent, cutoff dependent. To fix n_{cut}, we start by counting the total number of electrons in a TMD sample of area A. At half-filling, we get $2A/A_{\text{u.c.}}$, where $A_{\text{u.c.}} = \frac{\sqrt{3}}{2} a^2$ is the area of the hexagonal unit cell with lattice parameter $a \simeq 3.15$ Å [48]. Then, this number is divided by 4 (to account for spin and valley) and matched to the number of electronic states in n_{cut} LLs. Given the degeneracy of the LLs, $\frac{A}{2\pi l_B^2}$, we obtain that

$$n_{\text{cut}} = \frac{\pi l_B^2}{A_{\text{u.c.}}} \simeq \frac{24\,000}{B_0\ [\text{T}]} \quad (37)$$

is the number of filled LLs per spin and valley.

In the computations that follow, we use the material-dependent parameters listed in Table III.

TABLE III. List of parameters used in the numerical computation of the exchange self-energy corrections for different transition metal dichalcogenides. Values in the first and second, third and fourth, and last columns were taken from Refs. [5], [29], and [18], respectively.

	$\hbar v_F$(eV Å)	Δ(eV)	$\Delta^{\mathcal{V}}_{\text{SOC}}$(eV)	$\Delta^{\mathcal{C}}_{\text{SOC}}$(eV)	r_0(Å)
MoS_2	3.51	0.83	0.148	−0.003	41.5
WS_2	4.38	0.90	0.430	+0.029	37.9
$MoSe_2$	3.11	0.74	0.184	−0.021	51.7
WSe_2	3.94	0.80	0.466	+0.036	45.1

TABLE IV. Renormalization in energy of a selected set of optical transitions (described in the text) for different transition metal dichalcogenides and a magnetic field of 10 T: bare and exchange-corrected values (computed at zero absolute temperature) separated by commas, in the respective order. Results obtained for $\mathcal{T}^{K,s}_{\{0,\mathcal{V}\}\to\{1,\mathcal{C}\}}$ are equal to the ones for $\mathcal{T}^{K',-s}_{\{1,\mathcal{V}\}\to\{0,\mathcal{C}\}}$.

	$\mathcal{T}^{K,\uparrow}_{\{0,\mathcal{V}\}\to\{1,\mathcal{C}\}}$(eV)	$\mathcal{T}^{K,\downarrow}_{\{0,\mathcal{V}\}\to\{1,\mathcal{C}\}}$(eV)	$\mathcal{T}^{K,\uparrow}_{\{1,\mathcal{V}\}\to\{0,\mathcal{V}\}}$(meV)	$\mathcal{T}^{K',*}_{\{0,\mathcal{C}\}\to\{1,\mathcal{C}\}}$(meV)
MoS_2	1.587, 2.454	1.738, 2.717	2.4, 105.4	2.4, 103.5
WS_2	1.603, 2.567	2.003, 3.024	3.6, 107.9	2.9, 105.1
$MoSe_2$	1.380, 2.202	1.584, 2.433	2.1, 101.2	2.1, 100.7
WSe_2	1.388, 2.240	1.818, 2.729	3.4, 104.9	2.6, 102.9

C. Renormalized optical transition energies

As a direct application of the calculations presented above, we study how a selected set of optical transitions is renormalized in energy due to the exchange SE corrections, at $T = 0$. We consider different TMDs and focus on the following cases:

(i) Fermi level in the gap. Interband transitions: $\mathcal{T}^{K,s}_{\{0,\mathcal{V}\}\to\{1,\mathcal{C}\}} \equiv E^{K,s}_{1,\mathcal{C}} - E^{K,s}_{0,\mathcal{V}}$ and $\mathcal{T}^{K',s}_{\{1,\mathcal{V}\}\to\{0,\mathcal{C}\}} \equiv E^{K',s}_{0,\mathcal{C}} - E^{K',s}_{1,\mathcal{V}}$. From the renormalization of these transition energies, we obtain the renormalized energy thresholds that define the SOC plateau observed in the absorption spectrum of intrinsic TMDs (see Figs. 3 and 6). Evidently, the exchange-corrected value of $\mathcal{T}^{K,\uparrow}_{\{0,\mathcal{V}\}\to\{1,\mathcal{C}\}} = \mathcal{T}^{K',\downarrow}_{\{1,\mathcal{V}\}\to\{0,\mathcal{C}\}}$ corresponds to the renormalized band gap.

(ii) System doped with electrons or holes up to the first 0LL. Intraband transitions: $\mathcal{T}^{K,\uparrow}_{\{1,\mathcal{V}\}\to\{0,\mathcal{V}\}} \equiv E^{K,\uparrow}_{0,\mathcal{V}} - E^{K,\uparrow}_{1,\mathcal{V}}$ for p doping, and $\mathcal{T}^{K',*}_{\{0,\mathcal{C}\}\to\{1,\mathcal{C}\}} \equiv E^{K',*}_{1,\mathcal{C}} - E^{K',*}_{0,\mathcal{C}}$ for n doping, where $* = \uparrow$ if $\Delta^{\mathcal{C}}_{\rm SOC} > 0$ and vice versa. In this regime, these optical transitions lead to intraband peaks in the absorption spectrum that are spin- and valley-selective.

In the undoped case, both the interband optical spectrum and the exchange SE corrections are independent of T. For doped systems, the limit $T = 0$ is only valid as long as $T \lesssim 0.5B_0$ [T] K and provides an upper limit for the renormalization of the intraband transition energies.

In Table IV, we present the results obtained for $B_0 = 10$ T. These results show the usual tendency of the Hartree-Fock approximation to enhance energy gaps obtained through standard local density functional theory calculations. However, it must be noted that, in optical spectroscopic measurements, absorption occurs for photon energies below the exchange-corrected values due to excitonic effects.

For intrinsic TMDs, we find a band-gap correction whose magnitude is comparable to the renormalization of the direct band gap in the absence of external magnetic fields [20]. In the case of the intraband transitions between adjacent LLs, the exchange-corrected values obtained are most likely a severe overestimation of what should be observed in optical experiments. In fact, Kohn's theorem [49] states that the cyclotron resonance frequency of an electron gas is not altered by electron-electron interactions. Although this theorem ignores the coupling to the lattice [50], far-infrared spectroscopy probing the cyclotron frequency of the 2D electron gas formed in silicon inversion layers [51] has revealed a good agreement between the experiment and the independent-electron theory. The applicability of Kohn's theorem for Dirac electrons has been discussed in the literature [52].

Kohn's theorem implies the existence of interaction-independent collective modes that are relevant for optical spectroscopic measurements. However, this theorem does not preclude that the quasiparticle spectrum, probed directly through other experiments, can be strongly renormalized by interactions. Thus, scanning tunneling microscopy (STM) or a combination of angle-resolved photoemission spectroscopy (ARPES) and inverse ARPES could be used to investigate the renormalization of the LL energies due to Coulomb interactions.

D. Renormalization of the spin-orbit splitting

We now discuss an exchange-driven mechanism to enhance the spin-orbit splitting. Since the 0LLs do not disperse with the magnetic field, the energy difference between the two $n = 0$ LLs in the conduction/valence band is given by $\Delta^{\mathcal{C}/\mathcal{V}}_{\rm SOC}$. As shown in Table III, first-principle calculations predict values of $\Delta^{\mathcal{C}}_{\rm SOC}$ relatively small compared to those of $\Delta^{\mathcal{V}}_{\rm SOC}$. These first-principle results were obtained for undoped TMDs, in the absence of external fields. Here, we consider the renormalization of $\Delta^{\mathcal{C}}_{\rm SOC}$, due to SE corrections, for doped systems and in the presence of an out-of-plane magnetic field.

We take as example the case of a monolayer $MoSe_2$, for which $\Delta^{\mathcal{C}}_{\rm SOC} = -21$ meV in the undoped regime. At the Hartree-Fock level, it is clear that, in order to maximize the renormalization of this splitting, the Fermi level should lie between the two $n = 0$ LLs in the conduction band. For this matter, we consider the material doped with electrons up to the lowest-energy 0LL. In addition, the system should be cooled down such that there is no significant thermal activation of the unoccupied 0LL. For the calculations, we take $T = 0$, which is valid as long as $k_B T \ll \Delta^{\mathcal{C}}_{\rm SOC}$.

In the regime described above, the energy of the unoccupied 0LL is renormalized due to valence states only. On the other hand, the energy of the polarized 0LL is renormalized by states in the valence bands and in the 0LL itself. When computing the difference, the dominant contribution comes from the auto SE correction, i.e., the exchange SE correction to the occupied 0LL due to itself. The origin of the other contributions, which come from corrections due to the $n \neq 0$ LLs in the valence band that do not cancel each other, can be traced back to the presence of SOC interactions in the model.

In Fig. 7, we plot the evolution of the renormalized spin-orbit splitting of the 0LLs in the conduction band of $MoSe_2$, as a function of the magnetic field. We present results that include the complete SE corrections, the contribution

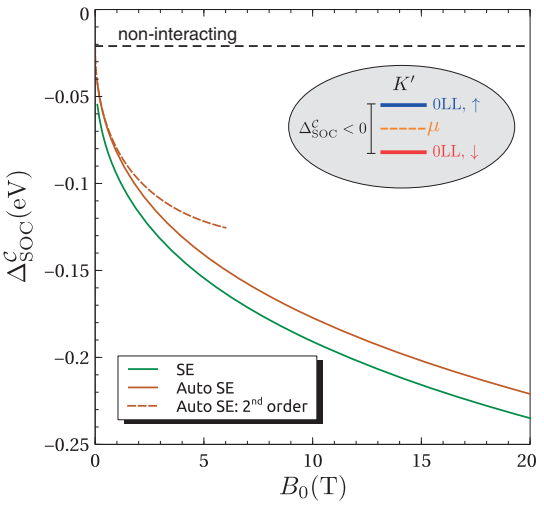

FIG. 7. Spin-orbit splitting of the zeroth Landau levels (0LLs) in the conduction band of $MoSe_2$, renormalized by the exchange self-energy (SE) corrections (computed at zero absolute temperature), as a function of the magnetic field. The Fermi level μ is kept between the two spin-split 0LLs in the conduction band, such that only the lowest-energy 0LL in the K' valley is polarized, as depicted in the cartoon. The horizontal black dashed line corresponds to the noninteracting reference, whereas the others correspond to exchange-corrected values that include the complete SE corrections (green solid line), the contribution of the auto SE only (brown solid line), and a low-field second-order Taylor expansion of the former (brown dashed line). These results reveal a large exchange-driven enhancement of the splitting, which increases with the intensity of the magnetic field and approaches the noninteracting value in the limit of zero field.

of the auto SE only, and a low-field approximation of the former (see derivations below). The carrier density implied to keep only the lowest-energy 0LL polarized is $\rho \simeq -2.4 \times 10^{10} B_0$ [T] cm^{-2}. The analytical expression for the auto SE correction reads as

$$\begin{aligned}\tilde{\Sigma}^{\eta}_{0\mathrm{LL}} &= -D^{\eta}_{\substack{0\mathrm{LL}\\0\mathrm{LL}}} I^{\eta}_{\substack{0\mathrm{LL}\\0\mathrm{LL}}} \\ &= -\frac{e^2}{4\pi\varepsilon_0}\frac{1}{l_B}\int_0^{+\infty} d\bar{q}\ \frac{e^{-\bar{q}^2/2}}{\frac{r_0}{l_B}\bar{q}+1} \\ &= -\frac{e^2}{4\pi\varepsilon_0}\frac{e^{-\frac{l_B^2}{2r_0^2}}}{2r_0}\left[\frac{\pi}{i}\mathrm{erf}\left(i\frac{l_B}{\sqrt{2}r_0}\right) - \mathrm{Ei}\left(\frac{l_B^2}{2r_0^2}\right)\right], \quad (38)\end{aligned}$$

where erf is the error function and Ei the exponential integral function. In the limit of small B_0, Eq. (38) can be simplified making a Taylor expansion around $\frac{r_0}{l_B} = 0$ which, up to second order, yields

$$\tilde{\Sigma}^{\eta}_{0\mathrm{LL}} \simeq -\frac{e^2}{4\pi\varepsilon_0}\frac{1}{r_0}\left(\frac{\sqrt{2\pi}}{2}\frac{r_0}{l_B} - \frac{r_0^2}{l_B^2}\right). \quad (39)$$

The validity of Eq. (39) is controlled by the ratio $\frac{r_0}{l_B}$, that scales as $0.2\sqrt{B_0\ [\mathrm{T}]}$ for $MoSe_2$.

The complete SE results show a large exchange-driven enhancement of Δ^C_{SOC}: even at a moderate field of 2 T, we obtain a renormalization in the order of 100 meV. It is also apparent that the exchange corrections are dominated by the auto SE contribution. Thus, it becomes clear why the spin-orbit splitting increases with the intensity of the magnetic field: as B_0 ramps up, so it does the density of electrons in the occupied 0LL and therefore the magnitude of the renormalization. Expectedly, we also observe that the exchange-corrected values approach the noninteracting reference as we decrease the intensity of the magnetic field. This is verified analytically through Eq. (39) by noticing the absence of zeroth-order terms in the low-field Taylor expansion of the auto SE correction.

The predictions of the Hartree-Fock calculations have to be contrasted with Larmor's theorem for spin-flip collective modes, excited with a zero-wave-vector perturbation [53]. Analogously to Kohn's theorem, this theorem states that electron-electron interactions do not renormalize the energy of the $q = 0$ spin-flip excitations, which must be equal to $g\mu_B B_0$. However, the theorem only holds for systems where the total spin is conserved, which is clearly not the case for TMDs, on account of the strong SOC interactions. On the other hand, vertex corrections are likely to reduce the large spin-flip energies predicted at the Hartree-Fock level [54]. In any case, experiments that probe the quasiparticle spectrum, such as STM and ARPES, might be able to capture the large shifts predicted by our calculations.

VIII. DISCUSSION AND CONCLUSIONS

We have provided a thorough theoretical study of the optical properties of semiconducting TMD monolayers, described within the massive Dirac model, under the influence of strong out-of-plane magnetic fields that quantize the energy spectrum into a set of LLs. We have analyzed in detail the longitudinal and transverse optical response, in both doped and undoped regimes, paying attention to the breakdown of the contributions coming from different spins and valleys. We have also addressed the role of electron-electron interactions, treated at the Hartree-Fock level.

A. Limits of the model

Here, we briefly discuss some limitations of the model Hamiltonian applied in this work. First, atomistic calculations [15,33] show a valley symmetry breaking of the LL spectrum that is not captured through Dirac models. Thus, the resulting magneto-optical spectra should feature a valley splitting of the peaks. Second, we have ignored the paramagnetic shift of the valence bands associated to the coupling between the magnetic field and the valley-dependent atomic orbital momentum $L_z = \tau 2$ of the highest-energy valence states [9]. This results in another valley-dependent contribution. Third, we have also ignored Zeeman splitting, that can be easily added to our results. Finally, we have not considered excitonic effects, that are expected to have a strong impact in the optical response. These are the scope of an incoming publication [28]. At charge neutrality, the excitonic effects not

considered in this work are known to renormalize strongly the optical response functions. Therefore, our results in the undoped regime are meant to be taken, at most, as a qualitative description. However, in the doped case, we expect our analysis to be robust against exciton formation. To sustain this statement, we first note that the exciton size in TMDs monolayers are not strongly affected by the presence of an out-of-plane magnetic field [28]. Then, we compare the $\boldsymbol{B} = \boldsymbol{0}$ exciton size, typically in the order of a few nanometers [20], with the 2D Thomas-Fermi screening length, which we have estimated to be $\sim$0.17 nm and independent of the carrier density. These numbers lead us to conclude that excitons in TMDs are effectively screened in any doped regime for which the Thomas-Fermi approximation holds.

B. Main results

We now summarize our main results. At $\boldsymbol{B} = \boldsymbol{0}$, TMDs are known to present valley-dependent circular dichroism [42]: photons with a given circular polarization induce transitions in a valley-selective manner. This permits to induce optical valley orientation. Given that TMDs have strong SOC interactions, valley orientation also implies spin orientation in these materials. In this work, we have found that the application of an out-of-plane magnetic field preserves these effects, although the resulting optical spectrum contains a much richer structure.

In the case of doped TMDs, the application of the magnetic field brings two main features that are absent in the undoped regime: (1) The lowest-energy peak in $\chi_{xx}(\omega)$ has dominant contributions from optical transitions within a single spin and valley [see Fig. 4(c)]. As a result, at that energy, linearly polarized light can induce both a valley and spin imbalance. This provides a mechanism for optical orientation, attained with linearly polarized light. (2) The ac Hall response is finite, as shown in Fig. 5(a). This implies a net circular dichroism, i.e., a net difference in absorption of σ^+ and σ^- photons.

The main consequences of the exchange SE interactions are the following: (1) In the intrinsic case, the effective band gap is severely renormalized, resulting in a larger value. (2) In n-doped systems with a spin-polarized ground state, our calculations show a strong exchange-driven renormalization of the spin-orbit splitting of the 0LLs in the conduction band, which exceeds 100 meV for $B_0 = 2$ T.

These results point out the strong influence of electron-electron interactions in the electronic and optical properties of doped TMDs. Future work will address spin and valley Stoner instabilities driven by Coulomb interactions in doped TMDs (see, for instance, Ref. [55]).

ACKNOWLEDGMENTS

We thank A. J. Chaves and L. Brey for fruitful discussions. G.C. thanks Departamento de Física Aplicada at Universidad de Alicante for their hospitality. G.C. and J.F.-R. acknowledge financial support from Fundação para a Ciência e a Tecnologia (FCT) for the Grant No. P2020-PTDC/FIS-NAN/4662/2014. J.H. acknowledges financial support by the QUSCOPE Center, sponsored by the Villum foundation. J.F.-R. acknowledges financial support from FCT for the Grants No. P2020-PTDC/FIS-NAN/3668/2014 and No. UTAP-EXPL/NTec/0046/2017, as well as Generalitat Valenciana funding Prometeo2017/139 and MINECO-Spain (Grant No. MAT2016-78625-C2). N.M.R.P. acknowledges financial support from the European Commission through the project "Graphene-Driven Revolutions in ICT and Beyond" (Ref. No. 785219) and the Portuguese Foundation for Science and Technology (FCT) in the framework of the Strategic Financing Grant No. UID/FIS/04650/2013. Additionally, N.M.R.P. acknowledges COMPETE2020, PORTUGAL2020, FEDER and the Portuguese Foundation for Science and Technology (FCT) for the Grants No. PTDC/FIS-NAN/3668/2013 and No. POCI-01-0145-FEDER-028114.

APPENDIX A: SOLUTION FOR THE NONINTERACTING EQUATION OF MOTION

Due to the optical selection rules, the solution for the time evolution of the polarization density operator can be broken down into the problem of solving the EOM of a specific set of general operators $\hat{T}^{\eta}_{\alpha,\alpha'}(t) \equiv \hat{c}^{\dagger}_{\alpha',\eta}(t)\hat{c}_{\alpha,\eta}(t)$. Introducing the notation

$$\hat{c}_{\alpha,\eta}(t) \equiv \begin{cases} \hat{\mathcal{C}}_n, & n \geqslant 1 \wedge \lambda = \mathcal{C} \\ \hat{\mathcal{V}}_n, & n \geqslant 1 \wedge \lambda = \mathcal{V} \\ \hat{a}_0, & \{n;\lambda\} = 0\mathrm{LL} \end{cases} \tag{A1}$$

where the dependency on t, k_y, and η is omitted to compress notation [56], the relevant set of pair of operators reads as follows:

(1) $\hat{a}^{\dagger}_0\hat{\mathcal{C}}_1$, $\hat{a}^{\dagger}_0\hat{\mathcal{V}}_1$ and Hermitian conjugates, for transitions that involve the 0LLs;

(2) $\hat{\mathcal{C}}^{\dagger}_n\hat{\mathcal{V}}_{n+1}$, $\hat{\mathcal{C}}^{\dagger}_{n+1}\hat{\mathcal{V}}_n$ and the Hermitian conjugates, for interband transitions between $n \neq 0$ LLs;

(3) $\hat{\mathcal{C}}^{\dagger}_n\hat{\mathcal{C}}_{n+1}$, $\hat{\mathcal{V}}^{\dagger}_n\hat{\mathcal{V}}_{n+1}$ and the Hermitian conjugates, for intraband transitions between $n \neq 0$ LLs.

In what follows, we will keep track of only one of these pairs, $\hat{a}^{\dagger}_0\hat{\mathcal{C}}_1$. The derivation for the others follows straightforwardly and the final result is trivial to generalize, as we mention below.

After some straightforward algebra, the EOM for $\hat{a}^{\dagger}_0\hat{\mathcal{C}}_1$ yields

$$\frac{\hbar}{i}\frac{d}{dt}(\hat{a}^{\dagger}_0\hat{\mathcal{C}}_1) = [\hat{H}_0(t), \hat{a}^{\dagger}_0\hat{\mathcal{C}}_1] + [\hat{H}_I(t), \hat{a}^{\dagger}_0\hat{\mathcal{C}}_1], \tag{A2}$$

where

$$[\hat{H}_0(t), \hat{a}^{\dagger}_0\hat{\mathcal{C}}_1] = \left(E^{\eta}_{0\mathrm{LL}} - E^{\eta}_{1,\mathcal{C}}\right)\hat{a}^{\dagger}_0\hat{\mathcal{C}}_1 \tag{A3}$$

and

$$\begin{aligned}[\hat{H}_I(t), \hat{a}^{\dagger}_0\hat{\mathcal{C}}_1] = -\boldsymbol{\mathcal{E}}(t)\cdot\big[&\boldsymbol{d}^{\eta\{1;\mathcal{C}\}}_{0\mathrm{LL}}(\hat{\mathcal{C}}^{\dagger}_1\hat{\mathcal{C}}_1 - \hat{a}^{\dagger}_0\hat{a}_0) + \boldsymbol{d}^{\eta\{1;\mathcal{V}\}}_{0\mathrm{LL}}\hat{\mathcal{V}}^{\dagger}_1\hat{\mathcal{C}}_1 \\ &- \boldsymbol{d}^{\eta\{1;\mathcal{C}\}}_{\{2;\mathcal{V}\}}\hat{a}^{\dagger}_0\hat{\mathcal{V}}_2 - \boldsymbol{d}^{\eta\{1;\mathcal{C}\}}_{\{2;\mathcal{C}\}}\hat{a}^{\dagger}_0\hat{\mathcal{C}}_2\big].\end{aligned} \tag{A4}$$

In order to simplify the previous EOM, we start by taking its average with respect to the unperturbed Hamiltonian $\hat{H}_0(t)$ and then approximate $\langle\hat{c}^{\dagger}_{\alpha,\eta}(t)\hat{c}_{\alpha,\eta}(t)\rangle_0 \simeq \langle\hat{c}^{\dagger}_{\alpha,\eta}\hat{c}_{\alpha,\eta}\rangle_0$, where $\hat{c}^{\dagger}_{\alpha,\eta}/\hat{c}_{\alpha,\eta}$ are the creation/annihilation fermionic operators in the Schrödinger representation. The first simplification occurs because the expectation value of the time-independent number

operator yields the Fermi-Dirac distribution

$$\langle \hat{c}^{\dagger}_{\alpha,\eta}\hat{c}_{\alpha,\eta}\rangle_0 = f\big(E^{\eta}_{n,\lambda}\big) = \frac{1}{e^{\beta(E^{\eta}_{n,\lambda}-\mu)}+1}, \tag{A5}$$

where μ is the Fermi level and $\beta \equiv 1/(k_B T)$ (k_B is the Boltzmann constant and T the absolute temperature). In addition to that, we use the fact that the average value of the terms which connect either (a) the same n but different λ, or (b) LL indexes that differ from ± 2, is null. This leads to

$$\frac{\hbar}{i}\frac{d}{dt}\langle \hat{a}^{\dagger}_0\hat{\mathcal{C}}_1\rangle_0 = \big(E^{\eta}_{0\mathrm{LL}} - E^{\eta}_{1,\mathcal{C}}\big)\langle \hat{a}^{\dagger}_0\hat{\mathcal{C}}_1\rangle_0 - \boldsymbol{\mathcal{E}}(t)\cdot \boldsymbol{d}^{\eta\{1;\mathcal{C}\}}_{0\mathrm{LL}}\big[f\big(E^{\eta}_{1,\mathcal{C}}\big) - f\big(E^{\eta}_{0\mathrm{LL}}\big)\big]. \tag{A6}$$

Regarding the validity of the approximations, both procedures are consistent with an expansion of the polarization density up to the first order in the electric field and are therefore valid within the linear response theory.

To solve Eq. (A6), we first express the electric field through its Fourier transform $\boldsymbol{\mathcal{E}}(\omega)$, where ω is the angular frequency. Then, considering the adiabatic regime, meaning that the external fields are switched on very slowly, we get

$$\langle \hat{a}^{\dagger}_0\hat{\mathcal{C}}_1\rangle_0 = \int_{\mathbb{R}} \frac{d\omega}{2\pi}\boldsymbol{\mathcal{E}}(\omega)\cdot \boldsymbol{d}^{\eta\{1;\mathcal{C}\}}_{0\mathrm{LL}}\frac{f\big(E^{\eta}_{1,\mathcal{C}}\big) - f\big(E^{\eta}_{0\mathrm{LL}}\big)}{E^{\eta}_{0\mathrm{LL}} - E^{\eta}_{1,\mathcal{C}} + \hbar\omega}e^{-i\omega t}, \tag{A7}$$

where we have imposed all averages to be null at t_0 (t_0 being the initial time in which the perturbation is turned on) and made $t_0 \to -\infty$, arguing that we have waited long enough for the transient terms to become negligible. In Eq. (A7), the substitution $\hbar\omega \to \hbar\omega + i\Gamma$, $\Gamma \to 0^+$ is implied due to the adiabatic limit. A finite empirical broadening parameter Γ is typically considered to account for disorder effects. As a final remark, we stress that this solution is straightforwardly generalizable for all the other pairs of operators. For example, if we want the expression for $\langle \hat{\mathcal{C}}^{\dagger}_n\hat{\mathcal{V}}_{n+1}\rangle_0$, we change from 0LL to $\{n;\mathcal{C}\}$ and from $\{1;\mathcal{C}\}$ to $\{n+1;\mathcal{V}\}$ in the right-hand side of Eq. (A7).

With the previous results, we can write the expectation value of the polarization density operator as

$$\begin{aligned}\langle \hat{\boldsymbol{P}}(t)\rangle_0 &= \sum_{\eta}\sum_{k_y}\sum_{\substack{\{n;\lambda\}\\ \{n';\lambda'\}}}\int_{\mathbb{R}}\frac{d\omega}{2\pi}e^{-i\omega t}\frac{f\big(E^{\eta}_{n',\lambda'}\big) - f\big(E^{\eta}_{n,\lambda}\big)}{A}\big(\boldsymbol{d}^{\eta\{n';\lambda'\}}_{\{n;\lambda\}}\big)^{*}\frac{\boldsymbol{\mathcal{E}}(\omega)\cdot \boldsymbol{d}^{\eta\{n';\lambda'\}}_{\{n;\lambda\}}}{E^{\eta}_{n,\lambda} - E^{\eta}_{n',\lambda'} + \hbar\omega}\\ &= \sum_{\eta}\sum_{\{n;\lambda\},\lambda'}\int_{\mathbb{R}}\frac{d\omega}{2\pi}e^{-i\omega t}\frac{f\big(E^{\eta}_{n+1,\lambda'}\big) - f\big(E^{\eta}_{n,\lambda}\big)}{2\pi l_B^2}\left[\big(\boldsymbol{d}^{\eta\{n+1;\lambda'\}}_{\{n;\lambda\}}\big)^{*}\frac{\boldsymbol{\mathcal{E}}(\omega)\cdot \boldsymbol{d}^{\eta\{n+1;\lambda'\}}_{\{n;\lambda\}}}{E^{\eta}_{n,\lambda} - E^{\eta}_{n+1,\lambda'} + \hbar\omega} + \boldsymbol{d}^{\eta\{n+1;\lambda'\}}_{\{n;\lambda\}}\frac{\boldsymbol{\mathcal{E}}(\omega)\cdot \big(\boldsymbol{d}^{\eta\{n+1;\lambda'\}}_{\{n;\lambda\}}\big)^{*}}{E^{\eta}_{n,\lambda} - E^{\eta}_{n+1,\lambda'} - \hbar\omega}\right],\end{aligned} \tag{A8}$$

where we have performed a trivial summation over k_y, which yields the degeneracy of the LLs, $\frac{A}{2\pi l_B^2}$. In addition, we clarify that the final expression is obtained employing the optical selection rules and rearranging the summations in a convenient manner.

APPENDIX B: DEMONSTRATION THAT $\chi_{yx}(\omega) = 0$ AT HALF-FILLING

We want to prove that

$$\chi_{yx}(\omega) = i\sum_{\eta}\sum_{\{n;\lambda\},\lambda'}\frac{f\big(E^{\eta}_{n+1,\lambda'}\big) - f\big(E^{\eta}_{n,\lambda}\big)}{2\pi l_B^2\varepsilon_0}\Big|d^{\eta\{n+1;\lambda'\}}_{x\,\{n;\lambda\}}\Big|^2\left(\frac{1}{E^{\eta}_{n,\lambda} - E^{\eta}_{n+1,\lambda'} + \hbar\omega + i\Gamma} - \frac{1}{E^{\eta}_{n,\lambda} - E^{\eta}_{n+1,\lambda'} - \hbar\omega - i\Gamma}\right) \tag{B1}$$

vanishes at half-filling.

Given that $k_B T \ll 2\Delta$ (even at room temperature), the Pauli exclusion principle implies that only interband transitions are allowed. As a consequence, we have

$$f\big(E^{\eta}_{n+1,\lambda'}\big) - f\big(E^{\eta}_{n,\lambda}\big) = \lambda\delta_{\lambda',-\lambda}. \tag{B2}$$

Using this result, we can write

$$\chi_{yx}(\omega) = \sum_{\eta}\chi^{\eta}_{yx}(\omega), \tag{B3}$$

with

$$\chi^{\eta}_{yx}(\omega) = i\sum_{\{n;\lambda\}}\frac{\lambda}{2\pi l_B^2\varepsilon_0}\Big|d^{\eta\{n+1;-\lambda\}}_{x\,\{n;\lambda\}}\Big|^2\left(\frac{1}{E^{\eta}_{n,\lambda} - E^{\eta}_{n+1,-\lambda} + \hbar\omega + i\Gamma} - \frac{1}{E^{\eta}_{n,\lambda} - E^{\eta}_{n+1,-\lambda} - \hbar\omega - i\Gamma}\right). \tag{B4}$$

In general, $\chi^{\eta}_{yx}(\omega)$ is not null, meaning that each valley and spin channel yields a finite Hall response. However, when summing over η, the contributions cancel out. In particular, the contribution from $\{\tau;s\}$ cancels out with the one from $\{-\tau;-s\}$, i.e., $\chi^{\tau,s}_{yx}(\omega) = -\chi^{-\tau,-s}_{yx}(\omega)$. To show this in a rigorous manner, it is helpful to take Eq. (B4) and split the sum over LLs in the cases $n = 0$, for which $\{n;\lambda\} = \{0;-\tau\}$, and $n \neq 0$, for which the sum runs over $n > 0$ and $\lambda = \pm$. Accordingly, we write

$$\chi^{\eta}_{yx}(\omega) = \underset{0\mathrm{LL}}{\chi^{\eta}_{yx}}(\omega) + \underset{n\neq 0}{\chi^{\eta}_{yx}}(\omega). \tag{B5}$$

Now, we make use of the identity that relates counterpart transitions, Eq. (21), along with the general relation

$$E^{\tau,s}_{n,\lambda} - E^{\tau,s}_{n+1,-\lambda} = -\left(E^{-\tau,-s}_{n,-\lambda} - E^{-\tau,-s}_{n+1,\lambda}\right), \tag{B6}$$

to show that

$$\begin{aligned}
\chi^{\tau,s}_{\substack{yx\\ 0\mathrm{LL}}}(\omega) &= i\frac{-\tau}{2\pi l_B^2\varepsilon_0}\left|d_x^{\tau,s\{1;\tau\}}_{\{0;-\tau\}}\right|^2\left(\frac{1}{E^{\tau,s}_{0,-\tau} - E^{\tau,s}_{1,\tau} + \hbar\omega + i\Gamma} - \frac{1}{E^{\tau,s}_{0,-\tau} - E^{\tau,s}_{1,\tau} - \hbar\omega - i\Gamma}\right)\\
&= i\frac{\tau}{2\pi l_B^2\varepsilon_0}\left|d_x^{-\tau,-s\{1;-\tau\}}_{\{0;\tau\}}\right|^2\left(\frac{1}{E^{-\tau,-s}_{0,\tau} - E^{-\tau,-s}_{1,-\tau} - \hbar\omega - i\Gamma} - \frac{1}{E^{-\tau,-s}_{0,\tau} - E^{-\tau,-s}_{1,-\tau} + \hbar\omega + i\Gamma}\right)\\
&= -\chi^{-\tau,-s}_{\substack{yx\\ 0\mathrm{LL}}}(\omega),
\end{aligned} \tag{B7}$$

$$\begin{aligned}
\chi^{\tau,s}_{\substack{yx\\ n\neq 0}}(\omega) &= i\sum_{n>0,\lambda=\pm}\frac{\lambda}{2\pi l_B^2\varepsilon_0}\left|d_x^{\tau,s\{n+1;-\lambda\}}_{\{n;\lambda\}}\right|^2\left(\frac{1}{E^{\tau,s}_{n,\lambda} - E^{\tau,s}_{n+1,-\lambda} + \hbar\omega + i\Gamma} - \frac{1}{E^{\tau,s}_{n,\lambda} - E^{\tau,s}_{n+1,-\lambda} - \hbar\omega - i\Gamma}\right)\\
&= i\sum_{n>0,\lambda=\pm}\frac{-\lambda}{2\pi l_B^2\varepsilon_0}\left|d_x^{\tau,s\{n+1;\lambda\}}_{\{n;-\lambda\}}\right|^2\left(\frac{1}{E^{\tau,s}_{n,-\lambda} - E^{\tau,s}_{n+1,\lambda} + \hbar\omega + i\Gamma} - \frac{1}{E^{\tau,s}_{n,-\lambda} - E^{\tau,s}_{n+1,\lambda} - \hbar\omega - i\Gamma}\right)\\
&= i\sum_{n>0,\lambda=\pm}\frac{\lambda}{2\pi l_B^2\varepsilon_0}\left|d_x^{-\tau,-s\{n+1;-\lambda\}}_{\{n;\lambda\}}\right|^2\left(\frac{1}{E^{-\tau,-s}_{n,\lambda} - E^{-\tau,-s}_{n+1,-\lambda} - \hbar\omega - i\Gamma} - \frac{1}{E^{-\tau,-s}_{n,\lambda} - E^{-\tau,-s}_{n+1,-\lambda} + \hbar\omega + i\Gamma}\right)\\
&= -\chi^{-\tau,-s}_{\substack{yx\\ n\neq 0}}(\omega).
\end{aligned} \tag{B8}$$

APPENDIX C: INTERACTING PROBLEM

1. Interacting equation of motion

The interacting EOM is obtained by adding the result of the commutator with $\hat{H}_{ee}(t)$ in the noninteracting EOM. As in Appendix A, we present the explicit calculations for only one of the relevant pairs of operators, $\hat{c}^\dagger_{\{0\mathrm{LL};k_y\},\eta}(t)\hat{c}_{\{1;\mathcal{C};k_y\},\eta}(t) \equiv \hat{a}^\dagger_0\hat{\mathcal{C}}_1$. The derivation for the other pairs follows analogously.

After some straightforward algebra, we get

$$[\hat{H}_{ee}(t), \hat{a}^\dagger_0\hat{\mathcal{C}}_1] = \&_1 + \&_2 + \&_3 + \&_4, \tag{C1}$$

where

$$\&_1 = \frac{1}{2}\sum_{s''}\sum_{\substack{\alpha_1,\alpha_2\\ \alpha_3}} U^{\tau,s,s''}_{\substack{\alpha_1,\alpha_2\\ \alpha_3,\{0\mathrm{LL};k_y\}}}\hat{c}^\dagger_{\alpha_1,\tau,s}(t)\hat{c}^\dagger_{\alpha_2,\tau,s''}(t)\hat{c}_{\alpha_3,\tau,s''}(t)\hat{\mathcal{C}}_1, \tag{C2}$$

$$\&_2 = -\frac{1}{2}\sum_{s'}\sum_{\substack{\alpha_1,\alpha_2\\ \alpha_4}} U^{\tau,s',s}_{\substack{\alpha_1,\alpha_2\\ \{0\mathrm{LL};k_y\},\alpha_4}}\hat{c}^\dagger_{\alpha_1,\tau,s'}(t)\hat{c}^\dagger_{\alpha_2,\tau,s}(t)\hat{c}_{\alpha_4,\tau,s'}(t)\hat{\mathcal{C}}_1, \tag{C3}$$

$$\&_3 = \frac{1}{2}\sum_{s'}\sum_{\substack{\alpha_1\\ \alpha_3,\alpha_4}} U^{\tau,s',s}_{\substack{\alpha_1,\{1;\mathcal{C};k_y\}\\ \alpha_3,\alpha_4}}\hat{a}^\dagger_0\hat{c}^\dagger_{\alpha_1,\tau,s'}(t)\hat{c}_{\alpha_3,\tau,s}(t)\hat{c}_{\alpha_4,\tau,s'}(t), \tag{C4}$$

$$\&_4 = -\frac{1}{2}\sum_{s''}\sum_{\substack{\alpha_2\\ \alpha_3,\alpha_4}} U^{\tau,s,s''}_{\substack{\{1;\mathcal{C};k_y\},\alpha_2\\ \alpha_3,\alpha_4}}\hat{a}^\dagger_0\hat{c}^\dagger_{\alpha_2,\tau,s''}(t)\hat{c}_{\alpha_3,\tau,s''}(t)\hat{c}_{\alpha_4,\tau,s}(t). \tag{C5}$$

2. Exchange self-energy terms

The interacting EOM contains four different types of terms, as seen in Eq. (C1). We first deal with $\&_1$.

Just like in the noninteracting case, it is implicit that, within the linear response limit, we take the average of the these terms with respect to the unperturbed Hamiltonian. The average of $\&_1$ implies the average of the product of four fermionic operators which, within the random phase approximation, yields

$$\begin{aligned}
&\left\langle\hat{c}^\dagger_{\alpha_1,\tau,s}(t)\hat{c}^\dagger_{\alpha_2,\tau,s''}(t)\hat{c}_{\alpha_3,\tau,s''}(t)\hat{\mathcal{C}}_1\right\rangle_0\\
&\quad= \left\langle\hat{c}^\dagger_{\alpha_1,\tau,s}(t)\hat{\mathcal{C}}_1\right\rangle_0\left\langle\hat{c}^\dagger_{\alpha_2,\tau,s''}(t)\hat{c}_{\alpha_3,\tau,s''}(t)\right\rangle_0\\
&\qquad- \left\langle\hat{c}^\dagger_{\alpha_1,\tau,s}(t)\hat{c}_{\alpha_3,\tau,s''}(t)\right\rangle_0\left\langle\hat{c}^\dagger_{\alpha_2,\tau,s''}(t)\hat{\mathcal{C}}_1\right\rangle_0.
\end{aligned} \tag{C6}$$

Among these terms, the ones that lead to a band renormalization, the so-called SE terms, are

$$\begin{aligned}
&\left\langle\hat{c}^\dagger_{\alpha_1,\tau,s}(t)\hat{c}^\dagger_{\alpha_2,\tau,s''}(t)\hat{c}_{\alpha_3,\tau,s''}(t)\hat{\mathcal{C}}_1\right\rangle^{\mathrm{SE}}_0\\
&\quad= \delta_{\alpha_1,\{0\mathrm{LL},k_y\}}\delta_{\alpha_2,\alpha_3}\langle\hat{a}^\dagger_0\hat{\mathcal{C}}_1\rangle_0 f\left(E^{\tau,s''}_{\alpha_2}\right)\\
&\qquad- \delta_{s,s''}\delta_{\alpha_1,\alpha_3}\delta_{\alpha_2,\{0\mathrm{LL},k_y\}}\langle\hat{a}^\dagger_0\hat{\mathcal{C}}_1\rangle_0 f\left(E^{\tau,s}_{\alpha_1}\right).
\end{aligned} \tag{C7}$$

This leads to

$$\langle\&_1\rangle^{\mathrm{SE}}_0 = \langle\&_1\rangle^{\mathrm{Hartree}}_0 + \langle\&_1\rangle^{\mathrm{Fock}}_0, \tag{C8}$$

where

$$\langle\&_1\rangle^{\mathrm{Hartree}}_0 = \frac{1}{2}\langle\hat{a}^\dagger_0\hat{\mathcal{C}}_1\rangle_0\sum_{s''}\sum_{\alpha_2} U^{\tau,s,s''}_{\substack{\{0\mathrm{LL};k_y\},\alpha_2\\ \alpha_2,\{0\mathrm{LL};k_y\}}} f\left(E^{\tau,s''}_{\alpha_2}\right) \tag{C9}$$

is the Hartree term and

$$\langle\&_1\rangle^{\mathrm{Fock}}_0 = -\frac{1}{2}\langle\hat{a}^\dagger_0\hat{\mathcal{C}}_1\rangle_0\sum_{\alpha_1} U^{\tau,s,s}_{\substack{\alpha_1,\{0\mathrm{LL};k_y\}\\ \alpha_1,\{0\mathrm{LL};k_y\}}} f\left(E^{\tau,s}_{\alpha_1}\right) \tag{C10}$$

is the Fock or exchange SE term.

By analogy with the Hartree-Fock approximation to the problem of the homogeneous electron gas [54], we argue that the Hartree term, which mixes spins, is canceled by the electron-ion background within the jellium model. To support this claim, we have verified that the limit $B_0 = 0$ in $\langle \&_1 \rangle_0^{\text{Hartree}}$ implies a null transferred momentum, i.e., $\delta_{\boldsymbol{q},\boldsymbol{0}}$. As a result, we keep only the Fock term, which couples the same spin flavors.

Repeating the same calculations, and making use of the identity

$$U^{\tau,s,s'}_{\substack{\alpha_1,\alpha_2\\ \alpha_3,\alpha_4}} = U^{\tau,s',s}_{\substack{\alpha_2,\alpha_1\\ \alpha_4,\alpha_3}}, \tag{C11}$$

it is immediate to show that $\langle \&_2 \rangle_0^{\text{Fock}} = \langle \&_1 \rangle_0^{\text{Fock}}$, which leads to

$$\langle \&_1 + \&_2 \rangle_0^{\text{Fock}} = -\langle \hat{a}_0^\dagger \hat{\mathcal{C}}_1 \rangle_0 \sum_{\alpha_1} U^{\tau,s,s}_{\substack{\alpha_1,\{0\text{LL};k_y\}\\ \alpha_1,\{0\text{LL};k_y\}}} f\big(E^{\tau,s}_{\alpha_1}\big). \tag{C12}$$

Similarly, we obtain

$$\langle \&_3 + \&_4 \rangle_0^{\text{Fock}} = \langle \hat{a}_0^\dagger \hat{\mathcal{C}}_1 \rangle_0 \sum_{\alpha_1} U^{\tau,s,s}_{\substack{\alpha_1,\{1;\mathcal{C};k_y\}\\ \alpha_1,\{1;\mathcal{C};k_y\}}} f\big(E^{\tau,s}_{\alpha_1}\big). \tag{C13}$$

We now observe that the interacting EOM is equivalent to the noninteracting one, Eq. (A6), with a renormalized energy difference, given by

$$\big(E^\eta_{0\text{LL}} - E^\eta_{1,\mathcal{C}}\big)_{\text{renorm}} = E^\eta_{0\text{LL}} - E^\eta_{1,\mathcal{C}} + \sum_{\alpha_1} f\big(E^{\tau,s}_{\alpha_1}\big) \times \left[U^{\tau,s,s}_{\substack{\alpha_1,\{1;\mathcal{C};k_y\}\\ \alpha_1,\{1;\mathcal{C};k_y\}}} - U^{\tau,s,s}_{\substack{\alpha_1,\{0\text{LL};k_y\}\\ \alpha_1,\{0\text{LL};k_y\}}} \right]. \tag{C14}$$

Generalizing these results for the other pairs of operators, we conclude that the energy bands are renormalized as

$$\big(E^\eta_\alpha\big)_{\text{renorm}} = E^\eta_\alpha + \Sigma^\eta_\alpha, \tag{C15}$$

where

$$\Sigma^\eta_\alpha = -\sum_{\alpha'} f\big(E^\eta_{\alpha'}\big) U^{\tau,s,s}_{\substack{\alpha',\alpha\\ \alpha',\alpha}} \tag{C16}$$

are the exchange SE corrections.

3. Coulomb integrals

The (general) expression for the exchange SE corrections, Eq. (C16), hides multiple integrals that can be solved analytically. Here, we provide some of the technical steps that lead to the simplification of this expression. We turn our attention to the following integral:

$$I_0 \equiv \int_{-\infty}^{+\infty} dx\, e^{iq_x x} \frac{e^{-(\frac{x}{l_B}+l_B k_y')^2/2}\; e^{-(\frac{x}{l_B}+l_B k_y)^2/2}}{\sqrt{\pi} l_B} \times \tilde{H}_{n'}\left(\frac{x}{l_B} + l_B k_y'\right) \tilde{H}_n\left(\frac{x}{l_B} + l_B k_y\right). \tag{C17}$$

This integral is relevant as its solution includes the nontrivial steps required to calculate the structure factors that lie inside the Coulomb integrals [see Eqs. (30) and (31)].

With the change of variables $u = \frac{x}{l_B} + l_B k_y'$, we obtain

$$I_0 = e^{-l_B^2(q_y^2/2 + iq_x k_y')} I_1, \tag{C18}$$

with

$$I_1 = \int_{-\infty}^{+\infty} \frac{du}{\sqrt{\pi}}\, e^{-u^2 + l_B(q_y + iq_x)u} \tilde{H}_{n'}(u) \tilde{H}_n(u - l_B q_y), \tag{C19}$$

where $q_y = k_y' - k_y$ is an implicit relation that comes from the trivial integration over dy in the structure factors.

At this point, we resort to a table of integrals (Ref. [57]), and invoke Eq. 7.377 which, with little manipulation, can be written as

$$\int_{-\infty}^{+\infty} \frac{du}{\sqrt{\pi}}\, e^{-u^2 + l_B(q_y+iq_x)u} \tilde{H}_n\left(u - \frac{l_B(q_y+iq_x)}{2} + p_0\right) \tilde{H}_{n'}\left(u - \frac{l_B(q_y+iq_x)}{2} + q_0\right) = e^{l_B^2(q_y+iq_x)^2/4} \sqrt{2^{n'-n}} \sqrt{\frac{n!}{n'!}}\, q_0^{n'-n} L_n^{n'-n}(-2p_0 q_0), \quad [n \leqslant n']. \tag{C20}$$

Given this relation, it is straightforward to show that

$$I_0 = e^{-l_B^2[\frac{q_x^2+q_y^2}{4} + iq_x(k_y' - \frac{q_y}{2})]} \sqrt{2^{|n'-n|}} \sqrt{\frac{\min(n,n')!}{\max(n,n')!}} \left[l_B \frac{\text{sign}(n'-n) q_y + iq_x}{2} \right]^{|n'-n|} L^{|n'-n|}_{\min(n,n')}\left(l_B^2 \frac{q_x^2 + q_y^2}{2}\right). \tag{C21}$$

The remaining steps required to simplify Eq. (C16) into Eqs. (34)–(36) follow straightforwardly.

[1] K. S. Novoselov, A. K. Geim, S. V. Morozov, D. Jiang, M. I. Katsnelson, I. V. Grigorieva, S. V. Dubonos, and A. A. Firsov, Nature (London) **438**, 197 (2005).

[2] K. S. Novoselov, A. Mishchenko, A. Carvalho, and A. H. C. Neto, Science **353**, aac9439 (2016).

[3] R. Roldán, L. Chirolli, E. Prada, J. A. Silva-Guillén, P. San-Jose, and F. Guinea, Chem. Soc. Rev. **46**, 4387 (2017).

[4] A. H. C. Neto, F. Guinea, N. M. R. Peres, K. S. Novoselov, and A. K. Geim, Rev. Mod. Phys. **81**, 109 (2009).

[5] D. Xiao, G.-B. Liu, W. Feng, X. Xu, and W. Yao, Phys. Rev. Lett. **108**, 196802 (2012).

[6] M. O. Goerbig, G. Montambaux, and F. Piéchon, Europhys. Lett. **105**, 57005 (2014).

[7] D. Xiao, W. Yao, and Q. Niu, Phys. Rev. Lett. **99**, 236809 (2007).

[8] M. Koshino and T. Ando, Phys. Rev. B **81**, 195431 (2010).

[9] K. Kośmider, J. W. González, and J. Fernández-Rossier, Phys. Rev. B **88**, 245436 (2013).

[10] G. Aivazian, Z. Gong, A. M. Jones, R.-L. Chu, J. Yan, D. G. Mandrus, C. Zhang, D. Cobden, W. Yao, and X. Xu, Nat. Phys. **11**, 148 (2015).

[11] A. Srivastava, M. Sidler, A. V. Allain, D. S. Lembke, A. Kis, and A. Imamoğlu, Nat. Phys. **11**, 141 (2015).

[12] R. Schmidt, A. Arora, G. Plechinger, P. Nagler, A. G. del Águila, M. V. Ballottin, P. C. M. Christianen, S. M. de Vasconcellos, C. Schüller, T. Korn, and R. Bratschitsch, Phys. Rev. Lett. **117**, 077402 (2016).

[13] Z. Wang, J. Shan, and K. F. Mak, Nat. Nanotechnol. **12**, 144 (2017).

[14] F. Rose, M. O. Goerbig, and F. Piéchon, Phys. Rev. B **88**, 125438 (2013).

[15] R.-L. Chu, X. Li, S. Wu, Q. Niu, W. Yao, X. Xu, and C. Zhang, Phys. Rev. B **90**, 045427 (2014).

[16] K. F. Mak, C. Lee, J. Hone, J. Shan, and T. F. Heinz, Phys. Rev. Lett. **105**, 136805 (2010).

[17] A. Splendiani, L. Sun, Y. Zhang, T. Li, J. Kim, C.-Y. Chim, G. Galli, and F. Wang, Nano Lett. **10**, 1271 (2010).

[18] T. C. Berkelbach, M. S. Hybertsen, and D. R. Reichman, Phys. Rev. B **88**, 045318 (2013).

[19] M. M. Ugeda, A. J. Bradley, S.-F. Shi, F. H. da Jornada, Y. Zhang, D. Y. Qiu, W. Ruan, S.-K. Mo, Z. Hussain, Z.-X. Shen, F. Wang, S. G. Louie, and M. F. Crommie, Nat. Mater. **13**, 1091 (2014).

[20] A. J. Chaves, R. M. Ribeiro, T. Frederico, and N. M. R. Peres, 2D Mater. **4**, 025086 (2017).

[21] G. Wang, A. Chernikov, M. M. Glazov, T. F. Heinz, X. Marie, T. Amand, and B. Urbaszek, Rev. Mod. Phys. **90**, 021001 (2018).

[22] Y. J. Zhang, T. Oka, R. Suzuki, J. T. Ye, and Y. Iwasa, Science **344**, 725 (2014).

[23] K. F. Mak, D. Xiao, and J. Shan, Nat. Photonics **12**, 451 (2018).

[24] L. Jiang, Y. Zheng, H. Li, and H. Shen, Nanotechnology **21**, 145703 (2010).

[25] J. G. Pedersen and T. G. Pedersen, Phys. Rev. B **84**, 115424 (2011).

[26] C. J. Tabert and E. J. Nicol, Phys. Rev. Lett. **110**, 197402 (2013).

[27] X. Li, T. Cao, Q. Niu, J. Shi, and J. Feng, Proc. Natl. Acad. Sci. USA **110**, 3738 (2013).

[28] J. Have, G. Catarina, T. G. Pedersen, and N. M. R. Peres, Phys. Rev. B **99**, 035416 (2019).

[29] G.-B. Liu, W.-Y. Shan, Y. Yao, W. Yao, and D. Xiao, Phys. Rev. B **88**, 085433 (2013).

[30] A. Kormányos, G. Burkard, M. Gmitra, J. Fabian, V. Zólyomi, N. D. Drummond, and V. Fal'ko, 2D Mater. **2**, 022001 (2015).

[31] H. Ochoa and R. Roldán, Phys. Rev. B **87**, 245421 (2013).

[32] J. L. Lado, J. W. González, and J. Fernández-Rossier, Phys. Rev. B **88**, 035448 (2013).

[33] J. L. Lado and J. Fernández-Rossier, 2D Mater. **3**, 035023 (2016).

[34] A. Ferreira, J. Viana-Gomes, Yu. V. Bludov, V. Pereira, N. M. R. Peres, and A. H. C. Neto, Phys. Rev. B **84**, 235410 (2011).

[35] N. M. R. Peres, R. M. Ribeiro, and A. H. C. Neto, Phys. Rev. Lett. **105**, 055501 (2010).

[36] This result is easily obtained using that $\langle\alpha'|\boldsymbol{r}|\alpha\rangle_\eta = \frac{\langle\alpha'|[\boldsymbol{r},H_0^\eta]|\alpha\rangle_\eta}{E_\alpha^\eta - E_{\alpha'}^\eta} = i\hbar v_F \frac{\langle\alpha'|(\tau\sigma_x,\sigma_y)|\alpha\rangle_\eta}{E_\alpha^\eta - E_{\alpha'}^\eta}$, for $\alpha \neq \alpha'$, followed by the spatial integration.

[37] V. P. Gusynin, S. G. Sharapov, and J. P. Carbotte, J. Phys.: Condens. Matter **19**, 026222 (2007).

[38] A. S. Nowick, *Crystal Properties Via Group Theory* (Cambridge University Press, Cambridge, 1995).

[39] F. Cadiz, E. Courtade, C. Robert, G. Wang, Y. Shen, H. Cai, T. Taniguchi, K. Watanabe, H. Carrere, D. Lagarde, M. Manca, T. Amand, P. Renucci, S. Tongay, X. Marie, and B. Urbaszek, Phys. Rev. X **7**, 021026 (2017).

[40] O. A. Ajayi, J. V. Ardelean, G. D. Shepard, J. Wang, A. Antony, T. Taniguchi, K. Watanabe, T. F. Heinz, S. Strauf, X.-Y. Zhu, and J. C. Hone, 2D Mater. **4**, 031011 (2017).

[41] W. Yao, D. Xiao, and Q. Niu, Phys. Rev. B **77**, 235406 (2008).

[42] T. Cao, G. Wang, W. Han, H. Ye, C. Zhu, J. Shi, Q. Niu, P. Tan, E. Wang, B. Liu, and J. Feng, Nat. Commun. **3**, 887 (2012).

[43] M. Ezawa, Phys. Rev. B **87**, 155415 (2013).

[44] X. Xu, W. Yao, D. Xiao, and T. F. Heinz, Nat. Phys. **10**, 343 (2014).

[45] N. W. Ashcroft and N. D. Mermin, *Solid State Physics* (Harcourt College, Fort Worth, TX, 1976).

[46] For the sake of clarity, we underline that each arrow in Fig. 4(d) represents two transitions, as there are two possible combinations of τ and s that yield $\tau s = +1$.

[47] P. Cudazzo, I. V. Tokatly, and A. Rubio, Phys. Rev. B **84**, 085406 (2011).

[48] Y. Ding, Y. Wang, J. Ni, L. Shi, S. Shi, and W. Tang, Physica B (Amsterdam) **406**, 2254 (2011).

[49] W. Kohn, Phys. Rev. **123**, 1242 (1961).

[50] T. Ando, A. B. Fowler, and F. Stern, Rev. Mod. Phys. **54**, 437 (1982).

[51] S. J. Allen, Jr., D. C. Tsui, and J. V. Dalton, Phys. Rev. Lett. **32**, 107 (1974).

[52] R. Roldán, J.-N. Fuchs, and M. O. Goerbig, Phys. Rev. B **82**, 205418 (2010).

[53] M. Dobers, K. v. Klitzing, and G. Weimann, Phys. Rev. B **38**, 5453 (1988).

[54] G. D. Mahan, *Many-particle Physics* (Springer, Berlin, 2013).

[55] L. Szulakowska, M. Bieniek, and P. Hawrylak, arXiv:1810.12402.

[56] There is no loss of generality in omitting k_y and η because the optical selection rules imply transitions that couple the same wave vector, valley, and spin.

[57] I. S. Gradshteyn and I. M. Ryzhik, *Table of Integrals, Series, and Products* (Academic, Hoboken, NJ, 2014).

Paper E

Excitonic magneto-optics in monolayer transition metal dichalcogenides: From nanoribbons to two-dimensional response

J. Have, N. M. R. Peres and T. G. Pedersen

Published in
Physical Review B **100**, 045411 (2019)

Excitonic magneto-optics in monolayer transition metal dichalcogenides: From nanoribbons to two-dimensional response

J. Have,[1,2,*] N. M. R. Peres,[3,4] and T. G. Pedersen[1,5]

[1]*Department of Materials and Production, Aalborg University, DK-9220 Aalborg East, Denmark*

[2]*Department of Mathematical Sciences, Aalborg University, DK-9220 Aalborg East, Denmark*

[3]*International Iberian Nanotechnology Laboratory (INL), 4715-330 Braga, Portugal*

[4]*Center and Department of Physics, and QuantaLab, University of Minho, Campus de Gualtar, 4710-057 Braga, Portugal*

[5]*Center for Nanostructured Graphene (CNG), DK-9220 Aalborg East, Denmark*

(Received 20 May 2019; revised manuscript received 24 June 2019; published 15 July 2019)

The magneto-optical response of monolayer transition metal dichalcogenides, including excitonic effects, is studied using a nanoribbon geometry. We compute the diagonal optical conductivity and the Hall conductivity. Comparing the excitonic optical Hall conductivity to results obtained in the independent-particle approximation, we find an increase in the amplitude corresponding to one order of magnitude when excitonic effects are included. The Hall conductivities are used to calculate Faraday rotation spectra for MoS_2 and WSe_2. Finally, we have also calculated the diamagnetic shift of the exciton states of WSe_2 in different dielectric environments. Comparing the calculated diamagnetic shift to recent experimental measurements, we find a very good agreement between the two.

DOI: 10.1103/PhysRevB.100.045411

I. INTRODUCTION

With the successful exfoliation of monolayers of transition metal dichalcogenides (TMDs) [1], a new group of interesting semiconducting materials became available for study and potential applications. The characteristics of monolayer TMDs include a direct band gap [1–3], broken inversion symmetry [4,5], strong spin-orbit coupling [6], and strongly bound excitons and excitonic complexes [7–10]. In addition to these characteristics, monolayer TMDs have also been shown to exhibit interesting magneto-optical properties such as valley polarized Landau levels [11–13], valley Zeeman splitting [14–18], and magnetic-field-induced rotation of the polarization state of light [19,20]. These properties have inspired potential new applications in areas such as optoelectronics [21] and valleytronics [22,23]. Magnetic fields have also been used to probe exciton properties, such as effective mass, size [24–26], and how they are affected by the dielectric environment [27].

So far, the theoretical analysis of TMD magnetoexcitons has relied on effective-mass models, such as the Wannier model [10,24,27,28]. We recently validated that the Wannier model can be used to accurately describe certain properties of magnetoexcitons [29]. However, in the Wannier model, the Bloch part of the wave function is replaced by a plane wave, which makes the task of computing the single-particle momentum matrix elements unfeasible. For the diagonal optical response there is a solution to this problem [30], but for the Hall conductivity no solution currently exists. Thus, the Wannier model cannot be applied to the task of calculating the Hall conductivity, which is a necessary step in computing the magneto-optical Kerr effect and the Faraday rotation [31,32]. The issue can be resolved in the independent-particle approximation (IPA) [13,33,34], but the optical properties of TMDs are dominated by excitonic effects. Hence, for an accurate description of the magneto-optical response of TMDs, excitons should be included.

The main computational difficulty in going beyond effective mass models when treating magnetoexcitons is that the external magnetic field breaks the translation symmetry of the single-particle Hamiltonian. Depending on the choice of magnetic vector potential gauge, translation symmetry will be broken in at least one direction. The translation symmetry can be restored by considering a magnetic supercell, but the size of the supercell is inversely proportional to the magnetic field strength [33]. Consequently, for experimentally obtainable field strengths, a very large supercell is needed, thus making the task of computing the excitonic properties unfeasible [35]. In the present work, we address this issue by using a system of finite width in the direction, for which translation symmetry is broken. This approach corresponds to considering wide TMD nanoribbons. By increasing the size of the system in the finite direction, we are able to recover the two-dimensional (2D) response, including excitonic effects. Using this approach, we then describe quantitatively the excitonic effects on both the diagonal conductivity and the Hall conductivity of monolayer TMDs perturbed by an external magnetic field. This allows us to compute Faraday rotation spectra as well as excitonic diamagnetic shifts.

The paper is structured as follows: In Sec. II, the tight-binding model used to describe the single-particle properties of both 2D monolayer TMDs and nanoribbons is introduced. In this section, we also check the width convergence of the nanoribbon optical response in the independent-particle approximation. In Sec. III, we include excitonic effects in our

*jh@nano.aau.dk

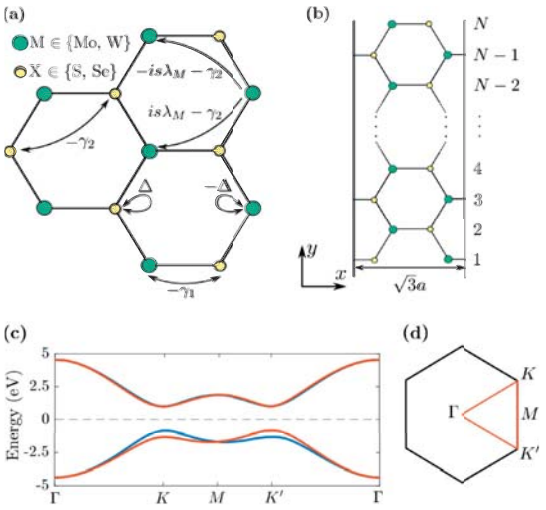

FIG. 1. (a) Schematic of the tight-binding couplings in the NNN-TB model for monolayer MX_2 TMDs. (b) Unit cell of a MX_2 armchair nanoribbon of width $(N-1)a/2$ and length $\sqrt{3}a$, where a is the lattice constant. (c) Band structure of WSe_2 along the path in the Brillouin zone specified by the letters. The blue and red lines are the spin-up and spin-down bands, respectively. (d) Brillouin zone of monolayer TMD.

model and check convergence of the optical response. Finally, in Sec. IV, the magneto-optical response including excitons is studied using our nanoribbon model. In this section, we also calculate the diamagnetic shift of excitons in WSe_2 and compare to recent experimental results.

II. SINGLE-PARTICLE PROPERTIES

In this section, we present the theoretical framework used to describe the single-particle properties of monolayer TMDs and nanoribbons. Two important characteristics of monolayer TMDs are the broken inversion symmetry and the strong spin-orbit coupling (SOC), which result in spin splitting of the conduction and valence band edge states [4,36–38]. In addition, TMDs also exhibit broken electron-hole symmetry, which leads to electrons and holes with different effective masses. To describe the single-particle properties of monolayer TMDs, we apply a tight-binding (TB) model. An orthogonal nearest-neighbor (NN) TB model always has electron-hole symmetry. Thus, in order to have different effective masses of electrons and holes, we need to use either a next-nearest-neighbor (NNN) model or include a finite overlap [31]. For this work, we have chosen to use a NNN TB model. The couplings used for a TMD with lattice constant a are illustrated in Fig. 1(a). Here, γ_1 and γ_2 are the NN and NNN hopping terms, respectively, and $-\Delta$ and Δ denote the on-site energies for transition metal (M) and chalcogen (X) atoms, respectively. Additionally, $is\lambda_M\eta$ is the SOC between NNN transition metal atoms, where $s=\pm1$ denotes the spin and $\eta=\pm1$ [39,40]. As shown for hBN systems in [39], the value of η depends on the rotation sense in a hexagon, $\eta=+1$ (-1) for clockwise (counterclockwise) orientation. This also holds for TMDs as they share the same point group as hBN [4,6,38]. For simplicity, we assume that the SOC between chalcogen atoms is negligible. The same couplings are used to describe both TMD monolayers and nanoribbons. Recently, a similar TB model was used in both the study of spin Hall effects in monolayer TMDs [40] and to compute the optical response of gapped and proximitized graphene [41].

We begin by considering a TMD monolayer placed in the xy plane. The couplings described above give the following two-band Hamiltonian for a state with wave vector $\mathbf{k}$:

$$\hat{H}=\begin{bmatrix}\Delta-\gamma_2 h & -\gamma_1 f\\ -\gamma_1 f^* & -\Delta-s\lambda_M g-\gamma_2 h\end{bmatrix}, \tag{1}$$

where

$$f(\mathbf{k})=e^{ik_x a/\sqrt{3}}+2e^{-ik_x a/2\sqrt{3}}\cos(k_y a/2), \tag{2}$$

$$g(\mathbf{k})=2\left[\sin\left(\frac{k_x a\sqrt{3}}{2}+\frac{k_y a}{2}\right)-\sin(k_y a)-\sin\left(\frac{k_x a\sqrt{3}}{2}-\frac{k_y a}{2}\right)\right], \tag{3}$$

$$h(\mathbf{k})=2\left[\cos\left(\frac{k_x a\sqrt{3}}{2}+\frac{k_y a}{2}\right)+\cos(k_y a)+\cos\left(\frac{k_x a\sqrt{3}}{2}-\frac{k_y a}{2}\right)\right]. \tag{4}$$

To determine the hopping parameters γ_1 and γ_2, we fit to the effective masses of electrons and holes in monolayer TMDs extracted from first-principles calculations in Ref. [42]. When doing this, we can assume that $\lambda_M=0$. This holds since λ_M is small compared to the band gap and, consequently, using a finite λ_M would only give a small correction to the hopping terms. Then, the energy bands are given by

$$E_\pm(\mathbf{k})=\gamma_2 h(\mathbf{k})\pm\sqrt{\Delta^2+\gamma_1^2|f(\mathbf{k})|^2}. \tag{5}$$

By expanding $E_\pm(\mathbf{k})$ around the K point $(k_x,k_y)=2\pi(1/\sqrt{3},1/3)/a$ in the Brillouin zone [illustrated in Fig. 1(d)], we get the following relations between the hopping parameters and the effective masses:

$$\frac{3a^2\gamma_1^2}{8\Delta}+\frac{3a^2}{4}\gamma_2=\frac{\hbar^2}{2m_e^*}, \tag{6}$$

$$\frac{3a^2\gamma_1^2}{8\Delta}-\frac{3a^2}{4}\gamma_2=\frac{\hbar^2}{2m_h^*}. \tag{7}$$

Here, $m^*_{e(h)}$ is the effective electron (hole) mass and $\hbar$ is the reduced Planck constant. Solving for γ_1 and γ_2 in Eqs. (6) and (7) gives the hopping parameters. The spin-dependent band gaps at the K and K' points are given by $E_g=2\Delta\mp3\sqrt{3}s\lambda_M$, where $+$ $(-)$ holds at the K (K') point. The value of the SOC parameter λ_M is determined by matching the split to the spin splitting of the valence band edge calculated in Ref. [42]. The resulting band structure for WSe_2 is plotted in Fig. 1(c). In Table I, we provide the complete set of parameters used for monolayer TMDs in the present paper.

TABLE I. Model parameters for the four common TMDs. The on-site energy, lattice constants, and screening lengths r_0 are taken from Ref. [42]. The SOC strengths are calculated from the spin splitting in Ref. [42], and the tight-binding couplings γ_1 and γ_2 are found by fitting to the electron and hole effective masses of Ref. [42].

	Δ (eV)	γ_1 (eV)	γ_2 (meV)	λ_M (meV)	a (Å)	r_0 (Å)
MoS_2	1.24	1.498	8.2	14.4	3.18	44.3
$MoSe_2$	1.09	1.359	92.5	18.3	3.32	51.2
WS_2	1.22	1.661	−51.7	43.3	3.19	39.9
WSe_2	1.04	1.444	−43.6	48.5	3.32	46.2

We introduce the external magnetic field by transforming the hopping integrals according to the Peierls substitution [43], which is simply the transformation $t \mapsto t_{ij} = te^{i\phi_{ij}}$, where t is equal to either γ_1, γ_2, or λ_M. The Peierls phase ϕ_{ij} is given by

$$\phi_{ij} = \frac{e}{\hbar}\int_{\mathbf{R}_i}^{\mathbf{R}_j} \mathbf{A}\cdot d\mathbf{l}. \tag{8}$$

Here, e is the elementary charge, $\mathbf{R}_i$ and $\mathbf{R}_j$ denote the location of atoms at site i and j, respectively, and $\mathbf{A}$ is the magnetic vector potential, related to the magnetic field by $\mathbf{B} = \nabla \times \mathbf{A}$. We take the magnetic field to be given by $\mathbf{B} = B\hat{z}$, where B is the magnetic field strength. For 2D systems the phase factor evidently breaks the periodicity of the tight-binding Hamiltonian, but it can be restored by using a suitable magnetic supercell [44]. As mentioned in Sec. I, the relation between field strength and the supercell size makes the calculation of excitonic properties unfeasible for experimentally obtainable fields. Indeed, with the current methodology (TB + BSE) and computer power available, magnetoexcitonic calculations are limited to field strengths of several thousand teslas. However, for a nanoribbon system, which is finite in the y direction, the Landau gauge, $\mathbf{A} = -By\hat{x}$, does not affect the translation symmetry of the system [35]. Hence, no restrictions on the magnetic field strength and no magnetic supercell are required. This is the motivation for using nanoribbons as a tool to describe the magneto-optical response of monolayer TMDs for arbitrary magnetic field strengths. We will consider armchair nanoribbons, which are infinite in the x direction and have a finite width of $W = (N-1)a/2$, where N is the number of dimer lines in the y direction. The unit cell is illustrated in Fig. 1(b). Since the nanoribbon system is finite in the x direction, edge states are expected to exist for all nanoribbon widths [45]. In Appendix A, we check the convergence of the electronic structure by examining the density of states (DOS). The edge states are found to have negligible effect on the electronic structure for $N \gtrsim 200$. Consequently, by increasing N, we expect the optical response of the nanoribbons to converge to that of the 2D system.

To calculate the linear optical conductivity, we make use of the following expression for the spin-up and spin-down contribution to the linear optical conductivity [33],

$$\sigma^s_{\alpha\beta}(\omega) = -\frac{ie^2\hbar^2\omega}{m^2A}\sum_{cvk}\frac{p^\alpha_{cvk,s}p^\beta_{vck,s}}{E^2_{cvk,s}(E_{cvk,s}-\hbar\omega-i\hbar\Gamma)}, \tag{9}$$

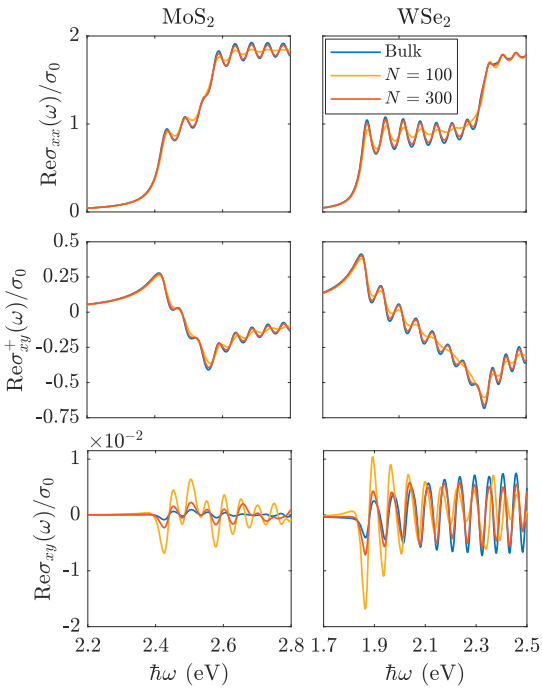

FIG. 2. Single-particle linear optical conductivities versus photon energy. The spectra are calculated for $B = 130$ T and $\hbar\Gamma = 25$ meV. The factor of 10^{-2} should be multiplied with the y axis directly underneath. The blue lines refer to the 2D conductivities and red and yellow lines to the nanoribbon case.

with $\alpha, \beta \in \{x, y\}$, $\hbar\omega$ the photon energy, $\hbar\Gamma$ a phenomenological broadening parameter, m the free electron mass, $A = WL$ the system area, where W is the system width and L is the system length, $p^\alpha_{cvk,s}$ the momentum matrix elements, and $E_{cvk,s} := E_c(k,s) - E_v(k,s)$ the transition energy. The sum runs over all combinations of conduction (c) and valence (v) bands and k points, and we have neglected the nonresonant term of the conductivity. In the nanoribbon geometry, the limit where L goes to infinity should be taken. In practice this is done by converting the sum over k points to an integral by using that the distance between two k points is equal to $\Delta k = 2\pi/L$. The linear optical conductivity tensor elements are then found by summing over spin, i.e., $\sigma_{\alpha\beta}(\omega) = \sigma^+_{\alpha\beta}(\omega) + \sigma^-_{\alpha\beta}(\omega)$. By symmetry, we have the relation $\sigma^+_{\alpha\alpha}(\omega) = \sigma^-_{\alpha\alpha}(\omega)$ for the diagonal elements, and $\sigma^+_{\alpha\beta}(\omega) = -\sigma^-_{\alpha\beta}(\omega)$ for the off-diagonal elements when $B = 0$ T. We note that the expression in Eq. (9) holds for both nanoribbons and 2D monolayers, but k denotes a scalar quantity in the former case and a vector quantity in the latter case.

In Fig. 2, we show the real part of the optical conductivity in the single-particle approximation for 2D monolayers and nanoribbons. All spectra are plotted in units of $\sigma_0 = e^2/4\hbar$ and calculated for a Brillouin zone discretized using 120 k points. In the particular case of Fig. 2, we plot the spectra with a broadening of 25 meV. This value is used in order to

clearly show the different features of the optical response and how they converge. Throughout, we focus on MoS_2 and WSe_2 as examples of monolayer TMDs, but similar results hold for other types of TMDs. In Fig. 2, the spectra are computed for a very strong magnetic field to make it possible to distinguish the peaks due to Landau levels (LLs). The LLs are clearly visible in both the diagonal and off-diagonal response. The plots also illustrate the finite off-diagonal conductivities, the so-called Hall conductivities, present when there is an external magnetic field. Comparing the response of the $N = 100$ and $N = 300$ nanoribbons to the bulk conductivity, we see that for $\sigma_{xx}(\omega)$ and $\sigma^{+}_{xy}(\omega)$ both nanoribbon widths capture the qualitative features. However, the wider nanoribbons more accurately capture the position of the higher Landau levels and the amplitudes of the peaks. In contrast, for $\sigma_{xy}(\omega)$ very wide nanoribbons are needed to obtain good convergence of the amplitudes. This is due to the fact that $\sigma_{xy}(\omega)$ is the sum of $\sigma^{+}_{xy}(\omega)$ and $\sigma^{-}_{xy}(\omega)$, both of which are much bigger in amplitude than $\sigma_{xy}(\omega)$. Thus, while the difference between the spin-dependent off-diagonal response of nanoribbons and 2D is small compared to the amplitude of $\sigma^{+}_{xy}(\omega)$ it is large compared to the amplitude of the Hall conductivity—consequently, making the Hall conductivity susceptible to poor convergence. The excitonic spectra are expected to show better convergence since the optical response is dominated by excitons and the excitons are strongly localized in TMDs [7,8,46]. Finally, we note that the valley Zeeman splitting is not described by the TB Hamiltonian in this paper.

III. EXCITONIC EFFECTS

In this section, we include excitonic effects in our description of TMD monolayers and nanoribbons. The approach follows that of Refs. [35,47]. We expand the excitonic wave function $|exc\rangle$ in a basis of singlets formed by excitations between a single pair of spin-dependent valence and conduction bands at k, such that the wave function is given by

$$|exc\rangle = \sum_{cvk,s} A^{s}_{cvk} |vks \to cks\rangle, \tag{10}$$

where A^{s}_{cvk} are the expansion coefficients and $|vks \to cks\rangle$ the singly excited states. Note that we only include excitations between bands of equal spin and that k can be either a vector or scalar quantity depending on the dimensionality of the system under consideration. The excitonic states are governed by the Bethe-Salpeter equation (BSE) [7], which for the expansion in Eq. (10) take the form

$$E_{cvk,s}A^{s}_{cvk} + \sum_{c'v'k',s'} W^{s,s'}_{cvk,c'v'k'} A^{s'}_{c'v'k'} = E A^{s}_{cvk}. \tag{11}$$

Here, $W^{s,s'}_{cvk,c'v'k'}$ is the electron-hole interaction matrix elements and E is the exciton energy. Note that we have neglected the exchange term in the BSE for simplicity. Then, the electron-hole interaction matrix elements are given by

$$W^{s,s'}_{cvk,c'v'k'} = \langle vks \to cks | U | v'k's' \to c'k's' \rangle, \tag{12}$$

where U is the electron-hole interaction potential defined below. Performing the spin integral in Eq. (12), we find

$$W^{s,s'}_{cvk,c'v'k'} = \delta_{s,s'} \iint d^3\mathbf{r} d^3\mathbf{r}' \phi^{*}_{cks}(\mathbf{r}) \phi_{vks}(\mathbf{r}') \times U(\mathbf{r} - \mathbf{r}') \phi_{c'k's}(\mathbf{r}) \phi^{*}_{v'k's}(\mathbf{r}'). \tag{13}$$

Here, $\phi_{\alpha ks}(\mathbf{r})$ are the tight-binding states with $\alpha \in \{c, v\}$. Equation (13) shows that the spin-up and spin-down equations decouple and can be solved independently.

In a strict 2D system the electron-hole interaction is not the usual Coulomb potential, but instead modeled by the Keldysh potential [48,49],

$$U(\mathbf{r}) = -\frac{e^2}{8\varepsilon_0 r_0}\left[H_0\left(\frac{\kappa r}{r_0}\right) - Y_0\left(\frac{\kappa r}{r_0}\right)\right]. \tag{14}$$

Here, ε_0 is the vacuum permittivity, H_0 and Y_0 are Struve and Neumann functions, respectively, $r = |\mathbf{r}|$, r_0 is an in-plane screening length, and κ is the average of the relative dielectric constant of the substrate and capping material. The values of r_0 used in this paper are listed in Table I. For the strict 2D system, a straightforward calculation of the matrix elements in Eq. (13) can be done using the approach of Ref. [47]. For the nanoribbon geometry, additional considerations are needed. We want the excitonic properties in the nanoribbon geometry to converge to those of the 2D system, when the ribbon width is sufficiently large. Thus, we need to modify the approach of Ref. [47] to work for structures, which are periodic in one direction, but have non-negligible width. The details are provided in Appendix B, but the main result is that for the nanoribbon geometry the matrix elements $W^{s,s}_{cvk,c'v'k'}$ can be computed from

$$W^{s,s}_{cvk,c'v'k'} = \sum_{n,m} I^{n,s}_{ck,c'k'} I^{m,s}_{v'k',vk} U^{k,k'}_{n,m}. \tag{15}$$

Here n and m run over the atomic sites in the unit cell and $I^{n,s}_{\alpha k,\beta k'} = C^{n*}_{\alpha ks} C^{n}_{\beta k's}$ is the Bloch overlap given by the product of the tight-binding eigenvector elements belonging to site n. Finally, the integral factor $U^{k,k'}_{n,m}$ is defined as

$$U^{k,k'}_{n,m} = -\frac{e^2}{2\pi L \varepsilon_0} \int_0^{\infty} dz K_0\left(\sqrt{r_0^2 z^2 + Y_{nm}^2}|k - k'|\right) e^{-\kappa z}, \tag{16}$$

where K_0 is a modified Bessel function of the second kind and $Y_{nm} = Y_n - Y_m$ is the difference between the y coordinates of the atoms belonging to orbitals n and m. The integral in Eq. (16) is computed numerically using a suitable Gauss quadrature.

The eigenvalue problem defined in Eq. (11) can be solved by diagonalization. Due to the decoupling of spin-up and spin-down equations, the matrix to be diagonalized is block diagonal. Thus, to obtain the full solution two eigenvalue problems of dimension $N_c N_v N_k$ have to be solved. Here, N_c and N_v are the number of conduction and valence bands, respectively, and N_k is the number of k points. For a magnetic field of 100 T the 2D magnetic supercell consists of roughly 2000 atoms, hence making diagonalization of the BSE problem computationally unfeasible. On the other hand, using nanoribbons as a theoretical tool the linear optical response converges to the bulk

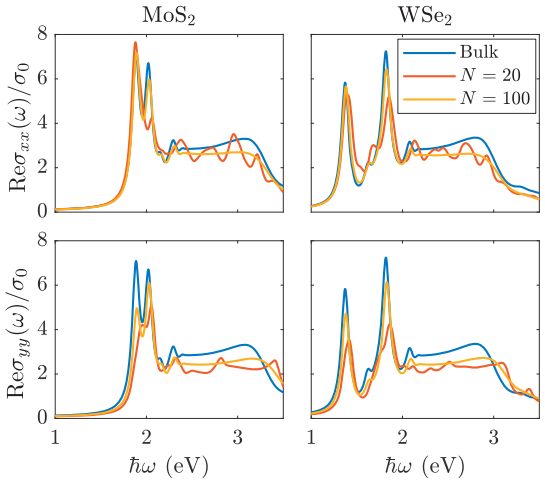

FIG. 3. Many-body diagonal conductivities versus photon energy, calculated for $B = 0$ T, $\hbar\Gamma = 50$ meV, and $\kappa = 1$. The blue lines refer to the 2D conductivities and yellow and red lines to the nanoribbon spectra.

2D response when the nanoribbon unit cell contains roughly 200 atoms. The result is that the computations are feasible, although still very demanding. However, if only the optical response and not the full eigenvalue decomposition is needed a significant reduction in computational complexity can be obtained by using the Lanczos approach in Refs. [35,47].

The Lanczos routine is based on the fact that the real part of the linear optical conductivity can be computed from the expression [47]

$$\mathrm{Re}\sigma_{\alpha\beta}(\hbar\omega) = -\frac{e^2}{m^2\omega A}\sum_s \mathrm{Im}\langle P_{\alpha s}|\hat{G}_s(\hbar\omega)|P_{\beta s}\rangle, \qquad (17)$$

with $\alpha, \beta \in \{x, y\}$, $\hat{G}_s(\hbar\omega)$ the many-body Green's function given below, and $P_{\alpha s}$ given by

$$|P_{\alpha s}\rangle := \hat{P}_\alpha|0, s\rangle = \sqrt{2}\sum_{cvk} A^s_{cvk} p^\alpha_{cvk,s}. \qquad (18)$$

Here, $|0, s\rangle$ is the many-body ground state, $\hat{P}_\alpha$ is the many-body momentum operator, and $p^\alpha_{cvk,s}$ denote the single-particle momentum matrix elements. The many-body Green's function in Eq. (17) is given by

$$\hat{G}_s(\hbar\omega) = \lim_{\hbar\Gamma\to 0^+}(\hbar\omega + i\hbar\Gamma - \hat{H}_s)^{-1}, \qquad (19)$$

where $\hat{H}_s$ is the many-body Hamiltonian. In practice, we allow a small, finite $\hbar\Gamma$ to add broadening to the spectra. The matrix elements of the Green's function in Eq. (17) are evaluated effectively as in Ref. [35], i.e., using the Lanczos-Haydock routine for tridiagonalization [50]. Computationally this is still a daunting task due to the size of the problem. For a nanoribbon with $N = 100$ and using a discretization with $N_k = 120$, the matrix that is to be tridiagonalized has dimension $(1.2 \times 10^6) \times (1.2 \times 10^6)$. We reduce the size of the problem by disregarding the top and bottom half of the conduction and valence bands, respectively, which primarily affect the high-energy part of the spectra.

In Fig. 3, we show the convergence of the nanoribbon conductivities to the 2D response in the unperturbed case ($B = 0$). The two main exciton peaks at 1.88 eV and 2.02 eV for MoS_2 and at 1.37 eV and 1.82 eV for WSe_2 are denoted by A and B, respectively. The results show a good convergence for the nanoribbon with $N = 100$. Both the A and B exciton peaks coincide with the bulk results and the peaks corresponding to the excited states also match the bulk results. The discrepancy at high photon energies is due to our disregarding some bands in the excitonic calculations. Regarding the amplitude of the peaks, we see that the amplitude is close to the bulk result for $\mathrm{Re}\sigma_{xx}$, while the $\mathrm{Re}\sigma_{yy}$ results could be improved by using wider nanoribbons. However, as our goal is to study the effect of an external magnetic field on the optical response, the convergence shown in Fig. 3 is satisfactory. Comparing to the spectra of unperturbed TMDs in Ref. [9], we see that the qualitative features agree well.

IV. RESULTS

In this section, we present the results obtained from the theoretical framework of Secs. II and III. All calculations are based on the nanoribbon geometry and are calculated for nanoribbons with $N = 100$. This corresponds to a ribbon width of 15.7 nm and 16.4 nm for MoS_2 and WSe_2, respectively. The one-dimensional Brillouin zone is discretized using 120 k points. For the spectra in this section, a broadening of $\hbar\Gamma = 50$ meV is used, which is at the high end of experimentally measured broadenings [51–53]. However, this value is needed in order to remove artifacts caused by the finite width of the system. The framework described in Sec. III is based on the assumption that the temperature is 0 K. However, as the thermal energy at room temperature ($\approx$25 meV) is smaller than the broadening, the band gap, and the exciton binding energy, we expect the spectra presented here to be good approximations at room temperature. It should be noted that the band gap tends to decrease with temperature. Consequently, the spectra should be shifted accordingly for comparison with room-temperature measurements.

The results presented in this paper are for magnetic field strengths of 10, 30, 65, and 130 T. Currently, measurements of magneto-optical properties of TMDs have been performed in fields up to 65 T and, thus, most of the results presented here are experimentally verifiable [24,27,28]. Moreover, destructive pulsed magnets can deliver fields as high as 130 T [54]. Another interesting approach is to study TMDs placed on a magnetic substrate. This has been shown to induce exchange fields in the TMD monolayer equivalent to extremely high magnetic fields [55,56].

In Fig. 4, the first row of plots shows the change of the real part of the diagonal conductivity as a function of the magnetic field strength relative to the zero-field case. To illustrate this, we have plotted the difference between the diagonal conductivity at a finite magnetic field strength and at 0 T. The plots show that the exciton peaks in MoS_2 and WSe_2 exhibit a small blueshift in response to the applied magnetic field. This small but important phenomena is what allows for experimental estimation of the spatial extent and

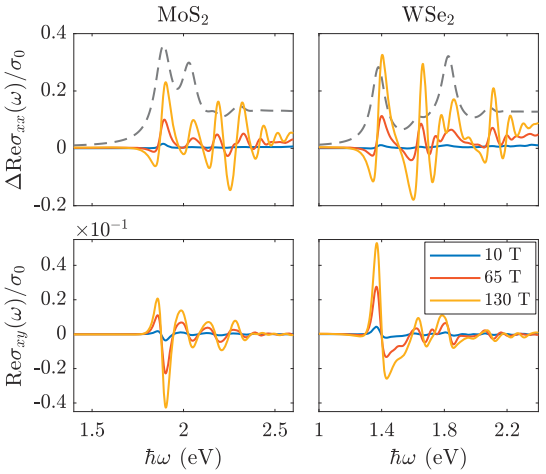

FIG. 4. Excitonic optical conductivity versus photon energy, for different magnetic field strengths. The first row illustrates $\Delta\mathrm{Re}\sigma_{xx}(\omega)$, which is the difference between the diagonal conductivity at a finite magnetic field strength and at 0 T. The dashed gray lines show the unperturbed spectra. The second row shows the Hall conductivities at different magnetic field strengths. Spectra are for nanoribbons with $N = 100$ and $\kappa = 1$. The factor 10^{-1} should be multiplied with the y axis directly underneath.

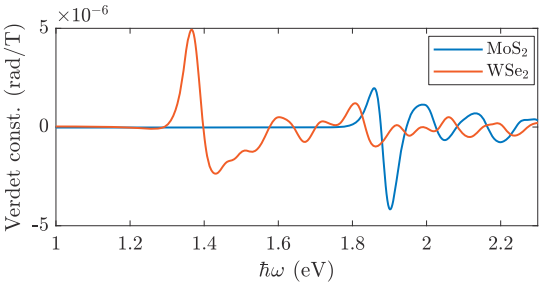

FIG. 5. Plot of the Verdet constant versus photon energy for normal incident light on a TMD monolayer in vacuum.

effective mass of excitons. We will evaluate the size of the shift and discuss this in detail below. In addition to the blueshift of the peaks, the amplitudes also increase slightly as the field strength increases. Comparing to the amplitude of the peaks in the unperturbed spectra in Fig. 3, the increase in amplitude due to the magnetic field is only a few percent for a field strength of 130 T. Thus, both effects are small changes relative to the unperturbed results. Finally, in the high-energy part of the spectra, the results show the emergence of an oscillating modulation appearing at strong magnetic fields. These oscillations correspond to transitions between Landau levels.

The second row of plots in Fig. 4 shows the Hall conductivities of MoS_2 and WSe_2. Similarly to the single-particle case, the time-reversal symmetry present in the absence of an external magnetic field ensures that the unperturbed excitonic Hall conductivities vanish identically; that is, $\sigma_{xy}(B = 0) = 0$. Consequently, they are not shown in Fig. 4. When time-reversal symmetry is broken by the external magnetic field, finite Hall conductivities are found even at small magnetic field strengths. Thus, we have $\sigma_{xy}(B > 0) \neq 0$. In other words, the Hall conductivity goes from being identically zero to having a finite magnitude when the magnetic field is turned on. Hence, the relative change of the Hall conductivities is very significant. In contrast, the relative change of the diagonal conductivity is only minor, as $\sigma_{xx}(B > 0)/\sigma_{xx}(B = 0) \approx 1$. Comparing the excitonic magneto-optical response in Fig. 4 to the IPA results in Fig. 2, we see that excitonic effects change the optical response significantly. In addition to changing the overall shape of the spectra, we also see that the excitonic Hall conductivities are approximately one order of magnitude larger than the IPA response. Hence, for an accurate description of the magneto-optical properties of monolayer TMDs, it is clearly important to account for excitons. Regarding the magnetic field dependence of the Hall conductivities in Fig. 4, we see that the amplitude scales linearly with the magnetic field strength. However, as we go to stronger fields, small changes in the shape of the spectra occur. These changes are due to the emergence of Landau levels and additional effects that are nonlinear in B, such as the diamagnetic shift.

The finite Hall conductivity, present when there is an external magnetic field, causes the system to exhibit a magneto-optical Kerr effect (MOKE) and a Faraday effect. The MOKE is a rotation of the polarization state of light when reflected off the surface of a magnetized material, while the Faraday effect is a rotation of the polarization of the transmitted light. Here, we compute the Faraday rotation angle θ for normal incidence of light on a single layer of TMD. The rotation angle for a single passage of the monolayer can be approximated by [32,57]

$$\theta = \frac{1}{(n_1 + n_2)c\varepsilon_0}\mathrm{Re}\sigma_{xy}(\omega), \tag{20}$$

where n_1 and n_2 are the refractive index of the substrate and capping material, respectively, and c is the speed of light. The expression in Eq. (20) is valid when $\sigma_{xx} \gg \sigma_{xy}$. As the Hall conductivity scales linearly with B at small field strengths, the Faraday rotation angle is often expressed as $\theta = VB$, where V is the so-called Verdet constant [31]. In Fig. 5, we have computed the Verdet constant for freestanding MoS_2 and WSe_2. As shown by the figure, the rotation for a single passage of the TMD monolayer is very small. However, this could be increased by placing the monolayer in an optical cavity in order to enhance the rotation by multiple passes [57,58].

As mentioned in Sec. III, the electron-hole interaction is screened by the substrate and capping materials. This screening is described by the κ parameter, which is simply the average of the relative dielectric constant of the substrate and capping material. In Fig. 6, the optical conductivity of WSe_2 is shown for κ values of 1, 1.55, and 4.5. These values correspond to WSe_2 placed in vacuum, on a SiO_2 substrate, or encapsulated in hBN, respectively [27,59]. It should be noted that an exchange self-energy correction to the single-particle band gap exists, and this effect is not included in our

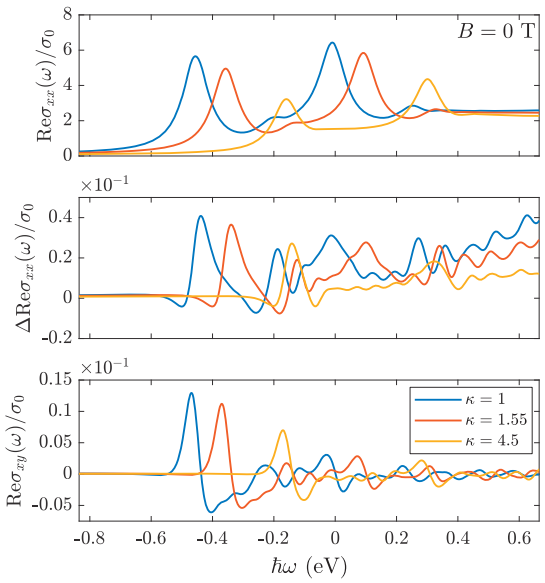

FIG. 6. Excitonic optical conductivity versus photon energy, calculated for WSe_2 in different dielectric environments. The top panel shows the diagonal conductivity in the unperturbed case. The middle panel shows the change in the diagonal conductivity from the unperturbed case to the $B = 30$ T case. The bottom panel shows the Hall conductivities calculated at $B = 30$ T. The factors of 10^{-1} should be multiplied with the y axes directly underneath.

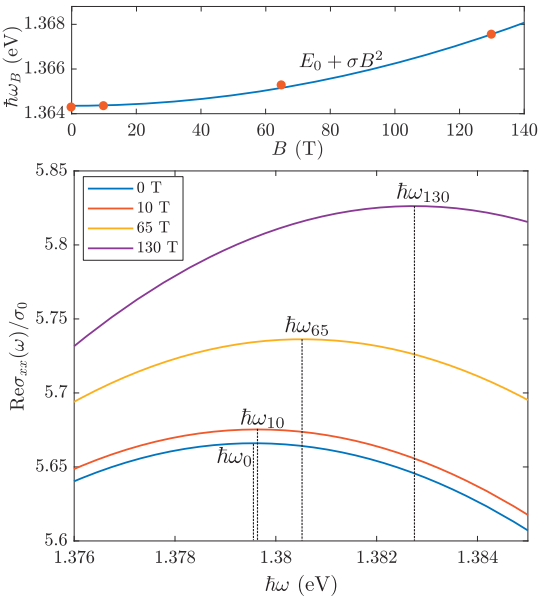

FIG. 7. Diamagnetic shift of the peak associated with the 1s state of the A exciton in WSe_2. The vertical dashed lines indicate the peak position at different magnetic field strengths. The upper panel illustrates the fit of the function $E_0 + \sigma B^2$ (blue line) to the peak positions marked by the red dots.

simple model. The self-energy correction decreases when the screening from the surroundings increases [29,34]. To account for this missing effect, the spectra in Fig. 6 are shifted by the band gap energy. This allows us to observe changes in exciton binding energy as a function of κ. The first plot is of the diagonal conductivity for $B = 0$ T, and the results show a blueshift of the exciton peaks as κ increases. This is due to a decrease in the exciton binding energy as the screening from the surroundings is increased. The binding energy decreases from 455 meV to 160 meV as κ increases from 1 to 4.5. The second row shows the change in the diagonal conductivity between the unperturbed case and the $B = 30$ T case. The plots show that the diamagnetic shift of the 2s exciton states becomes harder to observe at higher values of κ, and that the Landau levels are not affected by the dielectric environment. Finally, the last plot is of the Hall conductivities. Here, the same blueshift is observed as in the diagonal conductivity. When going to the limit $\kappa \to \infty$, we recover the IPA results, as has been checked numerically.

In the low-field limit, the magnetic field dependence of the energy of s-type excitons can be described by the relation $E_B \approx E_0 + \sigma B^2$, where E_0 is the unperturbed exciton energy and σ is the diamagnetic shift coefficient. The quadratic diamagnetic shift of the exciton peaks is illustrated in Fig. 7 for the A exciton in WSe_2. This coincides precisely with the small shift observed in the diagonal conductivities in Fig. 4. As mentioned, the value of σ is related to the spatial extent of the exciton. The relation is given by $\sigma = e^2\langle r^2\rangle/8\mu$, where $\sqrt{\langle r^2\rangle}$ is the root-mean-square (rms) radius of the exciton and μ is the reduced exciton mass. If μ is known, this relation allows for an experimental estimate of the exciton size. As the Lanczos method only provides the optical conductivity, and not the exciton energies, we compute the shift coefficient by following the exciton peak in the spectra as the field strength changes. The shift of the exciton peak is then fitted to a parabola, and the diamagnetic shift coefficient is found. Doing this for the A exciton peak of freestanding WSe_2, we find a σ value of 0.22 $\mu\mathrm{eV/T}^2$. Using the same effective masses as applied to find the TB parameters, we find an rms radius of 1.52 nm for the A exciton.

The dielectric environment is expected to affect the size of the diamagnetic shift. Increasing κ results in less tightly bound excitons, thus having a larger radius. This consequently results in larger diamagnetic shift coefficients. This effect was studied experimentally in Ref. [27]. In Table II, we summarize our findings with regard to the effect of the dielectric environment on the diamagnetic shift coefficient. We have also included values computed from the Wannier model presented in Ref. [29]. The Wannier model consistently underestimates σ, when comparing to the experimental values and the values computed using the nanoribbon approach. The explanation for this is found in the fact that the Bloch overlaps are disregarded in the Wannier model. This causes the excitons to be more strongly bound in the Wannier framework than in BSE framework and, consequently, have smaller diamagnetic shift coefficients. This shows the importance of including the

TABLE II. Calculated and experimental values of σ in units of $\mu eV/T^2$ for the 1s state of the A exciton in WSe_2. The first column gives the values calculated using the approach presented in this paper, while the second column gives the values calculated using the Wannier model from Ref. [29]. The κ values of 2.25 and 3.30 correspond to TMDs on a SiO_2 substrate capped by polybisphenol carbonate and hBN, respectively [27].

κ	σ (BSE)	σ (Wannier)	σ (Expt.)
1.00	0.22	0.13	
1.55	0.24	0.15	0.18 [27]
2.25	0.27	0.17	0.25 [27]
3.30	0.31	0.19	0.32 [27]
4.50	0.36	0.23	0.24 [26], 0.31 [24]

Bloch overlaps when modeling magnetoexcitons. Comparing the diamagnetic coefficients calculated using the nanoribbon approach to the experimental results, we observe a better agreement.

V. SUMMARY

In summary, we have used nanoribbons as a theoretical tool for the study of the magneto-optical response of monolayer TMDs. We have shown that by increasing the width of the nanoribbons the optical response will converge to that of a 2D monolayer. This has proven to be useful for including excitonic effects in the calculation of the magneto-optical response of TMDs, since a strict 2D calculation is not currently feasible. Beginning from a simple tight-binding model, we added excitonic effects in the framework provided by the Bethe-Salpeter equation. The linear optical conductivity was calculated effectively using the Lanczos-Haydock routine. We found that a 15–16 nm wide nanoribbon system is sufficient for a reasonable convergence of the optical response.

Using this approach, we are able to compute the excitonic Hall conductivity of monolayer TMDs. The calculated Hall conductivity spectra can be used to compute Faraday rotation in monolayer TMDs, an important magneto-optical effect. We also evaluated the diamagnetic shift coefficient, which provides a useful quantity for evaluating the size of excitons. So far, the experimentally determined diamagnetic shift coefficients have only been compared to theoretical results based on effective mass models. But our approach provides the option of going beyond effective mass models when analyzing experimental data. We compared the theoretical diamagnetic shift coefficient given by our calculation to values calculated using a Wannier model and to recent experimentally determined coefficients. The comparison with the values computed from the Wannier model showed the importance of including Bloch overlaps, while the comparison with experimental values showed a very good agreement between our calculations and the experimental results.

Finally, another potential use of the approach presented in this paper is as a benchmark for future strict 2D models. As it is currently not possible to compute the excitonic Hall conductivities in any 2D model, the Hall conductivity presented here can provide a reference when attempting to develop new models.

ACKNOWLEDGMENTS

J.H. and T.G.P. gratefully acknowledge financial support by the QUSCOPE Center, sponsored by the Villum Foundation. Additionally, T.G.P. is supported by the Center for Nanostructured Graphene (CNG), which is sponsored by the Danish National Research Foundation, Project No. DNRF103. N.M.R.P. acknowledges support from the European Commission through the project "Graphene-Driven Revolutions in ICT and Beyond" (Ref. No. 785219), COMPETE2020, PORTUGAL2020, FEDER, and the Portuguese Foundation for Science and Technology (FCT) through project POCI-01-0145-FEDER-028114 and in the framework of the Strategic Financing UID/FIS/04650/2013.

APPENDIX A: CONVERGENCE

In this Appendix, we examine the convergence of the electronic properties of the nanoribbon system. We need to ensure that the effect of edge states in the nanoribbon system is negligible. This is done by studying the DOS of the nanoribbons and comparing to that of the 2D system. The DOS is defined as

$$D(E) = \frac{1}{A}\sum_{\alpha,s,k}\delta(E - E_\alpha(k,s)), \tag{A1}$$

where α runs over all bands. In practice, the δ function in the DOS is approximated by a Lorentzian with 25 meV broadening.

In Fig. 8 the convergence of the nanoribbon DOS is illustrated. For nanoribbons with $N = 50$ and $N = 100$, oscillations in the DOS due to the finite width of the system are observed. In contrast, the DOS of the larger nanoribbons with $N = 200$ and $N = 300$ are almost identical to the 2D DOS except for two small small peaks around -3.3 and 3.5 eV. One of the peaks is illustrated in the inset in Fig. 8. The peaks corresponds to edge states in the nanoribbon system and, as we have checked numerically, will remain a feature of the nanoribbon DOS independently of the ribbon width. However, the photon energy needed for transitions from an edge state to a bulk state is approximately 4.3 eV (the energy difference between the valence edge states to the bottom of the conduction

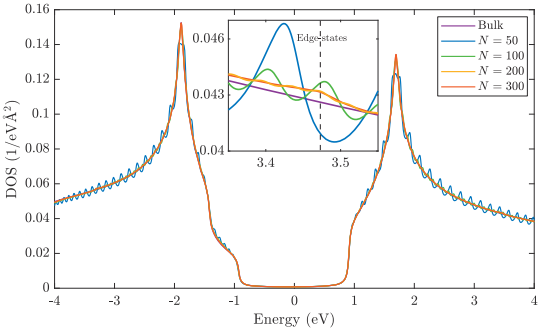

FIG. 8. DOS versus energy for WSe_2 plotted for a 2D monolayer and different nanoribbon widths. The inset shows a zoom of the DOS in the vicinity of the conduction edge states around 3.47 eV.

band). Consequently, edge states will not affect the optical response in the photon range considered in the present work.

APPENDIX B: ELECTRON-HOLE INTERACTION MATRIX ELEMENTS FOR NANORIBBONS

In this Appendix, we will find an expression for the matrix elements in Eq. (13) for the nanoribbon geometry. We begin by considering the product of two tight-binding states, such as the ones in Eq. (13). Exploiting the fact that the atomic orbitals are localized and orthogonal, we can write

$$\phi^*_{\alpha k s}(\mathbf{r})\phi_{\beta k' s}(\mathbf{r}) \approx \frac{1}{N_{uc}} \sum_{n,X} I^{n,s}_{\alpha k,\beta k} e^{i(k'-k)X} \varphi_n^2(\mathbf{r} - X\hat{x}), \quad \text{(B1)}$$

where N_{uc} is the number of unit cells, X is the location of the unit cell in the periodic direction, $I^{n,s}_{\alpha k,\beta k} = C^{n*}_{\alpha k s} C^{n}_{\beta k' s}$ are the products of the tight-binding eigenvector elements belonging to the nth atomic orbital, and φ_n are the atomic orbitals. The X sum runs over the location of the unit cells in the periodic direction. To evaluate the matrix elements, we need integrals of the form

$$U_{n,m}(X, X') = \iint \varphi_n^2(\mathbf{r} - X\hat{x}) U(\mathbf{r} - \mathbf{r}') \varphi_m^2(\mathbf{r}' - X'\hat{x}) d^3\mathbf{r} d^3\mathbf{r}'. \quad \text{(B2)}$$

For strongly localized atomic orbitals, we can assume the effective interaction

$$\begin{aligned} U_{n,m}(X, X') &\approx U^{\text{eff}}_{n,m}(X - X') \\ &\equiv -\frac{e^2}{8\varepsilon_0 r_0}\left[H_0\left(\frac{\kappa\sqrt{(X-X')^2 + Y^2_{nm}}}{r_0}\right) \right. \\ &\quad \left. - Y_0\left(\frac{\kappa\sqrt{(X-X')^2 + Y^2_{nm}}}{r_0}\right)\right]. \end{aligned} \quad \text{(B3)}$$

Here, Y_{nm} denotes the difference in y coordinates of the atomic site belonging to orbitals n and m. This effective interaction is validated by its ability to recover the 2D results, as shown in the paper. In the following, it is advantageous to rewrite $U^{\text{eff}}_{n,m}(X - X')$ using an integral form of the Keldysh potential [60]. This gives

$$U^{\text{eff}}_{n,m}(X - X') = -\frac{e^2}{4\pi\varepsilon_0} \int_0^\infty \frac{1}{\sqrt{(r_0 z)^2 + (X - X')^2 + Y^2_{nm}}} e^{-z\kappa} dz. \quad \text{(B4)}$$

The interaction matrix elements in Eq. (13) can then be approximated by

$$W^{s,s'}_{cvk,c'v'k'} \approx \delta_{s,s'} \sum_{n,m} I^{n,s}_{ck,c'k'} I^{m,s}_{v'k',vk} \frac{1}{L} \int e^{i(k'-k)X} U^{\text{eff}}_{n,m}(X) dX, \quad \text{(B5)}$$

where we have converted the sum over X to an integral and L denotes the length of the system. Finally, we have to do the X integration, which corresponds to taking the Fourier transform of the effective interaction. This gives

$$\begin{aligned} &\frac{1}{L} \int e^{i(k'-k)X} U^{\text{eff}}_{n,m}(X) dX \\ &\quad = -\frac{e^2}{2\pi L\varepsilon_0} \int_0^\infty dz K_0\left(\sqrt{r_0^2 z^2 + Y^2_{nm}}|k - k'|\right) e^{-\kappa z}, \end{aligned} \quad \text{(B6)}$$

where K_0 denotes a modified Bessel function of the second kind. The remaining integral over z can be evaluated numerically. Inserting Eq. (B6) into Eq. (B5), we obtain an expression for the interaction matrix elements in the nanoribbon geometry.

[1] K. F. Mak, C. Lee, J. Hone, J. Shan, and T. F. Heinz, Phys. Rev. Lett. **105**, 136805 (2010).

[2] A. Splendiani, L. Sun, Y. Zhang, T. Li, J. Kim, C.-Y. Chim, G. Galli, and F. Wang, Nano Lett. **10**, 1271 (2010).

[3] Y. Zhang, T.-R. Chang, B. Zhou, Y.-T. Cui, H. Yan, Z. Liu, F. Schmitt, J. Lee, R. Moore, Y. Chen *et al.*, Nat. Nanotechnol. **9**, 111 (2014).

[4] D. Xiao, G.-B. Liu, W. Feng, X. Xu, and W. Yao, Phys. Rev. Lett. **108**, 196802 (2012).

[5] X. Xu, W. Yao, D. Xiao, and T. F. Heinz, Nat. Phys. **10**, 343 (2014).

[6] G.-B. Liu, W.-Y. Shan, Y. Yao, W. Yao, and D. Xiao, Phys. Rev. B **88**, 085433 (2013).

[7] T. C. Berkelbach, M. S. Hybertsen, and D. R. Reichman, Phys. Rev. B **88**, 045318 (2013).

[8] M. M. Ugeda, A. J. Bradley, S.-F. Shi, H. Felipe, Y. Zhang, D. Y. Qiu, W. Ruan, S.-K. Mo, Z. Hussain, Z.-X. Shen *et al.*, Nat. Mater. **13**, 1091 (2014).

[9] A. Chaves, R. Ribeiro, T. Frederico, and N. Peres, 2D Mater. **4**, 025086 (2017).

[10] M. Van der Donck, M. Zarenia, and F. M. Peeters, Phys. Rev. B **97**, 195408 (2018).

[11] Z. Wang, J. Shan, and K. F. Mak, Nat. Nanotechnol. **12**, 144 (2017).

[12] F. Rose, M. O. Goerbig, and F. Piéchon, Phys. Rev. B **88**, 125438 (2013).

[13] R.-L. Chu, X. Li, S. Wu, Q. Niu, W. Yao, X. Xu, and C. Zhang, Phys. Rev. B **90**, 045427 (2014).

[14] Y. Li, J. Ludwig, T. Low, A. Chernikov, X. Cui, G. Arefe, Y. D. Kim, A. M. van der Zande, A. Rigosi, H. M. Hill *et al.*, Phys. Rev. Lett. **113**, 266804 (2014).

[15] D. MacNeill, C. Heikes, K. F. Mak, Z. Anderson, A. Kormányos, V. Zólyomi, J. Park, and D. C. Ralph, Phys. Rev. Lett. **114**, 037401 (2015).

[16] A. Srivastava, M. Sidler, A. V. Allain, D. S. Lembke, A. Kis, and A. Imamoğlu, Nat. Phys. **11**, 141 (2015).

[17] G. Wang, L. Bouet, M. Glazov, T. Amand, E. Ivchenko, E. Palleau, X. Marie, and B. Urbaszek, 2D Mater. **2**, 034002 (2015).

[18] G. Aivazian, Z. Gong, A. M. Jones, R.-L. Chu, J. Yan, D. G. Mandrus, C. Zhang, D. Cobden, W. Yao, and X. Xu, Nat. Phys. **11**, 148 (2015).

[19] R. Schmidt, A. Arora, G. Plechinger, P. Nagler, A. Granados del Águila, M. V. Ballottin, P. C. Christianen, S. Michaelis de

Vasconcellos, C. Schüller, T. Korn, and R. Bratschitsch, Phys. Rev. Lett. **117**, 077402 (2016).
[20] G. Wang, X. Marie, B. L. Liu, T. Amand, C. Robert, F. Cadiz, P. Renucci, and B. Urbaszek, Phys. Rev. Lett. **117**, 187401 (2016).
[21] Z. Sun, A. Martinez, and F. Wang, Nat. Photon. **10**, 227 (2016).
[22] C. Mai, A. Barrette, Y. Yu, Y. G. Semenov, K. W. Kim, L. Cao, and K. Gundogdu, Nano Lett. **14**, 202 (2013).
[23] J. R. Schaibley, H. Yu, G. Clark, P. Rivera, J. S. Ross, K. L. Seyler, W. Yao, and X. Xu, Nat. Rev. Mater. **1**, 16055 (2016).
[24] A. V. Stier, N. P. Wilson, K. A. Velizhanin, J. Kono, X. Xu, and S. A. Crooker, Phys. Rev. Lett. **120**, 057405 (2018).
[25] J. Zipfel, J. Holler, A. A. Mitioglu, M. V. Ballottin, P. Nagler, A. V. Stier, T. Taniguchi, K. Watanabe, S. A. Crooker, P. C. M. Christianen, T. Korn, and A. Chernikov, Phys. Rev. B **98**, 075438 (2018).
[26] E. Liu, J. van Baren, T. Taniguchi, K. Watanabe, Y.-C. Chang, and C. H. Lui, Phys. Rev. B **99**, 205420 (2019).
[27] A. V. Stier, N. P. Wilson, G. Clark, X. Xu, and S. A. Crooker, Nano Lett. **16**, 7054 (2016).
[28] A. V. Stier, K. M. McCreary, B. T. Jonker, J. Kono, and S. A. Crooker, Nat. Commun. **7**, 10643 (2016).
[29] J. Have, G. Catarina, T. G. Pedersen, and N. M. R. Peres, Phys. Rev. B **99**, 035416 (2019).
[30] T. G. Pedersen, Phys. Rev. B **94**, 125424 (2016).
[31] T. G. Pedersen, Phys. Rev. B **68**, 245104 (2003).
[32] T. Morimoto, Y. Hatsugai, and H. Aoki, Phys. Rev. Lett. **103**, 116803 (2009).
[33] J. G. Pedersen and T. G. Pedersen, Phys. Rev. B **84**, 115424 (2011).
[34] G. Catarina, J. Have, J. Fernández-Rossier, and N. M. R. Peres, Phys. Rev. B **99**, 125405 (2019).
[35] J. Have and T. G. Pedersen, Phys. Rev. B **97**, 115405 (2018).
[36] Z. Y. Zhu, Y. C. Cheng, and U. Schwingenschlögl, Phys. Rev. B **84**, 153402 (2011).
[37] T. Cheiwchanchamnangij and W. R. L. Lambrecht, Phys. Rev. B **85**, 205302 (2012).
[38] A. Kormányos, G. Burkard, M. Gmitra, J. Fabian, V. Zólyomi, N. D. Drummond, and V. Fal'ko, 2D Mater. **2**, 022001 (2015).
[39] D. Kochan, S. Irmer, and J. Fabian, Phys. Rev. B **95**, 165415 (2017).
[40] A. Taghizadeh and T. Pedersen, arXiv:1812.02596.
[41] T. G. Pedersen, Phys. Rev. B **98**, 165425 (2018).
[42] F. A. Rasmussen and K. S. Thygesen, J. Phys. Chem. C **119**, 13169 (2015).
[43] W. Kohn, Phys. Rev. **115**, 1460 (1959).
[44] J. G. Pedersen and T. G. Pedersen, Phys. Rev. B **87**, 235404 (2013).
[45] H. Rostami, R. Asgari, and F. Guinea, J. Phys.: Condens. Matter **28**, 495001 (2016).
[46] K. He, N. Kumar, L. Zhao, Z. Wang, K. F. Mak, H. Zhao, and J. Shan, Phys. Rev. Lett. **113**, 026803 (2014).
[47] M. L. Trolle, G. Seifert, and T. G. Pedersen, Phys. Rev. B **89**, 235410 (2014).
[48] L. V. Keldysh, Sov. Phys. JETP **29**, 658 (1979).
[49] M. L. Trolle, T. G. Pedersen, and V. Véniard, Sci. Rep. **7**, 39844 (2017).
[50] R. Haydock, Comput. Phys. Commun. **20**, 11 (1980).
[51] O. A. Ajayi, J. V. Ardelean, G. D. Shepard, J. Wang, A. Antony, T. Taniguchi, K. Watanabe, T. F. Heinz, S. Strauf, X. Zhu *et al.*, 2D Mater. **4**, 031011 (2017).
[52] G. Moody, C. K. Dass, K. Hao, C.-H. Chen, L.-J. Li, A. Singh, K. Tran, G. Clark, X. Xu, G. Berghäuser *et al.*, Nat. Commun. **6**, 8315 (2015).
[53] F. Cadiz, E. Courtade, C. Robert, G. Wang, Y. Shen, H. Cai, T. Taniguchi, K. Watanabe, H. Carrere, D. Lagarde *et al.*, Phys. Rev. X **7**, 021026 (2017).
[54] D. Nakamura, T. Sasaki, W. Zhou, H. Liu, H. Kataura, and S. Takeyama, Phys. Rev. B **91**, 235427 (2015).
[55] J. Qi, X. Li, Q. Niu, and J. Feng, Phys. Rev. B **92**, 121403(R) (2015).
[56] B. Scharf, G. Xu, A. Matos-Abiague, and I. Žutić, Phys. Rev. Lett. **119**, 127403 (2017).
[57] A. Ferreira, J. Viana-Gomes, Y. V. Bludov, V. Pereira, N. M. R. Peres, and A. H. Castro Neto, Phys. Rev. B **84**, 235410 (2011).
[58] H. Da, L. Gao, Y. An, H. Zhang, and X. Yan, Adv. Opt. Mater. **6**, 1701175 (2018).
[59] R. Geick, C. H. Perry, and G. Rupprecht, Phys. Rev. **146**, 543 (1966).
[60] P. Cudazzo, I. V. Tokatly, and A. Rubio, Phys. Rev. B **84**, 085406 (2011).

ISSN (online): 2446-1636
ISBN (online): 978-87-7210-480-5

AALBORG UNIVERSITY PRESS